# SYNTHESIS AND SELF-ASSEMBLY OF CARBOHYDRATE NAPHTHALIMIDE SCAFFOLDS FOR ELECTRONIC APPLICATIONS

**A THESIS SUBMITTED TO**

**NATIONAL INSTITUTE OF TECHNOLOGY WARANGAL**

**DOCTOR OF PHILOSOPHY**

**IN**

**CHEMISTRY**

**BY**

**RACHAMALLA ARUN KUMAR**

**(Roll No. 719117)**

**Under the supervision of**

**Prof. S. NAGARAJAN**

**&**

**Co-supervision of**

**Prof. JUGUN PRAKASH CHINTA**


**DEPARTMENT OF CHEMISTRY**

**NATIONAL INSTITUTE OF TECHNOLOGY WARANGAL**

**HANUMAKONDA-506004**

**TELANGANA, INDIA.**

**(JULY-2024)**

*Dedicated*
*To*
*My Beloved Family*
*&*
*My Supervisor*

Dr. S. NAGARAJAN ‖ डॉ. एस. नागराजन
Associate Professor ‖ सह - प्राध्यापक
Department of Chemistry ‖ रसायनिकी विभाग
e-mail: snagarajan@nitw.ac.in
Phone: 08702462660 (office) ‖ 9940430715 (mobile)

राष्ट्रीय प्रौद्योगिकी संस्थान वारंगल
National Institute of Technology Warangal
An Institute of National Importance
Hanumakonda – 506 004, Telangana State, India

# CERTIFICATE

This is to certify that the research work presented in this thesis entitled **"Synthesis and self-assembly of carbohydrate naphthalimide scaffolds for electronic applications,"** submitted by **Mr. Rachamalla Arun Kumar** for the degree of Doctor of Philosophy in Chemistry, National Institute of Technology Warangal (Telangana), under my supervision and that the same has not been submitted elsewhere for a degree.

Date: 25.07.2024
Place: NIT Warangal

**Dr. S. Nagarajan**
**Thesis Supervisor**

**Dr. Ch. Jugun Prakash**
Assistant Professor
Department of Chemistry
National Institute of Technology Warangal
Hanamkonda - 506 004
Telangana, India

Mobile: +91-9898625503
Email: jugun@nitw.ac.in

# CERTIFICATE

This is to certify that the research work presented in this thesis entitled **"Synthesis and self-assembly of carbohydrate naphthalimide scaffolds for electronic applications,"** submitted by **Mr. Rachamalla Arun Kumar** for the degree of Doctor of Philosophy in Chemistry, National Institute of Technology Warangal (Telangana), under my supervision and that the same has not been submitted elsewhere for a degree.

Date: 25.07.2024
Place: NIT Warangal

**Dr. Ch. Jugun Prakash**
**Thesis Co-Supervisor**

# ACKNOWLEDGEMENTS

The work presented in this thesis would not have been possible without my close association with many people. I take this opportunity to express my heartfelt thanks and deep gratitude to all the people mentioned here and others, whose names might have been omitted unintentionally.

It gives me immense pleasure and delight to express my deep sense of gratitude to my research supervisor, ***Dr. S. Nagarajan*****,** Associate Professor, Department of Chemistry, National Institute of Technology Warangal, for his inspiring and valuable guidance. His unfailing attention, unmitigated encouragement, and cooperation have helped me attain my goal. It would have been impossible to achieve this goal without his support and valuable advice. I am very fortunate to have worked under his mentorship, which significantly accelerated my career. I will hold his mentorship and support in the highest regard throughout my lifetime. He kept his words of saying that I am like your elder brother on the starting day of my Ph.D., and he supported me in all the ways possible.

I extend my heartfelt thanks to my research co-supervisor, ***Dr. Jugun Prakash Chinta***, Assistant Professor, Department of Chemistry, National Institute of Technology Warangal, for his continuous and unconditional support.

I am greatly indebted to ***Prof. Bidyadhar Subudhi*** (current) and ***Prof. N.V. Ramana Rao*** (former), Directors of the National Institute of Technology Warangal, for allowing me to carry out and submit my research work as a thesis. I gratefully acknowledge the financial assistance from the Government of India, Ministry of Education (MoE), in the form of an institute fellowship.

I am deeply grateful to ***Prof. Santosh Penta,*** Head of the Department of Chemistry, and ***Prof. D. Kashinath, Prof. Vishnu Shanker,*** *and* ***Prof. P. V. Srilakshmi,*** former Heads of the Department of Chemistry, National Institute of Technology Warangal for their valuable advice, help and support.

I am immensely grateful to the Doctoral Scrutiny Committee (DSC) members, ***Prof. V. Rajeswar Rao*** (former member), ***Dr. Raghu Chitta****,* ***Dr. K. Hari Prasad****,* Department of Chemistry, and ***Dr. Asim Bikas Das,*** Department of Biotechnology, for their support and valuable suggestions.

I owe a great debt of gratitude to ***Dr. R. Rakesh Kumar, Dr. Supraja Pottu***, ***Mr. M. Navaneeth***, Energy Materials and Devices Lab, Department of Physics, National Institute of Technology Warangal, for electrical characteristics and applications of triboelectric nanogenerator.

I am deeply grateful to ***Dr. Ravinder Pawar, Mr. Faizan,*** Department of Chemistry, for their DFT studies. My special thanks to ***Dr. K. Hari Prasad,*** Associate Professor, faculty in charge (Bruker-400 MHz NMR instrument), for rendering uninterrupted services to run the instrument.

I take this opportunity to express thanks to faculty members of the department, ***Prof. A. Ramachandraiah (Retd)***, ***Prof. K. Laxma Reddy (Retd)***, ***Prof. K. V. Gobi***, ***Prof. Venkatathri Narayanan***, ***Dr. B. Srinivas***, ***Dr. M. Raghasudha, Dr. Mukul Pradhan, Dr. G. Rajesh Khanna*** and ***Dr. V. Rajesh Kumar*** for their suggestions and encouragement.

I am very much delighted to work with my colleagues ***Ms. Tohira Banoo, Mr. Vara Prasad, Mr. Yogendra Kumar, Mr. J. Barathkumar, Mrs. Tanuja Das, and Mr. Venkateshwar Rao,*** I am very much thankful for their **s**upport and encouragement during my Ph.D. and this thesis would not have come to a successful completion without the help of these lab mates. I also thank project M.Sc. students, ***Mr. Atul, Mr. Devender, Ms. Arzu, Mr. Ramji, Ms. Saloni, Ms. Deepshika, and Ms. Rosalini*** for their help in my bench work.

I would like to especially thank ***Ms. Tohira Banoo*** for her continuous assistance and unconditional support during this thesis tenure.

Ph.D. journey gave me a lot of good friends, including ***Ms. Tohira Banoo, Ms. Akanksha Ashok Sangolkar***, ***Dr. Sanjeeva Thunga, Dr. Raju Chedupaka***, and ***Dr. Ambedkar Gandamalla,*** who were there beside me in all the ways possible in my Ph.D. tenure.

I am incredibly thankful to my seniors cum friends, ***Dr. Bhargava***, ***Dr. Siva Parvati***, ***Dr. Dhanunjay***, and ***Dr. Naveen*** for their support and for keeping me comfortable, especially during the early stages of my Ph.D.

I thank ***Dr. Parameshwara Chary*** and ***Dr. Shankara Chary*** for their invaluable guidance and support during my admission to Ph.D. at NITW.

Many colleagues have supported me and kept me sane throughout these trying years. I'm grateful for the jovial help from all of my research colleagues, whom I appreciate with great pleasure, ***Dr. K. Vimal Kumar, Dr. Suman, Dr. P. Sowmya, Dr. N. Satyanarayana, Dr. P. Babji, Dr. B. Prashanth, Dr. G. Sripal Reddy, G. Srinath, K. Sampath, T. Shirisha, Dr. P Venkatesham, R. Vara prasad, B. Anjaiah, Ch. Vijay, N. Nagaraju, Neetika, I. Madhu, Khushboo Agarwala, J. Swathi, K. Rambabu, Anshu Kari***, ***B. Srikanth Goud, B. Gayathri, Gargi, Subir, Sasi Sree, Pooja, Avinash Sharma, Akash, B. Apurba, Faizan, Arokiaraj, K. Ramakrishna, N. Sumit, B.***

***Thirupathi, Anindya Roy, Yogendra Kumar, P. Amala***, ***Amulya, D. Ravinder, C. Shruthilaya,*** and research scholars of various departments.

My special thanks to the non-teaching and technical supporting staff of the chemistry department ***G. Santhosh, K. Sreenivas, P. Heerulal, Md. Shaheen begum, T. Kiran Kumar, J. Praveen, A. Rajini, K. Keshavulu, B. Sadanandam, Ch. Ramesh Babu (late), P. S. Sunil Kumar, P. Abhivardhan, Shirshendu Mondal,*** and ***Atanu Sahoo*** for their help whenever needed.

I would like to convey my sincere gratitude to all my teachers who helped to build my career from an early age, special thanks to ***Dr. Vasantha, Dr. Annapuna, R. S. Butti, Dr. Prashanthi Dr. Roopa, Dr. Kalyani, Dr. M. Jyothi, and Dr. D. Ramesh.***

I am grateful to have best friends like ***Dr. Hitesh Kumar Reddy Medipally, Divya Jyothi***, and ***Sreeram***, they are and will always be there in bad and good times. Their support and encouragement towards my goals are invaluable.

I express my gratitude to ***Mr. Ravinder Reddy Danda*** and ***Dr. Rajesh Biogenesis*** for their tremendous teaching during my preparation for Ph.D. entrance exams.

It would be an understatement to say that I would not be the person I am today without my family. I am extremely grateful to my beloved father, ***Sri. Rachamalla Venkateswarlu*** for his moral support and inspiration to never give up, and to my beloved mother, ***Smt. Rachamalla Padma (late),*** who always dreamed of me reaching greater heights, I always miss her. I thank My Anna and Vadina: ***Rachamalla Anil*** and ***Purnima*** for considering my well-being. I am grateful to my Babai and Chinamma, ***R. Sikender*** and ***Shobha Rani,*** for their everlasting motivational support. I thank my stress busters, Sammi, Avvi, Jaswi, and Liswi, with whom I always find happiness. I am very happy to thank all my family members: ***R. Chandraiah, Bhagyalaxmi, Sunny, Bindu, Alivelu, Vijayalaxmi, Venkatesh, Prabhavathi (bhooju), Potti, N.Venkataiah, and N.Ravi*** for their inspiration, love and affection whose blessings made the journey worth effort. I owe everything to my family.

**(Rachamalla Arun Kumar)**

# ABSTRACT

A series of carbohydrate naphthalimide derivatives were synthesized in good yields using environmentally benign protocols. Self-assembly studies revealed that most of the synthesized compounds were able to form a gel in a diverse range of solvents and oils. Self-assembled carbohydrate naphthalimides were employed to develop flexible semiconductors and triboelectric nanogenerators (TENG). The fabricated TENG was used to construct self-powered electronics, humidity sensors, and the electrochemical system. It is worth mentioning that one of the fabricated TENG using self-assembled carbohydrate naphthalimide derivatives rendered a power density of 18.96 W/m$^2$. A small tuning of the molecular structure of assembled materials could bring big implications in electronics.

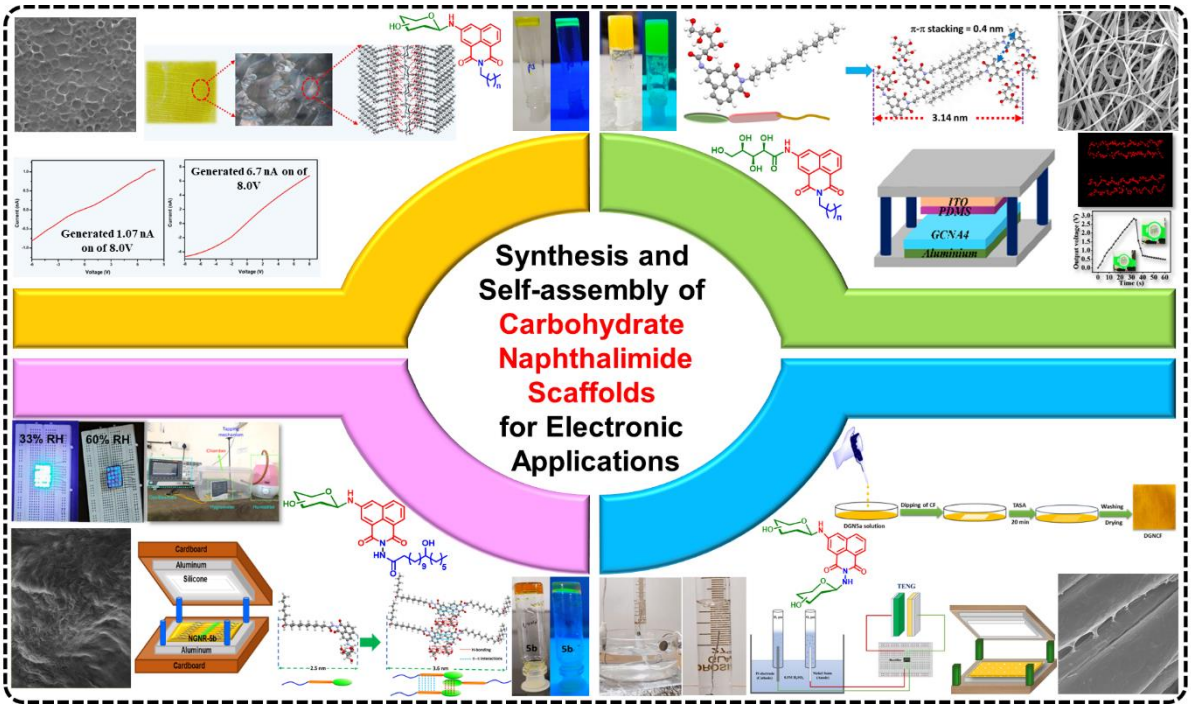

## Table of Contents

# LIST OF FIGURES

## Chapter I



## Chapter II

v/v), cyclohexane and xylene respectively. (c) A comparison of FT-IR spectra of compound **NGN5d** in (i) amorphous state and (ii) xerogel state (assembled state).

**Figure 2.5**. (a) NMR spectra of compound **NGN5d** in (i) DMSO-$d_6$, (ii) $D_2O$ 60% v/v (after shaking for 5 minutes), (iii and iv) gel form (after heating and cooling) at room temperature and 70 °C respectively. (b) XRD pattern of a xerogel obtained from compound **NGN5d**. (c) A schematic representation of molecular self-assembly of **NGN5d**. The dotted red line represents the H-bonding.

**Figure 2.6**. (a,b) UV-vis and Fluorescence titration of **NGN5d** dissolved in $CHCl_3$ respectively [$\lambda_{ex}$ = 250 nm].

**Figure 2.7**. SEM images of gel formed by (a-d) **NGN5d** in $CHCl_3$, (e-h) NGN5d in DMSO-$H_2O$ (40 % v/v) and (i-l) **NGN6d** in $CHCl_3$.

**Figure 2.8**. (a-d) Strain amplitude and angular frequency dependence of G′ and G″ of gel formed by compound **NGN5d** in $CHCl_3$ (a,b) and DMSO-$H_2O$ (c,d) respectively. (e-h) Thermal processability and thixotropic behaviour investigation using continuous temperature and strain ramp-up and ramp-down measurements of gel formed by compound **NGN5d** in $CHCl_3$ (e,f) and DMSO-$H_2O$ (g,h) respectively.

**Figure 2.9**. (a,b) Pictorial representation of (a) assembled semiconducting thin film formation of compound **NGN5d** by drop casting method, morphology, and I–V characteristics (b) formation of flexible semiconducting fabric by **NGN5d**, morphology, and I–V characteristics. (c,d) optical microscopic images of cotton fabric and (e) a Cyclic voltammogram of gelator **NGN5d** recorded in scanning rate from 100 to 800 mV/s at 298 K.

## Chapter III

**Figure 3.1**. Images of gel formed by compounds **GCNA3-7** in DMSO-$H_2O$ (40% v/v), (a) under normal light and b) UV light (CGC = 1% wt/v). (c) Concentration dependent gel to sol transition temperature ($T_g$) measurements of compounds **GCNA1-7**. (d) SEM images of xerogel formed by **GCNA4** in DMSO-$H_2O$ (40 % v/v)

**Figure 3.2**. (a) VT-NMR spectra of **GCNA4** in i) DMSO-$d_6$ at 25 °C, ii-v) DMSO-$d_6$ -$D_2O$ (40% v/v) at 80 °C, 85 °C, 90 °C, and 95 °C respectively (inset an opaque solid like gel in NMR tube). (b) A comparison of FT-IR spectra of compound **GCNA4** in the amorphous state (red) and xerogel state (black).

**Figure 3.3**. (a) XRD pattern of **GCNA4** xerogel (inset zoom in selected area). (b) UV-vis and (c) fluorescence titration of **GCNA4** dissolved in gelling solvent DMSO-$H_2O$ [$\lambda_{ex}$ = 250 nm].

(d) A schematic representation of bottom-up assembly of **GCNA4** to generate *J* type aggregated fibrillar network.

**Figure 3.4.** (a-b) Strain amplitude and Angular frequency dependence of G′ and G″. (c) thixotropic behaviour investigation using continuous strain ramp-up and ramp-down measurements of gel formed by compound **GCNA4** in DMSO-$H_2O$ (40% v/v).

**Figure 3.5**. (a) Fabrication steps of TENG and photograph of the actual fabricated TENG device. (b-c) Output voltage and current of GCNA4-TENG with different triboelectric layers. (d-e) Switching polarity test responses of **GCNA4**-TENG with PDMS. (f) Output current and the voltage across the different load resistances. (g) Instantaneous power density as a function of load resistance.

**Figure 3.6.** (a) open circuit voltage, and (b) short circuit current of amorphous **GCNA**-PDMS based TENG. (c) power density as a function of load resistance

**Figure 3.7**. (a) Working mechanism of GCNA4-PDMS TENG, (b) image of TENG powering-up 240 red LEDs (c-f) Powering-up small electric devices i. e. wristwatch, thermometer, and calculator with 4.7 μF capacitor and hygrometer with 47 μF capacitor, (g) Stability of the TENG over 2500 cycles (inset magnified view of a few cycles).

## Chapter IV

**Figure 4.1**. (a) Synthesis of *N*-glycosyl-3-amino-*N*-(ricinoleic acid hydrazide)-1,8-naphthalimides (NGNRs). (b) Pictorial representation of optimized flow reactor.

**Figure 4.2.** (a) The response of the product with respect to the temperature at flow rate of 100 μL/min. (b) Gel to sol transition temperature ($T_g$) measurements of **NGNR5a-7a** and **NGNR5b-7b** in different xylenes. (c) Concentration-dependent gel to sol transition temperature ($T_g$) measurements of **NGNR5a-7a** and **NGNR5b-7b** in *m*-xylene.

**Figure 4.3**. (a) Images of the gel formed by **NGNR5b-7b** in m-xylene under normal and UV light (CGC = 1% wt/v). (b) A comparison of FT-IR spectra of **NGNR5b** in xerogel state (red), and amorphous state (black). (c) The XRD pattern of a xerogel was obtained from **NGNR5b**. (d) UV-vis, and (e) fluorescence titration of **NGNR5b** dissolved in gelling solvent xylene [$\lambda_{ex}$ = 289 nm]. (f) A schematic representation of the bottom-up assembly of **NGNR5b** to generate *J*-type aggregated intertwined lamellar sheet structure

**Figure 4.4**. SEM images of the xerogel formed by **NGNR5b** (a–c) and **6b** (d-f) in *m*-xylene. (g) strain amplitude, and (h) angular frequency dependency of G' and G'' of the gel formed by

**NGNR5b** in *m*-xylene. (i) Thixotropic behavior investigation using continuous strain ramp-up and ramp-down measurements of the gel formed by **NGNR5b** in *m*-xylene.

**Figure 4.5**. Fabrication of vertical contact separation mode TENG. (a) NGNR-5b film coated on aluminium substrate and attached to a Cardboard. (b) Silicone attached aluminium sheet is attached to Cardboard. (c) final vertical contact separation mode TENG device. (d) Image of the TENG device after stability test.

**Figure 4.6**. (a) Schematic of the TENG device, (b) TENG response with different frictional layers; switching polarity results of (c) Voc, (d) Isc, (e) load resistance versus output voltage and current, (f) the instantaneous power density as a function of load resistance, (g) stability of TENG electrical response for 600 cycles of hand tapping, (h) photograph of the digital calculator continuously powered with TENG.

**Figure 4.7**. (a) Photograph of the humidity sensing set up, (b)-(c) TENG output voltage under different humidity conditions, (d) Photograph of the LEDs powered by TENG under two different humidity levels, (e) Response plot of TENG with humidity variation, (f) humidity sensing mechanism.

## Chapter V

**Figure 5.1**. Schematic representation of fabrication of DGNCF

**Figure 5.2**. (a). The XRD pattern of **CF**, **DGN5a**, **DGNCF**. (b) UV–vis, and (c) fluorescence spectra of **CF**, **DGN5a**, and **DGNCF** [$\lambda_{ex}$ = 420 nm].

**Figure 5.3**. SEM images of the (a) CF, and (b) DGNCF at different magnifications. (c) A schematic representation of TASA of **DGN5a** on **CF** to generate **DGNCF**

**Figure 5.4.** (a) Schematic representation of the fabricated TENG device. (b) TENG response of **DGNCF** with different frictional layers. (c) Area-dependent TENG response. (d-f) switching polarity results of (d) Voc, (e) Isc, (f) load resistance versus output voltage and current. (g) the instantaneous power density as a function of load resistance. (h,i) stability of TENG electrical response for 600 cycles of hand tapping.

**Figure 5.5**. (a) Schematic representation of the self-powered electrochemical workstation for the Hydrogen evolution reaction utilizing the fabricated TENG. (b) Production of $H_2$ gas with respect to time.

# LIST OF TABLES

# ABBREVIATIONS

| | | |
|---|---|---|
| *N*-Glycosyl naphthalimides | : | NGN |
| *N*-Glycosyl naphthalimide ricinoleate | : | NGNR |
| Diglycosyl naphthalimides | : | DGN |
| Gluconamide conjugated naphthalimide amphiphiles | : | GCNA |
| Diglycosyl naphthalimide cotton fabric | : | DGNCF |
| Cotton Fabric | : | CF |
| Internet of Things | : | IoTs |
| Triboelectric nanogenerator | : | TENG |
| Generally Recognized as Safe | : | GRAS |
| Food and Drug Administration | : | FDA |
| World Health Organization | : | WHO |
| Food and Agriculture Organization | : | FAO |
| Dimethyl sulfoxide | : | DMSO |
| Deuterated dimethyl sulfoxide | : | DMSO-$d_6$ |
| Ethyl acetate | : | EtOAc |
| Ethanol | : | EtOH |
| Methanol | : | MeOH |
| Chloroform | : | $CHCl_3$ |
| Iron(III)chloride | : | $FeCl_3$ |
| Water | : | $H_2O$ |
| Critical gelation concentration | : | CGC |
| Sol-to-gel transition temperature | : | $T_g$ |
| Hydrophilic Lipophilic Balance | : | HLB |
| Deoxyribonucleic acid | : | DNA |
| Ribonucleic acid | : | RNA |
| Attenuated Total Reflectance Fourier Transform Infrared Spectroscopy | : | ATR-FTIR |

| | | |
|---|---|---|
| X-Ray diffraction | : | XRD |
| Ultraviolet | : | UV |
| High-resolution mass spectrometry | : | HRMS |
| Aggregation Induced emission | : | AIE |
| Scanning electron microscopy | : | SEM |
| Nuclear Magnetic Resonance | : | NMR |
| Fourier-transform infrared spectroscopy | : | FT-IR |
| Linear viscoelastic region | : | LVE |
| Polymethyl methacrylate | : | PMMA |
| Fluorinated ethylene propylene | : | FEP |
| Alternating Current | : | AC |
| Direct current | : | DC |
| Relative humidity | : | RH |
| Milligram | : | mg |
| Minutes | : | min |
| Hours | : | h |
| Millilitre | : | mL |
| Milli mole | : | mmol |
| Molecular Iodine | : | $I_2$ |
| Molecular Oxygen | : | $O_2$ |
| Ammonium Sulphate | : | $(NH_4)_2SO_4$ |
| Hydrazine Hydrate | : | $N_2H_4.H_2O$ |
| Sodium carbonate | : | $Na_2CO_3$ |
| Tetramethyl silane | : | TMS |
| Thin Layer Chromatography | : | TLC |
| Polydimethylsiloxane | : | PDMA |
| Fluorinated ethylene propylene | : | FEP |

# DECLARATION

I hereby declare that the work embodied in this thesis entitled **"Synthesis and self-assembly of carbohydrate naphthalimide scaffolds for electronic applications"** is based entirely on the results of the investigations and research work carried out by me under the supervision of **Dr S. Nagarajan**, Department of Chemistry, National Institute of Technology Warangal. I declare that this work is original and has not been submitted in part or full for any degree or diploma to this or any other University.

Date: 25.07.2024 **(Rachamalla Arun Kumar)**

Place: NIT Warangal

# CHAPTER-I

# INTRODUCTION

# 1.1. Introduction

In the past few decades, synthetic materials have become prevalent across multiple fields, including pharmaceuticals, biomedical engineering, and organic electronics. Typically derived from petrochemical resources, these synthetic materials are employed in producing low-cost plastics, synthetic fibers, detergents, surfactants, value-added chemicals, and active pharmaceutical intermediates.[1,2] With the growing reliance on synthetic materials in everyday life, there is a rising demand for petrochemical building blocks. However, this increased consumption depletes fossil feedstocks, incurs high production costs, causes bio-incompatibility, and adversely affects environmental conditions. Synthetic materials face significant hurdles in biomedical and materials science applications, such as biocompatibility, biodegradability, and toxicity issues.[3] These challenges have driven researchers to seek alternative raw materials to address future shortages and the rising cost of conventional fossil raw materials.[4–6] Renewable resources offer a sustainable option for producing industrial chemicals and energy, potentially reducing reliance on fossil feedstocks and mitigating the increasing costs of petroleum-based building blocks.[7–12] Common examples of renewable resources include carbohydrates, proteins, fatty acids, and lipids.

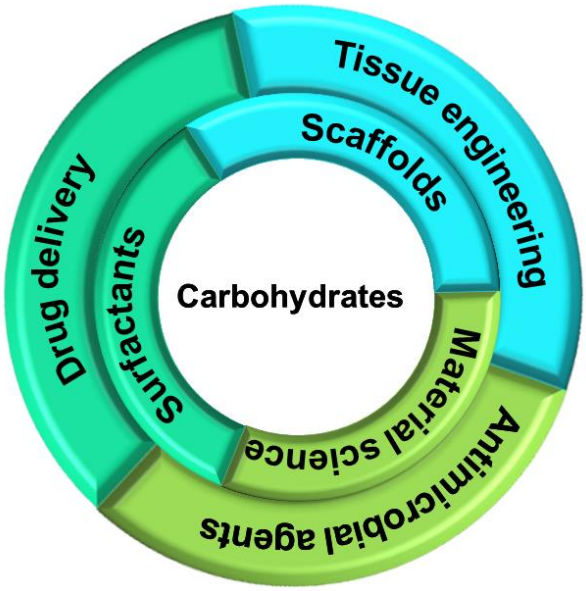


**Figure 1.1.** Applications of carbohydrates.

When compared to petroleum resources, carbohydrates have various advantages, including availability, low cost, unique molecular structure, environmental friendliness, and sustainability, highlighting their bright future. Carbohydrates and their derivatives, as fundamental building blocks in nature and the human body, have received major global attention as subjects for various studies and applications (**Figure 1.1**).[13–18]

Carbohydrates, including saccharides, glycoproteins, glycolipids, and proteoglycans, are among the most common and extensively distributed chemical molecules in nature. They are essential for energy metabolism, cell architecture, and molecular interactions. For example, glucose is the principal energy source, polysaccharides are important components of the plant cell wall, and glycoproteins on the cell surface are required for cell-cell contact. Since most carbohydrates possess multiple hydroxyl groups, each molecule presents numerous potential sites for various chemical reactions, such as alkylation,[19] acylation,[20] esterification,[21] oxidation,[22] and glycosylation.[23]

## 1.2. Chemistry of Glycosides

Carbohydrates, in their simplest form, generally referred to as either glycoside or glycoconjugates, display a broad range of applications in food, agriculture, cosmetics, health care, electronics, and pharmaceutical sectors.[24–28] Depending upon the type of atom linked to the anomeric carbon of the carbohydrate moiety, glycosides were classified into *C*, *N*, *S*, and *O*-glycosides.[29–32] Among these, *O*-glycosides are particularly noteworthy for their abundance and importance. Naturally occurring *O*-glycosides include notable antibiotics like vancomycin and chromomycin. Additionally, various glycosylated phenolic compounds of plant origin, such as sennoside A and glucofrangulin A are vital natural products (**Figure 1.2**). While the synthesis of *O*- and *C*-glycosides is well documented, the synthesis of *N*-glycosides remains less explored due to the challenge of stereoselective nitrogen scaffold induction at the anomeric position.[33] Despite this, there is growing interest in *N*-glycosides, as they are the key components in DNA, RNA, cofactors, proteoglycans, glycoproteins, peptidoglycans, and glycolipids.[34,35]

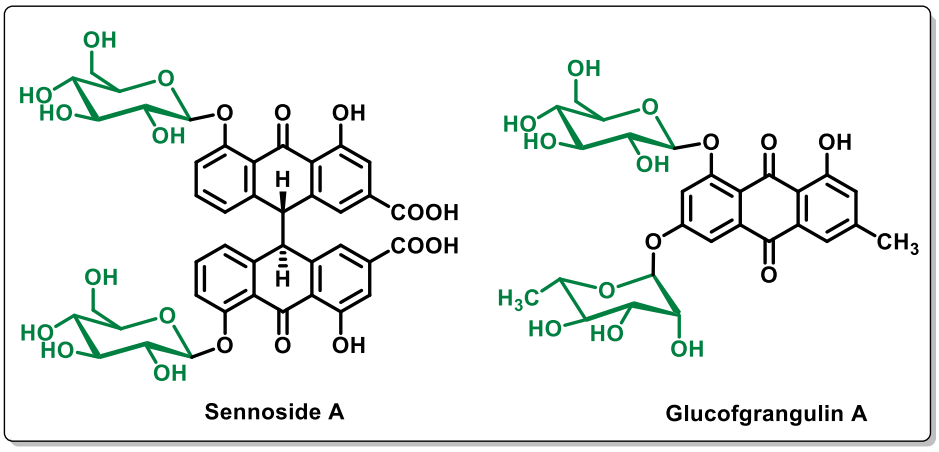


**Figure 1.2** Representative examples of naturally occurring *O*-glycosides.

With advancements in supramolecular self-assembly, naturally occurring carbohydrates can be harnessed to create sustainable materials through chemical modifications. The potential of carbohydrates in developing next-generation materials is significant, vast, and promising. Due

to their intrinsic bioactivities, compounds such as hyaluronic acid, heparin, and chitosan have already found applications in clinical and pharmaceutical industries. However, the preparation of precise carbohydrate assemblies for soft materials remains challenging due to the structural complexity and diversity of carbohydrates. Fabricating carbohydrate-based self-assembled materials with controllable molecular positions and functions is crucial for applications in medicine and advanced materials. Around the globe, to meet the demands of modern medicine and advanced biomaterials, other compounds such as polymers, dendrimers, peptides, lipids, proteins, and aromatic compounds are usually employed as scaffolds to synthesize carbohydrate assemblies (**Figure 1.3**).[36–44]

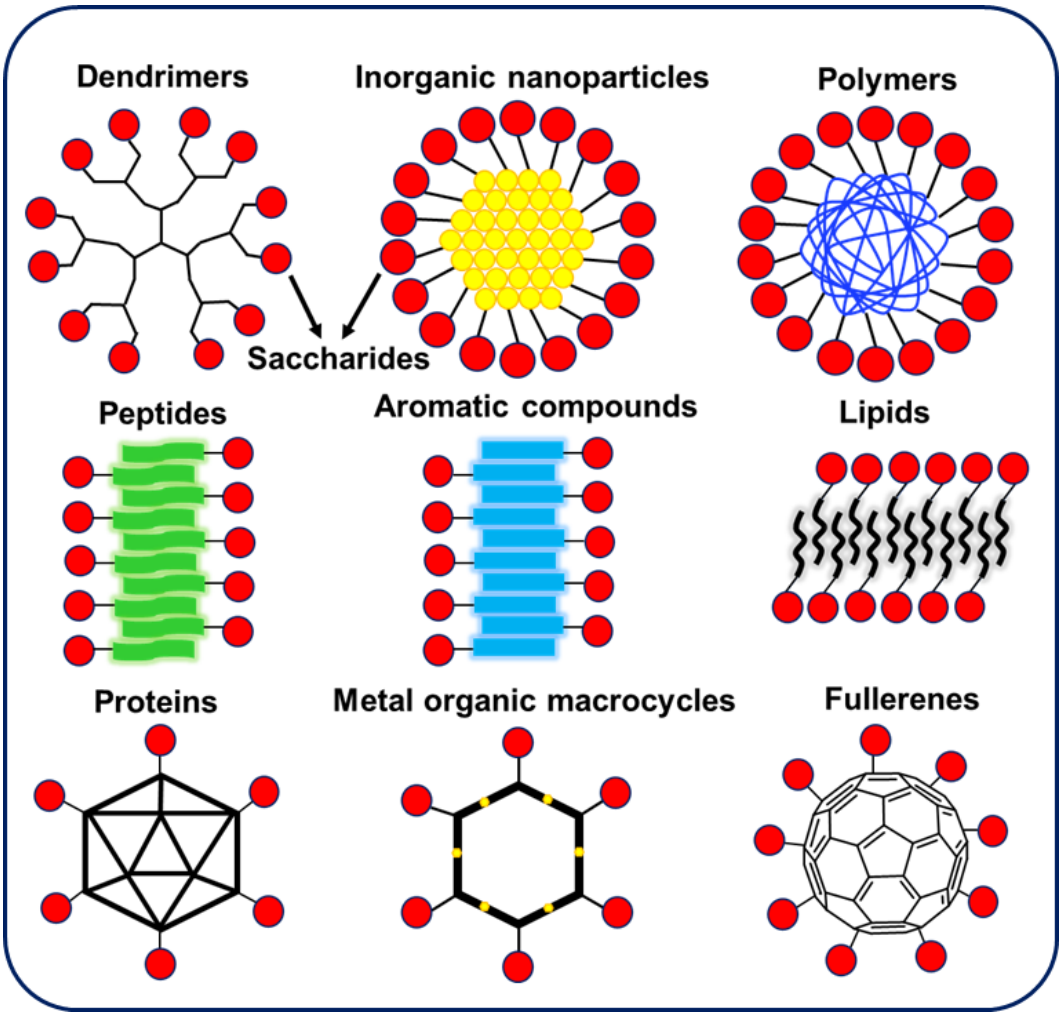


**Figure 1.3.** Illustration of precise display of multivalent carbohydrates by using other compounds as scaffolds.

## 1.3. Supramolecular chemistry

Supramolecular chemistry focuses on interactions that are non-covalent and is to be counted among the forefront subfields of chemistry during the twenty-first era. It is also known as "Chemistry beyond the molecules," wherein diverse units are attached together *via* intermolecular bonds to lead to a well-organized complex molecule or structure. Jean-Marie

Lehn, Charles Pedersen, and Donald Cram contributed significantly to the development of supramolecular chemistry and were awarded the 1987 Nobel Prize in supramolecular chemistry.[45] In conventional chemistry, covalent interactions are frequently observed with the sharing of electrons, whereas supramolecular chemistry shows supramolecular forces and electrostatic contact between the molecules or within the molecule. Thus, the subsequently formed supermolecule shows different properties in the combination of individual molecules' properties.

### 1.3.1. Self-Assembly

Self-assembly is the autonomous organization of molecules or particles into well-defined structures without external direction. This process is driven by the intrinsic properties of the molecules, such as shape, charge, and functional groups, which guide their interactions through non-covalent forces like hydrogen bonding, π–π interactions, van der Waals interactions, hydrophobic effects, and electrostatic forces. Self-assembly is a cornerstone in developing complex biological structures and advanced materials.[46]

### 1.3.2. Amphiphilic Molecules

Molecules that consist of both hydrophobic and hydrophilic part are called as amphiphiles. This attribute of amphiphiles in liquid medium allows them to self-assemble into diverse morphologies like vesicles, bilayers, micelles, nanosheets, nanotubes, nanofibres and aggregates of various shapes and sizes depending upon their hydrophilic-hydrophobic ratio (**Figure 1.4**).[45]

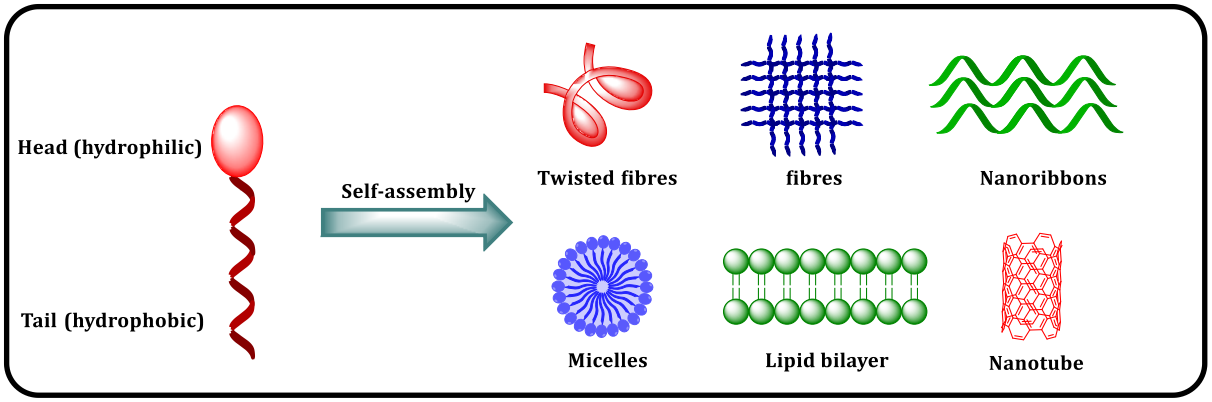


**Figure 1.4.** Representative Self-assembled structures of amphiphiles

### 1.3.3. Self-assembly in nature

In nature, self-assembly is a ubiquitous and essential phenomenon. For example, the lipid bilayers that form cell membranes result from amphiphilic molecules (phospholipids) self-assembling in an aqueous environment, creating a stable barrier fundamental for cellular function. Similarly, the intricate folding of proteins into specific three-dimensional shapes is driven by self-assembly, allowing them to perform diverse biological functions, from catalyzing reactions as enzymes to providing structural support as cytoskeleton components. Many of the following nano-scale structures are found in naturally occurring systems, and two of them are detailed below.

### 1.3.4. Chlorophyll molecule

In nature, chlorophyll molecule plays a vital part in the photosynthesis of plants., the process by which plants convert sunlight into usable energy. Two forms of chlorophyll molecules are found in the photosystems of green plants: chlorophyll a and b. Owing to their bulky nature and rigid aromaticity, these molecules undergo self-assembly in chloroplasts to facilitate energy transfer between molecules, which encourages the self-assembly phenomenon.[47,48] Inspiring by nature, various π-conjugated organic systems have been designed with directional hydrogen bonding groups, hydrophilic, hydrophobic, and ionic substituents as a building block for supramolecular self-assembly.

### 1.3.5. DNA

DNA comprises lengthy polynucleotide chains, each composed of a nucleotide with a five-carbon sugar (deoxyribose) chemically bonded to a phosphate group and a purine or pyrimidine base. All of the nucleotides are linked together in the shape of a chain that forms the DNA strand's backbone. DNA's three-dimensional structure arises from interactions between two strands through supramolecular forces. H-bonds are produced between the purine and pyrimidine bases in the complementary base pair present in two strands. DNA’s double helical is held via H-bonds between the nucleobases; guanine (G) arranges three H-bonds along with adenine (A), whereas cytosine (C) arranges two hydrogen bonds along with thymine (T). This helical structure consists of ten base pairs, and in each turn, it was created by coiling two nucleotide backbones around each other. This is a simple representation that H-bonding is present in DNA structure.[49]

## 1.4. Low Molecular Weight Gelators

Low molecular weight gelators (LMWGs) are small (molecular weight less than 3000 Da), typically organic molecules that can self-assemble into three-dimensional networks, forming gels.[50] Gels are classified based on the nature of the liquid used. Hydrogels are the gels in which liquid component is water, organogels are the gels in which gelators form a gel in organic solvents, similarly, oleogels are gels formed in oils. Schematic representation of supramolecular gelation is given in **figure 1.5**. These gels are characterized by their ability to immobilize large amounts of solvent within their network structure. The self-assembly of LMWGs into gels involves various non-covalent interactions, such as hydrogen bonding, π-π stacking, and van der Waals forces. The gels formed by LMWGs have gained significant attention due to their versatility and potential applications.[51–56] In the field of medicine, LMWG-based gels are explored for drug delivery systems where they can provide controlled release of therapeutics. In tissue engineering, these gels can serve as scaffolds that support cell growth and tissue regeneration due to their biocompatibility and tunable mechanical properties.

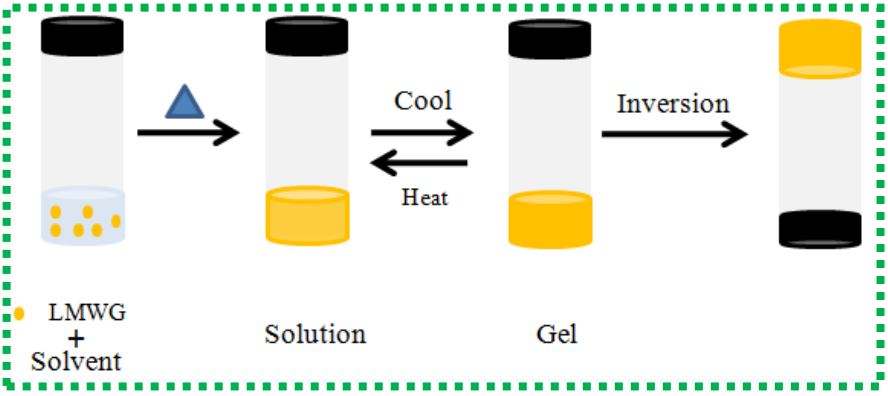


**Figure 1.5** Schematic representation of supramolecular gelation

The study of self-assembly, especially in the context of LMWGs, provides a deeper understanding of both natural processes and innovative technological applications. The principles governing self-assembly in biological systems inspire the design of new materials that mimic these natural processes. For instance, by understanding how proteins fold and assemble, researchers can design synthetic peptides and proteins that self-assemble into nanostructures with specific functions. Similarly, insights into the self-assembly of lipid bilayers can guide the development of synthetic vesicles for drug delivery. The interdisciplinary nature of this research area bridges chemistry, biology, and materials science, driving forward the development of novel solutions for challenges in medicine, biotechnology, and materials engineering.

## 1.4.1. Carbohydrate-based LMWGs

Carbohydrates have emerged as a promising feedstock for designing and synthesizing LMWGs, owing to their attractive features such as renewability, cost-effectiveness, and biocompatibility, with minimal environmental footprint. The structural diversity of natural monosaccharides has substantially enriched the molecular libraries for gelator design. Consequently, researchers have largely adopted a bottom-up strategy for developing LMWGs with tailored properties, leveraging the versatility of these natural precursors to create application-specific gelators. Carbohydrate-based molecular gelators have been extensively studied as a unique class of molecular assemblies (**Figure 1.6**). Carbohydrate assembling systems encompass a broad spectrum of materials and fields, with numerous reviews addressing the multifaceted roles of carbohydrates in contemporary scientific research. These include, for example, carbohydrate-based macromolecular materials,1 click chemistry and its applications in glycoscience, supramolecular chemistry and glycoconjugates. Seeberger and co-workers reviewed how carbohydrates intricately form molecular structures essential across diverse disciplines.[57]

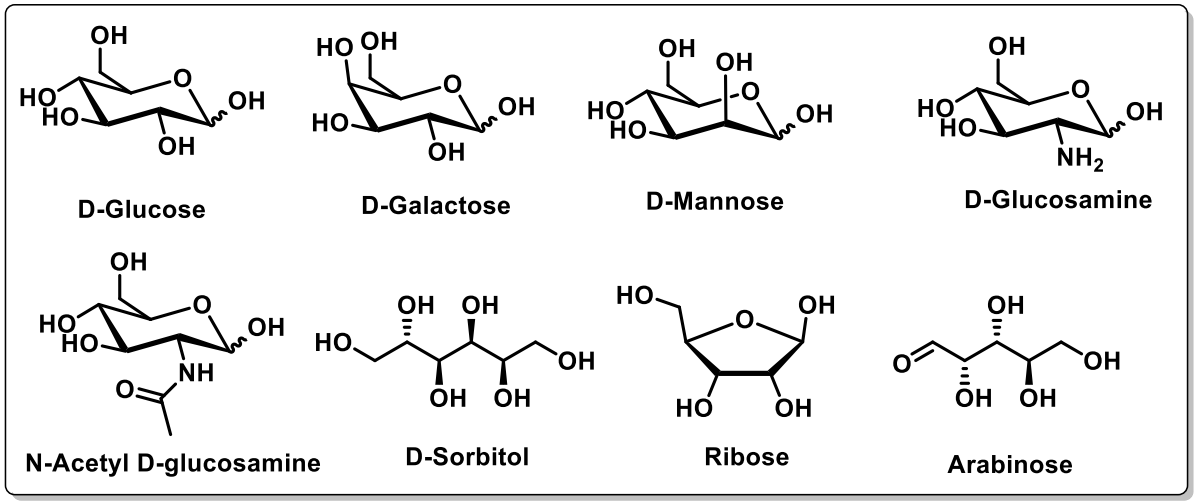


**Figure 1.6**. Molecular structures of carbohydrates are commonly used to design gelators.

*Wang et al*. summarized the sustainable and versatile nature of carbohydrate-derived surfactants in industrial and biomedical sectors.[58] Parshad and co-workers delved into the synthesis and functional applications of carbohydrate-derived amphiphiles, highlighting their efficacy in combating pathogens and enhancing drug delivery systems.[59] *Li et al.* explored advanced techniques for integrating carbohydrates to develop biomaterials with enhanced functionalities for biomedical applications.[60] *Zhang* and co-workers reviewed strategies to control chirality, crucial for drug delivery and catalysis advancements.[61] *Sagar* and co-workers showcased carbohydrates' cutting-edge applications in creating functional gels vital for biomedical and materials science.[62] *Wang et al.* delved into innovative methodologies for designing carbohydrate-based complex molecular assemblies, offering potential breakthroughs in

biomedicine and materials science. These reviews collectively highlight the pivotal role of carbohydrates in driving innovation across various scientific and technological fronts. Most of the literature reports on carbohydrate-based gelators focus on their use as biomaterials, while electronic applications are least explored. Representative examples of carbohydrate based self-assembled system and their applications are given in **figure 1.7**. [19,24-25,63–65]

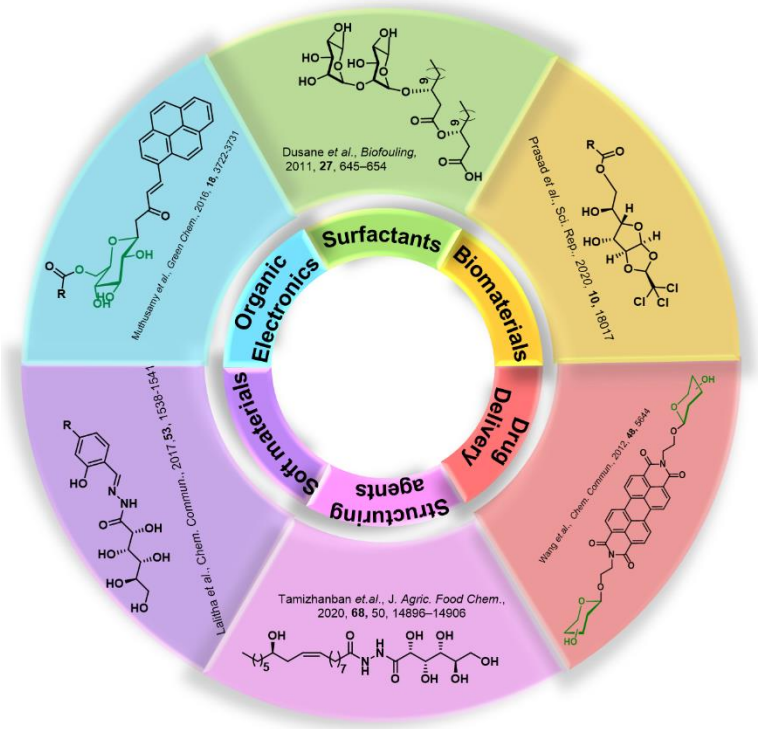


Figure 1.7. Representative examples of carbohydrate based self-assembled system and their applications

## 1.5. Naphthalimides

Naphthalimides, a class of organic compounds derived from naphthalene, have garnered significant attention in the scientific community due to their exceptional photophysical properties and versatile applications in various fields (**Figure 1.8**).[66–70] These compounds are characterized by their naphthalene core, which is functionalized with imide groups, resulting in a rigid, planar structure that is conducive to effective π-π stacking interactions. The unique combination of strong fluorescence, chemical stability, and conjugated system makes naphthalimides indispensable in developing advanced materials for various technological applications. Although simple naphthalimides have been extensively studied, the self-assembly properties of naphthalimides remain largely unexplored. According to the Scopus search, there are only 73 reports available on the naphthalimide-based self-assembled molecules.

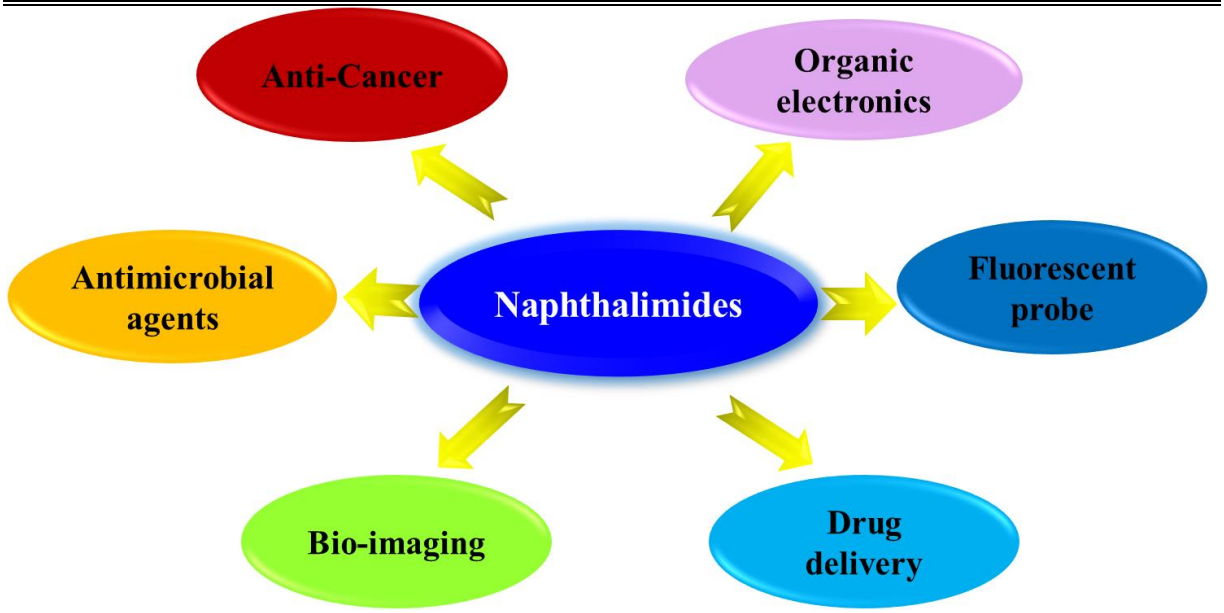


**Figure 1.8**. Applications of Naphthalimides.

### 1.5.1. Naphthalimides-based LMWGs

The rapid advancement of nanotechnology and material science has brought about significant interest in the self-assembly of organic molecules, particularly naphthalimides, because of their their exceptional structural and functional properties. Naphthalimides play a substantial role in supramolecular chemistry due to their ability to self-assemble into well-defined nanostructures. This self-assembly behavior is particularly advantageous for applications in organic electronics, where the organization of molecules at the nanoscale can significantly influence device performance. By leveraging the self-assembly properties of naphthalimides, researchers can design and fabricate materials with enhanced electronic characteristics and functionalities.

Self-assembled naphthalimides are distinguished by their ability to spontaneously organize into well-defined nanostructures through non-covalent interactions such as hydrogen bonding, π-π stacking, and van der Waals forces. This intrinsic property makes them ideal candidates for constructing supramolecular architectures with precise control over morphology and functionality. One of the primary areas where self-assembled naphthalimides have shown promise is in biological and medical applications, representative examples of self-assembled naphthalimides and their application is shown in **figure 1.9**. Enzyme-instructed self-assembly of naphthalimide-dipeptide structures, for instance, leads to the formation of hydrogel networks that can be tailored for specific chemical and biological functions, including drug delivery and tissue engineering.[68] In the realm of environmental and energy applications, naphthalimide derivatives have been effectively integrated into heterojunction systems with titanium dioxide to enhance photocatalytic performance.[69]

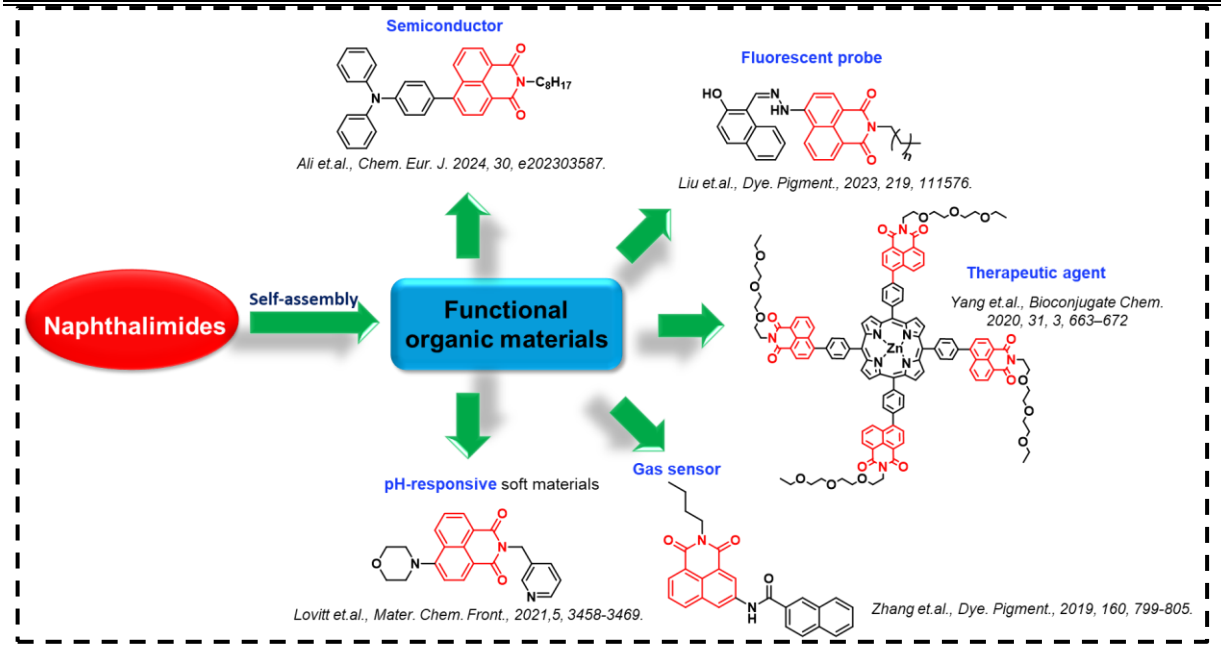


**Figure 1.9**. Pictorial representation of the various self-assembled naphthalimides and their applications.

This advancement is crucial for developing efficient photocatalysts for pollutant degradation and renewable energy production. Additionally, the ability of naphthalimides to form supramolecular structures, such as bowl-shaped motifs, opens new avenues for creating novel materials with unique electronic and optical properties.[70] Fluorescent naphthalimides have gained significant attention for their bioimaging and chemical sensing applications. Their strong fluorescence and selective binding properties make them excellent probes for detecting metal ions, anions, and other analytes. Furthermore, bis-naphthalimides self-assemble into organogels and nanofibers, which are valuable in chemical detection and creating soft materials with tunable properties. In medical science, self-assembled naphthalimide nanoparticles exhibit potential in anticancer therapies by binding to G-quadruplex DNA structures, thereby disrupting cancer cell proliferation. The aggregation-induced emission properties of naphthalimides are also leveraged for the sensitive detection of volatile organic compounds, highlighting their utility in environmental monitoring and safety.

Photoredox catalysis, another critical application, benefits from the self-assembly of naphthalimide nanoribbons, which facilitate hydrogen evolution a key process in renewable energy technologies. Additionally, naphthalimide-conjugated nanomaterials are explored for photodynamic and photothermal therapies, providing innovative approaches for non-invasive cancer treatment. Overall, the self-assembly of naphthalimides presents a rich and versatile platform for advancements across multiple disciplines. This thesis aims to delve into the self-assembly mechanisms, the resulting nanostructures' structural characteristics, and their wide-ranging applications.

## 1.6. Carbohydrate-naphthalimide derivatives

By considering the salient features of carbohydrates and naphthalimides, planned to work on the synthesis and self-assembly of carbohydrate naphthalimides. Structures and limitations in the synthesis of various sugar-based naphthalimides reported in the literature are given in **Table 1.1**.

**Table 1.1**. Synthesis of carbohydrate-naphthalimide derivatives

| S. No. | Structure | Summary of the methodology | Summary of application |
|---|---|---|---|
| 1 | 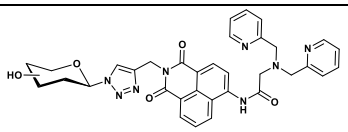 | 1. Only two derivatives were reported<br>2. Involves protection and deprotection of saccharide –OH groups<br>3. Multi-step synthesis<br>4. Involves column chromatography purification<br>5. Overall yield: Moderate | Li and co-workers: Enhanced aqueous sensitivity and lowered cytotoxicity of naphthalimide-based zinc ion fluorescence probe.[72] |
| 2 | 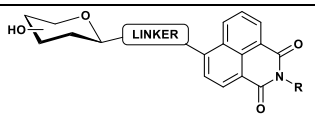 | 1. Limited substrate scope<br>2. Involves protection and deprotection of saccharide –OH groups<br>3. Multi-step synthesis<br>4. Involves column chromatography purification<br>5. Overall yield: Moderate to poor | Robinson and co-workers: Synthesis of amphiphilic sugar naphthalimide derivatives.<br>Tian and co-workers: Photochromic fluorescent glycoprobes.[73]<br>Zhang and co-workers: Fluorescent probe for intracellular imaging of hexosaminidase.[79] |
| 3 | 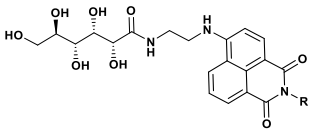 | 1. Only two derivatives were reported<br>2. Multi-step synthesis<br>3. Involves column chromatography purification<br>4. Overall yield: Poor | Yi and co-workers: Hydrogels as a hydrophilic drug delivery system.[74]<br>Yu and co-workers: construction of a $Eu^{3+}$-based metallogel *via* energy transfer in a supramolecular scaffold.[76] |
| 4 | 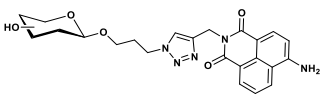 | 1. Involves protection and deprotection of saccharide –OH groups<br>2. Multi-step synthesis<br>3. Involves column chromatography purification<br>4. Overall yield: Poor | Scanlan and co-workers: Fluorescent probes for tumor cell imaging.[77] |

Recently, Fu *et al*. have developed a photochromic carbohydrate-modified naphthalimide-serum protein hybrid by adopting a simple host-guest assembly process, which displayed a

unique duplexed fluorescence blinking manner for precision bio-imaging.[71] In a similar line, Li and co-workers have adopted the click chemistry for the conjugation of glucose and galactose with a naphthalimide zinc ion probe, substantially increasing the aqueous sensitivity, specific cell targeting ability, and reduced cytotoxicity.[72] It is worth mentioning that Cavigiolio *et al*. has synthesized amphiphilic sugar and deoxy uridine conjugate of 1,8-naphthalimides by adopting protection and deprotection of sugar moiety and by using expensive catalysts.[73] It is proven that the molecular self-assembly of sugar-naphthalimide derivatives furnishes complex hierarchical luminescent aggregates, which paved the way for the development of advanced electronics, luminescent materials, and biomaterials.[74–79] Recently, Gudeika *et al.* has discussed the applications of naphthalimides in a way that can be useful for material scientists and electronic engineers.[80] Zhou and coworkers discussed the design and performance of naphthalimide and other imide-based semiconductors and demonstrated their utility in the organic field–effect transistors (OFET).[66]

## 1.7. Triboelectric Nanogenerator

The term ‘tribo’ originates from the Greek word for ‘friction’. Triboelectric nanogenerators (TENGs) are groundbreaking devices that capture and transform small amounts of frictional energy into usable electricity. This innovative technology offers a promising alternative for harvesting mechanical energy from the surrounding environment. When the two different materials come into contact, the triboelectric effect causes their surfaces to become electrically charged. As these materials move relatively to each other, friction generates an electrical potential difference between electrodes, producing electrical energy[81]. TENGs provide a method for converting mechanical energy from friction into electrical power, enabling energy scavenging from various environmental sources.

### 1.7.1. Fundamentals of TENGs

The triboelectric effect, widely seen in everyday life, takes place when two different materials come into contact, leading to the production of static charges. This effect is sometimes problematic in industries because it can ignite and cause dust explosions, dielectric breakdown, and electronic damage. The electrostatic charges then act as a capacitive energy storage device when they are separated; this is what led to the development of the early electrostatic generators such as “friction machines” or Van de Graaff generators[82].

In 2012, Wang’s group brought out a TENG which aims at efficiently capturing and converting ambient mechanical energy that is usually wasted in daily activities[81]. TENGs work on the principle of combining contact electrification where static charges are generated on surfaces of

materials that come into contact and electrostatic induction where mechanical energy is transformed into electrical energy through the shift of electrical potential during separation[83]. Over the past decade, the TENG concept has evolved to support various working modes suitable for different application scenarios, including mechanical vibrations, human motion, wind, and sea waves[84–86]. TENGs offer numerous advantages, such as the availability of a wide range of materials, lightweight design, low cost, and high efficiency even at low operational frequencies[87]. In theory, any material with a specific charge affinity can be used to create a TENG, leading to a diverse selection of high-performance materials across the triboelectric series (**Figure 1.10**)[88]. Commonly used materials for generating positive triboelectric charges include nylon and metal, while polytetrafluoroethylene (PTFE) and silicone are often employed for generating negative charges[89].

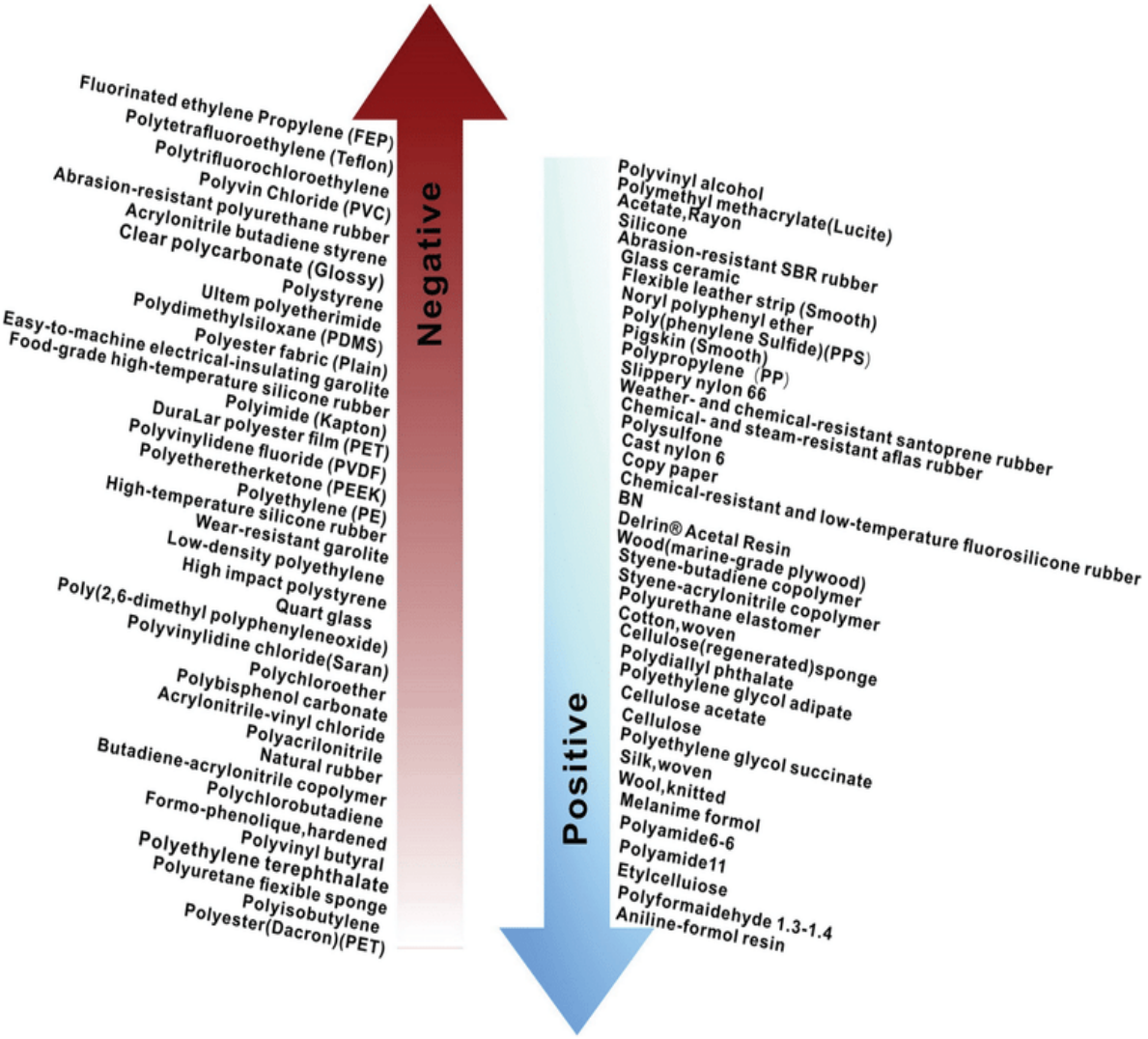


**Figure 1.10:** Triboelectric series. Reproduced from Liu *et al*., *Adv. Funct. Mater*., 2020, **30**, 2004714.[90]

Flexible polymers like nylon and PTFE are frequently chosen for constructing modern TENGs due to their ease of production, cost-effectiveness, and portability[91]. TENGs are made from durable ceramic materials for high-temperature applications to withstand extreme conditions[92]. TENGs can achieve a power density of up to 500 W/m², depending on the device's structure and active components, making them capable of powering small electronic devices and supporting the development of self-powered electronics networks[93]. In 2017, TENGs were proposed as "the energy for the new era" given the significant demand for sensors in the Internet of Things (IoT) era and the environmental concerns associated with large-scale battery replacement[94].

### 1.7.2. Working modes of TENG

Since the first introduction of TENG in 2012, four distinct operational modes for TENGs have been developed. These modes include vertical contact-separation (CS) mode, lateral-sliding mode, single-electrode mode, and freestanding triboelectric-layer (FT) mode, as illustrated in **Figure 1.11**[81]. Each mode is characterized by the direction of polarization changes and the specific electrode configuration.

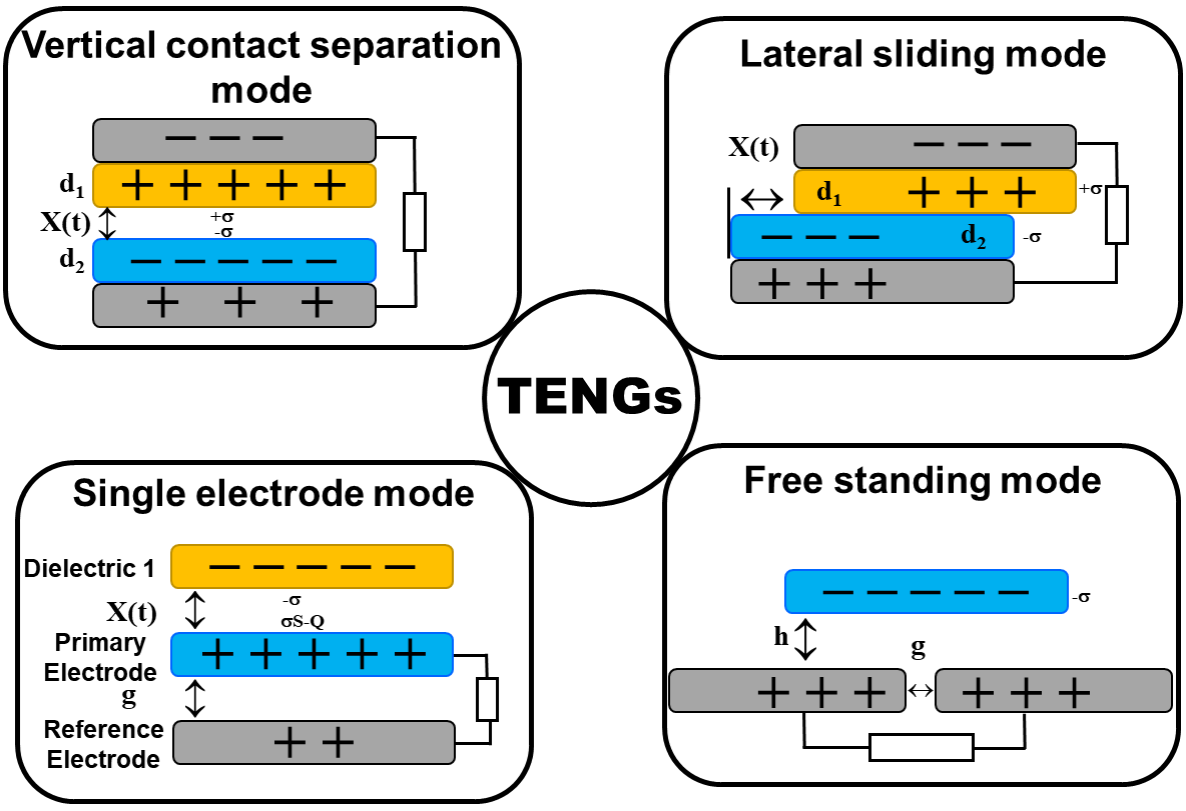


**Figure 1.11.** Working modes of TENG.

### 1.7.3. Contact-Separation Mode

The CS mode of Triboelectric Nanogenerators (TENGs) offers several advantages over other modes. It generates higher output power density and is more straightforward to fabricate. In this setup, two different dielectric films are paired and face each other. When these films make direct contact, charges transfer between their surfaces due to differences in triboelectric polarity, generating opposite charges on each layer. The mechanical motion then causes the layers to separate vertically, creating a potential drop between the electrodes on the films, allowing electrons to flow through an external circuit. As the layers come back together, the potential decreases, and electrons flow back to restore equilibrium. The CS mode provides better control of the contact area, leading to more consistent energy output and higher efficiency at low frequencies. It allows for a broader range of material combinations, enhancing flexibility and performance. Additionally, the CS mode is scalable and can be designed for more outstanding durability, making it suitable for diverse applications[95].

Integrating carbohydrate chemistry with naphthalimide derivatives represents a novel approach to the design of advanced materials. By harnessing the natural abundance and versatility of carbohydrates, combined with the unique photophysical properties of naphthalimide, this research aims to develop new materials with enhanced performance for electronic applications. The findings from this study could contribute to the development of sustainable and biocompatible electronic devices, addressing the growing demand for green technologies in the electronics industry. Moreover, this research bridges the gap between organic synthesis, material science, and electronics, offering a multidisciplinary approach to solving current challenges in developing advanced materials.

## 1.8. References

1. S. M. Al-Salem, P. Lettieri and J. Baeyens, *Waste Manag.*, 2009, **29**, 2625–2643.
2. J. C. Serrano-Ruiz, R. Luque and A. Sepúlveda-Escribano, *Chem. Soc. Rev.*, 2011, **40**, 5266–5281.
3. P. Pesode, S. Barve, S. V Wankhede and A. Ahmad, *Adv. Mater. Sci. Eng.*, 2023, **2023**, 6682892.
4. H. Alidrisi and A. Demirbas, *Energy Sources, Part A Recover. Util. Environ. Eff.*, 2016, **38**, 1419–1427.
5. K. Charubin, R. K. Bennett, A. G. Fast and E. T. Papoutsakis, *Metab. Eng.*, 2018, **50**, 173–191.

6. V. Rudovica, A. Rotter, S. P. Gaudêncio *et al*., *Front. Mar. Sci.*, 2021, **8**, 723333.
7. S. Ummartyotin and C. Pechyen, *Renew. Sustain. Energy Rev.*, 2016, **62**, 654–664.
8. K. N. Bharath and S. Basavarajappa, *Sci. Eng. Compos. Mater.*, 2016, **23**, 123–133.
9. B. Y. Karlinskii and V. P. Ananikov, *Chem. Soc. Rev.*, 2022, **52**, 836–862.
10. Y. Xie, S. Gao, D. Zhang, C. Wang and F. Chu, *Resour. Chem. Mater.*, 2023, **2**, 223–230.
11. G. Liao, E. Sun, E. B. G. Kana, H. Huang, I. A. Sanusi, P. Qu, H. Jin, J. Liu and L. Shuai, *Carbohydr. Polym.*, 2024, **341**, 122351.
12. S. Kumar, S. Krishnan, S. K. Samal, S. Mohanty and S. K. Nayak, *Polym. Int.*, 2017, **66**, 1349–1363.
13. O. Oyelaran and J. C. Gildersleeve, *Expert Rev. Vaccines*, 2007, **6**, 957–969.
14. A. M. Faísca Phillips, *European J. Org. Chem.*, 2014, **2014**, 7291–7303.
15. H. Jiang, X. Qin, Q. Wang, Q. Xu, J. Wang, Y. Wu, W. Chen, C. Wang, T. Zhang, D. Xing, D. Xing and R. Zhang, *Eur. J. Med. Chem.*, 2021, **223**, 113633.
16. J. A. Batool, K. Rehman, A. Qader and M. S. H. Akash, *Curr. Pharm. Des.*, 2022, **28**, 1669–1687.
17. R. K, V. K. S, P. Saravanan, R. Rajeshkannan, M. Rajasimman, H. Kamyab and Y. Vasseghian, *Environ. Res.*, 2024, **240**, 117521.
18. B. S. Hariprasad, R. Lakshmi Priya and S. Ganesh Babu, *Eur. Polym. J.*, 2024, **214**, 113178.
19. K. Muthusamy, V. Sridharan, C. U. Maheswari and S. Nagarajan, *Green Chem.*, 2016, **18**, 3722–3731.
20. S. David and S. Hanessian, *Tetrahedron*, 1985, **41**, 643–663.
21. S. E. Denmark and G. L. Beutner, *Angew. Chemie Int. Ed.*, 2008, **47**, 1560–1638.
22. A. S. Perlin, *Adv. Carbohydr. Chem. Biochem.*, 2006, **60**, 183.
23. A. Thamizhanban, K. Lalitha, G. P. Sarvepalli, C. U. Maheswari, V. Sridharan, J. B. B. Rayappan and S. Nagarajan, *J. Mater. Chem. B*, 2019, **7**, 6238–6246.
24. Y. S. Prasad, S. Miryala, K. Lalitha et al., *Sci. Rep.*, 2020, **10**, 18017.
25. A. Thamizhanban, S. Balaji, K. Lalitha, Y. S. Prasad, R. V. Prasad, R. A. Kumar, C. U. Maheswari, V. Sridharan and S. Nagarajan, *J. Agric. Food Chem.*, 2020, **68**, 14896–14906.
26. A. Bernardi, J. Jiménez-Barbero, A. Casnati *et al*.,, *Chem. Soc. Rev.*, 2013, **42**, 4709–4727.
27. J. Xie and N. Bogliotti, *Chem. Rev.*, 2014, **114**, 7678–7739.
28. B. Kang, T. Opatz, K. Landfester and F. R. Wurm, *Chem. Soc. Rev.*, 2015, **44**, 8301–8325.

29. K. Lalitha, K. Muthusamy, Y. S. Prasad, P. K. Vemula and S. Nagarajan, *Carbohydr. Res.*, 2015, **402**, 158–171.
30. B. Piniello, E. Lira-Navarrete, H. Takeuchi, M. Takeuchi, R. S. Haltiwanger, R. Hurtado-Guerrero and C. Rovira, *ACS Catal.*, 2021, **11**, 9926–9932.
31. V. Kelemen, M. Csávás, J. Hotzi, M. Herczeg, Poonam, B. Rathi, P. Herczegh, N. Jain and A. Borbás, *Chem. – An Asian J.*, 2020, **15**, 876–891.
32. K. Villadsen, M. C. Martos-Maldonado, K. J. Jensen and M. B. Thygesen, *ChemBioChem*, 2017, **18**, 574–612.
33. F. T. Ndombera, G. C. Vanhecke, S. Nagi and Y. H. Ahn, *Bioorganic Med. Chem. Lett.*, 2016, **26**, 1452–1456.
34. P. J. Berti and J. A. B. McCann, *Chem. Rev.*, 2006, **106**, 506–555.
35. R. Sangwan, A. Khanam and P. K. Mandal, *European J. Org. Chem.*, 2020, **2020**, 5949–5977.
36. Y. Liu, Y. Zhang, Z. Wang, J. Wang, K. Wei, G. Chen and M. Jiang, *J. Am. Chem. Soc.*, 2016, **138**, 12387–12394.
37. B. M. Seifried, W. Qi, Y. J. Yang, D. J. Mai, W. B. Puryear, J. A. Runstadler, G. Chen and B. D. Olsen, *Bioconjug. Chem.*, 2020, **31**, 554–566.
38. Y. Anraku, H. Kuwahara, Y. Fukusato *et al*., *Nat. Commun.*, 2017, **8**, 1001.
39. Y. Chang, Y. Lv, P. Wei, P. Zhang, L. Pu, X. Chen, K. Yang, X. Li, Y. Lu, C. Hou, Y. Pei, W. Zeng and Z. Pei, *Adv. Funct. Mater.*, 2017, **27**, 1703083.
40. V. Ladmiral, M. Semsarilar, I. Canton and S. P. Armes, *J. Am. Chem. Soc.*, 2013, **135**, 13574–13581.
41. B. Parshad, P. Yadav, Y. Kerkhoff, A. Mittal, K. Achazi, R. Haag and S. K. Sharma, *New J. Chem.*, 2019, **43**, 11984–11993.
42. S.-J. Kwon, D. H. Na, J. H. Kwak *et al*., *Nat. Nanotechnol.*, 2017, **12**, 48–54.
43. A. P. V Moura, L. C. B. Santos, C. R. N. Brito *et al*., *ACS Cent. Sci.*, 2017, **3**, 1026–1031.
44. S.-J. Richards, A. N. Baker, M. Walker and M. I. Gibson, *Biomacromolecules*, 2020, **21**, 1604–1612.
45. J. -M. Lehn, *Angew. Chemie Int. Ed. English*, 1988, **27**, 89–112.
46. G. M. Whitesides and B. Grzybowski, *Science*, 2002, **295**, 2418–2421.
47. M. R. Wasielewski, *Acc. Chem. Res.*, 2009, **42**, 1910–1921.
48. S. Sengupta and F. Würthner, *Acc. Chem. Res.*, 2013, **46**, 2498–2512.
49. P. W. K. Rothemund, *Nature*, 2006, **440**, 297–302.
50. E. R. Draper and D. J. Adams, *Chem*, 2017, **3**, 390–410.
51. N. Hara, R. Yamazaki, N. Kimura and H. Suzuki, in *Polymer,* 2006, **55**, 3528.

52. P. Sahoo, D. Krishna Kumar, D. R. Trivedi and P. Dastidar, *Tetrahedron Lett.*, 2008, **49**, 3052–3055.
53. A. R. Hirst, I. A. Coates, T. R. Boucheteau *et al*., *J. Am. Chem. Soc.*, 2008, **130**, 9113–9121.
54. A. R. Hirst, B. Escuder, J. F. Miravet and D. K. Smith, *Angew. Chemie - Int. Ed.*, 2008, **47**, 8002–8018.
55. Q. Yu, C. Yu, F. Guo, J. Wang, S. Jiao, S. Gao, H. Li and L. Zhao, *Energy Environ. Sci.*, 2012, **5**, 6151–6155.
56. M. Bielejewski, A. Łapiński and O. Demchuk, *J. Colloid Interface Sci.*, 2017, **490**, 279–286.
57. M. Delbianco, P. Bharate, S. Varela-Aramburu and P. H. Seeberger, *Chem. Rev.*, 2016, **116**, 1693–1752.
58. L. Wang and Y. Queneau, *Carbohydrate-Based Amphiphiles: Resource for Bio-based Surfactants. Green Chemistry and Chemical Engineering*, 2019.
59. A. Mittal, Krishna, Aarti, S. Prasad, P. K. Mishra, S. K. Sharma and B. Parshad, *Mater. Adv.*, 2021, **2**, 3459–3473.
60. L. Li and G. Chen, *J. Am. Chem. Soc.*, 2022, **144**, 16232–16251.
61. Y. Yao, X. Meng, C. Li, K. V. Bernaerts and K. Zhang, *Small*, 2023, **19**, 2208286.
62. G. Wang, A. Chen, P. Aryal and J. Bietsch, *Org. Biomol. Chem.*, 2024, 5470–5510.
63. Y. V. N. V. P. V. A. R. K. Devendra H. Dusane Vinay S. Pawar and S. S. Zinjarde, *Biofouling*, 2011, **27**, 645–654.
64. K.-R. Wang, H.-W. An, L. Wu, J.-C. Zhang and X.-L. Li, *Chem. Commun.*, 2012, **48**, 5644–5646.
65. K. Lalitha, V. Sridharan, C. U. Maheswari, P. K. Vemula and S. Nagarajan, *Chem. Commun.*, 2017, **53**, 1538–1541.
66. M. Liao, J. Duan, P. Peng, J. Zhang and M. Zhou, *RSC Adv.*, 2020, **10**, 41764–41779.
67. A. Zhang, Y. Zhang, Z. Xu, Y. Li, X. Yu and L. Geng, *RSC Adv.*, 2017, **7**, 25673–25677.
68. R. D. Chakravarthy, M. Mohammed and H.-C. Lin, *Chem. – An Asian J.*, 2020, **15**, 2696–2705.
69. D. Liu, Y. Chen, R. Guan, J. Zhao, H. Jin, S. Zhang and Q. Shang, *Chemosphere*, 2022, **296**, 134046.
70. R. Renner, M. Stolte and F. Würthner, *ChemistryOpen*, 2020, **9**, 32–39.
71. Y. Fu, H.-H. Han, J. Zhang, X.-P. He, B. L. Feringa and H. Tian, *J. Am. Chem. Soc.*, 2018, **140**, 8671–8674.
72. L. Dong, Y. Zang, D. Zhou, X.-P. He, G.-R. Chen, T. D. James and J. Li, *Chem.*

*Commun.*, 2015, **51**, 11852–11855.

73. G. Cavigiolio, J. L. Morgan, B. H. Robinson and J. Simpson, *Aust. J. Chem.*, 2004, **57**, 885–894.
74. Z. Ma, P. Zhang, X. Yu, H. Lan, Y. Li, D. Xie, J. Li and T. Yi, *J. Mater. Chem. B*, 2015, **3**, 7366–7371.
75. J. Zhang, Y. Fu, H.-H. Han, Y. Zang, J. Li, X.-P. He, B. L. Feringa and H. Tian, *Nat. Commun.*, 2017, **8**, 987.
76. T. Wang, Z. Wang, D. Xie, C. Wang, X. Zhen, Y. Li and X. Yu, *RSC Adv.*, 2015, **5**, 107694–107699.
77. E. Calatrava-Pérez, S. Acherman, L. Stricker *et al*., *Org. Biomol. Chem.*, 2020, **18**, 3475–3480.
78. E. Calatrava-Pérez, S. A. Bright, S. Achermann *et al*., *Chem. Commun.*, 2016, **52**, 13086–13089.
79. L. Dong, S. Shen, H. Lu, S. Jin and J. Zhang, *ACS Sensors*, 2019, **4**, 1222–1229.
80. D. Gudeika, *Synth. Met.*, 2020, **262**, 116328.
81. F. R. Fan, Z. Q. Tian and Z. Lin Wang, *Nano Energy*, 2012, **1**, 328–334.
82. R. Zhang, M. Hummelgård, J. Örtegren, M. Olsen, H. Andersson, Y. Yang, H. Zheng and H. Olin, *Nano Energy*, 2021, **86**, 106041.
83. S. Mishra, S. Potu, R. S. Puppala, R. K. Rajaboina, P. Kodali and H. Divi, *Mater. Today Commun.*, 2022, **31**, 103292.
84. C. Rodrigues, M. Ramos, R. Esteves *et al*., *Nano Energy*, 2021, **84**, 105890.
85. Y. Zeng, H. Xiang, N. Zheng, X. Cao, N. Wang and Z. L. Wang, *Nano Energy*, 2022, **91**, 106601.
86. H. Yong, J. Chung, D. Choi, D. Jung, M. Cho and S. Lee, *Sci. Rep.*, 2016, **6**, 33977.
87. R. Walden, C. Kumar, D. Mulvihill and S. Pillai, *Chem. Eng. J. Adv.*, 2021, **9**, 100237.
88. H. Zou, Y. Zhang, L. Guo et al., *Nat. Commun.*, 2019, **10**, 1427.
89. S. Pan and Z. Zhang, *Friction*, 2019, **7**, 2–17.
90. Y. Liu, J. Mo, Q. Fu, Y. Lu, N. Zhang, S. Wang and S. Nie, *Adv. Funct. Mater.*, 2020, **30**, 2004714.
91. A. Chen, C. Zhang, G. Zhu and Z. L. Wang, *Adv. Sci.*, 2020, **7**, 2000186.
92. P. Zhang, W. Zhang, L. Deng and H. Zhang, *Nano Energy*, 2021, **87**, 106176.
93. H. Wu, S. Wang, Z. Wang and Y. Zi, *Nat. Commun.*, 2021, **12**, 5470.
94. Z. L. Wang, T. Jiang and L. Xu, *Nano Energy*, 2017, **39**, 9–23.
95. H. Zou, L. Guo, H. Xue, Y. Zhang, X. Shen, X. Liu, P. Wang, X. He, G. Dai, P. Jiang, H. Zheng, B. Zhang, C. Xu and Z. L. Wang, *Nat. Commun.*, 2020, **11**, 2093.

# CHAPTER-II

## Assembled *N*-glycosyl naphthalimides as a flexible semiconductor

# 2.1. Introduction

Carbohydrates have attracted significant interest from academia and industry as one of the promising molecules widely abundant in nature in simple and complex architecture, performing various brilliant tasks.[1–6] In addition to the energy storage and structure imparting properties, carbohydrates act as an active component in various coenzymes and genetic molecules.[2,7–9] In particular, carbohydrates in their simplest form, generally referred to as either glycoside or glycoconjugates display a broad range of applications in food, agriculture, cosmetics, health care, electronics, and pharmaceutical sectors.[10–19] Depending upon the type of atom linked to the anomeric carbon of the carbohydrate moiety, glycosides were classified into *C*, *N*, *S*, and –*O* glycosides.[20–24] Among the various glycosides reported in the literature, *N*-glycosides received special attention among researchers because of their existence as an important component in DNA, RNA, cofactor, and a large variety of signaling molecules.[25,26] By considering the salient feature of *N*-glycosides in the field of pharmaceutical science and molecular materials, in this paper, we have synthesized a library of *N*-glycosides from monosaccharides, generally referred as a chiral pool and naphthalimides.

The selection of naphthalimide as an aglycon part is due to the presence of a highly conjugated system and immense pharmacological properties.[27-29] A patent review by Kamal *et al*. revealed the potential applications of naphthalimide-based functional materials as therapeutic agents and fluorescent probes.[28] Conjugation of active naphthalimide derivatives with other functional components has become an interesting area of research.[30] Recently Fu *et al*. have developed a photochromic carbohydrate-modified naphthalimide-serum protein hybrid by adopting a simple host-guest assembly process, which displayed a unique duplexed fluorescence blinking manner for precision bio-imaging.[31] In a similar line, Li and co-workers have adopted the click chemistry for the conjugation of glucose and galactose with a naphthalimide zinc ion probe, which substantially increases the aqueous sensitivity, specific cell targeting ability, and reduced cytotoxicity.[32] It is worth mentioning that Cavigiolio *et al*. has synthesized amphiphilic sugar and deoxy uridine conjugate of 1,8-naphthalimides by adopting protection and deprotection of sugar moiety and by using expensive catalysts.[33] It is proven that the molecular self-assembly of sugar-naphthalimide derivatives furnishes complex hierarchical luminescent aggregates, which paved the way for the development of advanced electronics, luminescent materials, and biomaterials.[34–39]. Recently, Gudeika has discussed the applications of naphthalimides in a way that can be useful for material scientists and electronic engineers.[40] Zhou and coworkers discussed the design and performance of naphthalimide and other imide-based semiconductors and demonstrated their utility in the organic field–effect transistors (OFET). However,

bendability, deformability, and smartness are the key features for the fabrication of flexible devices, which display wide applications in electronics and optoelectronics. The intrinsic brittleness exhibited by the assembled naphthalimides restricts their use in the field of flexible semiconductors.[41]

There is no report on the fabrication of flexible semiconductors based on the self-assembly of glycosyl naphthalimides, which is achieved by anchoring glycosyl naphthalimides on cotton fabric through hydrogen bonding. The demonstrated flexible organic semiconducting material obtained via a more sustainable pathway would provide an opportunity to fabricate green electronics. It is worth mentioning that the reported methods for the synthesis of sugar-naphthalimide derivatives involve limited substrate scope and the use of highly complex protection and deprotection strategies or expensive catalysts. To overcome the existing limitations in synthesizing sugar-conjugated naphthalimides, this report adopts a simple N-glycosylation method with a broad substrate scope. In addition to the synthesis of sugar-conjugated naphthalimides, we have explored the molecular self-assembly in various solvents utilizing the non-covalent interactions such as H-bonding, π–π interaction, and van der Waals forces and proposed self-assembly mechanism. The semiconducting property of structurally stable molecular architecture in thin film and flexible fabric form was evaluated, which is crucial in the development of organic electronics.

## 2.2. Results and discussion

Naphthalimides are a potential candidate for the development of optoelectronic devices. In particular, theoretical and experimental investigation on aggregated naphthalimides revealed the existence of improved electronic coupling, which results in enhanced charge transport ability and photo-conducting properties.[42] In the recent past, there has been an ever-increasing effort towards conjugating carbohydrates with other functional molecules due to their crucial role in supramolecular assembly. In this chapter, we have judiciously conjugated representative monosaccharides with naphthalimides using simple synthetic protocol, which displays a significant advance in green chemistry. Although several methods have been reported for synthesizing sugar-conjugated naphthalimides, a simple and green protocol integrating the concept of static molecular assembly has yet to be reported. The condensation of 3-nitro-1,8-naphthalic anhydride **1** with various n-alkylamines **2a-g** in methanol under reflux condition followed by reduction using Fe in MeOH-AcOH in one pot furnished the corresponding 5-amino-2-alkyl-naphthalimides **3a-g** in 90-95% yield.[43] In order to establish a suitable reaction

condition for the synthesis of *N*-glycosyl naphthalimides, optimization studies were performed using D-glucose **4a** and 5-Amino-2-decyl-naphthalimide **3b** as model substrates (**Table 2.1**).

At the outset, to check the feasibility of the *N*-glycosylation reaction, initially, the reaction was performed in water, ethanol, methanol, glycerol, ethylene glycol, PEG-200, dioxane, acetonitrile, and tetrahydrofuran, without any catalyst (**Table 2.1, Entry 1-12**). Unfortunately, polar and nonpolar aprotic solvents, including the green reaction medium and water, did not render the desired product at room temperature. Nevertheless, the use of polar protic solvents furnished the desired *N*-glycosyl naphthalimide in traces. To further improve the yield, the reaction was screened in the presence of weak acids, including AcOH (pKa = 4.76), Pyridine in AcOH (pKa = 5.23), and Lewis acids such as $InCl_3$, $Sc(OTf)_3$, and $BF_3.OEt_2$ in methanol at reflux condition. It is worth mentioning that decomposition of the substrate was observed in strong acids, and the use of weak acid generated traces of product along with undesired products. In contrast, Lewis acids delivered the desired product in 22-35% (**Table 2.1, entry 15-17**). The reaction performed in the presence of organic bases such as pyridine, piperidine, pyrrolidine, and TEA furnished the *N*-glycosyl naphthalimide in low yields (12-21%), even the prolonged reaction time did not improve the yield significantly (**Table 2.1, Entry 18-21**). To our surprise, the use of $(NH_4)_2SO_4$ generated the desired product in an excellent yield of 91%, whereas bases such as KOH, NaOH, $K_2CO_3$, and $NaHCO_3$ delivered the *N*-glycosyl naphthalimide in poor yield even at elevated temperature and prolonged reaction time or with undesired products.

However, after establishing a suitable reaction condition, further investigation into why the use of $(NH_4)_2SO_4$ furnished an excellent yield and why other acids, bases, and salts failed to do so. To probe the responsible component of $(NH_4)_2SO_4$ (either ammonium ion or sulphate ion) in the process of *N*-glycosylation, $NH_4Cl$, and $NH_4OH$, catalysts providing ammonium ion, and $Na_2SO_4$, a catalyst providing sulphate ion were chosen. However, all the tested salts failed to provide good yields (**Table 2.1, Entry 22-24**). Furthermore, the reaction was checked in various salts such as $NH_4Cl$ (pH = 4.6), ammonium oxalate (pH = 6.4), and ammonium phosphate (pH = 4.0), where their pH is in the range of $(NH_4)_2SO_4$ (pH = 5.5) and observed the poor yields. Hence, the arrived optimized condition to generate N-glycosyl naphthalimides is methanol, $(NH_4)_2SO_4$ (0.1 mmol), 65 °C, 24h. Low yield was observed when the reaction was performed at room temperature, and the elevated temperature, 65 °C, and prolonged reaction time did not improve the yield significantly (**Table 2.1**).

**Table 2.1**. Optimization of the reaction conditions for the synthesis of *N*-glycosyl naphthalimides using D-glucose and 5-Amino-2-decyl-naphthalimide **3c** as a model substrates.[a]

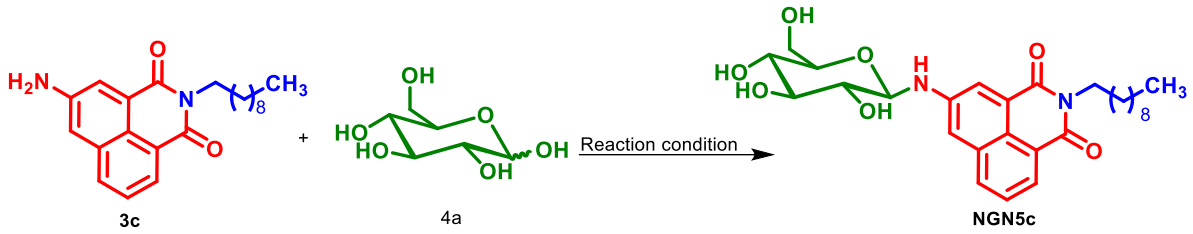


| S.No | Solvent | Temp (°C) | Catalyst | Time (h) | Yield (%)[b] |
|---|---|---|---|---|---|
| 1 | Toluene | 25 | - | 24 | NR |
| 2 | DCM | 25 | - | 24 | NR |
| 3 | THF | 25 | - | 24 | NR |
| 4 | Dioxane | 25 | - | 24 | NR |
| 5 | MeOH | 25 | - | 24 | Trace[c] |
| 6 | EtOH | 25 | - | 24 | Trace[c] |
| 7 | $CH_3CN$ | 25 | - | 24 | NR |
| 8 | DMF | 25 | - | 24 | NR |
| 9 | $H_2O$ | 25 | - | 24 | NR |
| 10 | Glycerol | 25 | - | 24 | Trace[c] |
| 11 | Ethylene glycol | 25 | - | 24 | Trace[c] |
| 12 | PEG-200 | 25 | - | 24 | Trace[c] |
| 13 | MeOH | 65 | AcOH | 24 | Trace[e] |
| 14 | MeOH | 65 | Pyridine/AcOH | 24 | Trace[e] |
| 15 | MeOH | 65 | $InCl_3$ | 24 | 22 |
| 16 | MeOH | 65 | $Sc(OTf)_3$ | 24 | 35 |
| 17 | MeOH | 65 | $BF_3.OEt_2$ | 24 | 27 |
| 18 | MeOH | 65 | Pyridine | 24 | 15 |
| 19 | MeOH | 65 | Piperidine | 24 | 18 |
| 20 | MeOH | 65 | Pyrrolidine | 24 | 21 |
| 21 | MeOH | 65 | TEA | 24 | 12 |
| 22 | MeOH | 65 | $NH_4OH$ | 24 | 18 |
| 23 | MeOH | 65 | $(NH_4)_2SO_4$ (pH = 5.5) | 24 | 91[d] |
| 24 | MeOH | 65 | $Na_2SO_4$ | 24 | 14 |
| 25 | MeOH | 65 | $(NH_4)_3PO_4$ (pH = 4.0) | 24 | 12 |
| 26 | MeOH | 65 | $(NH_4)_2C_2O_4$ (pH = 6.4) | 24 | 17[e] |
| 27 | MeOH | 65 | $NH_4Cl$ (pH = 4.6) | 24 | 24 |
| 28 | EtOH | reflux | $(NH_4)_2SO_4$ | 24 | 84 |
| 29 | $CH_3CN$ | reflux | $(NH_4)_2SO_4$ | 24 | Trace[c] |
| 30 | DMF | 90 | $(NH_4)_2SO_4$ | 24 | Trace[c,e] |
| 31 | $H_2O$ | 90 | $(NH_4)_2SO_4$ | 24 | NR |
| 32 | Glycerol | 90 | $(NH_4)_2SO_4$ | 24 | Trace[c] |
| 33 | Ethylene glycol | 90 | $(NH_4)_2SO_4$ | 24 | 43 |
| 34 | PEG-200 | 90 | $(NH_4)_2SO_4$ | 24 | 25 |
| 35 | MeOH | 25 | $(NH_4)_2SO_4$ | 24 | 24 |
| 36 | MeOH | 65 | $(NH_4)_2SO_4$ | 48 | 93 |

[a] all the reactions were carried out with 5-Amino-2-decyl-naphthalimide **3c** (1 mmol), and D-glucose **4a** (1.5 mmol) in 10 mL of MeOH. [b] Isolated yields. [c] trace product was observed in TLC, where the starting materials were not consumed even after a prolonged reaction time. [d] Optimized reaction condition for the synthesis of *N*-glycosyl naphthalimides. [e] other than the desired product formed.

After establishing a suitable reaction condition for the synthesis of *N*-glycosyl naphthalimides, the scope and limitations of the protocol are studied with a variety of unprotected monosaccharides (**4a-c**) and 5-amino-2-alkyl-naphthalimides **3a-g**. In the recent past, exploring the potential utility of unprotected monosaccharides, a molecule displaying a pool of abundant chiral centers has once again become the thrust area of research to develop advanced organic smart materials. In this chapter, glycosylation of unprotected monosaccharides (**4a-c**) with 7 different 5-amino-2-alkyl-naphthalimides **3a-g** furnished the selective *β*-anomeric product in high yields (**Figure 2.1a)**. The key components for the achievement of a selective product are the activation of the anomeric hydroxyl group and the added nucleophilicity of the substrate. However, the optimized condition using $(NH_4)_2SO_4$ provides selectively *β*-anomeric products and mechanism that were computationally validated. All the 21 different *N*-glycosyl naphthalimides were characterized by NMR, IR, and mass spectral studies.

The existence of *β*-anomeric form was identified by calculating the coupling constant of the anomeric proton of compound **NGN7a**, which displayed doublet after $D_2O$ exchange and resonated at 4.58 ppm with the coupling constant of $J = 8.0$ Hz. It is worth mentioning that, for the synthesis of *N*-glycosyl naphthalimides, we have adopted the best possible green protocol, such as the use of substrate obtained from renewable resources, green solvent, and catalyst and reducing the number of steps and side products. In the entire reaction sequence, the only side product obtained is 2 molecules of water and one molecule of oxygen, with an excellent yield of the desired product even without column chromatography purification. Fortunately, the $(NH_4)_2SO_4$ catalyst used in this reaction is generally recognized as safe (GRAS) by the United States Food and Drug Administration (FDA). A plausible mechanism for the reaction of D-glucose and 5-amino-2-alkyl-naphthalimide in the presence of ammonium sulfate has been proposed and theoretically investigated using the Gaussian 16 program.[44]

The nucleophilic attack of the 5-amino-2-alkyl-naphthalimide on the carbonyl carbon of D-glucose in the presence and absence of $(NH_4)_2SO_4$ have been compared to assess the role of the catalyst. The reaction mechanism in the presence of the catalyst is given in **Figure 2.1b**. The mechanism involves the simultaneous protonation and nucleophilic attack on carbonyl group of the D-glucose to give the IM1 via TS1. Further deprotonation followed by dehydration of IM1 furnish IM2 and IM3, respectively. Free hydroxyl group at C-5 position of glucose moiety undergoes ring closure to give the corresponding desired product.

The geometries of various reactants, catalysts, intermediates, transition states (TSs), and products were fully optimized without any geometrical/symmetrical constraints. Density functional theory (DFT) calculations were performed using B3LYP functional employing a 6-

31G* basis set.[45,46] The TSs were confirmed by the characteristic single imaginary frequency with displacement vectors in the bond formation and breaking direction. The energetics of the reactions were calculated in the gas phase at 298.15 K and 1 atm pressure. Zero-point energy correction was also included in the calculated relative energies.

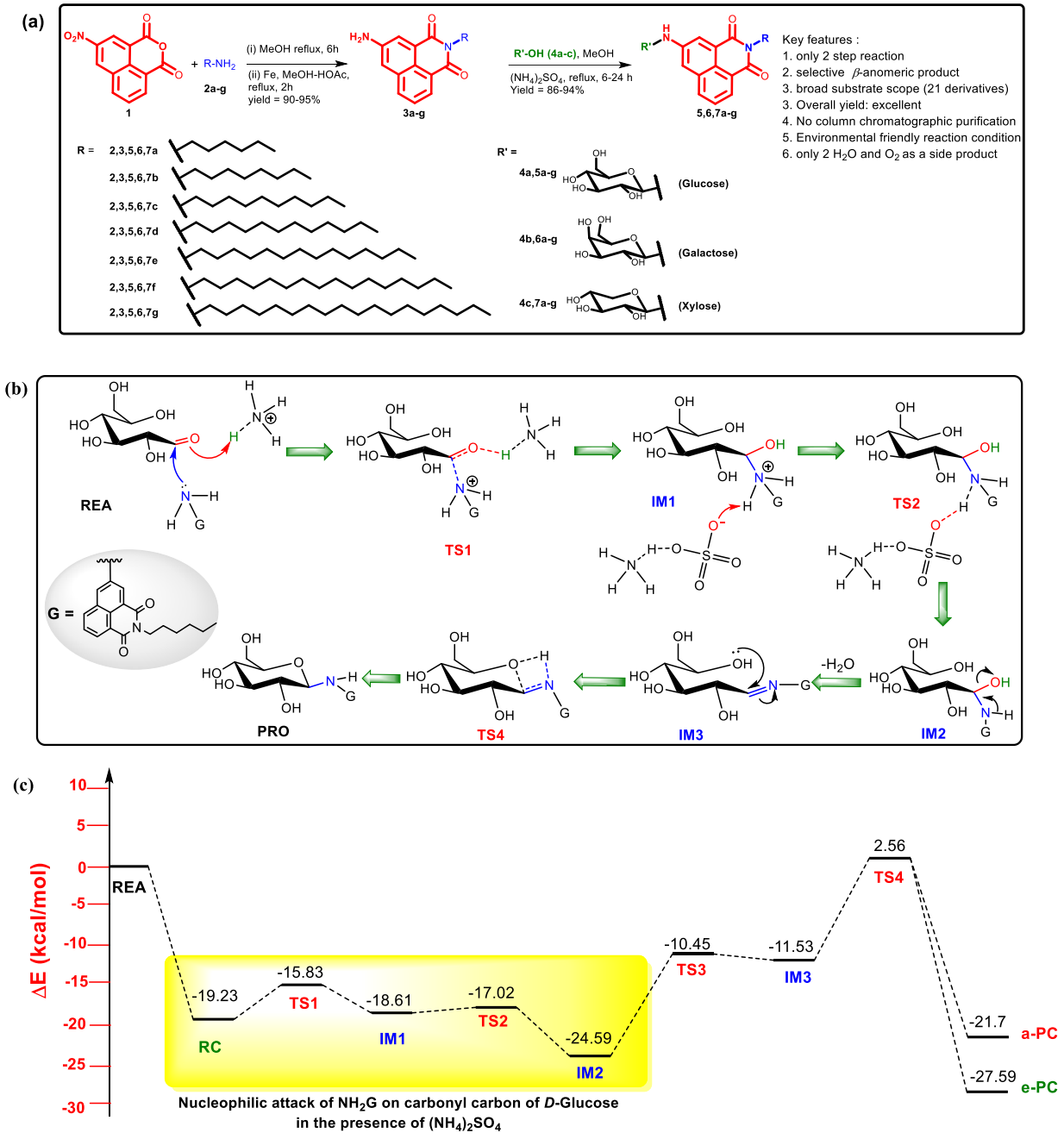


**Figure 2.1**. (a) Synthesis of *N*-glycosyl naphthalimides **NGN5-7(a-g)**. (b,c) Proposed mechanism and relative energy profile diagram for *N*-glycosylation of D-glucose **4a** and 5-amino-2-hexyl-naphthalimide **3a** in the presence of $(NH_4)_2SO_4$, respectively. REA: reactants, RC: reactant complex, TS: transition state, IM: intermediate, PRO: product, a-PC: axial product (α-anomeric product) and e-PC: equatorial product (*β*-anomeric product).

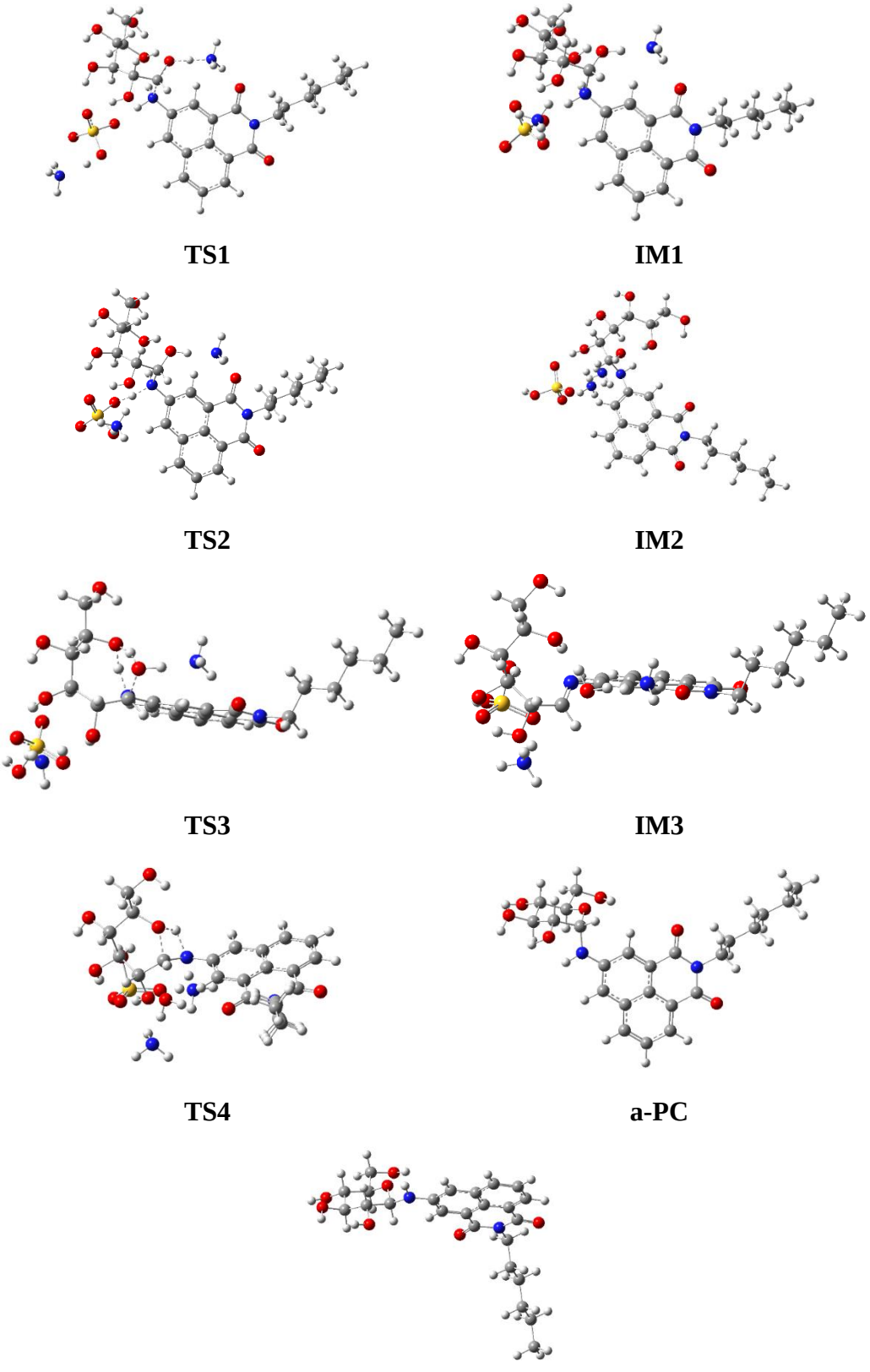


**Figure 2.2**. Images of the optimized geometries of the TSs, IM, and products obtained in the reaction between D-glucose and *N*-alkyl-3-aminonapthlimide in the presence of ammonium sulphate. TS, transition state; IM, intermediate; a-PC, axillary product ($\alpha$-anomeric product); e-PC, equatorial product ($\beta$-anomeric product).

The relative energy profile for the proposed mechanism and the reaction in the absence of ammonium sulphate are shown in **Figure 2.1c**, and **Figure 2.3a**, respectively. Images of the

optimized geometries of the TSs, IM, and products obtained in the reaction between D-glucose and 5-amino-2-alkyl-naphthalimide in the presence and absence of $(NH_4)_2SO_4$ are given in **Figure 2.2 and 2.3**. The formation of IM1 via TS1 requires 3.4 kcal/mol and deprotonation of IM1 to give a stable intermediate IM2 via TS2 requires only 1.58 kcal/mol. The relative energy for IM2 is -24.59 kcal/mol, which is lower than that of the RC. Interestingly, the energy profile diagram of the *N*-glycosylation reaction in the absence of the catalyst (**Figure 2.3a**) proceeding via TS and IM2 requires 30.26 kcal/mol, which is relatively higher than that of the reaction proceeding in the presence of the catalyst (**Figure 2.3**). Thus, the $(NH_4)_2SO_4$ makes the nucleophilic attack of 5-amino-2-alkyl-naphthalimide more feasible. Furthermore, the IM2 loses a water molecule to give a relatively less stable intermediate IM3, which could furnish either axial or equatorial products or even both upon cyclization. The relative energy for the axial product is observed as -21.7 kcal/mol and the equatorial product is -27.59 kcal/mol. Thus, the equatorial product is more stable than the axial product. It is worth mentioning that the relative energy of the axial product is more than the stable intermediate IM2. Thus, the theoretical investigation clearly reveals the exclusive formation of equatorial product (*β*-anomer), which strongly compliments the experimental outcome of the reaction emphasizing the role of ammonium sulfate.

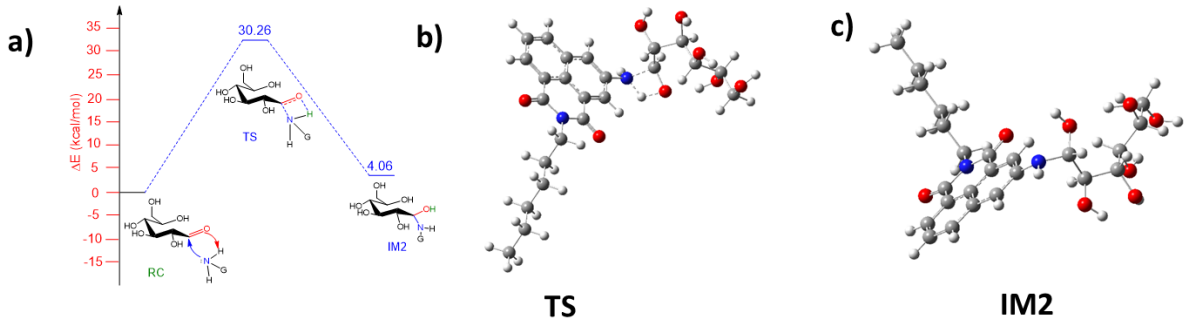


**Figure 2.3**. (a)Relative energy profile diagram for *N*-glycosylation of D-glucose **4a** and 5-amino-2-hexyl-naphthalimide **3a** in the absence of $(NH_4)_2SO_4$. (RC: reactant complex, TS: transition state, IM: intermediate). Images of the optimized geometries of the TS (b) and IM2 (c) obtained in the reaction between D-glucose and *N*-alkyl-3-aminonapthlimide in the absence of ammonium sulphate. TS, transition state; IM, intermediate.

Supramolecular self-assembly of molecules in various living organisms generated a broad range of functional architectures performing brilliant tasks including complex biological functions.[47–52] In the self-assembly phenomenon, individual components organize spontaneously through specific interactions to generate the desired architecture with greater precision, flexibility, and error correction capacity through the "bottom-up" fabrication method.[53–57] In particular, the self-assembly of carbohydrates, one of the important naturally occurring biocompatible and biodegradable molecules, renders an opportunity to arrive at different functional architectures that hold potential applications in the electronic and bio sectors.[58–65] Seeberger and coworkers

have summarized the advances in carbohydrate supramolecular chemistry emphasizing carbohydrates as stabilizers of complex architectures.[66] Owing to the fascinating applications of assembled carbohydrate amphiphiles, the self-assembly studies were performed for a series of amphiphilic *N*-Glycosyl Naphthalimides (NGN) judiciously designed by incorporating the salient structural features such as hydroxyl and amide linkage for hydrophilicity, alkyl chain to induce hydrophobicity and naphthalimide moiety for π- π staking. Initially, the gelation behaviour of NGN (**5, 6, 7a-g**) bearing the varying degree of hydrophilic-lipophilic balance (HLB) was studied by the "stable to inversion method", which involved heating the sample in conquer amount of solvent followed by cooling the resultant solution to room temperature. While cooling, NGN starts to self-assemble into the anisotropic structure, which then further entangles to give a network wherein solvents are immobilized through surface tension and capillary forces. The gelation ability of NGN in various solvents and oils was summarized in **Table 2.2**. Among the various NGN tested, epimers **NGN5d-g** and **NGN6d-g** derived from glucose and galactose displayed excellent gelation behaviour. Gel images of **NGN5d-g** in $CHCl_3$ under normal and UV light are shown in **Figure 2.4a**. Interestingly, these compounds exhibited hydrogelation in DMSO-$H_2O$ (40% v/v) with critical gelation concentration (CGC) of 0.5% (wt/v) and organogelation in chloroform, cyclohexane, and xylene with CGC of 0.3, 0.8 and 0.6 % (wt/v) respectively. Representative images of gel formed by compound **NGN5d** in DMSO-$H_2O$, cyclohexane, and xylene are given in **Figure 2.4b**. In the case of **NGN7a-g**, NGN derived from xylose, hydrogelation (CGC: 0.6% wt/v) was observed in all the derivatives irrespective of HLB ratio and oleogelation in olive oil (0.6 % wt/v) was observed in **NGN7f** and **NGN7g**, where hydrophobicity is comparatively more in that series. Investigation on the gelation behaviour of **NGN5a-g** and **NGN6a-g** revealed that the tuning of the molecular level orientation of the C4–OH group didn't affect the gelation behaviour, whereas compounds **NGN7a-g** displayed a change in gelation behaviour because of the absence of one of the hydroxyl groups. The thermo-reversible nature of hydrogel, organogel, and oleogel were studied by repeated heating and cooling cycles and found stable even after 25 cycles. To visualize the strength of the gel, the sol-to-gel transition temperature, $T_g$ for a hydrogel formed by **NGN5c**, **6c,** and **7c** was determined. The representative examples possess the decyl group as hydrophobic tail, naphthalimide as π- π staking unit, and glucose, galactose, and xylose as hydrophilic head group respectively. $T_g$ of hydrogel derived from **NGN5c**, **6c**, and **7c** at CGC was determined as 69, 86, and 73 °C, respectively, which gradually increase with the increase in the gelator concentration.

**Table 2.2**. Gelation Studies of Compound **NGN5-7a-g** in Various Solvents and Vegetable Oils.

| Solvent/Oils | 5a | 5b | 5c | 5d | 5e | 5f | 5g | 6a | 6b | 6c | 6d | 6e | 6f | 6g | 7a | 7b | 7c | 7d | 7e | 7f | 7g |
|---|---|---|---|---|---|---|---|---|---|---|---|---|---|---|---|---|---|---|---|---|---|
| linseed oil | S | S | S | S | S | S | S | S | S | S | S | S | S | S | S | S | S | S | S | S | S |
| olive oil | PG | PG | PG | PG | PG | PG | PG | PG | PG | PG | PG | PG | PG | PG | PG | PG | PG | PG | PG | G(0.6) | G(0.6) |
| paraffin light | PG | PG | PG | PG | PG | PG | PG | PG | PG | PG | PG | PG | PG | PG | S | S | S | S | S | S | S |
| PEG | PG | PG | PG | PG | PG | PG | PG | PG | PG | PG | PG | PG | PG | PG | S | S | S | S | S | S | S |
| chloroform | S | S | PG | G (0.3) | G (0.3) | G (0.3) | G (0.3) | S | S | PG | G (0.3) | G (0.3) | G (0.3) | G (0.3) | S | S | S | S | S | S | S |
| DMSO | S | S | S | S | S | S | S | S | S | S | S | S | S | S | S | S | S | S | S | S | S |
| DMSO+$H_2O$ | G(0.5) | G(0.5) | G(0.5) | G(0.5) | G(0.5) | G(0.5) | G(0.5) | G(0.5) | G(0.5) | G(0.5) | G(0.5) | G(0.5) | G(0.5) | G(0.5) | G(0.6) | G(0.6) | G(0.6) | G(0.6) | G(0.6) | G(0.6) | G(0.6) |
| cyclohexane | I | I | S | G (0.8) | G (0.8) | G (0.8) | G (0.8) | I | S | S | G (0.8) | G (0.8) | G (0.8) | G (0.8) | I | I | S | S | S | S | S |
| Toulene | PG | PG | PG | PG | PG | PG | PG | PG | PG | PG | PG | PG | PG | PG | PG | PG | PG | PG | PG | PG | PG |
| N-Methyl-2-pyrrolidone (NMP) | P | P | P | P | P | P | P | P | P | P | P | P | P | P | P | P | P | P | P | P | P |
| 1,4-dioxane | S | S | S | S | S | S | S | S | S | S | S | S | S | S | S | S | S | S | S | S | S |
| EtOH | P | P | P | P | P | P | P | P | P | P | P | P | P | P | P | P | P | P | P | P | P |
| methanol | P | P | P | P | P | P | P | P | P | P | P | P | P | P | P | P | P | P | P | P | P |
| isopropanol | S | S | S | S | S | S | S | S | S | S | S | S | S | S | S | S | S | S | S | S | S |
| xylene | S | S | S | G(08) | G(0.6) | G(0.6) | G(0.6) | S | S | S | G(0.8) | G(0.6) | G(0.6) | G(0.6) | S | S | S | S | S | S | S |
| water | I | I | I | I | I | I | I | I | I | I | I | I | I | I | I | I | I | I | I | I | I |

CGC, critical gelation concentration is given in % w/v. S, soluble; G, Gel; PG, partial gel; P, precipitation

It is observed that the hydrogel of **NGN6c**, derived from galactose exhibited higher $T_g$ (86 ºC) when compared to its epimer **NGN5c**, derived from glucose. This result clearly reveals that the epimerization process could substantially alter the gel strength either by intermolecular interactions or entanglement of the assembled structure. The increased $T_g$ displayed by hydrogel

obtained from **NGN7c**, where one -OH group is lesser than **NGN5c** discloses that the gel strength is not directly proportional to the number of hydroxyl groups, instead it is related to the strength of the intermolecular interaction exhibited by the molecule. Gelation and $T_g$ studies reveal that **NGN5c** and **NGN6c** display the same level of HLB-formed gel with almost the same CGC, whereas its strength varies because of the orientation of the -OH group in the 3D lattice, which is responsible for intermolecular H-bonding. Recently, self-assembly concepts emerged as a fascinating area and hold the attention of many researchers working in the field of advanced electronics and biomaterials because of their tuneable properties arising at the molecular level.[67–69] Until today, no clear-cut molecule design parameters suitable for self-assembly have been reported because of their difficulty in probing and understanding molecular-level interactions. However, several researchers have correlated the crystallization process to gelation because both involve intermolecular interaction at different levels. This study generated a library of compounds and correlated their structure-assembly behaviour. To gain further insight into self-assembly, Fourier-Transform Infra-red Spectroscopy (FT-IR) is one of the best methods to explain intermolecular interactions effectively. Nevertheless, a comparison of FT-IR spectra of the compound in an amorphous and assembled state, generally referred to as the xerogel state could provide a direct measure of the degree of H-bonding and other intermolecular interactions, even though there is an influence on the existence of some degree of interaction in amorphous state. FTIR spectra of compound **NGN5d** in amorphous and xerogel states were recorded and shown in **Figure 2.4c** to capture the formation of intermolecular interactions in the gelator molecule and during the gelation process. The characteristic peak in the FTIR spectra of **NGN5d** in amorphous state displayed peaks at 3419, 3322, 2848, 1693, 1655, 1628, 1291, 1088 and 1028 $cm^{-1}$, which corresponds to –OH, -NH, -CH (alkane), amide I, amide II, -C=C (conjugated alkene), -C-N (Aromatic amine), -C-O (secondary alcohol) and –C-O (primary alcohol) respectively. Generally, in an amorphous state, various functional group, alkyl moiety, and aryl system orient randomly in a 3-dimensional lattice, however, the probability of intermolecular aggregation or interaction is much less. Interestingly, compound **NGN5d** in xerogel state displayed a sensitive molecular arrangement due to intermolecular interactions and directly reflected on the Attenuated total reflection-IR analysis. In xerogel state, peaks observed at 3372, 3271, 2852, 1699, 1649, 1622, 1286, 1073 and 1019 $cm^{-1}$, which corresponds to –OH, -NH, -CH (alkane), amide1, amide 2, -C=C (conjugated alkene), -C-N (Aromatic amine), -C-O (secondary alcohol) and –C-O (primary alcohol) respectively.

A careful analysis of IR data revealed that the characteristic peaks of functional groups responsible for intermolecular interaction such as -OH, -NH, and C=O displayed a shift and

were in well accord with the principle of IR spectroscopy. Another characteristic signal corresponding to C=C stretching of conjugated alkenes and C-O stretching of primary alcohol and secondary alcohol also displayed a shift to the lower frequency region, which implies that the existence of π-π staking in naphthalimide moiety and the involvement of oxygen in intermolecular H-bonding (**Figure 2.4c**).

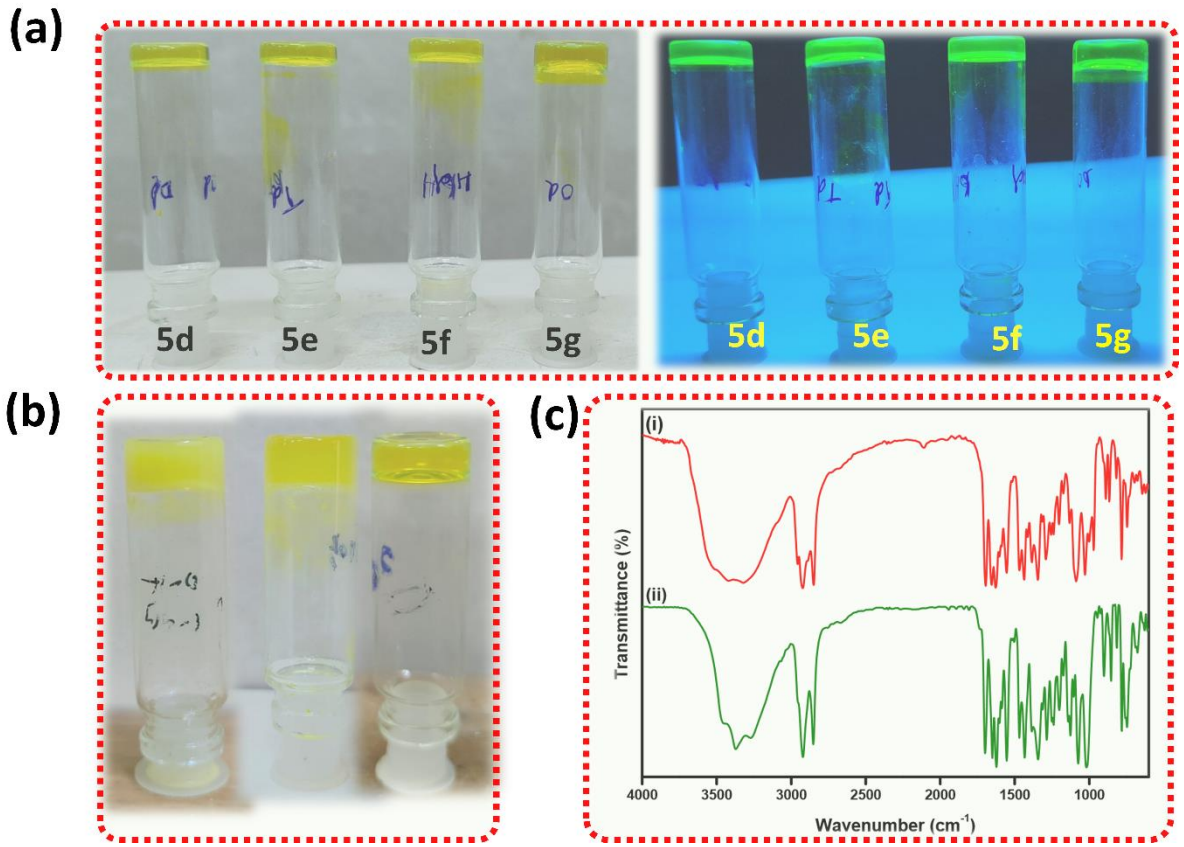


**Figure 2.4**. (a) Images of gel formed by compounds **NGN5d-g** in $CHCl_3$ under normal and UV light (CGC = 0.3% wt/v. (b) images of gel formed by compound **NGN5d** in DMSO-$H_2O$ (40% v/v), cyclohexane and xylene respectively. (c) A comparison of FT-IR spectra of compound **NGN5d** in (i) amorphous state and (ii) xerogel state (assembled state).

The influence of various groups in molecular assembly can be examined by concentration-dependent and variable temperature NMR studies. Fortunately, most of the compounds form gel in the DMSO-$H_2O$ system (40%v/v), which opens a gateway to probe the intermolecular interactions. $^1$H NMR spectra of **NGN5d** in DMSO-$d_6$ displayed signal at δ 8.11 (two aromatic protons $H_c$, $H_e$ got merged), 8.07, 7,66, 7.44 and 7.18 ppm, which represent $H_{c,e}$, $H_a$, $H_d$, $H_b$ and NH protons respectively (**Figure 2.5a**). Upon the addition of $D_2O$ (60% v/v), the broadening of signals corresponding to aromatic and carbohydrate protons was observed without displaying any appreciable shift. Interestingly, a clear gel formation is observed when the solution is heated and cooled to room temperature, which is then subjected to variable temperature NMR studies (**Figure 2.5a**). $^1$H NMR spectra of gel formed by **NGN5d** in DMSO-$d_6$-$D_2O$ displayed the disappearance of exchangeable protons, downfield shift of $H_b$ and $H_e$ signals, and upfield shift

of $H_a$ signal clearly establish the participation of aryl group in π-π staking (**Figure 2.5a**). Generally, hydrogen atom experiencing greater electron density make larger opposition to the applied magnetic field, as a consequence, they feel a lower magnetic field and resonate at a lower frequency or shielding zone. During the process of self-assembly, the downfield shift of the $H_b$ and $H_e$ signals and the upfield shift of the $H_a$ signal disclose the substantial decrease and increase in electron densities, respectively. In order to investigate the thermo-responsive character of molecules in the gel state, we have performed variable temperature NMR studies. An increase in the temperature of gel up to 70 °C did not display any appreciable shift in signal, suggesting the strength of intermolecular interactions in gel.

Prediction of molecular arrangement in supramolecular gel is highly challenging because the structure and properties rely on building blocks' geometry and 3-D arrangement.[70–72] However, with the established intermolecular interactions between the individual gelator molecules, packing can be demonstrated from a small angle of XRD. Xerogel obtained from compound **NGN5d** displayed 2θ = 2.9, 7.6, 8.6, 13.1, 15.8, 18.7, 19.9, 22.4 and 26.5° corresponding to the interplanar spacing (d-spacing) at 3.01, 1.16, 1.03, 0.67, 0.56, 0.47, 0.44, 0.39 and 0.33 nm respectively (**Figure 2.5b**). Intermolecular interactions facilitate the molecular self-assembly resulting in the formation of 3-D fibrillar network architecture bearing the length of 3.01 nm as identified from SAXRD, which is higher than the end-end molecular length of compound **NGN5d**. The energy-minimized structure of **NGN5d** revealed the end-to-end molecular length as 2.1 nm, which is lower than the d-spacing value of 3.01, suggesting a double layer stabilized by intermolecular H- H-bonding (**Figure 2.5c**). Subsequently, XRD recorded for the gel formed by **NGN5d** in chloroform suggests that the hydrophobic tail is projecting outwards, and the bilayer is stabilized by intermolecular H-bonding. It is worth mentioning that peaks observed at 0.67 and 0.56 nm represent hydrophobic interactions, 0.47 and 0.44 represent π-π staking, and 0.39 and 0.33 nm stand for H-bonding, all these values are in good agreement with Bragg's law (**Figure 2.5b**). Based on the FTIR, NMR, and SAXRD data, we have proposed a molecular self-assembly mechanism, as shown in **Figure 2.5c**.

Conventionally, materials derived from a compound possessing conjugated π-bonds absorb light at a lower wavelength of higher energy and emit light at a higher wavelength of lower energy, which is referred to as a fluorescent material. In particular, fluorescent gels (hydrogel, oleogel, organogel) differ from conventional fluorescent solutions and solids because of their dynamic and reversible nature achieved by means of molecular self-assembly utilizing various non-covalent interactions such as H-bonding, π–π interaction, and van der Waals forces, which leads to interesting optoelectronic properties. Recently, Loh and co-workers have provided an

overview of the recent development in the field of fluorescent gel materials, including physical and chemical properties and their laboratory applications.[73]

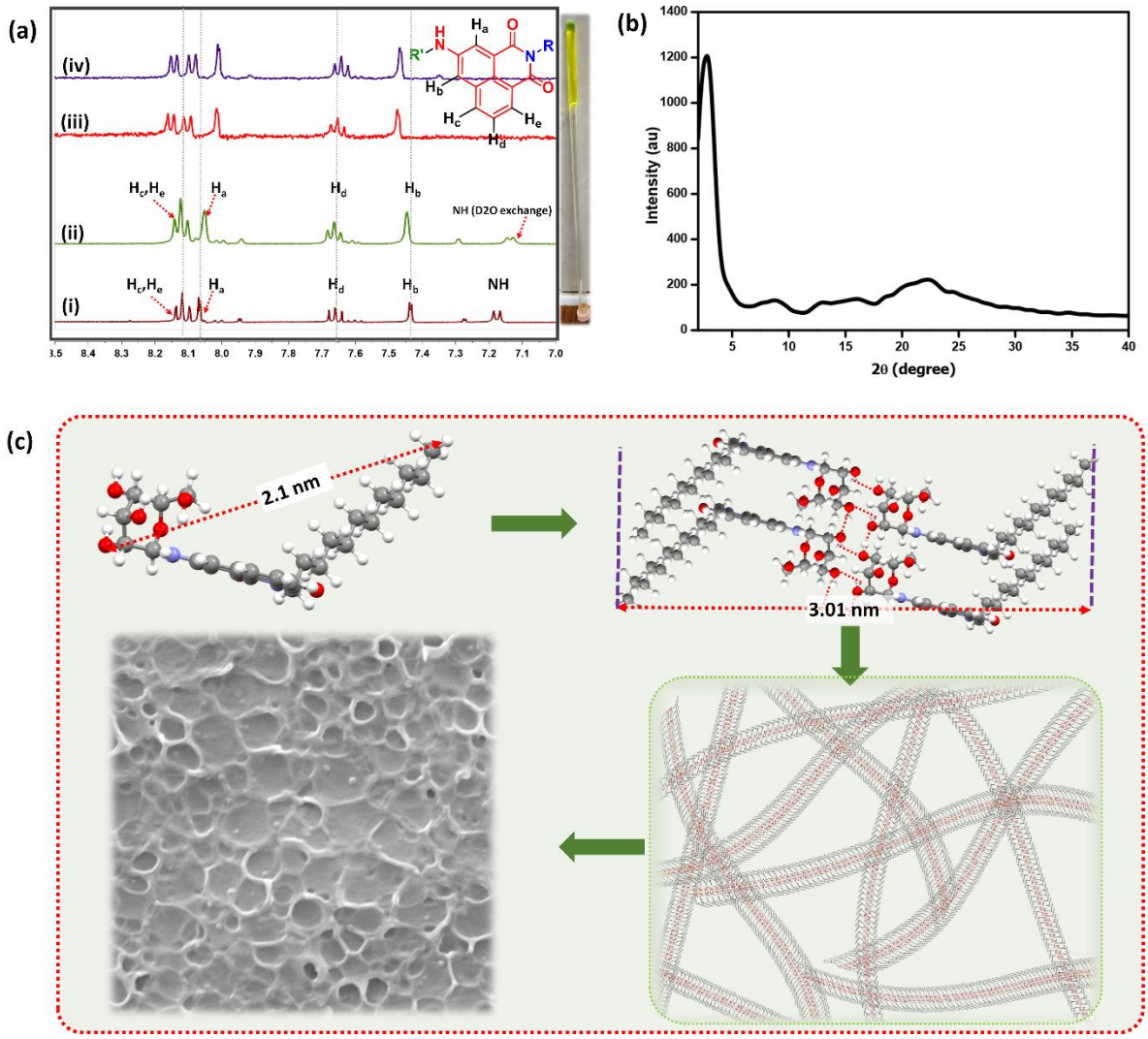


**Figure 2.5**. (a) NMR spectra of compound **NGN5d** in (i) DMSO-$d_6$, (ii) $D_2O$ 60% v/v (after shaking for 5 minutes), (iii and iv) gel form (after heating and cooling) at room temperature and 70 °C respectively. (b) XRD pattern of a xerogel obtained from compound **NGN5d**. (c) A schematic representation of molecular self-assembly of **NGN5d**. The dotted red line represents the H-bonding.

A common fluorescent gel fabrication technique includes the incorporation of fluorophore in the molecule itself or by intercalation into a non-fluorescent gel. Nevertheless, in the aspect of stability and reproducibility of fabricated material is a concern, covalently linking a fluorophore in a gelator is most preferred, and UV-visible spectroscopy is the most appropriate and sensitive method to investigate aggregation as a function of concentration. Absorption spectra of **NGN5d** in a gelling solvent, $CHCl_3$ are given in **Figure 2.6a**. Compound **NGN5d** in $CHCl_3$ ($5 \times 10^{-5}$M) displayed two well-resolved bands centered at 230 and 351 nm, which are assigned to $\pi$ -$\pi^*$ and n-$\pi^*$ transition of naphthalimide and amide groups, respectively. When compared to the UV-vis spectra of **NGN5d** in the dilute state, an increase in the concentration of the gelator

displayed a distinct change in the absorption band due to molecular aggregation. Interestingly, an increase in the concentration of the gelator displayed a bathochromic shift of the band centered at 230 nm to 257 nm with an increase in absorption intensity suggesting the existence of *J*-aggregate as a result of supramolecular organization. Spontaneous emission of light upon absorption of UV-vis radiation is termed "Luminescence", which has received a great application in photo-physics, chemistry, materials science, and biology. Generally, intermolecular interactions in the assembled molecules slowly disappear by dilution phenomenon and could be easily identified by fluorescence spectrophotometer. **Figure 2.6b** represents the emission behaviour of gelator **NGN5d** in $CHCl_3$ at various dilutions. Upon dilution, a gradual increase in emission intensity suggests the existence of "aggregation-caused quenching" due to π-π stacking of highly conjugated planar naphthalimide moiety.

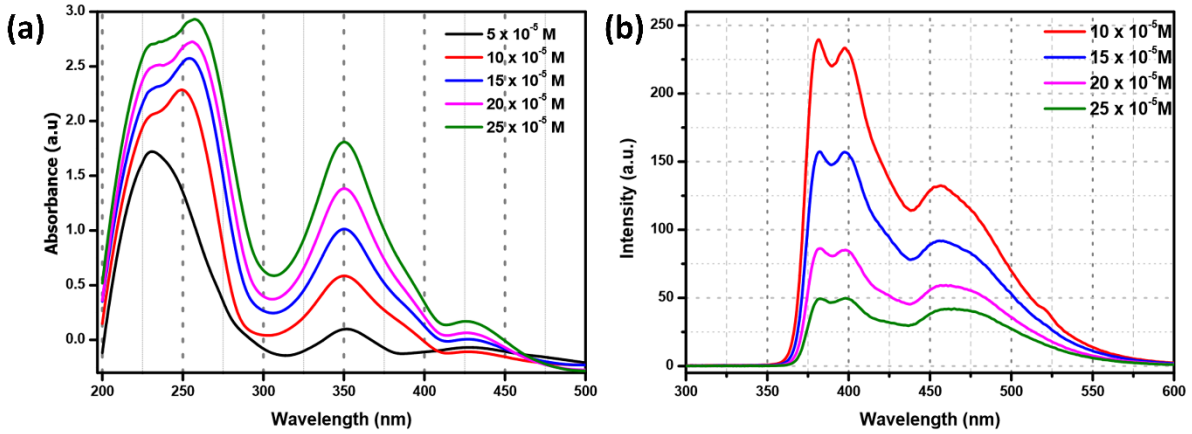


**Figure 2.6**. (a,b) UV-vis and Fluorescence titration of **NGN5d** dissolved in $CHCl_3$ respectively [$\lambda_{ex}$ = 250 nm].

Having established the assembly mechanism and photophysical behaviour of compound **NGN5d**, the morphology of gels was further investigated. Optical microscopy image of gel formed by **NGN5d** in $CHCl_3$ revealed the formation of a 3-dimensional fibrous network structure. To further probe the detailed gel architecture, SEM analysis of xerogel was performed, which furnished the existence of a fibrillar network structure with a width ranging from 50-150 nm wherein the solvent is trapped in the bore diameter of ~900 nm (**Figure 2.7a-d**). It is worth mentioning that the morphology of gel formed by compound **NGN5d** in DMSO-$H_2O$ displayed thin sheets with widths ranging from 100 to 200 nm (**Figure 2.7e-h**). This result clearly reveals that the solvent environment plays a key role in regulating the supramolecular self-assembly of the gelator into a gel material via intermolecular interactions, which can reflect in microscopic structure.[74] Interestingly, the gel formed by **NGN6d** in $CHCl_3$ displayed tubular architecture, whereas its epimer **NGN5d** exhibited a fibrillar network structure (**Figure 2.7**). Even though the use of the same solvent, $CHCl_3$, with fine-tuning in the 3D-orientation of -OH

group drastically influences the non-covalent interactions exhibited by the molecule, thereby greatly affecting the morphology of assembled materials.

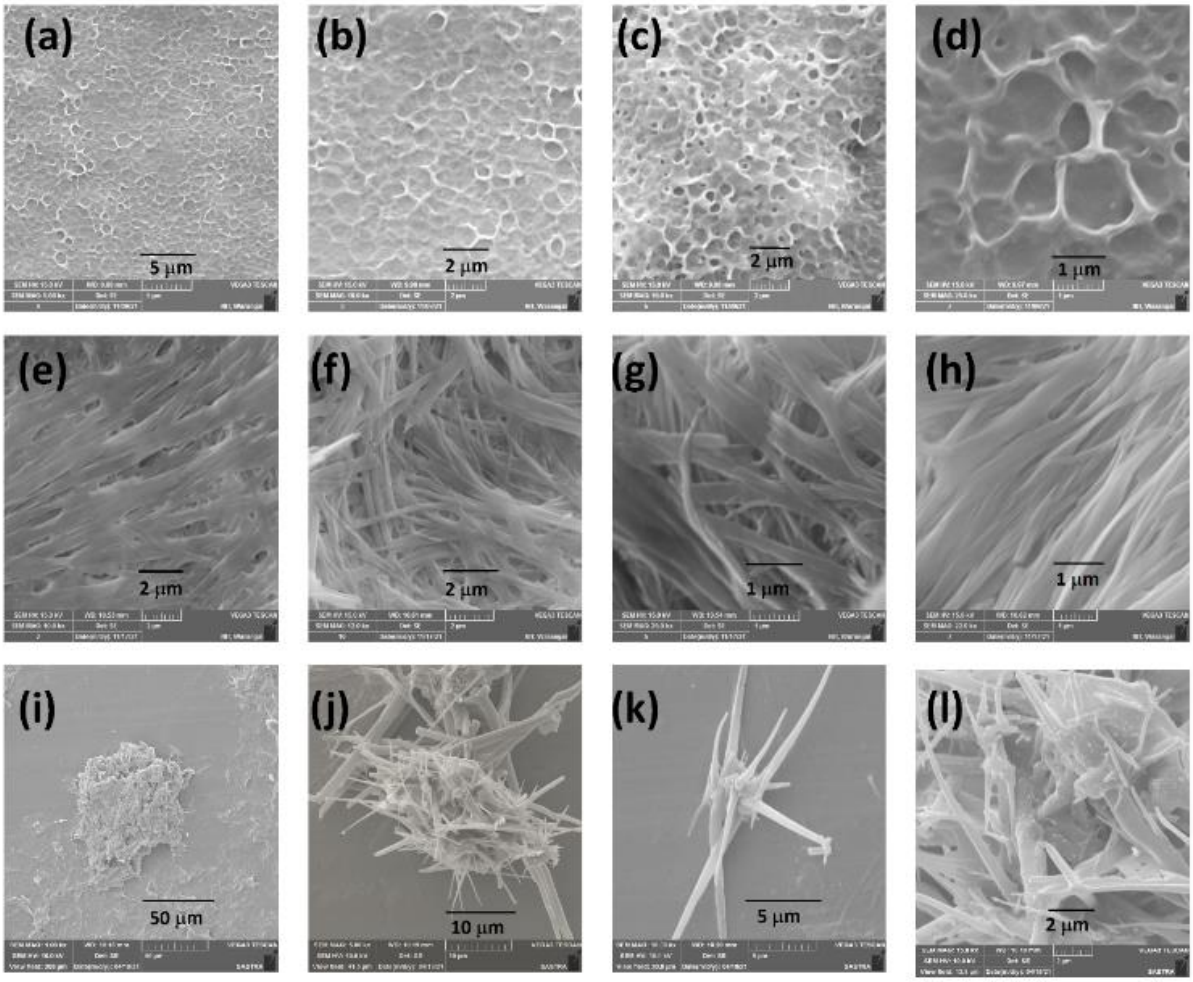


**Figure 2.7**. SEM images of gel formed by (a-d) **NGN5d** in $CHCl_3$, (e-h) NGN5d in DMSO-$H_2O$ (40 % v/v) and (i-l) **NGN6d** in $CHCl_3$.

Rheological measurement is generally defined as the extent of deformation of a material from its original structure in response to a force applied.[75–77] The rheology of solids, liquids, nano-composites, and polymeric materials is well established; nevertheless, soft materials derived from the molecular assembly are unique and do not behave like ideal solids or liquids.[78] In the aspect of materials engineering, it is essential to study the flow and viscoelastic behaviour of such soft material by measuring the storage modulus G′ (elastic) and the loss modulus G″ (viscous) in response to the strain. Soft material deformation in response to stress or strain is associated with the pattern of supra-molecular arrangement and degree of intermolecular interactions, and in some cases, the interaction of solvents with the assembled structure also plays a vital role. Bringing out a defined correlation in soft material properties displaying such a molecular level-to-atomic level phenomenon is a tedious task, hence heaps of the questions

associated with micro/nanostructure and viscoelastic behaviour remain unreciprocated. To realize the processability of these gels in materials fabrication, a trenchant understanding of soft material rheology is necessitated. The gel formed by **NGN5d** in $CHCl_3$ and DMSO-$H_2O$ was considered for our investigation. **Figure 2.8a-d** displays the response of G′ and G″ against strain sweep and frequency sweep. In both the gels, the greater value of storage modulus G′ as compared to loss modulus G″ within the range of linear viscoelastic region (LVE) suggests good mechanical strength as identified from strain amplitude sweep measurements. In the frequency sweep test, throughout the entire range analysis, the greater value of G′ than G″ clearly establishes the stability and good tolerance towards the external forces (**Figure 2.8b,d**).

In gel formed by the **NGN5d** in $CHCl_3$ and DMSO-$H_2O$, a slight deformation or fold in supramolecular structure is observed beyond the critical strain (γc) value of 0.002 and 0.005 % and complete gel to sol transformation was observed at γ = 0.04%, and 0.07% respectively (**Figure 2.8a, c**). Assembled systems derived from macromolecules, small molecules, and inorganic composites were widely used in the development of advanced materials for electronic and medical applications.[57,60,68] Nevertheless, thermo-reversible and self-healing at room temperature are important parameters for materials manufacturing and have received great attention among scientists because of their resemblance with living systems. To validate the thermal processability of gel in the field of material fabrication, continuous temperature ramp-up and ramp-down experiments for **NGN5d** in $CHCl_3$ were performed in view of electronic applications and **NGN5d** in DMSO-$H_2O$ for medical applications. The thixotropic behaviour of both gels was studied by a continuous step-strain experiment (**Figure 2.8f,h**).

Both the gels displayed good thermal stability and processability even after several temperature ramp-ups and down cycles (**Figure 2.8e,g**). The thermally reversible mechanism involves breaking network structure upon heating and rebuilding intermolecular interactions upon cooling by following the principle of microscopic reversibility. Upon the application of high strain (100%), storage modulus G′ is found to be lower than the loss modulus G″ indicating the development of folds followed by the destruction of 3D-network. Once the strain is reduced to 1%, a higher G′ value is observed, which clearly reveals the rapid recovery of gel to its original structure by the reconstruction of the fibrillar network.

Generally, organic semi-conductors are molecular crystals or amorphous thin films composed of molecules having conjugated π-bonds and hetero atoms (*N*, *O,* and *S*), which are nearly insulators and behave like semiconductors upon photo-excitation or doping or appropriate adjoining with electrodes.[79] In particular, the development of the organic semiconductor field can make a breakthrough in electronic industries by bringing a wide variety of molecular

structures with tuneable properties and flexibility.[80,81] Recently, many organic semiconductors have been explored, with the scope of replacing rigid crystalline silicon-based semiconductors, which require extremely high purity and precise processing technology.[82,83,84]

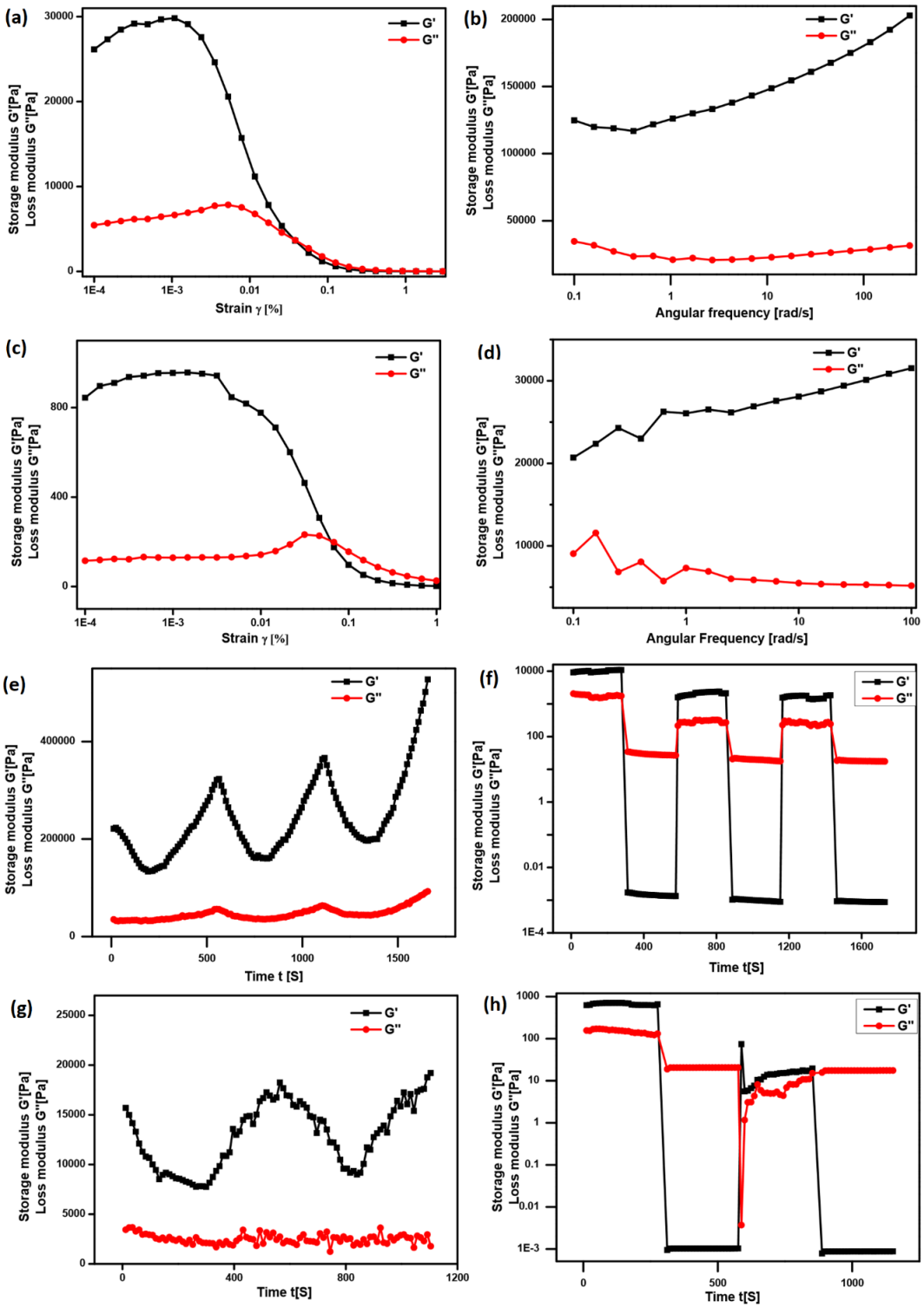


**Figure 2.8**. (a-d) Strain amplitude and angular frequency dependence of G′ and G″ of gel formed by compound **NGN5d** in $CHCl_3$ (a,b) and DMSO-$H_2O$ (c,d) respectively. (e-h) Thermal processability and thixotropic behaviour investigation using continuous temperature and strain ramp-up and ramp-down measurements of gel formed by compound **NGN5d** in $CHCl_3$ (e,f) and DMSO-$H_2O$ (g,h) respectively.

The Electronic Industries Alliance (EIA) composed of electronic manufacturers, has developed a standard for semiconductors, which should have surface resistivity in the range of $10^5$-$10^{13}$ Ω/sq. In particular, a highly conjugated system such as perylenes, pentacenes, phenylene vinylenes, pyrenes, and naphthalene derivatives was largely explored, however, the use of the concept of molecular self-assembly of naphthalimides in semiconductor fabrication is limited. Long and coworkers recently synthesized naphthalimide-based bola amphiphiles and fabricated supramolecular metal-insulator-semiconductor nanostructures.[85] Based on the self-assembly process; Li *et al*. have developed solar cells composed of naphthalimide derivatives.[85] By carefully looking at the molecular structure of the synthesized compounds and assembly phenomenon, the semiconducting property of gel formed by **NGN5d** in $CHCl_3$ was investigated. The current vs voltage characteristics of xerogel prepared by drop casting of gel on a glass plate clearly revealed the semiconducting behaviour, which generated 1.07 nA current upon the application of 8.0V (**Figure 2.9a**).

Based on the assembly pattern displayed by naphthalimide derivatives, a flexible semiconductor using cotton fabric as a template-assisted self-assembly process was developed. In this experiment, initially, cotton fabric was dipped into a hot solution of **NGN5d** in $CHCl_3$ at CGC of 0.3% w/v and allowed to cool down to room temperature. Upon cooling, hydroxyl groups of **NGN5d** form multiple hydrogen bonds with cellulose fibers of cotton, thereby generating a stable assembled pattern with strong adherence. After completion of the assembly process, as identified by the "stable to inversion method", the dipped cloth was taken out and rinsed very well with distilled water to ensure the complete removal of any adhered substances and dried under a desiccator. The four probe *I-V* measurement of semiconducting flexible fabric generated a 6.7 nA on the application of 8.0V, which is sixfold greater in performance than the assembled thin film semiconductor generated on a glass substrate (**Figure 2.9b**). The enhanced performance exhibited by the semiconducting fabric follows the instructed assembly mechanism between the gelator and cellulose through hydrogen bonding, which makes the molecule stack more intact than the thin film formed by the drop-casting method. Interestingly, the semiconducting fabric developed by the self-assembly process was stable for 6 months and did not leach out in water as identified from UV–vis spectroscopy. **Figures 2.9c** and **d** represent the optical microscopic images of cotton cloth, which is used for the comparison of the morphology of glass-coated and fabric-coated semiconductor materials.

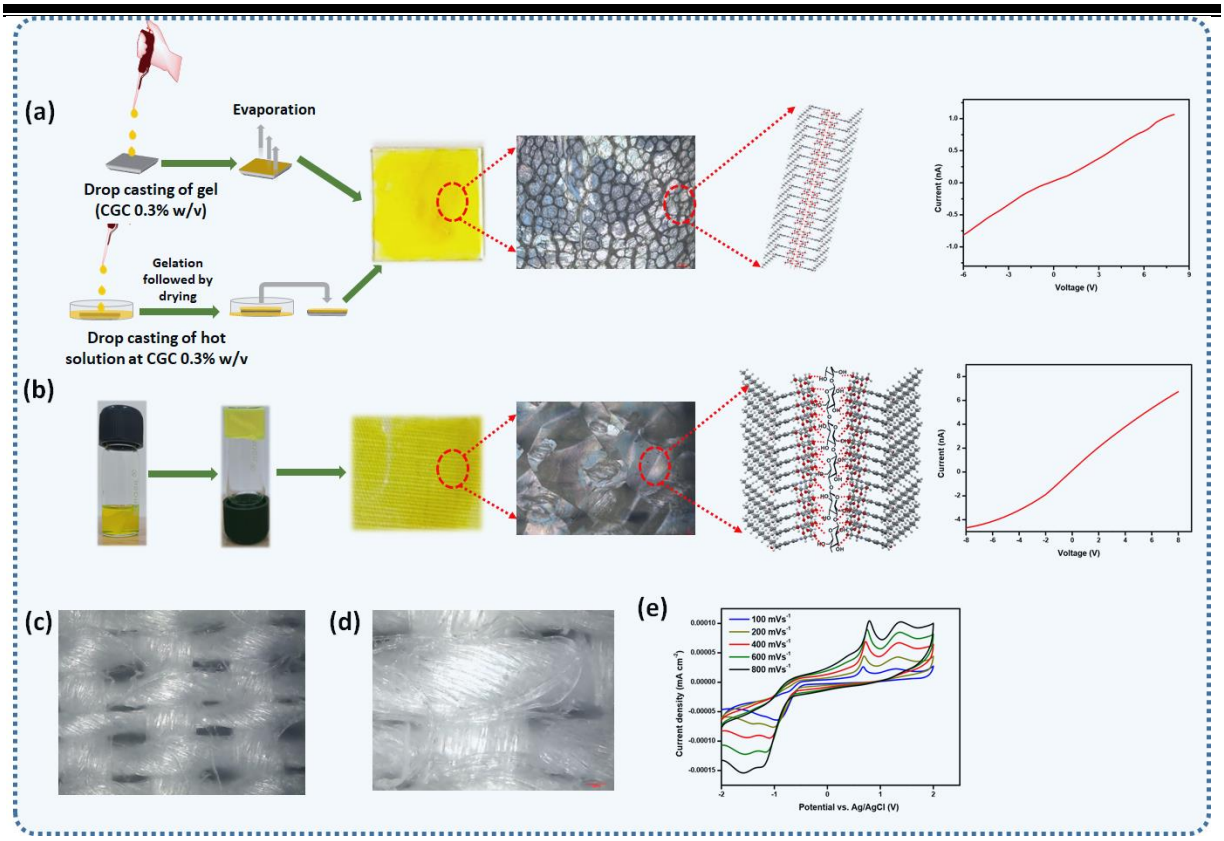


**Figure 2.9**. (a,b) Pictorial representation of (a) assembled semiconducting thin film formation of compound **NGN5d** by drop casting method, morphology, and I–V characteristics (b) formation of flexible semiconducting fabric by **NGN5d**, morphology, and I–V characteristics. (c,d) optical microscopic images of cotton fabric and (e) a Cyclic voltammogram of gelator **NGN5d** recorded in scanning rate from 100 to 800 mV/s at 298 K.

To understand the accessible potential window, redox potential, and stability of the gelator **NGN5d** well, a cyclic voltammogram was recorded at 298 K. In the test window of -2 to 2.5V, two peaks of oxidation and reduction were observed at 0.67, 1.28, -1.2, and -0.9 V, respectively, which clearly indicated the redox activity. An increase in the scanning rate from 100 to 800 mV/s resulted in the gradual increase in the anodic potential from 0.67 and 1.28 V to 0.79 and 1.39 V respectively.

Similarly, the corresponding cathodic peak potential appeared at -1.2 and -0.9 V displayed a decrease in value to -1.6 and -1.22 V (**Figure 2.9e**). Small changes in anodic and cathodic potential suggest the independent nature of the gelator with respect to scan rate and environment. The reversible redox reaction of gelator **NGN5d** is identified by the symmetric shape of anodic and cathodic peaks and the ratio of peak potential is almost equal to 1 in all scanning rates. The compounds used for the generation of semiconducting fabric are not harmful and displayed exceptional stability. Our innovative demonstration displays the potential of the assembly process in applied science and technology.

# 2.3. Experimental Section

## 2.3.1. General Information

All reagents and solvents used for the synthesis of NGN were purchased from commercial suppliers such as Merck, Himedia, and Avra chemicals and were used without purification. We have used LR-grade solvents for recrystallization and AR-grade solvents for gelation studies. The progress of the reactions was monitored by thin-layer chromatography (TLC) using pre-coated Merck silica gel 60 F254 plates and visualized by UV detection or using sulfuric acid spray or molecular iodine. Melting points were recorded on Stuart SMP30 melting point apparatus in capillaries and are uncorrected. $^{1}$H- and $^{13}$C NMR spectra were recorded on a Bruker Avance III spectrometer operating at 400 MHz and 100 MHz respectively. $^{1}$H and $^{13}$C NMR spectra recorded in either $CDCl_3$ or DMSO-$d_6$ at room temperature. Chemical shifts (δ) are expressed in parts per million (ppm) using TMS as an internal standard and coupling constants (*J*) are given in Hz. Proton multiplicity is assigned using the following abbreviations: singlet (s), doublet (d), triplet (t), quartet (q), and multiplet (m). Infrared (IR) spectra were recorded using Perkin Elmer spectrum 100 spectrophotometers from 400 – 4000 $cm^{-1}$ using KBr. High-resolution MS analysis was performed on an Agilent Q-TOF 6230 instrument by dissolving the solid sample in methanol or acetonitrile.

## 2.3.2. General procedure for the synthesis of 5-amino-2-alkyl-naphthalimides (3a-g):

To a stirred solution of 3-nitro-1,8-napthalic anhydride **1** (1 mmol) in 5 mL of methanol, n-alkylamine **2** (2 mmol) was added and refluxed for 6h. After the completion of the reaction as identified by TLC, the reaction mixture is directly subjected to reduction using Fe powder in MeOH-HOAc and continued the reflux for 4h. After the completion of the reduction reaction, as identified using TLC, the reaction mixture was cooled to room temperature, neutralized with saturated $Na_2CO_3$ solution, and extracted with ethyl acetate. The organic layer was dried over $Na_2SO_4$ and the solvent was removed under reduced pressure using a rotary evaporator. A pure 5-amino-2-alkyl-naphthalimides (3a-g) was obtained as an amorphous yellow solid.

## 2.3.3. General procedure for the synthesis of *N*-glycosyl naphthalimides NGN5-7a-g

To a stirred solution of 5-amino-2-alkyl-naphthalimide 3a-g (1.0 mmol) in MeOH (10 mL) was added monosaccharide 4a-c (1.5 mmol) followed by $(NH_4)_2SO_4$ (0.1mmol). The reaction

mixture was stirred at 65 ºC for 24h in an oil bath. During the progress of the reaction, a pale-yellow solid precipitated out was filtered and washed with cold methanol and recrystallized in ethanol.

### 2.3.4. Gelation Studies

The gelation ability of N-glycosyl naphthalimides was determined by the "stable to inversion" method and a wide range of solvents were used for the gelation test. The critical gelation concentration (CGC) in %wt/v (i.e., mg/100 μL) was identified by heating a known amount of gelator taken in a vial with an appropriate volume of solvent. The contents in the vial were heated until the gelator got completely soluble and then cooled to room temperature. Upon cooling, the gelator undergoes molecular self-assembly to form a fibrillar network structure wherein the solvent is immobilized by capillary action. Compound-forming gel is referred to as "G", solution is denoted as "S" and precipitate is denoted as "P".

### 2.3.5. Morphological Study

The morphology of the gels was investigated using optical microscopy and Scanning Electron Microscopy. The gel was prepared at critical gelation concentration placed over a glass plate and viewed using Carl Zeiss Axio Scope A1 fluorescent/phase-contrast microscope. Xerogel was used for SEM analysis.

### 2.3.6. X-ray Diffraction and Molecular Modelling

For SAXRD analysis, a small portion of xerogel was placed and a diffraction pattern was obtained on a BRUKER-binary V3 diffractometer system. ChemDraw Professional 16 and Mercury - The Cambridge Crystallographic Data Centre (CCDC) software were used to obtain MM2 energy minimized diagram and 3-D structure visualization respectively.

### 2.3.7. Rheological Measurements

The visco-elastic behaviour of the gels was identified using a stress-controlled rheometer (Anton Paar 302 rheometer) equipped with steel-coated parallel plate geometry of 25 mm diameter. The rheological behaviour of the gels was investigated by keeping the gel sample over the parallel plate at 23 °C. 1 mm gap was maintained between two parallel plates and the excess gel squeezing out of the parallel plate was trimmed and the measurements were done.

## 2.4. Characterization Data

**Compound 3a**: Amorphous yellow solid; yield: 92% (0.770 g)[86]

**5-amino-2-octyl-1*H*-benzo[*de*]isoquinoline-1,3(2*H*)-dione (3b)**:

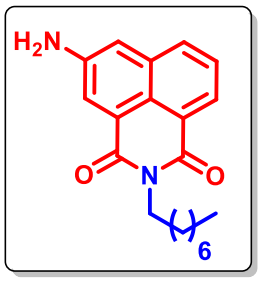


Amorphous yellow solid; yield: 93% (0.301g); mp: 105-107 °C. IR (neat): 3433, 3356, 2922, 2850, 1690 and 1650 $cm^{-1}$. $^{1}H$ NMR (400 MHz, DMSO-$d_6$): $\delta$ 8.07 (d, $J$ = 6.0 Hz, 1H), 8.02 (d, $J$ = 8.0 Hz, 1H), 7.97 (d, $J$ = 2.4 Hz, 1H), 7.60 (t, $J$ = 7.8 Hz, 1H), 7.28 (d, $J$ = 2.4 Hz, 1H), 5.99 (s, 2H), 4.0 (t, $J$.= 7.4 Hz, 2H), 1.65 – 1.56 (m, 2H), 1.9-1.23 (m, 10H), 0.84 (t, $J$ = 6.8 Hz, 3H). $^{13}C$ NMR (100 MHz, DMSO-$d_6$) δ 164.20, 164.02, 148.34, 134.01, 131.89, 127.38, 125.83, 123.03, 122.23, 122.17, 121.03, 112.14, 31.68, 29.17, 29.04, 27.96, 26.99, 22.52, 14.38.

**5-amino-2-decyl-1*H*-benzo[*de*]isoquinoline-1,3(2*H*)-dione (3c)**:

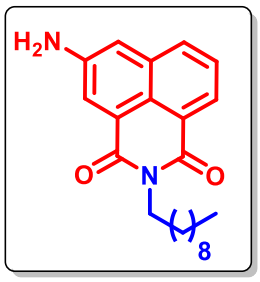


Amorphous yellow solid; yield: 92% (0.324 g); mp: 95-97 °C. IR (neat): 3471, 3371, 2918, 2849, 1682 and 1647 $cm^{-1}$. $^{1}H$ NMR (400 MHz, DMSO-$d_6$): δ 8.06 (d, $J$ = 7.2 Hz, 1H), 8.03 (d, $J$ = 8.0 Hz, 1H), 7.97 (d, $J$ = 2.0 Hz, 1H), 7.60 (t, $J$ = 7.8 Hz, 1H), 7.28 (d, $J$ = 2.1 Hz, 1H), 5.98 (s, 2H), 3.99 (t, $J$.= 7.4 Hz, 2H), 1.65 – 1.55 (m, 2H), 1.34 - 1.28 (m, 4H), 1.25 – 1.19 (m, 10H), 0.83 (t, $J$ = 6.8 Hz, 3H). $^{13}C$ NMR (101 MHz, DMSO-$d_6$) δ 164.20, 164.02, 148.35, 134.01, 131.89, 127.37, 125.83, 123.03, 122.23, 122.17, 121.03, 112.14, 31.73, 29.39, 29.37, 29.19, 29.13, 27.95, 26.97, 22.54, 14.39.

**5-amino-2-dodecyl-1*H*-benzo[*de*]isoquinoline-1,3(2*H*)-dione (3d)**:

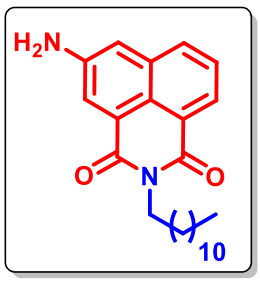


Amorphous yellow solid; yield: 93% (0.353 g); mp: 89-91°C. IR (neat): 3470, 3367, 2918, 2848, 1702, and 1658 $cm^{-1}$. $^{1}H$ NMR (400 MHz, DMSO-$d_6$): δ 8.07 (d, $J$ = 6.4 Hz, 1H), 8.02 (d, $J$ = 8.4 Hz, 1H), 7.97 (d, $J$ = 2.4 Hz, 1H), 7.60 (t, $J$ = 7.8 HZ, 1H), 7.28 (d, $J$ = 2.4 HZ, 1H), 5.98 (s, 2H), 4.0 (t, $J$ = 7.4 Hz, 2H), 1.65 – 1.55 (m, 2H), 1.33 – 1.27 (m, 4H), 1.25 – 1.19 (m, 14H), 0.84 (t, $J$ = 6.8 Hz, 3H). $^{13}C$ NMR (101 MHz, DMSO-$d_6$) δ 164.20, 164.02, 148.35, 134.02, 131.90, 127.37, 125.83, 123.03, 122.23, 122.18, 121.03, 112.14, 31.75, 29.47, 29.45, 29.42, 29.35, 29.19, 29.15, 27.95, 26.96, 22.55, 14.40.

**5-amino-2-tetradecyl-1*H*-benzo[*de*]isoquinoline-1,3(2*H*)-dione (3e)**:

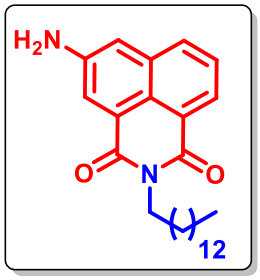


Amorphous yellow solid; Yield: 90%(0.367 g); mp: 91-93 °C. IR (neat): 3460, 3359, 2916, 2848, 1697, and 1651 $cm^{-1}$. $^{1}H$ NMR (400 MHz, DMSO-$d_6$) δ 8.06 (d, $J$ = 6.4 Hz, 1H), 8.02 (d, $J$ = 8.0 Hz, 1H), 7.97 (d, $J$ = 2.4 Hz, 1H), 7.60 (t, $J$ = 7.8 Hz, 1H), 7.28 (d, $J$ = 2.4 Hz, 1H), 5.98 (s, 2H), 3.99 (t, $J$ = 7.4 Hz, 2H), 1.67-1.54 (m, 2H), 1.32-1.20 (m, 22H), 0.84 (t, $J$ = 6.8 Hz, 3H). $^{13}C$ NMR (101 MHz, DMSO-$d_6$) δ 168.95, 168.77, 153.10, 138.77, 136.65, 132.12, 130.58, 127.78, 126.98, 125.79, 116.90, 36.50, 34.21, 34.16, 34.09, 33.94, 33.91, 32.71, 31.71, 31.04, 27.30, 19.14.

**5-amino-2-hexadecyl-1*H*-benzo[*de*]isoquinoline-1,3(2*H*)-dione (3f)**:

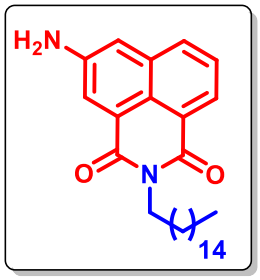


Amorphous yellow solid; Yield: 91%(0.396 g); mp: 84-86 °C. IR (neat): 3459, 3358, 2916, 2848, 1696 and 1650 $cm^{-1}$. $^{1}H$ NMR (400 MHz, DMSO-$d_6$) δ 8.06 (d, $J$ = 6.4 Hz, 1H), 8.01 (d, $J$ = 8.4 Hz, 1H), 7.96 (d, $J$ = 2.4 Hz, 1H), 7.59 (t, $J$ = 7.8 Hz, 1H), 7.27 (d, $J$ = 2.4 Hz, 1H), 5.98 (s, 2H), 3.99 (t, $J$ = 7.4 Hz, 2H), 1.65 – 1.55 (m, 2H), 1.30 – 1.18 (m, 26H), 0.83 (t, $J$ = 6.8 Hz, 3H). $^{13}C$ NMR (101 MHz, DMSO-$d_6$) δ 164.19, 164.01, 148.35, 134.01, 131.88, 127.35, 125.81, 123.02, 122.23, 122.18, 121.03, 112.14, 31.75, 29.46, 29.35, 29.17, 27.96, 26.97, 22.55, 14.38.

**5-amino-2-octadecyl-1*H*-benzo[*de*]isoquinoline-1,3(2*H*)-dione (3g)**: Amorphous yellow solid; Yield: 95% (0.440 g); mp: 76 - 78 °C. IR (neat): 3470, 3368, 2915, 2847, 1699 and 1657 $cm^{-1}$. $^{1}H$ NMR (400 MHz, DMSO-$d_6$) δ 8.06 (d, $J$ = 7.2 Hz, 1H), 8.02 (d, $J$ = 8.4 Hz, 1H), 7.96 (d, $J$ = 2.4 Hz, 1H), 7.60 (t, $J$ = 7.8 Hz, 1H), 7.27 (d, $J$ = 2.0 Hz, 1H), 5.98 (s, 2H), 4.0 (t, $J$ = 7.4 Hz, 2H), 1.65 – 1.55 (m, 2H), 1.33 – 1.27 (m, 4H), 1.25 – 1.19 (m, 26H), 0.83 (t, $J$ = 6.8 Hz, 3H). $^{13}C$ NMR (101 MHz, DMSO-$d_6$) δ 164.19, 164.02, 148.35, 134.02, 131.89, 127.36, 125.82, 123.03, 122.23, 122.18, 121.04, 112.14, 31.75, 29.46, 29.34, 29.16, 27.96, 26.97, 22.55, 14.38

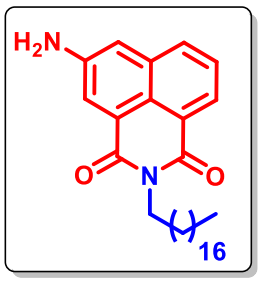

**5-*N*-glucosyl-2-hexyl-1*H*-benzo[*de*]isoquinoline-1,3(2*H*)-dione (NGN5a)**:

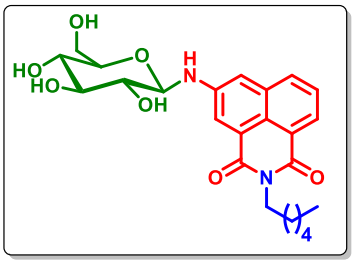

Amorphous yellow solid; yield: 93% (0.425 g); mp: 147 – 149 °C. IR (KBr, $cm^{-1}$): 3376, 2924, 2853, 1699, 1649. $^1$H NMR (400 MHz, DMSO-$d_6$) δ 8.14 (d, $J$ = 7.6 Hz, 1H), 8.11 (d, $J$ = 8.8 Hz, 1H), 8.09 (d, $J$ = 2.4 Hz, 1H), 7.66 (t, $J$ = 8.0 Hz, 1H), 7.44 (d, $J$ = 2.0 Hz, 1H), 7.20 (d, $J$ = 7.6 Hz, 1H), 5.03 (d, $J$ = 4.8 Hz, 1H), 4.96 (dd, $J$ = 11.6, 5.2 Hz, 2H), 4.58 (t, $J$ = 8.0 Hz, 1H), 4.46 (t, $J$ = 6.0 Hz, 1H), 4.01 (t, $J$ = 7.6 Hz, 2H), 3.73 – 3.67 (m, 1H), 3.52 – 3.46 (m, 1H), 3.37 (m, 1H), 3.30 – 3.14 (m, 3H), 1.65 – 1.57 (m, 2H), 1.28 – 1.34 (m, 6H), 0.86 (t, $J$ = 7.2 Hz, 3H). $^{13}$C NMR (100 MHz, DMSO-$d_6$) δ 164.14, 163.92, 146.66, 133.78, 132.60, 127.53, 126.50, 122.82, 122.27, 122.16, 121.70, 111.58, 85.12, 78.24, 77.98, 73.52, 70.56, 61.35, 31.44, 27.95, 26.68, 22.47, 14.39. HRMS (ESI, m/z): $[M+H]^+$ calcd. for $C_{24}H_{31}N_2O_7$: 459.2131; found: 459.2155.

**5-*N*-glucosyl-2-octyl-1*H*-benzo[*de*]isoquinoline-1,3(2*H*)-dione (NGN5b)**:

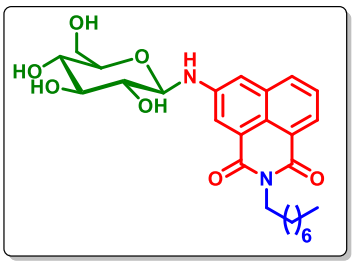

Amorphous yellow solid; yield: 89% (0.432 g); mp: 152-154 °C. IR (KBr, $cm^{-1}$): 3376, 2924, 2824, 1699, 1649.$^1$H NMR (400 MHz, DMSO-$d_6$) δ 8.14 (d, $J$ = 7.6 Hz, 1H), 8.10 (s, 1H), 8.09 (d, $J$ = 2.4 Hz, 1H), 7.66 (t, $J$ = 8.0 Hz, 1H), 7.44 (d, $J$ = 2.0 Hz, 1H), 7.20 (d, $J$ = 7.6 Hz, 1H), 5.03 (d, $J$ = 4.4 Hz, 1H), 4.96 (dd, $J$ = 10.8, 5.2 Hz, 2H), 4.58 (t, $J$ = 8.0 Hz, 1H), 4.46 (t, $J$ = 6.0 Hz, 1H), 4.01 (t, $J$ = 7.6 Hz, 2H), 3.71 – 3.68 (m, 1H), 3.52 – 3.46 (m, 1H), 3.42 – 3.35 (m, 1H), 3.31 – 3.13 (m, 3H), 1.66 – 1.56 (m, 2H), 1.36-1.30 (m, 4H), 1.28 – 1.22 (m, 6H), 0.85 (t, J = 6.8 Hz, 3H). $^{13}$C NMR (100 MHz, DMSO-$d_6$) δ 164.16, 163.94, 146.69, 133.80, 132.60, 127.54, 126.51, 122.86, 122.28, 122.20, 121.73, 111.61, 85.15, 78.24, 77.99, 73.53, 70.58, 61.36, 31.70, 29.18, 29.06, 27.98, 27.03, 22.55, 14.42. HRMS (ESI, m/z): $[M+H]^+$ calcd. for $C_{26}H_{35}N_2O_7$: 487.2444; found: 487.2471.

**5-*N*-glucosyl-2-decyl-1*H*-benzo[*de*]isoquinoline-1,3(2*H*)-dione (NGN5c)**:

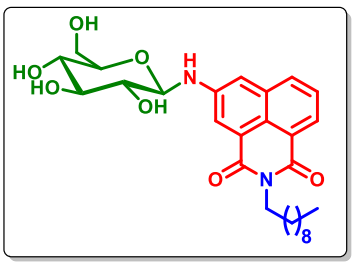

Amorphous yellow solid; yield: 91% (0.467 g); mp: 159-161°C. IR (KBr, $cm^{-1}$): 3375, 2953, 2851, 1691, 1650. $^1$H NMR (400 MHz, DMSO-$d_6$) δ 8.13 (d, $J$ = 7.2 Hz, 1H), 8.10 (s, 1H), 8.09 (d, $J$ = 2.4 Hz, 1H), 7.66 (t, $J$ = 7.6 Hz, 1H), 7.44 (d, $J$ = 2.0 Hz, 1H), 7.20 (d, $J$ = 7.6 Hz, 1H), 5.03 (d, $J$ = 4.4 Hz, 1H), 4.96 (dd, $J$ = 10.8, 5.2 Hz, 2H), 4.58 (t, $J$ = 8.0 Hz, 1H), 4.46 (t, $J$ = 6.0

Hz, 1H), 4.01 (t, *J* = 7.6 Hz, 2H), 3.71 – 3.68 (m, 1H), 3.52 – 3.46 (m, 1H), 3.39 – 3.35 (m, 1H), 3.29 – 3.16 (m, 3H), 1.65 – 1.57 (m, 2H), 1.31 (m, J = 2.8 Hz, 4H), 1.23 (m, 10H), 0.84 (t, J = 6.8 Hz, 3H). $^{13}$C NMR (100 MHz, DMSO-$d_6$) δ 164.18, 163.96, 146.71, 133.83, 132.62, 127.57, 126.52, 122.88, 122.28, 122.22, 121.74, 111.60, 85.14, 78.24, 77.99, 73.52, 70.56, 61.34, 31.76, 29.42, 29.39, 29.21, 29.15, 27.98, 27.01, 22.57, 14.44. HRMS (ESI, m/z): $[M+H]^+$ calcd. for $C_{28}H_{39}N_2O_7$: 515.2757; found: 515.2775.

**5-*N*-glucosyl-2-dodecyl-1*H*-benzo[*de*]isoquinoline-1,3(2*H*)-dione (NGN5d)**:

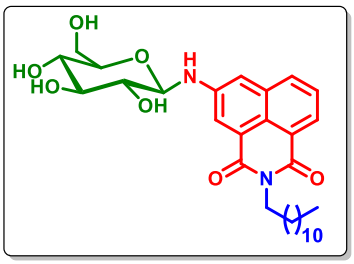


Amorphous yellow solid; yield: 88% (0.476 g); mp: 137-139 °C. IR (KBr, $cm^{-1}$): 3325, 2922, 2849, 1694, 1654 $^1$H NMR (400 MHz, DMSO-$d_6$) δ 8.13 (d, *J* = 7.2 Hz, 1H), 8.10 (s, 1H), 8.09 (d, *J* = 2.0 Hz, 1H), 7.66 (t, *J* = 8.0 Hz, 1H), 7.44 (d, *J* = 2.0 Hz, 1H), 7.20 (d, *J* = 7.6 Hz, 1H), 5.03 (d, *J* = 4.4 Hz, 1H), 4.96 (dd, *J* = 10.4, 5.2 Hz, 2H), 4.58 (t, J = 8.0 Hz, 1H), 4.46 (t, J = 6.0 Hz, 1H), 4.01 (t, *J* = 7.6 Hz, 2H), 3.71 – 3.68 (m, 1H), 3.52-3.46 (m, 1H), 3.36 (m, 1H), 3.28 – 3.18 (m, 3H), 1.65 – 1.56 (m, 2H), 1.31 (m, 4H), 1.23 (m, 14H), 0.85 (t, J = 7.2 Hz, 3H). $^{13}$C NMR (100 MHz, DMSO-$d_6$) δ 164.16, 163.94, 146.67, 133.80, 132.61, 127.54, 126.51, 122.83, 122.27, 121.72, 111.59, 85.14, 78.23, 77.98, 73.52, 70.55, 61.34, 31.76, 29.40, 29.22, 29.16, 27.98, 27.01, 22.58, 14.44. HRMS (ESI, m/z): $[M+H]^+$ calcd. for $_{C30}H_{43}N_2O_7$: 543.3070; found: 543.3092.

**5-*N*-glucosyl-2-tetradecyl-1*H*-benzo[*de*]isoquinoline-1,3(2*H*)-dione (NGN5e)**:

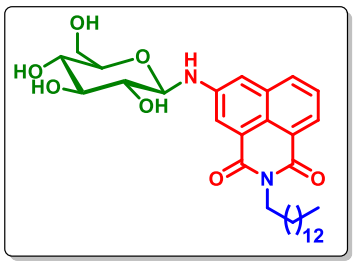


Amorphous yellow solid; yield: 86% (0.490 g); mp: 129-131 °C. IR (KBr, $cm^{-1}$): 3323, 2922, 2849, 1695, 1654 $^1$H NMR (400 MHz, DMSO-$d_6$) δ 8.13 (d, *J* = 7.6 Hz, 1H), 8.10 (s, 1H), 8.09 (d, *J* = 2.4 Hz, 1H), 7.66 (t, *J* = 7.66 Hz, 1H), 7.44 (d, *J* = 2.0 Hz, 1H), 7.20 (d, *J* = 7.6 Hz, 1H), 5.03 (d, *J* = 4.4 Hz, 1H), 4.96 (dd, *J* = 10.4, 5.2 Hz, 2H), 4.58 (t, *J* = 8.0 Hz, 1H), 4.46 (t, *J* = 6.0 Hz, 1H), 4.01 (t, *J* = 7.2 Hz, 2H), 3.73 – 3.66 (m, 1H), 3.52 – 3.46 (m, 1H), 3.36 (m, 1H), 3.30 – 3.16 (m, 3H), 1.61 – 1.59 (m, 2H), 1.31 (m, 4H), 1.22 (m, 18H), 0.84 (t, *J* = 6.8 Hz, 3H). $^{13}$C NMR (100 MHz, DMSO-$d_6$) δ 164.23, 163.96, 146.71, 141.22, 133.83, 132.62, 127.57, 126.52, 122.89, 122.28, 111.59, 85.14, 78.24, 77.99, 73.52, 70.55, 61.33, 31.77, 29.48, 29.18, 27.98, 27.01, 22.58, 14.45. HRMS (ESI, m/z): $[M+H]^+$ calcd. for $C_{32}H_{47}N_2O_7$: 571.3383; found: 571.3414.

**5-*N*-glucosyl-2-hexadecyl-1*H*-benzo[*de*]isoquinoline-1,3(2*H*)-dione (NGN5f)**:

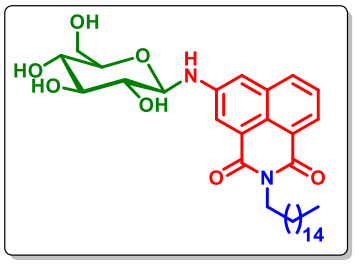

Amorphous yellow solid; yield: 89% (0.532 g); mp: 126-128 °C. IR (KBr, $cm^{-1}$): 3324, 2921, 2849, 1694, 1654 $^1$H NMR (400 MHz, DMSO-$d_6$) δ 8.13 (d, *J* = 7.6 Hz, 1H), 8.10 (s, 1H), 8.08 (d, *J* = 2.0 Hz, 1H), 7.66 (t, *J* = 8.0 Hz, 1H), 7.44 (d, *J* = 2.0 Hz, 1H), 7.20 (d, *J* = 7.6 Hz, 1H), 5.03 (d, *J* = 4.8 Hz, 1H), 4.96 (dd, *J* = 10.8, 5.2 Hz, 2H), 4.58 (t, *J* = 8.0 Hz, 1H), 4.46 (t, *J* = 6.0 Hz, 1H), 4.01 (t, *J* = 7.2 Hz, 2H), 3.73 – 3.67 (m, 1H), 3.52 – 3.46 (m, 1H), 3.36 (m, 1H), 3.29 – 3.15 (m, 3H), 1.64 – 1.57 (m, 2H), 1.31 (m, 4H), 1.22 (m, 22H), 0.84 (t, J = 6.8 Hz, 3H). $^{13}$C NMR (100 MHz, DMSO-$d_6$) δ 164.18, 163.96, 146.70, 133.83, 132.63, 127.57, 126.52, 122.88, 122.28, 122.22, 121.74, 111.60, 85.15, 78.23, 77.99, 73.52, 70.56, 61.34, 31.77, 29.48, 29.38, 29.18, 27.98, 27.02, 22.57, 14.44. HRMS (ESI, m/z): $[M+H]^+$ calcd. for $C_{34}H_{51}N_2O_7$: 599.3696; found: 599.3720.

**5-*N*-glucosyl-2-octadecyl-1*H*-benzo[*de*]isoquinoline-1,3(2*H*)-dione (NGN5g)**:

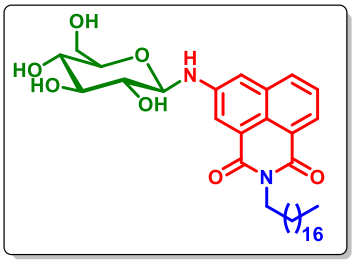

Amorphous yellow solid; yield: 88% (0.550 g); mp: 139-141°C. IR (KBr, $cm^{-1}$): 3323, 2921, 2849, 1691, 1654. $^1$H NMR (400 MHz, DMSO-$d_6$) δ 8.13 (d, *J* = 7.2 Hz, 1H), 8.10 (s, 1H), 8.09 (d, *J* = 3.2 Hz, 1H), 7.66 (t, *J* = 8.0 Hz, 1H), 7.44 (d, *J* = 2.0 Hz, 1H), 7.20 (d, *J* = 7.2 Hz, 1H), 5.03 (d, *J* = 4.4 Hz, 1H), 4.96 (dd, *J* = 10.4, 5.2 Hz, 2H), 4.58 (t, *J* = 8.0 Hz, 1H), 4.46 (t, *J* = 5.6 Hz, 1H), 4.01 (t, *J* = 7.2 Hz, 2H), 3.72 – 3.67 (m, 1H), 3.52 – 3.46 (m, 1H), 3.36 (m, 1H), 3.28 – 3.16 (m, 3H), 1.63 – 1.59 (m, 2H), 1.31 (m, 4H), 1.22 (m, 26H), 0.84 (t, *J* = 6.8 Hz, 3H). $^{13}$C NMR (100 MHz, DMSO-$d_6$) δ 164.17, 163.95, 146.71, 132.61, 127.56, 126.51, 122.88, 122.29, 122.23, 121.74, 111.60, 85.16, 78.24, 77.99, 73.52, 70.56, 61.34, 31.77, 29.48, 29.19, 27.99, 27.02, 22.58, 14.43. HRMS (ESI, m/z): $[M+H]^+$ calcd. for $C_{36}H_{55}N_2O_7$: 627.4009; found: 627.4036.

**5-*N*-galactosyl-2-hexyl-1*H*-benzo[*de*]isoquinoline-1,3(2*H*)-dione (NGN6a)**:

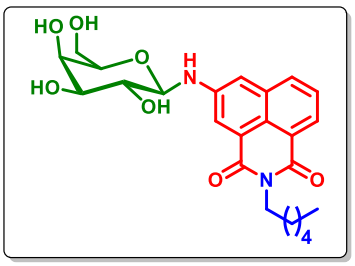

Amorphous yellow solid; yield: 94% (0.430 g); mp: 142-144 °C. IR (KBr, $cm^{-1}$): 3369, 2954, 2857, 1700, 1654. $^1$H NMR (400 MHz, DMSO-$d_6$) δ 8.13 (d, *J* = 7.2 Hz, 1H), 8.10 (s, 1H), 8.09 (d, *J* = 4.4 Hz, 1H), 7.66 (t, *J* = 7.6 Hz, 1H), 7.45 (d, *J* = 2.0 Hz, 1H), 7.18 (d, *J* = 7.6 Hz, 1H), 4.81 (d, *J* = 5.2 Hz, 2H), 4.60 – 4.52 (m, 2H), 4.45 (d, *J* = 4.0 Hz, 1H), 4.01 (t, *J* = 7.6 Hz, 2H), 3.78 (t,

*J* = 3.6 Hz, 1H), 3.64 – 3.53 (m, 3H), 3.50 – 3.45 (m, 2H),1.66 – 1.56 (m, 2H), 1.31 (m, 6H), 0.86 (t, *J* = 7.2 Hz, 3H). $^{13}$C NMR (100 MHz, DMSO-$d_6$) δ 164.17, 163.96, 146.80, 133.78, 132.53, 127.56, 126.47, 122.85, 122.24, 122.19, 121.67, 111.61, 85.61, 76.23, 74.82, 70.59, 68.84, 60.95, 31.44, 27.94, 26.67, 22.47, 14.39. HRMS (ESI, m/z): $[M+H]^+$ calcd. for $C_{24}H_{31}N_2O_7$: 459.2131; found: 459.2151.

**5-*N*-galactosyl-2-octyl-1*H*-benzo[*de*]isoquinoline-1,3(2*H*)-dione (NGN6b)**:

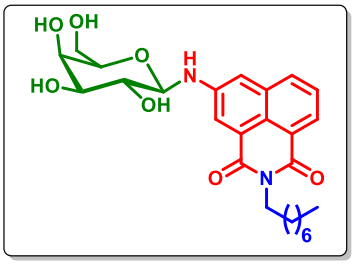

Amorphous yellow solid; yield: 87% (0.422 g); mp: 140-142 °C. IR (KBr, cm$^{-1}$): 3372, 2924, 2853, 1700, 1653. $^1$H NMR (400 MHz, DMSO-$d_6$) δ 8.13 (d, *J* = 6.8 Hz, 1H), 8.10 (s, 1H), 8.09 (d, *J* = 4.0 Hz, 1H), 7.66 (t, *J* = 8.0 Hz, 1H), 7.45 (d, *J* = 2.0 Hz, 1H), 7.18 (d, *J* = 8.0 Hz, 1H), 4.81 (d, *J* = 5.2 Hz, 2H), 4.61 – 4.52 (m, 2H), 4.45 (d, J = 4.0 Hz, 1H), 4.01 (t, J = 7.2 Hz, 2H), 3.78 (t, *J* = 3.6 Hz, 1H), 3.61 – 3.55 (m, 3H), 3.51 – 3.43 (m, 2H), 1.64 – 1.57 (m, 2H), 1.31 (m, 4H), 1.24 (m, 6H), 0.85 (t, *J* = 6.8 Hz, 3H). $^{13}$C NMR (100 MHz, DMSO-$d_6$) δ 164.16, 163.95, 146.79, 133.77, 132.51, 127.52, 126.45, 122.85, 122.22, 122.19, 121.68, 111.63, 85.64, 76.23, 74.81, 70.58, 68.84, 60.95, 31.67, 29.15, 29.03, 27.95, 26.99, 22.52, 14.38. HRMS (ESI, m/z): $[M+H]^+$ calcd. for $C_{26}H_{35}N_2O_7$: 487.2444; found: 487.2469.

**5-*N*-galactosyl-2-decyl-1*H*-benzo[*de*]isoquinoline-1,3(2*H*)-dione (NGN6c)**:

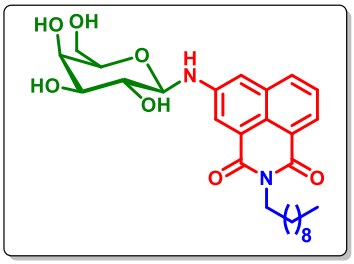

Amorphous yellow solid; yield: 90% (0.462 g); mp: 168-170 °C. IR (KBr, cm$^{-1}$): 3382, 2922, 2850, 1703, 1651. $^1$H NMR (400 MHz, DMSO-$d_6$) δ 8.16 – 8.07 (m, 3H), 7.66 (t, *J* = 7.8 Hz, 1H), 7.45 (s, 1H), 7.17 (d, *J* = 7.4 Hz, 1H), 4.82 (d, *J* = 5.2 Hz, 2H), 4.61-4.53 (m, 2H), 4.46 (d, *J* = 4.0 Hz, 1H), 4.01 (t, *J* = 7.2 Hz, 2H), 3.78 (s, 1H), 3.63 – 3.48 (m, 5H), 1.61 (d, *J* = 0.8 Hz, 2H), 1.31 (s, 4H), 1.23 (s, 10H), 0.83 (t, *J* = 6.8 Hz, 3H). $^{13}$C NMR (100 MHz, DMSO-$d_6$) δ 164.16, 163.95, 146.80, 133.77, 132.50, 127.52, 126.44, 122.85, 122.23, 122.19, 121.68, 111.63, 85.65, 76.23, 74.82, 70.59, 68.83, 60.94, 31.73, 29.38, 29.36, 29.19, 29.12, 27.95, 26.98, 22.54, 14.40. HRMS (ESI, m/z): $[M+H]^+$ calcd. for $C_{28}H_{39}N_2O_7$: 515.2757; found: 515.2774.

**5-*N*-galactosyl-2-dodecyl-1*H*-benzo[*de*]isoquinoline-1,3(2*H*)-dione (NGN6d)**:

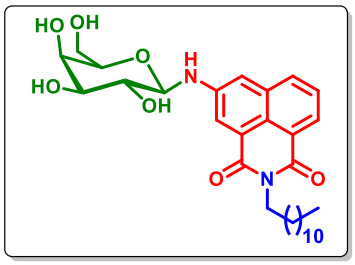

Amorphous yellow solid; yield: 88% (0.476 g); mp: 141-143 °C. IR (KBr, $cm^{-1}$): 3386, 2922, 2851, 1701, 1653. $^1$H NMR (400 MHz, DMSO-$d_6$) δ 8.13 (d, *J* = 7.2 Hz, 1H), 8.10 (s, 1H), 8.09 (d, *J* = 4.4 Hz, 1H), 7.66 (t, *J* = 8.0 Hz, 1H), 7.45 (d, *J* = 2.0 Hz, 1H), 7.18 (d, *J* = 7.6 Hz, 1H), 4.81 (d, *J* = 5.6 Hz, 2H), 4.60 – 4.52 (m, 2H), 4.45 (d, *J* = 4.0 Hz, 1H), 4.01 (t, *J* = 7.2 Hz, 2H), 3.78 (t, *J* = 3.6 Hz, 1H), 3.63 – 3.54 (m, 3H), 3.51 – 3.44 (m, 2H), 1.64 – 1.57 (m, 2H), 1.31 (m, 4H), 1.22 (m, 14H), 0.84 (t, *J* = 6.8 Hz, 3H). $^{13}$C NMR (100 MHz, DMSO-$d_6$) δ 164.15, 163.94, 146.80, 133.78, 132.51, 127.52, 126.43, 122.84, 122.24, 122.19, 121.68, 111.59, 85.63, 76.23, 74.83, 70.59, 68.82, 60.93, 31.77, 29.48, 29.40, 29.23, 29.19, 27.98, 27.02, 22.58, 14.43. HRMS (ESI, m/z): $[M+H]^+$ calcd. for $C_{30}H_{43}N_2O_7$: 543.3070; found: 543.3089

**5-*N*-galactosyl-2-tetradecyl-1*H*-benzo[*de*]isoquinoline-1,3(2*H*)-dione (NGN6e)**:

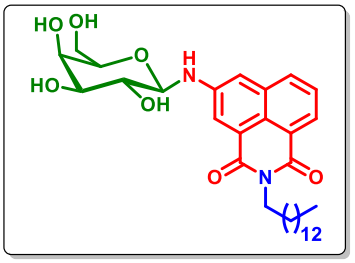

Amorphous yellow solid; yield: 87% (0.495 g); mp: 133-135 °C. IR (KBr, $cm^{-1}$): 3389, 2922, 2851, 1702, 1651. $^1$H NMR (400 MHz, DMSO-$d_6$) 8.13 (d, *J* = 7.2 Hz, 1H), 8.10 (s, 1H), 8.09 (d, *J* = 4.4 Hz, 1H), 7.66 (t, *J* = 8.0 Hz, 1H), 7.45 (d, *J* = 2.4 Hz, 1H), 7.18 (d, *J* = 7.6 Hz, 1H), 4.81 (d, *J* = 5.2 Hz, 2H), 4.60 – 4.52 (m, 2H), 4.44 (d, *J* = 4.4 Hz, 1H), 4.01 (t, *J* = 7.6 Hz, 2H), 3.78 (t, J = 3.6 Hz, 1H), 3.63 – 3.54 (m, 3H), 3.50 – 3.44 (m, 2H), 1.65 – 1.57 (m, 2H), 1.31 (m, 4H), 1.22 (m, 18H), 0.84 (t, *J* = 7.2 Hz, 3H). $^{13}$C NMR (100 MHz, DMSO-$d_6$) δ 164.16, 163.95, 146.81, 133.79, 132.52, 127.53, 126.44, 122.86, 122.24, 122.20, 121.69, 111.60, 85.64, 76.23, 74.83, 70.58, 68.82, 60.93, 31.77, 29.49, 29.39, 29.22, 29.19, 27.98, 27.02, 22.58, 14.43. HRMS (ESI, m/z): $[M+H]^+$ calcd. for $C_{32}H_{47}N_2O_7$: 571.3383; found: 571.3406.

**5-*N*-galactosyl-2-hexadecyl-1*H*-benzo[*de*]isoquinoline-1,3(2*H*)-dione (NGN6f)**:

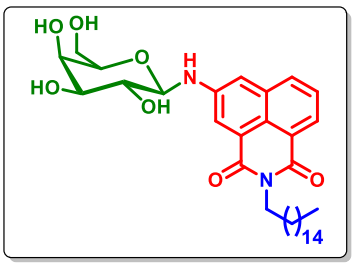

Amorphous yellow solid; yield: 89% (0.532 g); mp: 131-133 °C. IR (KBr, $cm^{-1}$): 3388, 2920, 2849, 1702, 1654. $^1$H NMR (400 MHz, DMSO-$d_6$) δ 8.13 (d, *J* = 7.2 Hz, 1H), ), 8.10 (s, 1H), 8.09 (d, *J* = 4.4 Hz, 1H), 7.66 (t, *J* = 7.6 Hz, 1H), 7.44 (d, *J* = 1.6 Hz, 1H), 7.18 (d, *J* = 7.6 Hz, 1H), 4.80 (d, *J* = 5.6 Hz, 2H), 4.59 – 4.53 (m, 2H), 4.44 (d, *J* = 4.0 Hz, 1H), 4.01 (t, *J* = 7.2 Hz, 2H), 3.78 (t,

*J* = 3.6 Hz, 1H), 3.59 – 3.54 (m, 3H), 3.50 – 3.43 (m, 2H), 1.65 – 1.57 (m, 2H), 1.30 (m, 4H), 1.22 (m, 22H), 0.84 (t, *J* = 7.2 Hz, 3H). $^{13}$C NMR (100 MHz, DMSO-$d_6$) δ 164.14, 163.94, 146.79, 133.77, 132.51, 127.51, 126.43, 122.83, 122.18, 121.68, 111.60, 85.63, 76.21, 74.82, 70.58, 68.81, 60.92, 31.77, 29.49, 29.39, 29.22, 29.19, 27.98, 27.03, 22.58, 14.42. HRMS (ESI, m/z): $[M+H]^+$ calcd. for $C_{34}H_{51}N_2O_7$: 599.3696; found: 599.3715.

**5-*N*-galactosyl-2-octadecyl-1*H*-benzo[*de*]isoquinoline-1,3(2*H*)-dione (NGN6g)**:

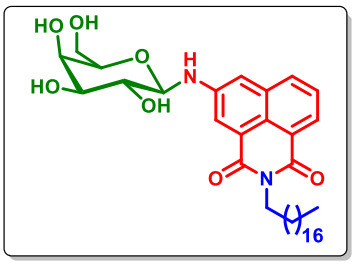

Amorphous yellow solid; yield: 86% (0.538 g); mp: 140-142 °C. IR (KBr, cm$^{-1}$): 3388, 2922, 2850, 1702, 1651. $^1$H NMR (400 MHz, DMSO-$d_6$) δ 8.13 (d, *J* = 7.2 Hz, 1H), ), 8.10 (s, 1H), 8.09 (d, *J* = 4.4 Hz, 1H), 7.66 (t, *J* = 8.0 Hz, 1H),7.44 (d, *J* = 2.0 Hz, 1H), 7.18 (d, J = 7.6 Hz, 1H), 4.80 (d, *J* = 5.2 Hz, 2H), 4.60 – 4.51 (m, 2H), 4.44 (d, *J* = 4.4 Hz, 1H), 4.01 (t, *J* = 7.6 Hz, 2H), 3.78 (t, *J* = 3.6 Hz, 1H), 3.61 – 3.54 (m, 3H), 3.50 – 3.43 (m, 2H), 1.64 – 1.57 (m, 2H), 1.31 (m, 4H), 1.22 (m, 26H), 0.84 (t, *J* = 7.2 Hz, 3H). $^{13}$C NMR (100 MHz, DMSO-$d_6$) δ 164.14, 163.94, 146.80, 133.78, 132.51, 127.51, 126.43, 122.84, 122.24, 122.19, 121.68, 111.60, 85.64, 76.22, 74.82, 70.58, 68.81, 60.92, 31.78, 29.49, 29.40, 29.23, 29.19, 27.99, 27.03, 22.58, 14.42. HRMS (ESI, m/z): $[M+H]^+$ calcd. for $C_{36}H_{55}N_2O_7$: 627.4009; found: 627.4036

**5-*N*-xylosyl-2-hexyl-1*H*-benzo[*de*]isoquinoline-1,3(2*H*)-dione (NGN7a)**:

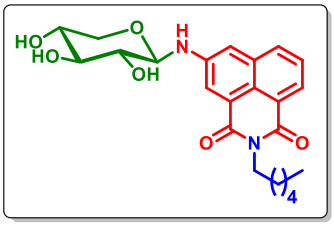

Amorphous yellow solid; yield: 93% (0.398 g); mp: 183-185 °C. IR (KBr, cm$^{-1}$): 3431, 3329, 2929, 2855, 1703, 1651. $^1$H NMR (400 MHz, DMSO-$d_6$) δ 8.15 (d, *J* = 2.4 Hz, 1H), 8.13 (s, 1H), 8.07 (d, *J* = 2.4 Hz, 1H), 7.67 (t, *J* = 8.0 Hz, 1H), 7.44 (d, *J* = 2.0 Hz, 1H), 7.19 (d, *J* = 8.0 Hz, 1H), 5.08 (d, *J* = 4.0 Hz, 1H), 5.01 (t, *J* = 4.8 Hz, 2H), 4.56 (t, *J* = 8.0 Hz, 1H), 4.01 (t, *J* =7.6, 2H), 3.73 (dd, J = 10.0, 4.4 Hz, 1H), 3.42 – 3.34 (m, 1H), 3.30– 3.21 (m, 3H), 1.66 – 1.56 (m, 2H), 1.32 (m, 6H), 0.86 (t, *J* = 6.8 Hz, 3H). $^{13}$C NMR (100 MHz, DMSO-$d_6$) δ 164.11, 163.91, 146.50, 133.73, 132.55, 127.56, 126.55, 122.90, 122.19, 122.10, 121.74, 111.50, 85.72, 78.16, 73.39, 70.31, 67.04, 31.45, 27.94, 26.68, 22.47, 14.39. HRMS (ESI, m/z): $[M+H]^+$ calcd. for $C_{23}H_{29}N_2O_6$: 429.2026; found: 429.2041.

**5-*N*-xylosyl-2-octyl-1*H*-benzo[*de*]isoquinoline-1,3(2*H*)-dione (NGN7b)**:

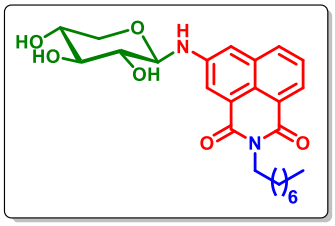

Amorphous yellow solid; yield: 91% (0.414 g); mp: 182-184 °C. IR (KBr, $cm^{-1}$): 3427, 3328, 2925, 2852, 1703, 1651. $^1$H NMR (400 MHz, DMSO-$d_6$) δ 8.15 (d, *J* = 2.4 Hz, 1H), 8.13 (d, *J* = 1.2 Hz, 1H), 8.07 (d, *J* = 2.4 Hz, 1H), 7.67 (t, *J* = 8.0 Hz, 1H), 7.44 (d, *J* = 2.4 Hz, 1H), 7.19 (d, *J* = 8.0 Hz, 1H), 5.08 (d, *J* = 4.4 Hz, 1H), 5.01 (t, *J* = 4.8 Hz, 2H), 4.56 (t, *J* = 8.0 Hz, 1H), 4.01 (t, *J* =7.6, 2H), 3.73 (dd, J = 10.0, 4.4 Hz, 1H), 3.41 – 3.34 (m, 1H), 3.30– 3.20 (m, 3H), 1.66 – 1.55 (m, 2H), 1.30 (m, 4H), 1.25 (m, 6H), 0.85 (t, *J* = 6.8 Hz, 3H). $^{13}$C NMR (100 MHz, DMSO-$d_6$) δ 164.09, 163.87, 146.27, 133.63, 132.27, 127.16, 126.53, 122.94, 122.26, 122.12, 121.99, 111.57, 86.00, 79.37, 79.05, 78.72, 77.91, 73.18, 70.22, 66.93, 31.76, 29.28, 29.14, 28.08, 27.12, 22.59, 14.34. HRMS (ESI, m/z): $[M+H]^+$ calcd. for $C_{25}H_{33}N_2O_6$: 457.2339; found: 457.2362.

**5-*N*-xylosyl-2-decyl-1*H*-benzo[*de*]isoquinoline-1,3(2*H*)-dione (NGN7c)**:

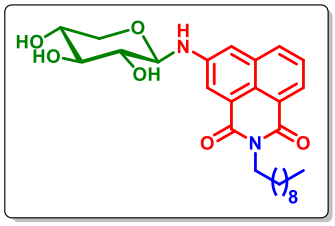

Amorphous yellow solid; yield: 94% (0.454 g); mp: 175-177 °C. IR (KBr, $cm^{-1}$): 3427, 3335, 2923, 2852, 1703, 1650. $^1$H NMR (400 MHz, DMSO-$d_6$) δ 8.15 (d, *J* = 2.8 Hz, 1H), 8.13 (d, *J* = 1.6 Hz, 1H), 8.07 (d, *J* = 2.4 Hz, 1H), 7.67 (t, *J* = 8.0 Hz, 1H), 7.44 (d, *J* = 2.0 Hz, 1H), 7.19 (d, *J* = 8.0 Hz, 1H), 5.08 (d, *J* = 4.0 Hz, 1H), 5.01 (t, *J* = 5.2 Hz, 2H), 4.55 (t, *J* = 8.0 Hz, 1H), 4.01 (t, *J* = 7.6 Hz, 2H), 3.73 (dd, *J* = 10.4, 4.4 Hz, 1H), 3.39 – 3.34 (m, 1H), 3.30 – 3.21 (m, 3H), 1.62 (m, 2H), 1.31 (m, 4H), 1.23 (m, 10H), 0.84 (t, *J* = 6.8 Hz, 3H). $^{13}$C NMR (100 MHz, DMSO-$d_6$) δ 164.12, 163.92, 146.51, 133.75, 132.55, 127.55, 126.54, 122.92, 122.20, 122.10, 121.76, 111.50, 85.73, 78.16, 73.39, 70.31, 67.04, 31.75, 29.40, 29.22, 29.15, 27.97, 27.01, 22.57, 14.42. HRMS (ESI, m/z): $[M+H]^+$ calcd. for $C_{27}H_{37}N_2O_6$: 485.2652; found: 485.2669

**5-*N*-xylosyl-2-dodecyl-1*H*-benzo[*de*]isoquinoline-1,3(2*H*)-dione (NGN7d)**:

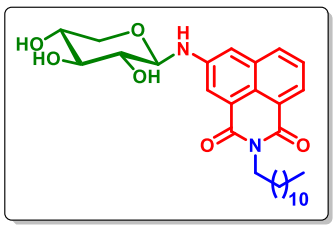

Amorphous yellow solid; yield: 89% (0.455 g); mp: 177-179°C. IR (KBr, $cm^{-1}$): 3426, 3329, 2921, 2851, 1704, 1651. $^1$H NMR (400 MHz, , DMSO-$d_6$) δ 8.15 (d, *J* = 2.4 Hz, 1H), 8.13 (d, *J* = 1.2 Hz, 1H), 8.06 (d, *J* = 2.4 Hz, 1H), 7.67 (t, *J* = 7.6 Hz, 1H), 7.44 (d, *J* = 2.0 Hz, 1H), 7.19 (d, *J* = 8.0 Hz, 1H), 5.07 (d, *J* = 4.0 Hz, 1H), 5.01 (t, *J* = 5.6 Hz, 2H), 4.55 (t, *J* = 8.0 Hz, 1H), 4.04 – 3.97

(m, 2H), 3.73 (dd, J = 10.4, 4.4 Hz, 1H), 3.40 – 3.34 (m, 1H), 3.30 – 3.22 (m, 3H), 1.66 – 1.55 (m, 2H), 1.31 (m, 4H), 1.22 (m, 14H), 0.84 (t, *J* = 6.8 Hz, 3H). $^{13}$C NMR (100 MHz, DMSO-$d_6$) δ 164.15, 163.94, 146.54, 146.09, 133.77, 132.57, 127.58, 126.55, 122.95, 122.24, 122.11, 121.78, 111.52, 85.73, 78.16, 73.39, 70.31, 67.05, 31.77, 29.47, 29.38, 29.22, 29.18, 27.97, 27.00, 22.57, 14.43. HRMS (ESI, m/z): $[M+H]^+$ calcd. for $C_{29}H_{41}N_2O_6$: 513.2965; found: 513.2984.

**5-*N*-xylosyl-2-tetradecyl-1*H*-benzo[*de*]isoquinoline-1,3(2*H*)-dione (NGN7e)**:

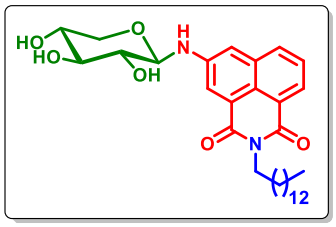


Amorphous yellow solid; yield: 91% (0.491 g); mp: 159-161 °C. IR (KBr, $cm^{-1}$): 3426, 3333, 2920, 2850, 1704, 1650.$^1$H NMR (400 MHz, DMSO-$d_6$) δ 8.15 (d, *J* = 2.4 Hz, 1H), 8.13 (s, 1H), 8.06 (d, *J* = 2.0 Hz, 1H), 7.66 (t, *J* = 8.0 Hz, 1H), 7.44 (d, *J* = 2.0 Hz, 1H), 7.18 (d, *J* = 8.0 Hz, 1H), 5.07 (d, *J* = 4.0 Hz, 1H), 5.01 (t, *J* = 6.0 Hz, 2H), 4.55 (t, *J* = 7.6 Hz, 1H), 4.05 – 3.96 (m, 2H), 3.73 (dd, *J* = 10.0, 4.4 Hz, 1H), 3.41 – 3.34 (m, 1H), 3.29 – 3.21 (m, 3H), 1.66 – 1.57 (m, 2H), 1.30 (m, 4H), 1.22 (m, 18H), 0.84 (t, *J* = 7.2 Hz, 3H). $^{13}$C NMR (100 MHz, DMSO-$d_6$) δ 164.16, 163.95, 162.74, 146.54, 133.78, 132.58, 127.59, 126.57, 122.96, 122.24, 122.11, 121.78, 111.53, 85.72, 78.15, 73.39, 70.31, 67.04, 31.77, 29.48, 29.36, 29.18, 27.96, 27.00, 22.57, 14.43, 0.59. HRMS (ESI, m/z): $[M+H]^+$ calcd. for $C_{31}H_{45}N_2O_6$: 541.3275; found: 541.3299.

**5-*N*-xylosyl-2-hexadecyl-1*H*-benzo[*de*]isoquinoline-1,3(2*H*)-dione (NGN7f)**:

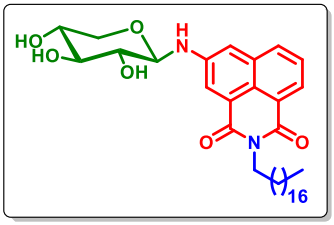


Amorphous yellow solid; yield: 86% (0.488 g); mp: 158-160 °C. IR (KBr, $cm^{-1}$): 3426, 3332, 2920, 2850, 1704, 1651.$^1$H NMR (400 MHz, DMSO-$d_6$) δ 8.15 (d, *J* = 2.4 Hz, 1H), 8.13 (s, 1H), 8.06 (d, *J* = 2.0 Hz, 1H), 7.66 (t, J = 8.0 Hz, 1H), 7.44 (d, *J* = 2.4 Hz, 1H), 7.18 (d, *J* =8.0 Hz, 1H), 5.08 (d, *J* = 4.0 Hz, 1H), 5.01 (t, *J* = 5.6 Hz, 2H), 4.55 (t, *J* = 8.0 Hz, 1H), 4.04 – 3.97 (m, 2H), 3.73 (dd, *J* = 10.4, 4.4 Hz, 1H), 3.37 – 3.34 (m, 1H), 3.29 – 3.22 (m, 3H), 1.65 – 1.56 (m, 2H), 1.30 (m, 4H), 1.22 (m, 22H), 0.84 (t, J = 6.8 Hz, 3H). $^{13}$C NMR (100 MHz, DMSO-$d_6$) δ 164.16, 163.95, 146.53, 133.78, 132.58, 127.60, 122.96, 122.24, 122.11, 121.77, 111.52, 85.71, 78.14, 73.38, 70.30, 67.03, 31.77, 29.47, 29.35, 29.18, 27.96, 26.99, 22.57, 14.43. HRMS (ESI, m/z): $[M+H]^+$ calcd. for $C_{33}H_{49}N_2O_6$: 569.3591; found: 569.3610.

**5-*N*-xylosyl-2-octadecyl-1H-benzo[*de*]isoquinoline-1,3(2*H*)-dione (NGN7g)**:

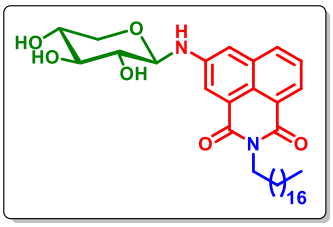

Amorphous yellow solid; yield: 88% (0.524 g); mp: 153-155 °C. IR (KBr, $cm^{-1}$): 3427, 3329, 2920, 2850, 1704, 1651.$^1$H NMR (400 MHz, DMSO-$d_6$) δ 8.15 (d, $J$ = 2.4 Hz, 1H), 8.13 (s, 1H), 8.06 (d, $J$ = 2.0 Hz, 1H), 7.66 (t, $J$ = 7.6 Hz, 1H), 7.44 (d, $J$ = 2.0 Hz, 1H), 7.18 (d, $J$ = 8.0 Hz, 1H), 5.07 (d, $J$ = 4.0 Hz, 1H), 5.01 (t, $J$ = 6.0 Hz, 2H), 4.55 (t, $J$ = 8.0 Hz, 1H), 4.04 – 3.97 (m, 2H), 3.73 (dd, $J$ = 10.4, 4.4 Hz, 1H), 3.41 – 3.34 (m, 1H), 3.30 – 3.20 (m, 3H), 1.64 – 1.56 (m, 2H), 1.30 (m, 4H), 1.22 (m, 26H), 0.84 (t, $J$ = 7.2 Hz, 3H). $^{13}$C NMR (100 MHz, DMSO-$d_6$) δ 163.95, 146.53, 133.78, 132.59, 127.60, 126.57, 122.96, 122.23, 122.11, 121.77, 111.52, 85.71, 78.14, 73.38, 70.30, 67.03, 31.77, 29.47, 29.35, 29.18, 27.96, 26.99, 22.57, 14.43. HRMS (ESI, m/z): $[M+H]^+$ calcd. for $C_{35}H_{52}N_2O_6$: 597.3904; found: 597.3910.

## 2.5. Conclusions

In summary, this chapter reports an environmentally benign protocol for the synthesis of amphiphilic N-glycosyl naphthalimides starting from readily available raw materials in good yields. The use of FDA-approved GRAS chemical $(NH_4)_2SO_4$ as a catalyst for N-glycosylation reaction exclusively generated *β*-anomeric product. The theoretical investigation of the role of catalysts and plausible reaction mechanisms is in agreement with the experimental outcome. Supramolecular self-assembly of N-glycosyl naphthalimides in both hydrophilic and hydrophobic solvents furnished gel. Molecular level interactions such as H-bonding, π-π stacking, and van der Waals forces in the gel were identified using FT-IR, NMR, SAXRD, UV-vis, and Fluorescence spectral methods and a suitable self-assembly mechanism has been proposed. Investigation of the morphology, microstructure, and mechanical strength disclose the suitability of the soft material in the fabrication of materials. As designed, the self-assembly of the gelator molecule in $CHCl_3$ generated a fibrillar network structure in such a way that the hydrophobic moiety projected outwards with the stacking of naphthalimide moiety. Assembled thin film generated by drop casting of NGN displayed semiconducting properties. In order to visualize the advancement at the interface of supramolecular science and technology, a highly flexible semiconducting fabric via self-assembly of NGN on cotton fabric anchoring through H-bonding is developed. Interestingly, the semiconducting fabric displayed more enhanced conductivity than the assembled thin film, which could display fidelity in the sustainable development of flexible organic electronics.

## 2.6. References


1. S. J. Danishefsky and J. R. Allen, *Angew. Chemie - Int. Ed.*, 2000, **39**, 836-863.
2. K. C. Nicolaou and H. J. Mitchell, *Angew. Chemie - Int. Ed.*, 2001, **40**, 1576–1624.
3. B. Ernst and J. L. Magnani, *Nat. Rev. Drug Discov.*, 2009, **8**, 661–677.
4. R. D. Astronomo and D. R. Burton, *Nat. Rev. Drug Discov.*, 2010, **9**, 308–324.
5. M. Nishio, *Phys. Chem. Chem. Phys.*, 2011, **13**, 13873–13900.
6. L. T. Mika, E. Cséfalvay and Á. Németh, *Chem. Rev.*, 2018, **118**, 505–613.
7. R. M. Nelson, A. Venot, M. P. Bevilacqua, R. J. Linhardt and I. Siamenkovic, *Annu. Rev. Cell Dev. Biol.*, 1995, **11**, 601–631.
8. B. Ernst, G. W. Hart and P. Sinay, *Carbohydrates in chemistry and biology*, 2008, vol. **1–4**.
9. E. C. O'Neill and R. A. Field, Front. *Bioeng. Biotechnol.*, 2015, **3**, 23-27.
10. Y. S. Prasad, S. Miryala, K. Lalitha, B. Saritha, C. U. Maheswari, V. Sridharan, C. S. Srinandan and S. Nagarajan, *Sci. Rep.*, 2020, **10**, 18017.
11. A. Thamizhanban, S. Balaji, K. Lalitha, Y. S. Prasad, R. V. Prasad, R. A. Kumar, C. U. Maheswari, V. Sridharan and S. Nagarajan, *J. Agric. Food Chem.*, 2020, **68**, 14896–14906.
12. T. S. Zatsepin and T. S. Oretskaya, *Chem. Biodivers.*, 2004, **1**, 1401–1417.
13. T. Freire, S. Bay, S. Vichier-Guerre, R. Lo-Man and C. Leclerc, *Mini-Reviews Med. Chem.*, 2006, **6**, 1357–1373.
14. E. H. Song and N. L. Pohl, *Curr. Opin. Chem. Biol.*, 2009, **13**, 626–632.
15. R. K. Shukla and A. Tiwari, *Carbohydr. Polym.*, 2012, **88**, 399–416.
16. J. Xie and N. Bogliotti, *Chem. Rev.*, 2014, **114**, 7678–7739.
17. B. Kang, T. Opatz, K. Landfester and F. R. Wurm, *Chem. Soc. Rev.*, 2015, **44**, 8301–8325.
18. S. Gim, Y. Zhu, P. H. Seeberger and M. Delbianco, *Wiley Interdiscip. Rev. Nanomedicine Nanobiotechnology*, 2019, **11**.
19. H. Jiang, X. Qin, Q. Wang, Q. Xu, J. Wang, Y. Wu, W. Chen, C. Wang, T. Zhang, D. Xing and R. Zhang, *Eur. J. Med. Chem.*, 2021, **223**, 256-261.
20. K. Lalitha, K. Muthusamy, Y. S. Prasad, P. K. Vemula and S. Nagarajan, *Carbohydr. Res.*, 2015, **402**, 158–171.
21. D. Teze, J. Coines, F. Fredslund, K. D. Dubey, G. N. Bidart, P. D. Adams, J. E. Dueber, B. Svensson, C. Rovira and D. H. Welner, *ACS Catal.*, 2021, **11**, 1810–1815.
22. V. Kelemen, M. Csávás, J. Hotzi, M. Herczeg, Poonam, B. Rathi, P. Herczegh, N. Jain and A. Borbás, *Chem. - An Asian J.*, 2020, **15**, 876–891.
23. K. Villadsen, M. C. Martos-Maldonado, K. J. Jensen and M. B. Thygesen, *ChemBioChem*, 2017, **18**, 574–612.

24. E. M. Sánchez-Fernández, R. Gonçalves-Pereira, R. Rísquez-Cuadro, G. B. Plata, J. M. Padrón, J. M. García Fernández and C. Ortiz Mellet, *Carbohydr. Res*., 2016, **429**, 113–122.
25. P. J. Berti and J. A. B. McCann, *Chem. Rev*., 2006, **106**, 506–555.
26. R. Sangwan, A. Khanam and P. K. Mandal, *European J. Org. Chem*., 2020, **2020**, 5949–5977.
27. M. Lv and H. Xu, *Curr. Med. Chem*., 2009, **16**, 4797–4813.
28. A. Kamal, N. R. Bolla, P. S. Srikanth and A. K. Srivastava, *Expert Opin. Ther. Pat*., 2013, **23**, 299–317.
29. A. S. Oshchepkov, M. S. Oshchepkov, M. V. Oshchepkova, A. Al-Hamry, O. Kanoun and E. A. Kataev, *Adv. Opt. Mater*., 2021, **9**, 303-306.
30. M. Sawa, T. L. Hsu, T. Itoh, M. Sugiyama, S. R. Hanson, P. K. Vogt and C. H. Wong, *Proc. Natl. Acad. Sci. U. S. A*., 2006, **103**, 12371–12376.
31. Y. Fu, H. H. Han, J. Zhang, X. P. He, B. L. Feringa and H. Tian, *J. Am. Chem. Soc*., 2018, **140**, 8671–8674.
32. L. Dong, Y. Zang, D. Zhou, X. P. He, G. R. Chen, T. D. James and J. Li, *Chem. Commun*., 2015, **51**, 11852–11855.
33. G. Cavigiolio, J. L. Morgan, B. H. Robinson and J. Simpson, *Aust. J. Chem*., 2004, **57**, 885–894.
34. Z. Ma, P. Zhang, X. Yu, H. Lan, Y. Li, D. Xie, J. Li and T. Yi, *J. Mater. Chem. B*, 2015, **3**, 7366–7371.
35. T. Wang, Z. Wang, D. Xie, C. Wang, X. Zhen, Y. Li and X. Yu, *RSC Adv*., 2015, **5**, 107694–107699.
36. E. Calatrava-Pérez, S. Acherman, L. Stricker, G. McManus, J. Delente, A. D. Lynes, A. F. Henwood, J. I. Lovitt, C. S. Hawes, K. Byrne, W. Schmitt, O. Kotova, T. Gunnlaugsson and E. M. Scanlan, *Org. Biomol. Chem*., 2020, **18**, 3475–3480.
37. E. Calatrava-Pérez, S. A. Bright, S. Achermann, C. Moylan, M. O. Senge, E. B. Veale, D. C. Williams, T. Gunnlaugsson and E. M. Scanlan, *Chem. Commun*., 2016, **52**, 13086–13089.
38. L. Dong, S. Shen, H. Lu, S. Jin and J. Zhang, *ACS Sensors*, 2019, **4**, 1222–1229.
39. J. Zhang, Y. Fu, H.-H. Han, Y. Zang, J. Li, X.-P. He, B. L. Feringa and H. Tian, *Nat. Commun*., 2017, **8**, 987.
40. D. Gudeika, *Synth. Met*., 2020, **262**.
41. M. Liao, J. Duan, P. Peng, J. Zhang and M. Zhou, *RSC Adv*., 2020, **10**, 41764–41779.

42. I. Arrechea-Marcos, P. De Echegaray, M. J. Mancheño, M. C. Ruiz Delgado, M. M. Ramos, J. A. Quintana, J. M. Villalvilla, M. A. Díaz-García, J. T. López Navarrete, R. Ponce Ortiz and J. L. Segura, *Phys. Chem. Chem. Phys*., 2017, **19**, 6206–6215.
43. S. Diab, T. Teo, M. Kumarasiri, P. Li, M. Yu, F. Lam, S. K. C. Basnet, M. J. Sykes, H. Albrecht, R. Milne and S. Wang, *ChemMedChem*, 2014, **9**, 962–972.
44. 2016. Gaussian 16, Revision C.01, M. J. Frisch, G. W. Trucks, H. B. Schlegel, G. E. Scuseria, M. A. Robb, J. R. Cheeseman, G. Scalmani, V. Barone, G. A. Petersson, H. Nakatsuji, X. Li, M. Caricato, A. V. Marenich, J. Bloino, B. G. Janesko, R. Gomperts, B. Mennu, Gaussian, Inc., Wallingford CT.
45. C. Lee, W. Yang and R. G. Parr, *Phys. Rev. B*, 1988, **37**, 785–789.
46. A. D. Becke, *J. Chem. Phys*., 1993, **98**, 5648–5652.
47. D. Lombardo, M. A. Kiselev, S. Magazù and P. Calandra, *Adv. Condens. Matter Phys*., 2015, **2015**, 1-20.
48. J. M. Zayed, N. Nouvel, U. Rauwald and O. A. Scherman, *Chem. Soc. Rev*., 2010, **39**, 2806–2816.
49. Y. Zhao, F. Sakai, L. Su, Y. Liu, K. Wei, G. Chen and M. Jiang, *Adv. Mater*., 2013, **25**, 5215–5256.
50. A. C. Mendes, E. T. Baran, R. L. Reis and H. S. Azevedo, *Wiley Interdiscip. Rev. Nanomedicine Nanobiotechnology*, 2013, **5**, 582–612.
51. A. M. Castilla, W. J. Ramsay and J. R. Nitschke, *Acc. Chem. Res*., 2014, **47**, 2063–2073.
52. C. Yuan, W. Ji, R. Xing, J. Li, E. Gazit and X. Yan, *Nat. Rev. Chem*., 2019, **3**, 567–588.
53. M. Shimomura and T. Sawadaishi, *Curr. Opin. Colloid Interface Sci*., 2001, **6**, 11–16.
54. S. Zhang, *Nat. Biotechnol*., 2003, **21**, 1171–1178.
55. A. Biswas, I. S. Bayer, A. S. Biris, T. Wang, E. Dervishi and F. Faupel, *Adv. Colloid Interface Sci*., 2012, **170**, 2–27.
56. K. Ariga, Y. Yamauchi, G. Rydzek, Q. Ji, Y. Yonamine, C. W. Kevin and J. P. Hill, *Chem. Lett*., 2014, **43**, 36–68.
57. D. Xiang, X. Wang, C. Jia, T. Lee and X. Guo, *Chem. Rev*., 2016, **116**, 4318–4440.
58. B. S. Kim, D. J. Hong, J. Bae and M. Lee, *J. Am. Chem. Soc*., 2005, **127**, 16333–16337.
59. R. A. Pires, Y. M. Abul-Haija, D. S. Costa, R. Novoa-Carballal, R. L. Reis, R. V. Ulijn and I. Pashkuleva, *J. Am. Chem. Soc*., 2015, **137**, 576–579.
60. C. Lin, S. Maisonneuve, R. Métivier and J. Xie, *Chem. - A Eur. J*., 2017, **23**, 14996–15001.
61. S. Abb, N. Tarrat, J. Cortés, B. Andriyevsky, L. Harnau, J. C. Schön, S. Rauschenbach and K. Kern, *Angew. Chemie - Int. Ed*., 2019, **58**, 8336-8340.

62. S. Wong, J. Zhao, C. Cao, C. K. Wong, R. P. Kuchel, S. De Luca, J. M. Hook, C. J. Garvey, S. Smith, J. Ho and M. H. Stenzel, *Nat. Commun*., 2019, **10**, 582.
63. A. Mittal, Krishna, Aarti, S. Prasad, P. K. Mishra, S. K. Sharma and B. Parshad, *Mater. Adv*., 2021, **2**, 3459–3473.
64. A. Brito, S. Kassem, R. L. Reis, R. V. Ulijn, R. A. Pires and I. Pashkuleva, *Chem*, 2021, **7**, 2943–2964.
65. P. K. Vemula and G. John, *Acc. Chem. Res*., 2008, **41**, 769–782.
66. M. Delbianco, P. Bharate, S. Varela-Aramburu and P. H. Seeberger, *Chem. Rev*., 2016, **116**, 1693–1752.
67. S. Magazù and D. Lombardo, *Materials* (Basel), 2020, **13**, 1458.
68. D. Lombardo, M. A. Kiselev, L. Pasqua, G. Pellicane and P. Calandra, *J. Nanomater*., 2021, **2021**, 1-6.
69. L. Wågberg and J. Erlandsson, *Adv. Mater*., 2021, **33**.
70. K. Lalitha, Y. S. Prasad, C. U. Maheswari, V. Sridharan, G. John and S. Nagarajan, *J. Mater. Chem*. *B*, 2015, **3**, 5560–5568.
71. K. Muthusamy, V. Sridharan, C. U. Maheswari and S. Nagarajan, *Green Chem*., 2016, **18**, 3722–3731.
72. K. Lalitha, V. Sridharan, C. U. Maheswari, P. K. Vemula and S. Nagarajan, *Chem. Commun*., 2017, **53**, 1538–1541.
73. Y. Li, D. J. Young and X. J. Loh, *Mater. Chem. Front*., 2019, **3**, 1489–1502.
74. A. R. Hirst and D. K. Smith, *Langmuir*, **2004**, 20, 10851–10857.
75. P. Fischer and E. J. Windhab, *Curr. Opin. Colloid Interface Sci*., 2011, **16**, 36–40.
76. S. Odenbach, *Arch. Appl. Mech*., 2016, **86**, 269–279.
77. H. Askari and K. Kamrin, *Nat. Mater*., 2016, **15**, 1274–1279.
78. D. T. N. Chen, Q. Wen, P. A. Janmey, J. C. Crocker and A. G. Yodh, *Annu. Rev. Condens. Matter Phys*., 2010, **1**, 301–322.
79. V. Coropceanu, J. Cornil, D. A. da Silva Filho, Y. Olivier, R. Silbey and J. L. Brédas, *Chem. Rev*., **2007**, 107, 926–952.
80. C. R. Newman, C. D. Frisbie, D. A. Da Silva Filho, J. L. Brédas, P. C. Ewbank and K. R. Mann, *Chem. Mater*., 2004, **16**, 4436–4451.
81. A. Mishra and P. Bäuerle, *Angew. Chemie - Int. Ed*., 2012, **51**, 2020–2067.
82. Y. Zhang, A. Chen, M. W. Kim, A. Alaei and S. S. Lee, *Chem. Soc. Rev*., 2021, **50**, 9375–9390.
83. D. Burmeister, M. G. Trunk and M. J. Bojdys, *Chem. Soc. Rev*., 2021, **50**, 11559–11576.

84. B. P. Krishnan, S. Mukherjee, P. M. Aneesh, M. A. G. Namboothiry and K. M. Sureshan, *Angew. Chemie - Int. Ed.*, 2016, **55**, 2345–2349.

85. H. Lin, Z. Ma, J. Zhao, Y. Liu, J. Chen, J. Wang, K. Wu, H. Jia, X. Zhang, X. Cao, X. Wang, X. Fu and J. Long, *Angew. Chemie - Int. Ed.*, 2021, **60**, 1235–1243.

86. S. Kotowicz, M. Korzec, M. Siwy, S. Golba, J. G. Malecki, H. Janeczek, S. Mackowski, K. Bednarczyk, M. Libera and E. Schab-Balcerzak, *Dye. Pigment.*, 2018, **158**, 65–78.

## 2.7. Selected NMR ($^{1}$H & $^{13}$C), and Mass spectra

**$^{1}$H NMR Spectrum of compound NGN5d (400 MHz, DMSO-*d*$_6$)**

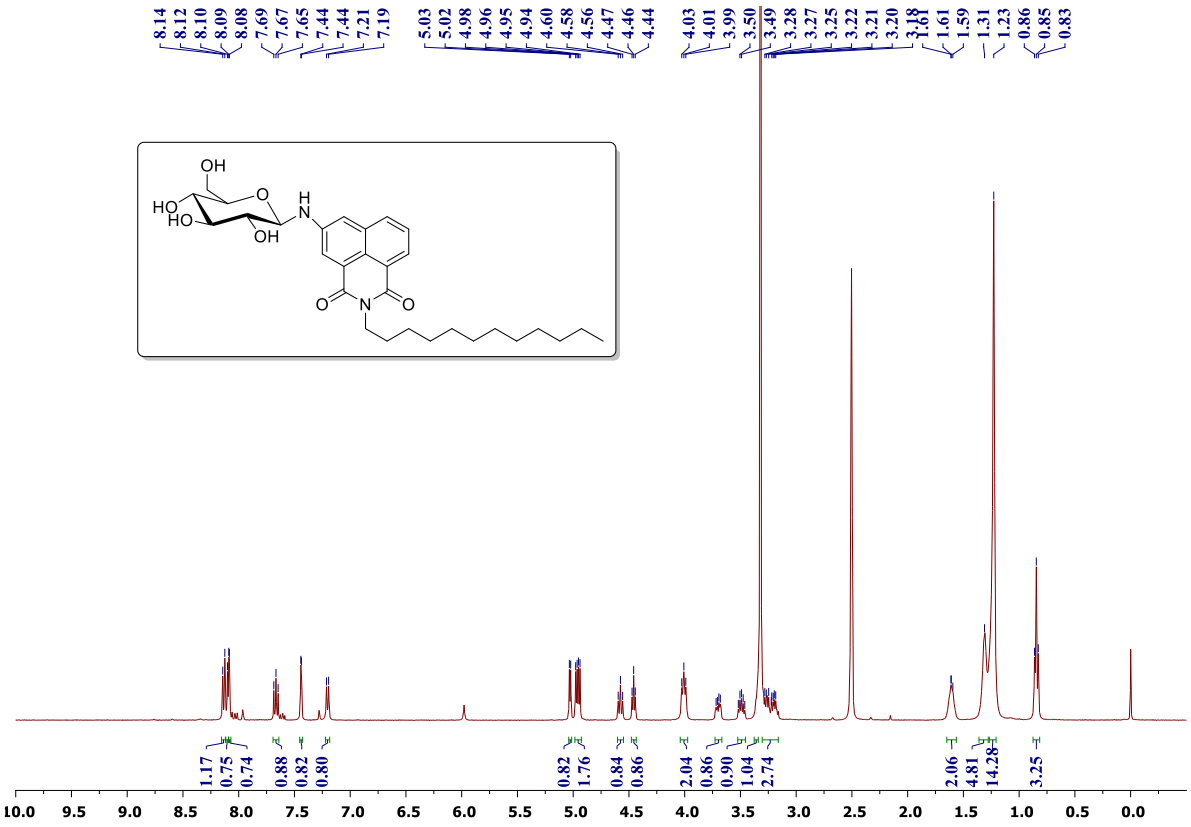

## $^{13}$C NMR Spectrum of compound NGN5d (100 MHz, DMSO-*d*$_6$)

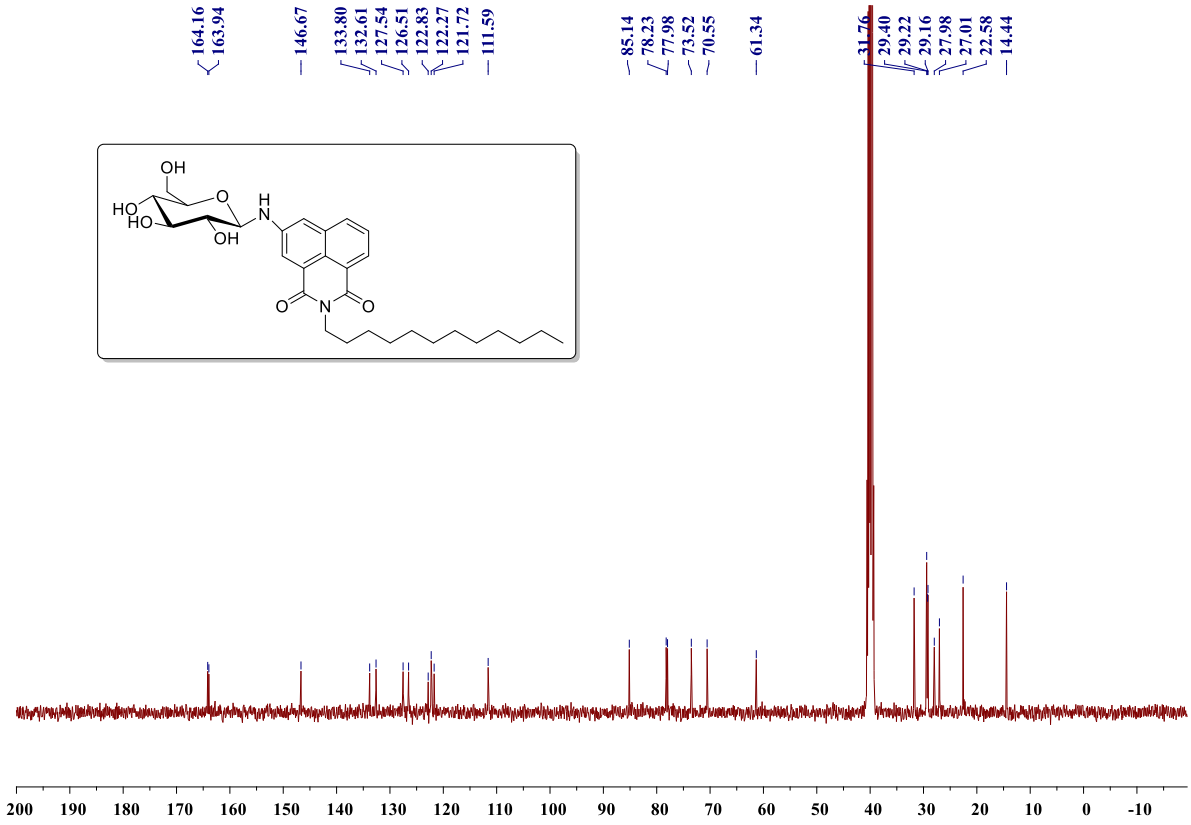


## HRMS spectrum of NGN5d

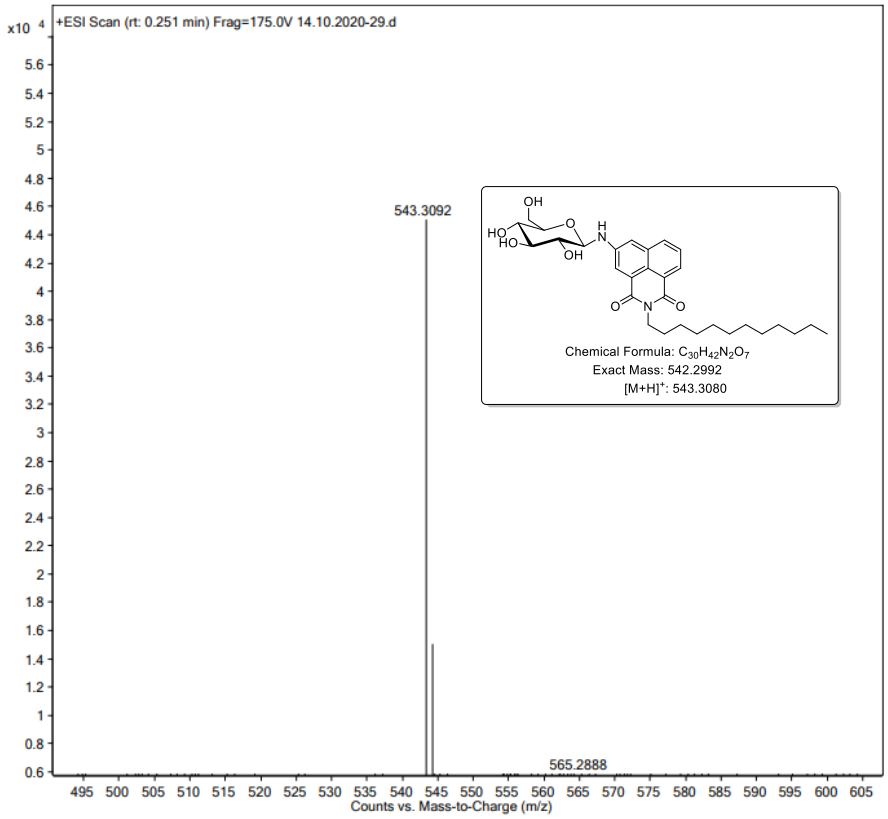

## $^{1}$H NMR Spectrum of compound NGN6d (400 MHz, DMSO-$d_6$)

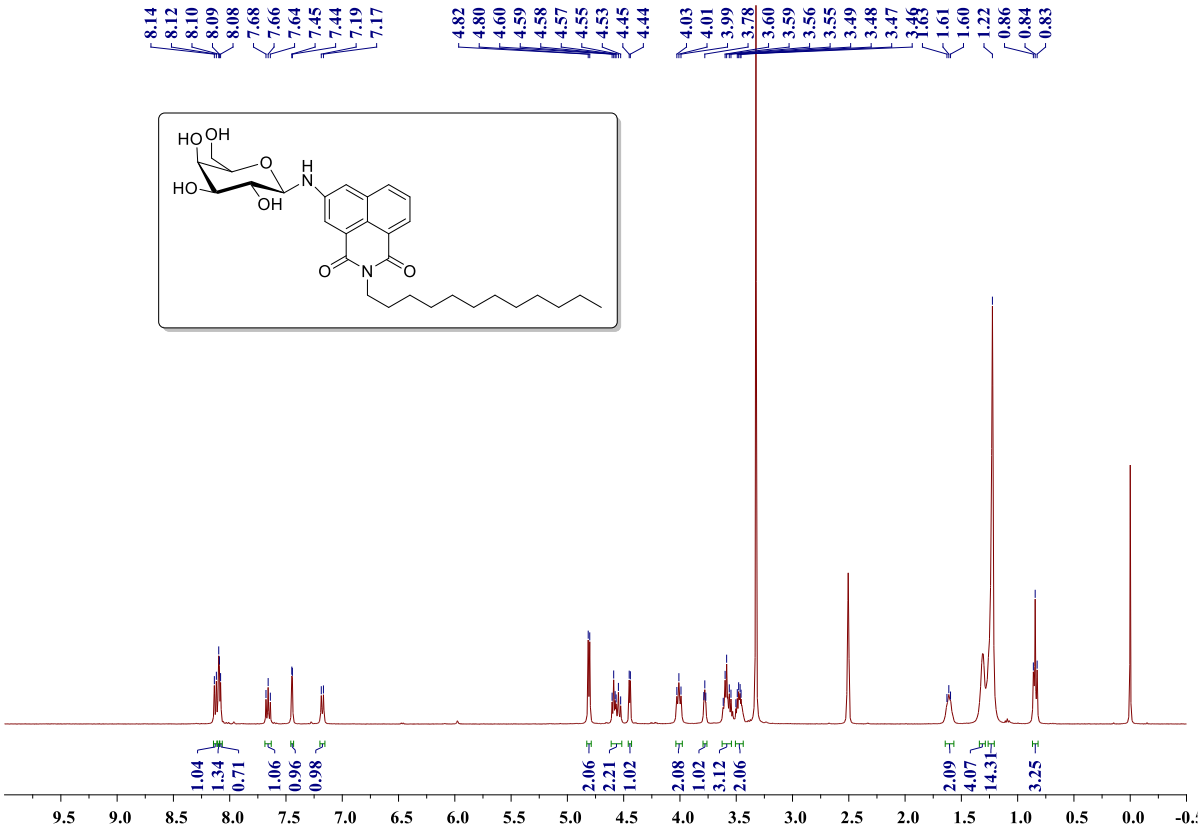


## $^{13}$CNMR Spectrum of compound NGN6d (100 MHz, DMSO-$d_6$)

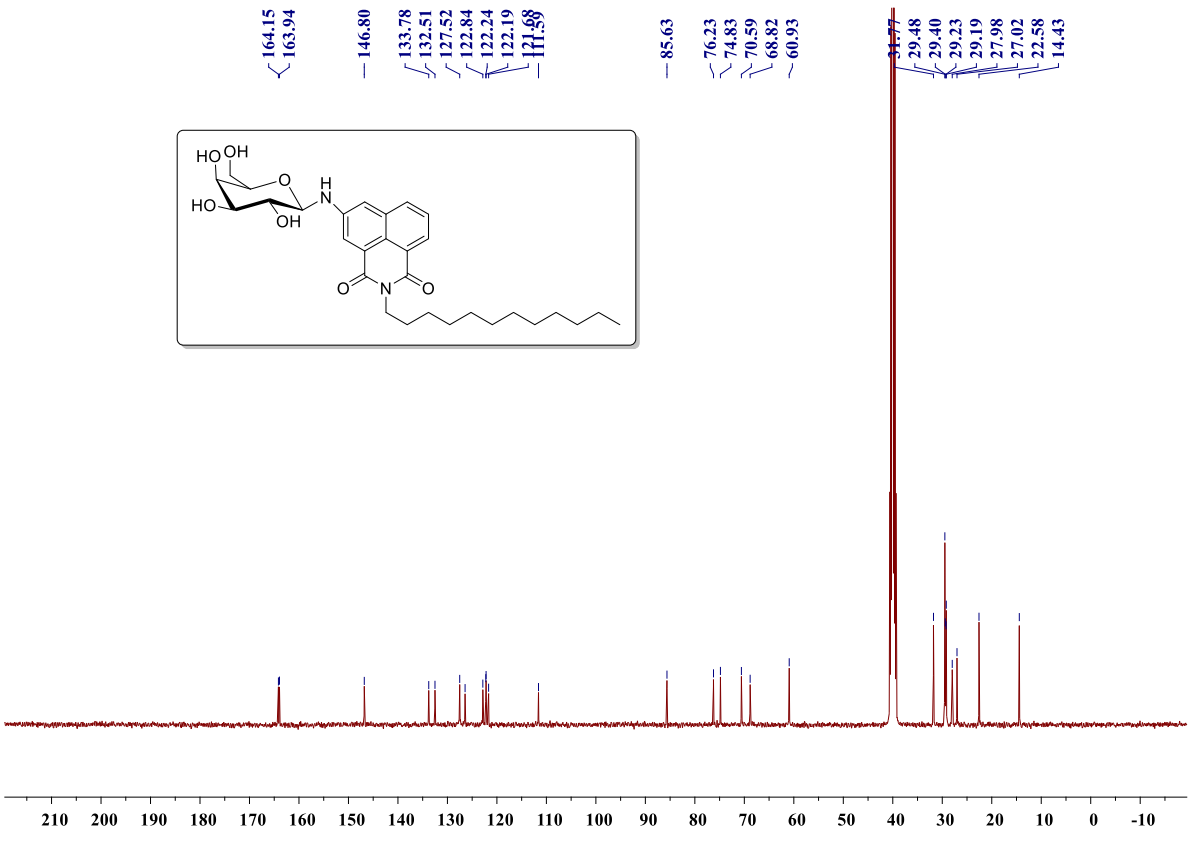

## HRMS spectrum of NGN6d

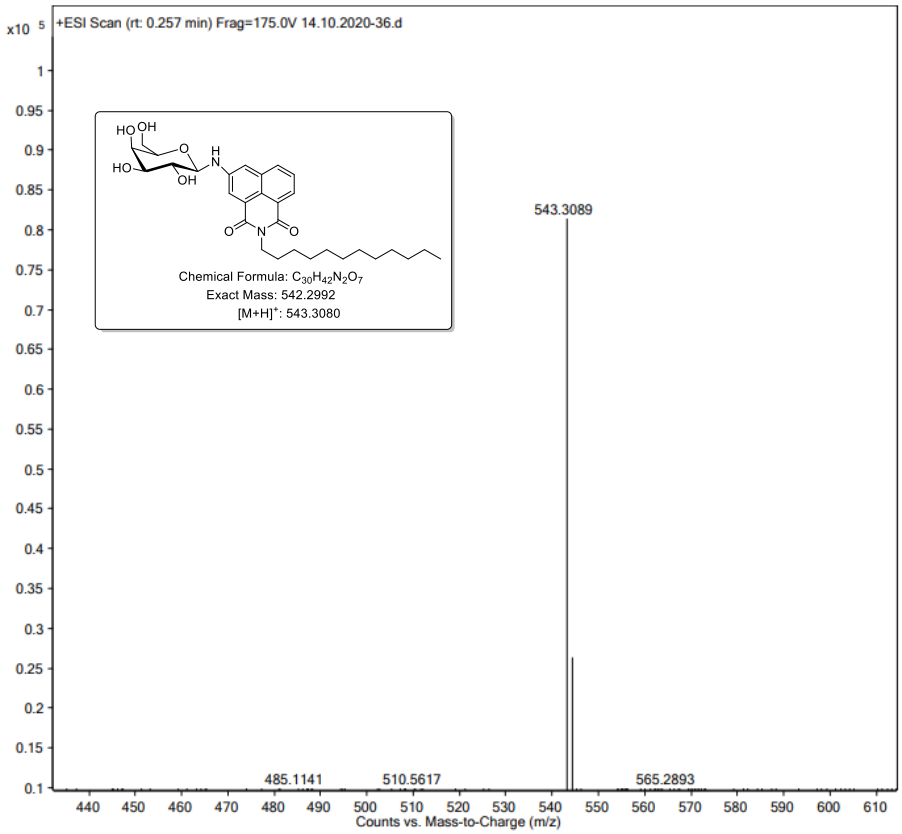


## $^1$H NMR Spectrum of compound NGN7d (400 MHz, DMSO-$d_6$)

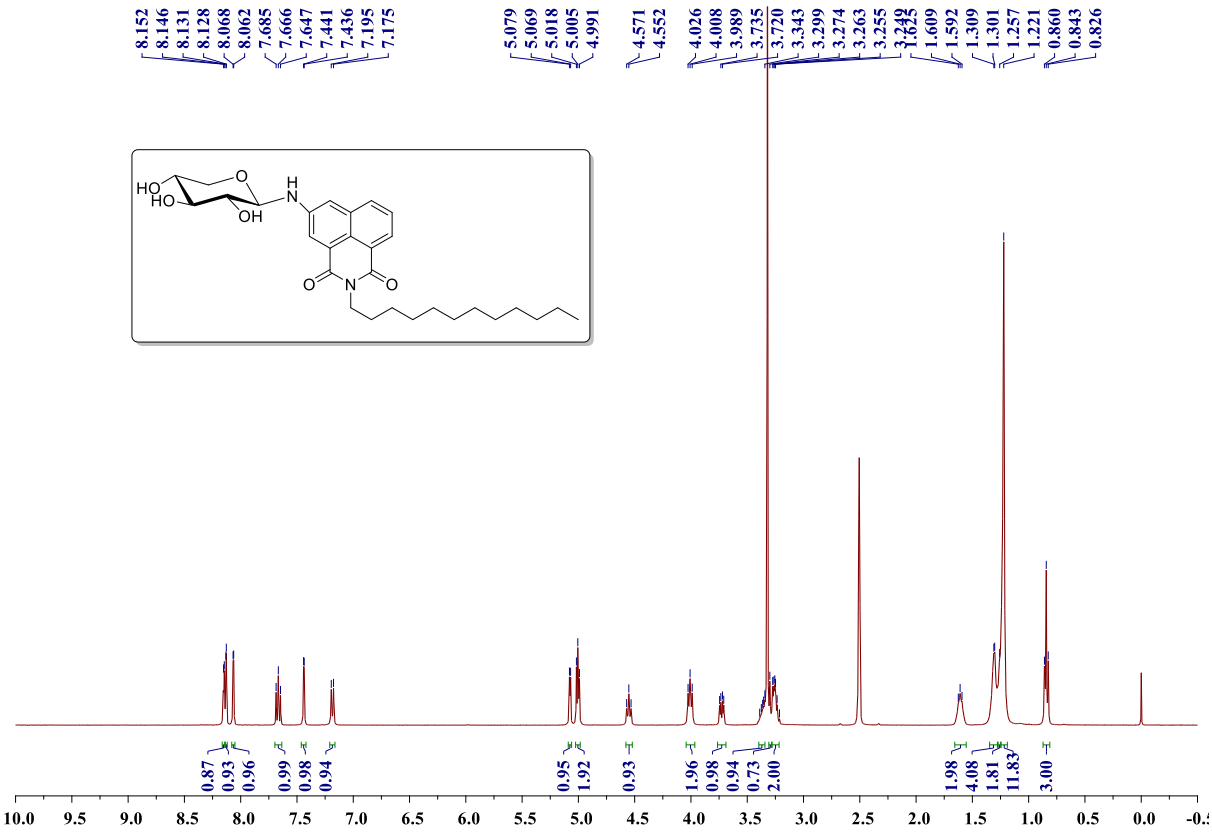

## $^{13}$CNMR Spectrum of compound NGN7d (100 MHz, DMSO-$d_6$)

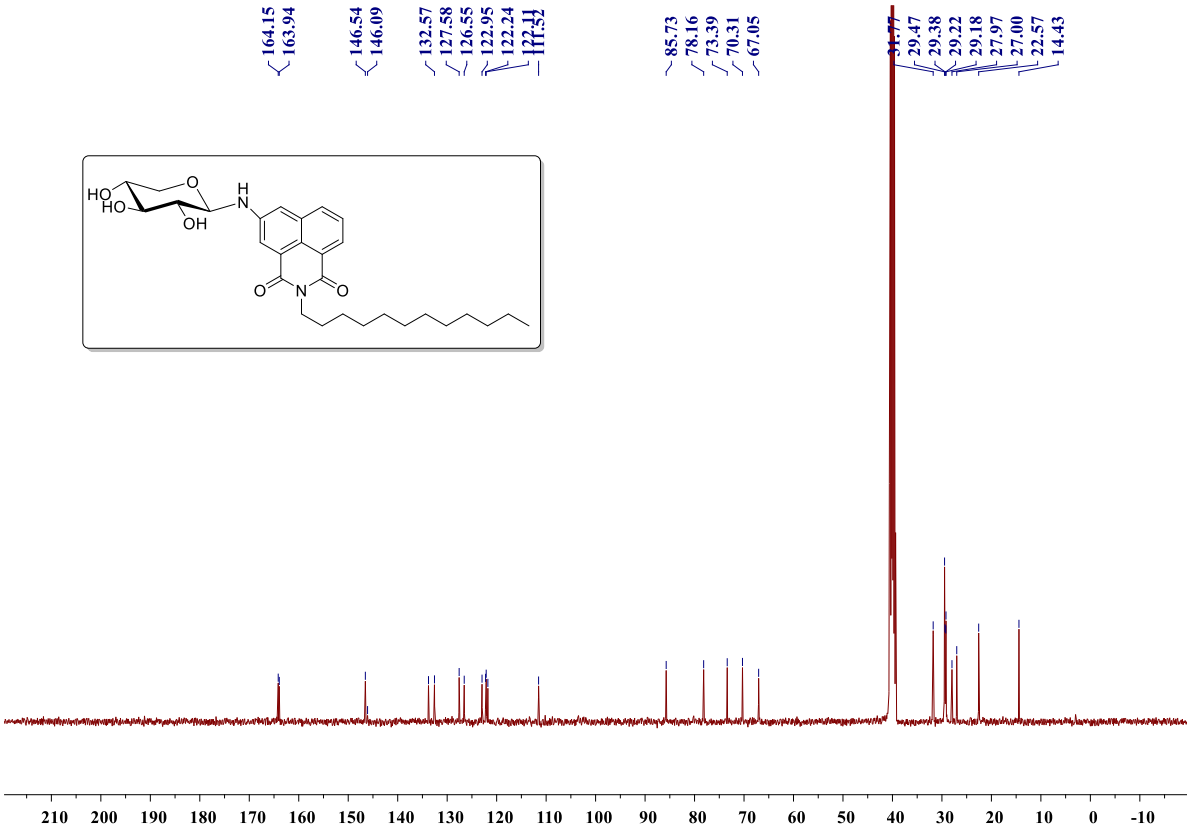


## HRMS spectrum of NGN7d

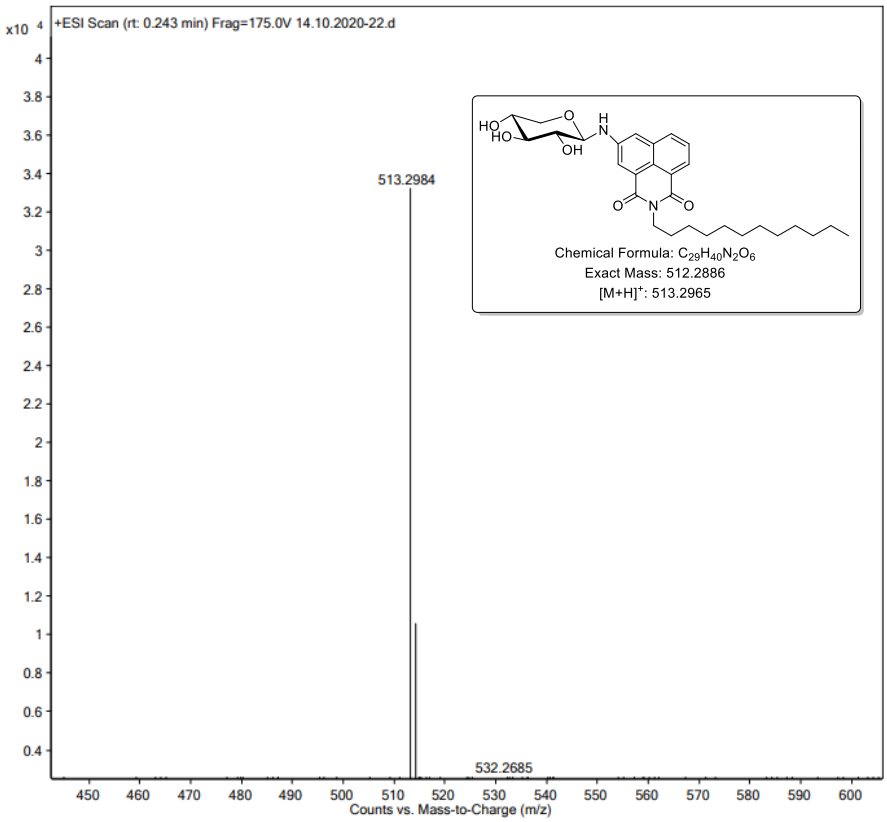

# CHAPTER-III

## Electronically robust self-assembled gluconamide conjugated naphthalimides for the fabrication of triboelectric nanogenerator

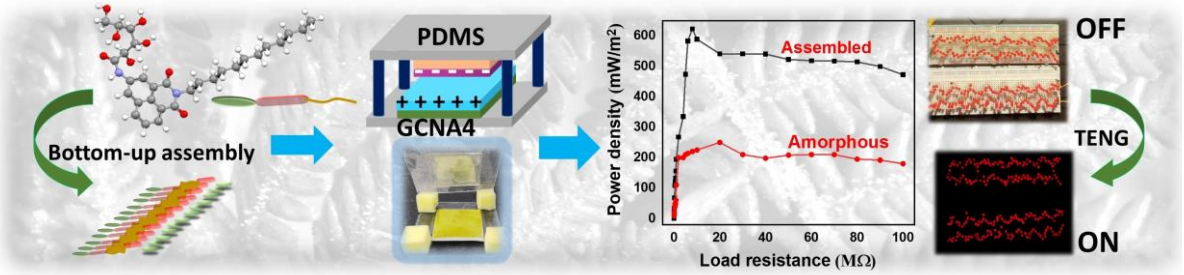

# 3.1. Introduction

Supramolecular assembly is a ubiquitous phenomenon in nature in which molecules spontaneously form aggregates via non-covalent interactions, even without human intervention.[1-4] It is astonishing to see the existence of life in the living organism is facilitated by the supramolecular self-assembly process, where molecules are fundamentally designed and build themselves by a sequential bottom-up organization of disordered collection of individual units.[5-8] Even though ample footprints of highly precise and well-programmed nature's assembly processes were documented in science, technology, and medicine, the topic has emerged as a discrete field of investigation because of its scope to exploit further in chemistry, physics, biology, materials science, nanoscience and technology, advanced manufacturing, biotechnology, and bioengineering.[9–13] It is worth mentioning that the self-assembling chiral natural molecules utilizing non-covalent inter- and intramolecular interactions could offer new clues on life's origin, evolution, and existence.[14–17] In particular, nanoenergy required for the function of various organs, especially in plants and animals, are self-generated by means of mechanical movement assisted by wind, rain, pressure, and flow velocity, to name a few.[18–21] Recently, Gammaitoni and co-workers have demonstrated the utility of nano energy generated in the cell membrane for the operation of wireless communication system.[22] Advances in triboelectric nanogenerators (TENG) demonstrated by Wang and co-workers using live plants model could establish a green and sustainable energy harvesting, which can boost the industrial revolution towards Internet of Things (IoT), next-generation wireless networks and self-powered electronics.[23]

Traditional TENG, in practice, are polymer materials derived from non-renewable resources, which are not cost-effective and biodegradable.[24–27] Hence, to improve the quality of modern life, industrialization, and medicine, a more reliable nano energy harvesting system[28–31] based on organic molecules, which constitute more than 90% of the living system, should be developed. In this regard, a series of low molecular weight organic molecules was generated using an efficient green synthetic protocol from renewable resources. Among the various classes of natural organic compounds that exist in nature, carbohydrates are the most abundant, displaying structural diversity, biodegradability, biocompatibility, and eco-friendliness, and hence we have selected them as one of the starting materials for the synthesis and fabrication of TENG. The massive growth of electronic technology has adopted miniaturization and portable and wearable functionality.[32–35] However, traditional power supplies are not suitable for this type of equipment because they are rigid and complicated to use, have a large size, and are not environmentally friendly. Hence, the near future development is the fabrication of small-

sized electronics operated with nanoenergy. Generally, piezoelectric and triboelectric effects were used to harvest low-magnitude mechanical energies, [36–45] however, the conversion of mechanical energy into electricity utilizing electrostatic induction and triboelectrification using organic molecules is not reported.

In this chapter, biologically relevant small molecules were selected for constructing amphiphiles. Glucono-$\delta$-lactone is a food additive with an E number of E575 and is also classified as Generally Recognised as Safe (GRAS) by the Food and Drug Administration (FDA)[46] and naphthalimide, which displays electrical conductivity through substantial π-π stacking interactions.[47–50] Consequently, the fabrication of miniature devices using the designed amphiphiles could have a broad range of applications. To the best of our knowledge, this is the first report on the fabrication of triboelectric nanogenerators based on the self-assembly of Gluconamide Conjugated Naphthalimide Amphiphiles (GCNA), which is being achieved by coating the hydrogel of GCNA on an aluminium sheet. The demonstrated flexible triboelectric nanogenerator obtained through a more sustainable pathway would open a gateway to fabricating green electronics. In this chapter, a series of GCNA were generated in good yields using sustainable protocol and studied the molecular self-assembly in various solvents. In the bottom-up assembly process, the electron density in π-π stacking unit is studied with respect to molecular structure and arrived at a plausible self-assembly mechanism. Further, the use of GCNA in the energy harvesting application and the mechanism of TENG were investigated in depth.

## 3.2. Results and Discussion

Thus far, various methodologies have been proposed for nano energy harvesting from the local environment, which includes light, heat, electromagnetic radiations, molecular vibration, and mechanical actions.[51–53] Since from inception of the TENG concept, scientists have devoted efforts and found that electrical energy can be generated by rubbing the different metallic or inorganic or polymeric semiconductors. However, molecular design and mechanistic studies are crucial parameters in TENG, which have not yet been studied.[54–57] At the most fundamental level of supramolecular materials design and fabrication, molecules should be minimalistic mimics of biological systems displaying dynamic porosity and hierarchical organization facilitated by various intermolecular interactions.[58,59] Thus, supramolecular self-assembly of carbohydrate derivatives could be an ideal system to unveil the mechanism of TENG in biological materials. Taking the prerequisite into account in our molecular design, a carbohydrate unit is conjugated with naphthalimides bearing varying hydrophobic alkyl chains

to obtain intermolecular H-bonding interaction and- electron delocalization. To establish a suitable reaction condition for the synthesis of GCNA, optimization studies were performed using Glucono-$\delta$-lactone and 5-Amino-2-decyl-naphthalimide **2c** as model substrates (**Table 3.1**).

**Table 3.1**. Optimization of the reaction conditions for the synthesis of gluconamide conjugated naphthalimide amphiphiles using Glucono-$\delta$-lactone and 5-amino-2-decyl-naphthalimide **2c** as a model substrate

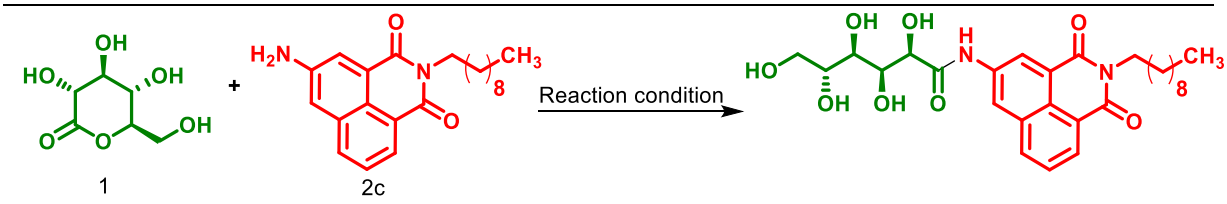


1 2c

| S.No | Solvent | Temp (°C) | Catalyst | Time (h) | Yield (%)[b] |
|---|---|---|---|---|---|
| 1 | Toluene | rt | __ | 24 | NR |
| 2 | DCM | rt | __ | 24 | NR |
| 3 | THF | rt | __ | 24 | NR |
| 4 | Dioxane | rt | __ | 24 | NR |
| 5 | MeOH | rt | __ | 24 | NR |
| 6 | EtOH | rt | __ | 24 | NR |
| 7 | $CH_3CN$ | rt | __ | 24 | NR |
| 8 | DMF | rt | __ | 24 | NR |
| 9 | Glycerol | rt | __ | 24 | NR |
| 10 | Ethylene glycol | rt | __ | 24 | NR |
| 11 | PEG-400 | rt | __ | 24 | NR |
| 12 | $H_2O$ | rt | __ | 24 | NR |
| 13 | MeOH | 65 | __ | 24 | NR |
| 14 | MeOH | 65 | TEA | 24 | NR |
| 15 | MeOH | 65 | Pyridine | 24 | NR |
| 16 | MeOH | 65 | Piperidine | 24 | NR |
| 17 | MeOH | 65 | Pyrrolidine | 24 | NR |
| 18 | MeOH | 65 | $(NH_4)_2SO_4$ | 24 | NR |
| 20 | MeOH | 65 | AcOH | 24 | NR |
| 21 | MeOH | 65 | Pyridine/AcOH | 24 | NR |
| 19 | MeOH | 65 | $I_2$ | 24 | 94[c] |
| 22 | MeOH | 65 | $Sc(OTf)_3$ | 24 | 47 |
| 23 | MeOH | 65 | $InCl_3$ | 24 | 60 |
| 24 | MeOH | 65 | $BF_3OEt_2$ | 24 | 32 |
| 25 | MeOH | 65 | $AlCl_3$ | 24 | 38 |
| 26 | MeOH | 65 | $FeCl_3$ | 24 | 41 |
| 27 | MeOH | 65 | $ZnCl_2$ | 24 | 28 |

[a]all the reactions were carried out with 5-Amino-2-decyl-naphthalimide **2c** (1 mmol) and Glucono-$\delta$-lactone (1.5 mmol) in 10 mL of MeOH. [b]Isolated yields. [c]Optimized reaction condition for the synthesis of GCNA.

At the outset, to check the feasibility of the reaction, initially, the reaction was performed in water, ethanol, methanol, glycerol, ethylene glycol, PEG-200, dioxane, acetonitrile, and tetrahydrofuran, dichloromethane without any catalyst (**Table 3.1, Entry 1-13**). Unfortunately, polar and nonpolar aprotic solvents, including the green reaction medium and water, did not

render the desired product at room temperature. The reaction performed in the presence of organic bases such as pyridine, piperidine, pyrrolidine, TEA, and weak acids, including AcOH (pKa = 4.76), Pyridine in AcOH (pKa = 5.23), did not furnish the desired product. The reaction was screened in the presence of Lewis acids such as $InCl_3$, $Sc(OTf)_3$, and $BF_3.OEt_2$, $AlCl_3$, $FeCl_3$, and $ZnCl_2$ in methanol at reflux condition delivered the desired product in 28-60% yield. It is noteworthy that the conjugation of gluconolactone with 5-amino-2-alkylnaphthalimide has proceeded well using Iodine as a catalyst in MeOH and furnished the **GCNA1-7** in excellent yield without complicated workup and column chromatographic purification (**Scheme 3.1**).

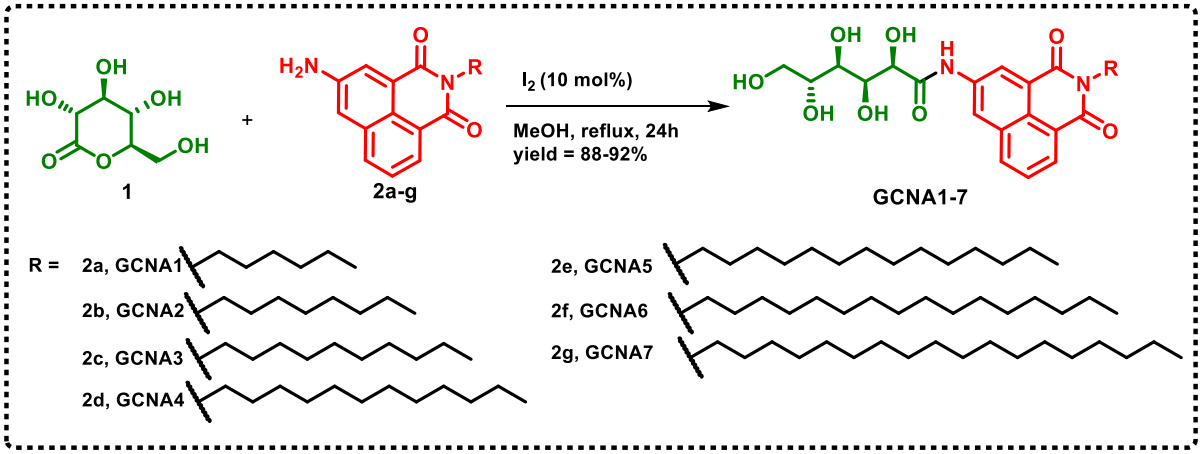


**Scheme 3.1.** Synthesis of gluconamide conjugated naphthalimide amphiphiles, **GCNA1-7**.

Nevertheless, the energy harvested in a bio cell directly from cell membrane potential has been used to perform micro-scale physiological activities.[22,60] In most biological systems, molecular self-assembly phenomena displaying various surface morphologies such as fibers, wires, and porous micro and nano-patterns act as primary sources of mechanical energy harvesting through triboelectrification. To mimic the pattern of a natural system, molecular self-assembly of **GCNA1-7** in various solvents was performed. Owing to the existence of salient structural features of **GCNA1-7,** such as hydroxyl and amide linkage to induce hydrophilicity, naphthalimide moiety for π-π stacking, and alkyl chain to induce hydrophobicity, the individual component can organize spontaneously into the desired architecture with more flexibility and precision.

It is worth mentioning that the bottom-up fabrication method adopted here was in line with the nature assembly process, displaying error correction capacity and tunability with respect to the environment.[61] A typical "stable to inversion" method is used to identify the existence of supramolecular architecture in the solvent environment via the generation of anisotropic structure,[62,63] which then entangle to generate a network wherein solvent was trapped to form gel at room temperature. Initially, a broad range of solvents was used to check the gelation of GCNA1-7 bearing varying degrees of hydrophilic-lipophilic balance (HLB) with a loading of

2 % wt/v (**Table 3.2**). Almost all the tested organic solvents did not display gelation; rather, it remains insoluble or solution or precipitate. The use of vegetable oils as a gelation medium rendered a satisfactory result, however, the initial nucleation and further growth into gel network via intermolecular interactions are found to be frail, and even little vibrations could commute gel into viscous solution. It should be noted that in linseed oil, although a complete dissolution is observed upon heating, a degree of direct interaction between GCNA is restricted because of the presence of more unsaturation, which in turn directly reflects on the polarity of the solvent. For gelation, molecules should be soluble leastwise at elevated temperature, and upon assembly influenced by the environmental factor furnish the supramolecular architecture.

**Table 3.2.** Gelation studies of compounds **GCNA1-7** in various solvents and vegetable oils

| **S.No** | **Solvent/Oils** | **GCNA 1** | **GCNA 2** | **GCNA 3** | **GCNA 4** | **GCNA 5** | **GCNA 6** | **GCNA 7** |
|---|---|---|---|---|---|---|---|---|
| | | | | | | | | |
| 1 | linseed oil | S | S | S | S | S | S | S |
| 2 | olive oil | S | S | PG | PG | PG | PG | PG |
| 3 | paraffin light | S | S | S | PG | PG | PG | PG |
| 4 | polyethylene glycol(PEG) | S | S | S | S | S | S | S |
| 5 | chloroform | I | I | I | I | I | I | I |
| 6 | DMSO | S | S | S | S | S | S | S |
| 7 | chloroform + DMSO | | | | | | | G |
| **8** | **DMSO+$H_2O$** | **G(1)** | **G(1)** | **G(1)** | **G(0.7)** | **G(0.7)** | **G(0.7)** | **G(0.7)** |
| 9 | cyclohexane | I | I | I | I | I | I | I |
| 10 | toluene | I | I | I | I | I | I | I |
| 11 | N-Methyl-2-pyrrolidone | S | S | S | S | S | S | S |
| 12 | 1,4-dioxane | S | S | S | S | S | S | S |
| 13 | ethanol | P | P | P | P | P | P | P |
| 14 | methanol | P | P | P | P | P | P | P |
| 15 | butanol | P | P | P | P | P | P | P |
| 16 | isopropanol | S | S | S | S | S | S | S |
| 17 | xylene | S | S | S | S | S | S | S |
| 18 | water | I | I | I | I | I | I | I |
| 19 | diesel | S | S | PG | PG | PG | PG | PG |
| 20 | 1,2-dichlorobenzene | P | P | P | P | P | P | P |
| 21 | $CH_3CN$ | I | I | I | I | I | I | I |
| 22 | THF | I | I | I | I | I | I | I |
| 23 | 1,2-dichloroethane | I | I | I | I | I | I | I |
| 24 | DCM | I | I | I | I | I | I | I |

CGC, critical gelation concentration is given in %wt/v (parentheses). S, soluble; G, Gel; PG, partial gel; I, insoluble; P, precipitation.

Initially, the use of water as a solvent for the bottom-up assembly of **GCNA1-7** did not provide encouraging results because of less solubility. Indeed, our trial with the dissolution of **GCNA1-7** using DMSO followed by the addition of water furnished excellent gelation with the critical gelation concentration (CGC) of 0.7% and 1.0 % wt/v (**Table 3.2**). Representative images of the gel formed by **GCNA3-7** at CGC 1% wt/v is given in **Figure 3.1a,b**. GCNA hydrogel developed here is thermo-reversible and opaque in nature, which indicates the organization of molecules at room temperature. Concentration-dependent gel-to-sol transition temperature ($T_g$) measurements show a gradual increase, and a plateau is obtained upon attaining the saturation level of **GCNA1-7** solution (**Figure 3.1c**). Interestingly, the length of the hydrophobic chain in GCNA, the nature of the solvent, and the amount of unsaturation in the vegetable oil dramatically impacted the molecular assembly process, which in turn influenced the materials' properties. Among the series of GCNA synthesized, **GCNA4** displayed higher $T_g$ with CGC of 0.7 % wt/v, and hence, for further investigation, we have selected **GCNA4** as a model substrate.

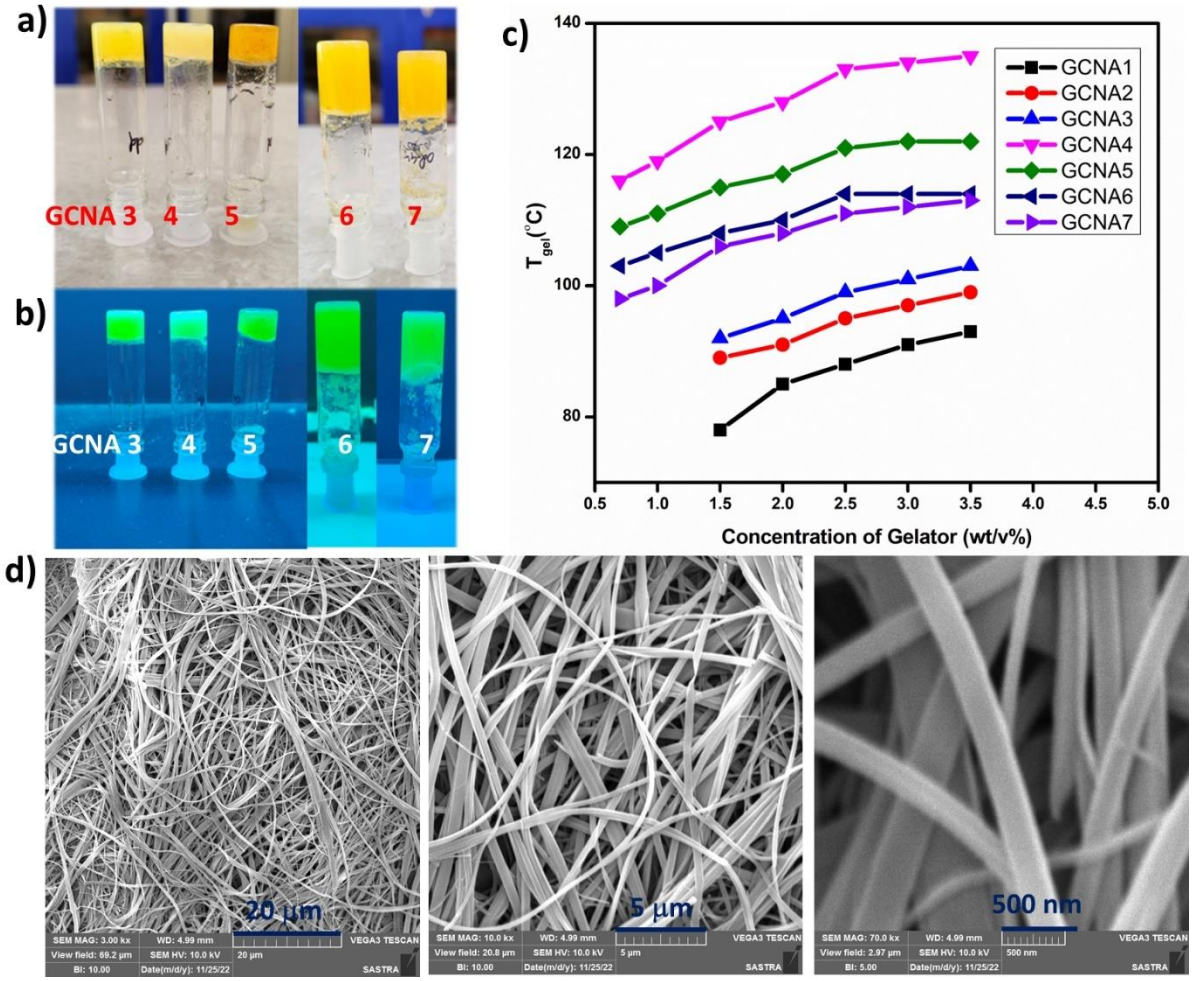


**Figure 3.1**. Images of gel formed by compounds **GCNA3-7** in DMSO-$H_2O$ (40% v/v), (a) under normal light and b) UV light (CGC = 1% wt/v). (c) Concentration dependent gel to sol transition temperature ($T_g$) measurements of compounds **GCNA1-7**. (d) SEM images of xerogel formed by **GCNA4** in DMSO-$H_2O$ (40 % v/v)

The hypothesis of the formation of fibrillar network by molecular self-assembly is confirmed by SEM analysis. Morphological analysis of **GCNA4** gel revealed that the existence of intertwined fibrillar structure having a width ranging from 200-300 nm (**Figure 3.1d**). The formation of the fibrillar network by sugar-based amphiphiles is already well documented in literature,[64-68] however, the contributing factors for the bottom-up assembly process, such as gelator design, solvent effect, temperature, and assembly pattern, requires a thorough investigation.[69] In GCNA system, the electronic environment in the naphthalimide unit is considered as crucial, which exclusively contributes to the TENG. $^1$H NMR is one of the best, readily available, and reliable techniques to investigate the electronic environment of an assembling molecule. Proton in different electronic environments absorbs at different frequencies; however, the intramolecular contributors such as inductive and mesomeric effect or strong intermolecular interactions such as hydrogen bonding, π-π, anionic-π, cationic-π and halogen-π interactions can tune the absorbance frequency marginally.

$^1$H NMR spectra of **GCNA4** dissolved in DMSO-$d_6$ at 25 ºC displayed well-resolved signals at δ 8.85, 8.80, 8.36 and 7.81 ppm for $H_a$-$H_e$ protons of naphthalimide moiety (**Figure 3.2a**). Upon addition of $D_2O$ to DMSO-$d_6$ in the ratio of 6:4, an opaque solid-like gel network with significant upfield shift in $H_a$, $H_b$, and $H_e$ signals and tenuous upfield shift in $H_c$ and $H_d$ signals is noted. The observed signal shift can be attributed to two factors: the interaction of polar protic solvent with **GCNA4** or the bottom-up assembly of **GCNA4** facilitated by intermolecular interactions. To validate the interaction of solvent with **GCNA4** is the main cause for the upfield shift of the naphthalimide unit signal, a comparison with its analogous molecule, *N*-glycosyl naphthalimide (**NGN**), was made. $^1$H NMR spectra of **NGN** was recorded in solution and gel state (**Figure 2.5a**). The **NGN** under similar experimental conditions displayed a significant downfield shift of $H_b$ and $H_c$ protons, and tenuous upfield shift of $H_a$ proton. Suppose the interaction of $D_2O$ with naphthalimide unit of **GCNA4** is the contributing factor for the upfield shift, then the structural analogue, **NGN** also should show the similar shift pattern. Nevertheless, the distinct shift pattern displayed by the protons of naphthalimide unit of **GCNA4** and **NGN** clearly revealed that the solvent interaction is not only the factor for the upfield shift of NMR signals. Since the solvent effect is ruled out, the one and only factor contributing factor is molecular assembly by means of intermolecular interactions. In assembling system, electronic environment of stacking unit by means of π-π interaction is not clearly established, and the influence of such effect in materials properties also left unanswered. The collected NMR data for **GCNA4** and analysis could provide solution for the above-mentioned problems.[70] Generally, chemical shift of a proton is based on the electronic

environment, which influences the applied magnetic field ($B_o$) thereby the proton can resonate in lower or higher frequency region. Upon the molecular assembly of **GCNA4**, in the vicinity of nucleus of $H_a$, $H_b$ and $H_e$, the circulating π-electron of naphthalimide unit increase the electronic density, which in turn increase the induced magnetic field of respective proton. The induced magnetic field of $H_a$, $H_b$ and $H_e$ protons opposes the applied magnetic field strength ($B_o$), thereby the proton feels the relatively weaker magnetic field and hence lower frequency is needed for the resonance.

It is worth mentioning that the electronic environment of $H_c$ and $H_d$ are slightly influenced by molecular assembly. **GCNA4** in well dispersed and aggregated state display change in energy of $4.77x10^{-32}$ J, $7.315x10^{-32}$ J, $-0.3445x10^{-32}$J, $0.9806x10^{-32}$J and $2.6106x10^{-32}$J for $H_a$-$H_e$ protons respectively. Because of the existence of different electronic environment in naphthalimide moiety, C-H and C-C bonds has been identified as anisodesmic. In VT-NMR studies, a tenuous upfield shift of all the protons of naphthalimide moiety at 90 °C, the temperature lower than $T_g$, revealed the increase in the electron density around $H_a$-$H_e$ by isodesmic fashion (**Figure 3.2a**).

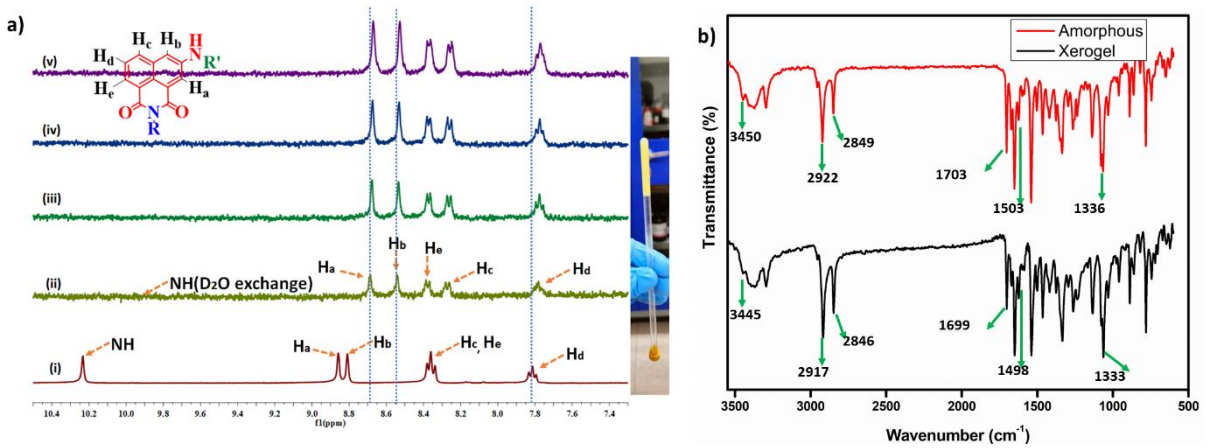


**Figure 3.2**. (a) VT-NMR spectra of **GCNA4** in i) DMSO-$d_6$ at 25 °C, ii-v) DMSO-$d_6$ -$D_2O$ (40% v/v) at 80 °C, 85 °C, 90 °C, and 95 °C respectively (inset an opaque solid like gel in NMR tube). (b) A comparison of FT-IR spectra of compound **GCNA4** in the amorphous state (red) and xerogel state (black).

A comparative NMR analysis of **GCNA4** and **NGN** revealed that a small change in hydrophilic moiety can drastically influence π–π stacking of naphthalimide moiety. Under these circumstances, it is worth investigating the intermolecular forces responsible for the bottom-up molecular assembly of **GCNA4**. ATR-FTIR studies is one of the readily available methods to investigate the intermolecular interaction.[71,72] **GCNA4** in the amorphous form displayed characteristic absorption frequencies of -OH, amide I, amide II, amide III, and alkyl at 3450, 1703, 1503, 1336, 2922 and 2849 $cm^{-1}$, respectively. Even though a random arrangement of molecules in a 3D lattice is pronounced in the amorphous state, a marginal intermolecular interaction would also be displayed. Nevertheless, the bottom-up assembly of **GCNA4** displays

a sensitive molecular arrangement in the 3D lattice by means of regular intermolecular interaction, which in turn reflect in the absorption frequencies of -OH, amide I, amide II, amide III, and alkyl at 3445, 1699, 1498, 1333, 2917 and 2846 $cm^{-1}$ respectively (**Figure 3.2b**).

Having established the various groups such as hydroxyl, amide, aryl and alkyl chain responsible for the intermolecular interactions, it is mandatory to establish the mode of aggregation. Generally, the performance of organic electronics or energy devices relies on the functional properties of organic molecules and their mode of assembly in solid state.[73] To study the mechanism of energy harvesting in artificial scaffolds, various synthetic mimics of natural systems were generated, wherein coherently coupled supramolecular aggregates play a vital role.[74,75] Depending upon the spatial arrangement and the relative orientation of molecules, aggregation pattern is termed as *J*-type, a head to tail type or slipped type arrangement and *H*-type, a parallel arrangement. To gain a deep insight into the mode of aggregation, absorption, and emission spectra were recorded at various concentrations. **GCNA4** dissolved in $H_2O$-DMSO (6:4 ratio) at 25 x $10^{-6}$ M displayed an absorbance at 253 nm, which, upon aggregation by the influence of the addition of **GCNA4** displayed a bathochromic shift of $\lambda_{max}$ to 260 nm (**Figure 3.3b**). The red shift displayed by **GCNA4** in concentration-dependent UV-vis studies indicates the formation of *J*-type aggregates. In the concentration dependent emission studies, upon increasing the concentration of **GCNA4**, a gradual decrease in emission intensity is observed. Such type of fluorescence quenching is likely facilitated through the *J*-type aggregation of **GCNA4** (**Figure 3.3c**).

To predict the 3D arrangement of building blocks,[76,77] small angle XRD of xerogel of GCNA4 was recorded (**Figure 3.3a**). The formation of gel in hydrophilic solvent suggests that hydrophilic group is projected outwards and hydrophobic alkyl chains were projected inside the fibrillar architecture, arranged in a slipped *J*-type mode. It is worth mentioning that the interplanar spacing follows a Bragg's reflection progression ratio of 1:1/2, 1/3, 1/4, 1/5, 1/6, 1/7 and 1/8 suggest the regular arrangement of **GCNA4** during the bottom-up assembly process in a *J*-type pattern.

In addition, the close spacing of peaks at low angle region, especially between $2\theta$ = 9.1-12.9° implies the existence of large unit cell with different H-bonding faces of carbohydrate unit and amide bond (**Figure 3.3a**). The energy-minimized structure of **GCNA4** furnished an end-to-end molecular length of 2.2 nm, which is lower than the value obtained from XRD, suggesting the intercalated *J*-type aggregation. Based on the VT-NMR, IR, UV-Vis, and emission studies experimental data, a schematic representation of the bottom-up assembly mechanism of **GCNA4** is given in **Figure 3.3d.**

In the field of engineering, especially during the device fabrication process, the material used should not undergo deformation; even such deformation of a lower magnitude will affect the performance of the device.[78,79] The strength and processability of gel has been confirmed by rheological measurements.

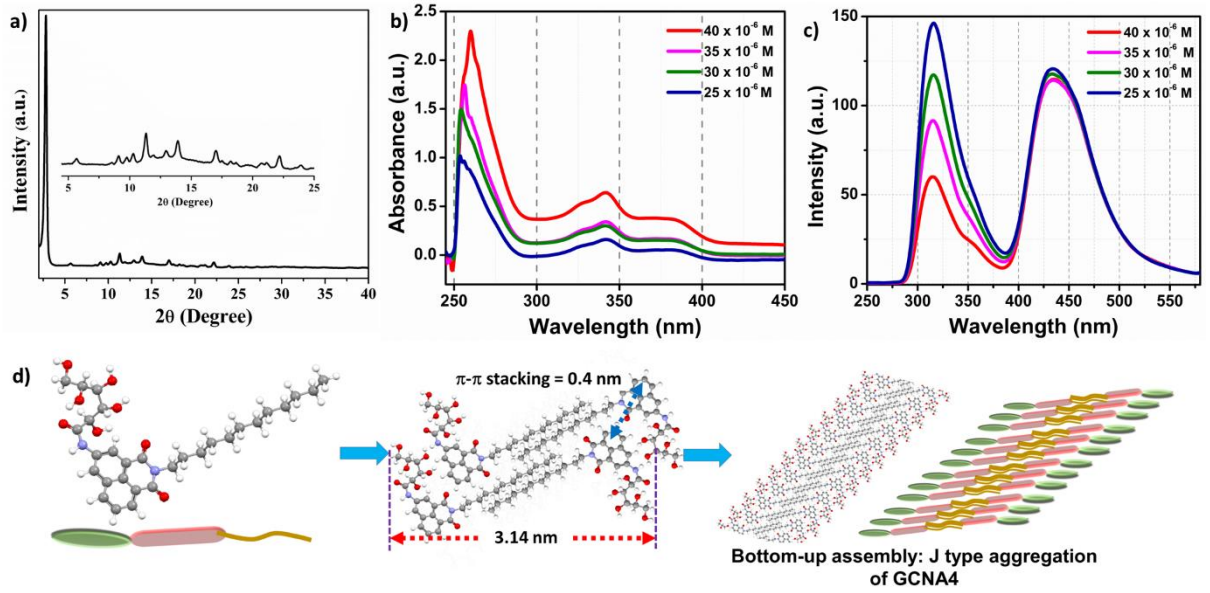


**Figure 3.3**. (a) XRD pattern of **GCNA4** xerogel (inset zoom in selected area). (b) UV-vis and (c) fluorescence titration of **GCNA4** dissolved in gelling solvent DMSO-$H_2O$ [$\lambda_{ex}$ = 250 nm]. (d) A schematic representation of bottom-up assembly of **GCNA4** to generate *J* type aggregated fibrillar network.

Strain amplitude and angular frequency dependence of **GCNA4** gel displayed higher storage modulus G' as compared to the loss modulus G'' within the range of linear viscoelastic region (**Figure 3.4a-b**). It is observed that the gel strength increases as the progression of angular frequency. To evaluate the rapid recovery of **GCNA4** gel, a series of shear stress loop test were conducted. The consecutive application of high strain and low strain on the gel reveals the destruction of gel network followed by a rapid recovery of its original structure without any deformation, which accounts the high stability and processability (**Figure 3.4c**).

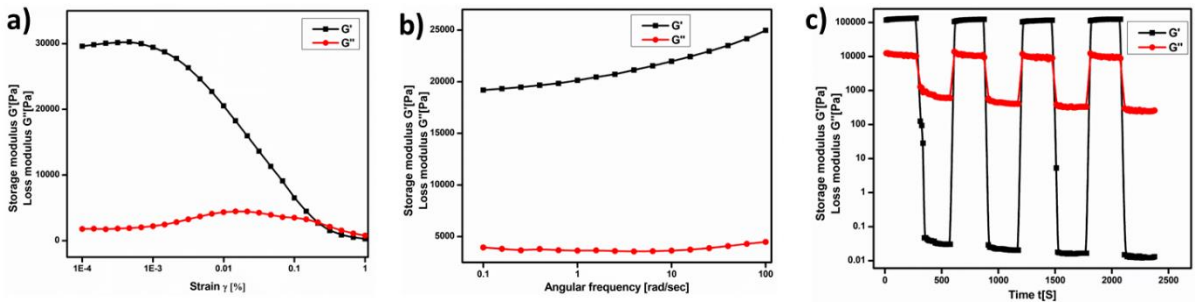


**Figure 3.4.** (a-b) Strain amplitude and Angular frequency dependence of G′ and G″. (c) thixotropic behaviour investigation using continuous strain ramp-up and ramp-down measurements of gel formed by compound **GCNA4** in DMSO-$H_2O$ (40% v/v).

Having established the molecular assembly process, the potential of increased electron density in naphthalimide unit is further asserted by fabricating TENG device. The schematic of the device fabrication steps is presented in **Figure 3.5a**. Initially, aluminium and indium tin oxide-coated polyethylene terephthalate (ITO-PET) sheets (5x5 $cm^2$) were taken as electrode materials. Onto the aluminium sheet of dimension 5x4 $cm^2$, **GCNA4** film of ~ 80 µm thickness is coated by drop casting method, and PDMS was attached to ITO electrodes as shown in **Figure 3.5a**. Further, triboelectric layers attached electrodes are attached to the acrylic sheets (7x7 $cm^2$) with strong glue, as shown in **Figure 3.5a**. Finally, the above two acrylic layers are placed one over the other with the help of a sponge spacer to form the vertical contact separation mode of the TENG operation. The final TENG device has an active area of 5x4 $cm^2$ and spacing of ~1.2 cm between the triboelectric layers.

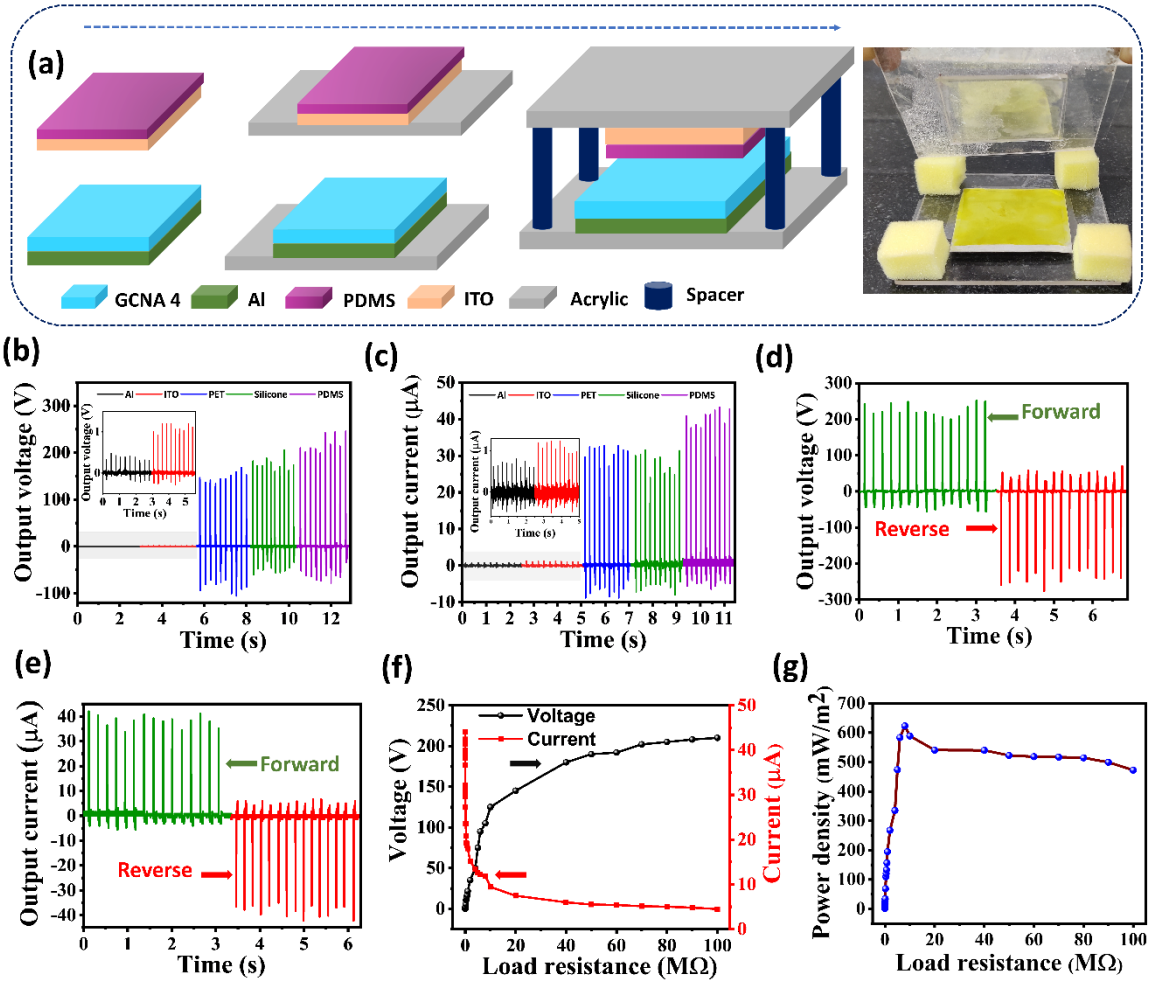


**Figure 3.5**. (a) Fabrication steps of TENG and photograph of the actual fabricated TENG device. (b-c) Output voltage and current of GCNA4-TENG with different triboelectric layers. (d-e) Switching polarity test responses of **GCNA4**-TENG with PDMS. (f) Output current and the voltage across the different load resistances. (g) Instantaneous power density as a function of load resistance.

For TENG device fabrication, keeping **GCNA4** coated aluminium sheet as a constant triboelectric layer, we have chosen Al, ITO, PET, silicone, polydimethylsiloxane (PDMS) as

other triboelectric layers. To test the potential of mechanical energy harvesting, TENG is connected to the measuring instrument with the help of two conducting wire connections. The output voltage and current against hand slapping force are measured using a digital storage oscilloscope (DSO, MSO 5204) and current preamplifier (SRS 570), respectively. The open circuit voltage and short circuit of **GCNA4**-TENG with different opposite triboelectric layers under the hand tapping force is shown in **Figure 3.5b,c**.

Among the various opposite triboelectric layers such as Al, ITO, PET, silicone, and PDMS tested, the combination of **GCNA4-PDMS** triboelectric system generated a maximum output voltage and current. The open-circuit voltage and short-circuit currents of ~250 V, and 40 μA were observed in **GCNA4**-PDMS TENG system. Further, **GCNA4**-PDMS TENG output has also been recorded under reverse connections to the measuring instrument to confirm the origin of output voltage and current. **Figure 3.5d,e** shows the **GCNA4**-PDMS TENG output under normal and reverse connections, and the results assert that the response is coming only from TENG and not from any noise. [80,81] Further, the electrical behaviour of **GCNA4**-PDMS TENG was tested under different external load resistances, and the responses are shown in F**igure 3.5f,g**. The output voltage increased with load resistance up to 80 MΩ and thereafter attained a plateau. The saturated output voltage value is close to the open circuit voltage since the circuit acts like an open circuit at such high load resistance values. On the contrary, the output current is decreased with the load resistance due to ohmic losses. The behavior of TENG with load is similar to the reported literature.[82,83] From the load characteristic curves, instantaneous power density (Pd=(VI/A) has been calculated and presented in **Figure 3.5g**. The Pd values increased with load resistance and reached a peak value of ~622 mW/m$^2$ at 8 MΩ and decreased later.[81,84] The maximum power observed at 8 MΩ is considered as load-matching condition, where the device delivers maximum energy to the load.

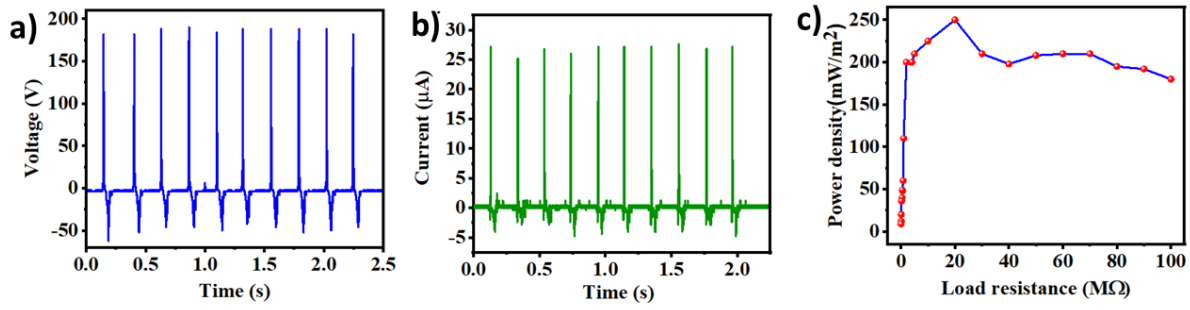


**Figure 3.6.** (a) open circuit voltage, and (b) short circuit current of amorphous **GCNA**-PDMS based TENG. (c) power density as a function of load resistance

To verify the crucial role of bottom-up assembly of **GCNA4** in TENG, another TENG device was fabricated under similar conditions using amorphous **GCNA4** and PDMS as triboelectric

layers and tested its response. The output voltage, current, and power density of amorphous **GCNA4** displayed ~ 180 V, 26 μA, and 250 mW/m$^2$, respectively (**Figure 3.6**). The high performance of assembled **GCNA4**-PDMS TENG over the amorphous **GCNA4**-PDMS system-based TENG is attributed to the increase in the electron density of naphthalimide moiety by *J*-type aggregation. The working mechanism of GCNA4-PDMS is schematically presented (**Figure 3.7a**). Before applying any force on the TENG, triboelectric layers are in a separated state and therefore, no potential difference is observed (**Figure 3.7a**). Upon applying force on top of TENG, friction between the layers is generated upon contact, and they exchange charges based on their electronic affinities and get charged. The increased electron density observed in the aggregated naphthalimide moiety facilitates the electron donating tendency, and the strongly electronegative PDMS accepts the electrons donated; and hence, it attains a negative charge of equivalent quantity (**Figure 3.7a-ii**). Consequently, when both the layers are separated, the materials posse static charges on their surfaces by which a potential difference is established. The developed potential drives the electrons to flow from the top electrode to the bottom electrode and reaches an equilibrium state (**Figure 3.7a (iii-iv**)). When both the layers started moving closer again, the electrons started flowing in the reverse direction (**Figure 3.7a (v)**). The repeated process of contacting and separating the triboelectric layer produces an alternating voltage/current in the external load.

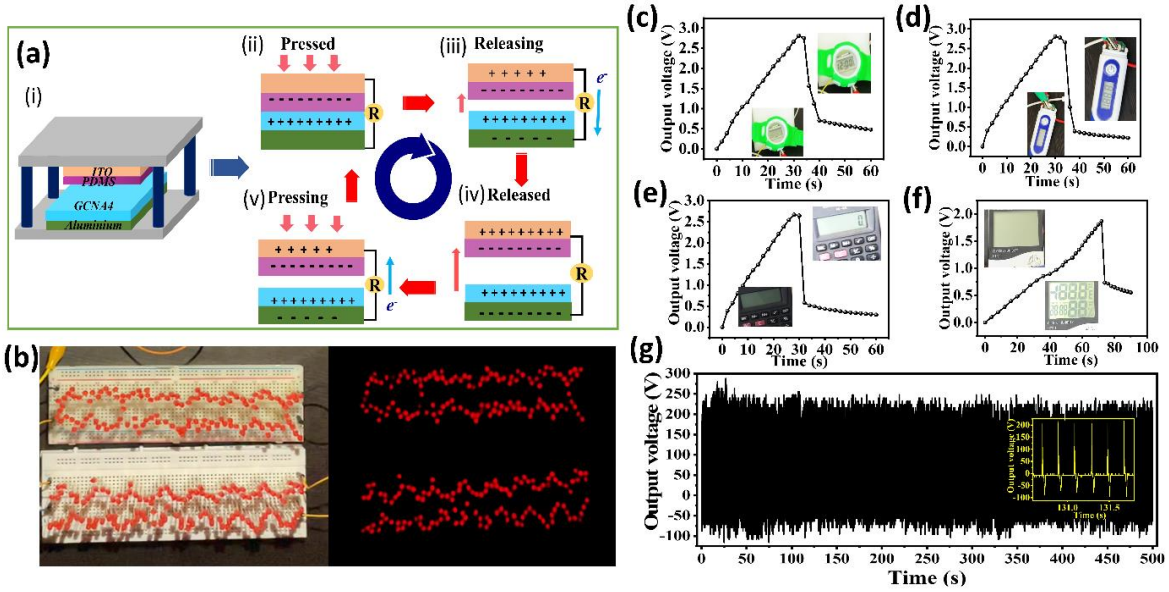


**Figure 3.7**. (a) Working mechanism of GCNA4-PDMS TENG, (b) image of TENG powering-up 240 red LEDs (c-f) Powering-up small electric devices i. e. wristwatch, thermometer, and calculator with 4.7 μF capacitor and hygrometer with 47 μF capacitor, (g) Stability of the TENG over 2500 cycles (inset magnified view of a few cycles).

Finally, different applications of the proposed TENG are presented in **Figure 3.7b-f**. The AC output of the TENG was rectified using a bridge rectifier, and the rectified output was given to a series-connected 240 red LEDs. **Figure 3.7b** shows the Off and On state of the 240 LEDs

powered by TENG under repeated hand tapping. Further, the DC output of the TENG was stored in a capacitor and powered small electronic devices such as wristwatch, thermometer, calculator, and hygrometer respectively. **Figures 3.7c-f** show the charging and discharging curves of the capacitor before and after powering the projected. The stability and durability of the TENG device are important parameters from the device's point of view. To study the stability of the TENG device, TENG was tested for ~2500 cycles of repeated hand tapping at a frequency of ~ 4Hz with 1 minute interval. **Figure 3.7g** clearly reveal that the fabricated TENG displays a stable output voltage for all the cycles. For clarity, an enlarged view of a few cycles is shown in the inset of **Figure 3.7g**. The device response was tested over three months, and a stable response was found.

## 3.3. Experimental

### 3.3.1. General Information

A detailed general information is given in Chapter 2.

### 3.3.2. General procedure for the synthesis of gluconamide conjugated naphthalimide amphiphiles GCNA1-7

To a stirred solution of 5-amino-2-alkyl-naphthalimide 3a–g (1.0 mmol) in MeOH (10 mL) was added glucono-δ-lactone 4 (1.5 mmol) followed by $I_2$ (0.1 mmol). The reaction mixture was stirred at 65 ºC for 24 h in an oil bath. During the progress of the reaction, a pale-yellow solid precipitated out was filtered and washed with water, cold methanol and diethyl ether. Recrystallized in ethanol to get the pure product.

Complete details on gelation studies, morphological analysis, X-ray diffraction, molecular modelling, and rheological studies are given in Chapter 2.

## 3.4. Characterization Data

**(2R,3S,4R,5R)-N-(2-hexyl-1,3-dioxo-2,3-dihydro-1H-benzo[de]isoquinolin-5-yl)-2,3,4,5,6-pentahydroxyhexanamide (GCNA1)**:

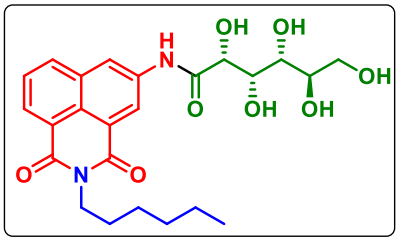


Amorphous yellow solid; yield: 96% (0.454 g); mp: 196-198 ºC. IR (neat): 3449, 2922, 2849, 1703, 1672, 1503, 1336, and 1031 $cm^{-1}$. $^1H$ NMR (400 MHz, DMSO-$d_6$): δ 10.25 (s, 1H), 8.86 (d, $J$ = 2.0 Hz, 1H), 8.82 (d, $J$ = 2.0 Hz, 1H), 8.35 (m, 2H), 7.80 (t, $J$ = 7.6 Hz, 1H), 5.78 (s, 1H), 4.60 (s, 3H), 4.29

(d, *J* = 3.6 Hz, 1H), 4.09 – 4.06 (m, 1H), 4.03 (t, *J* = 7.4 Hz, 2H), 3.63 – 3.58 (m, 1H), 3.56 – 3.53 (m, 2H), 3.44 – 3.41 (m, 2H), 1.68 – 1.58 (m, 2H), 1.31 (s, 6H), 0.86 (t, *J* = 7.0 Hz, 3H). $^{13}$C NMR (100 MHz, DMSO-$d_6$) δ 172.99, 163.87, 163.65, 137.94, 134.15, 132.40, 129.51, 127.98, 125.25, 124.60, 122.97, 122.31, 122.16, 74.74, 72.58, 72.02, 70.99, 63.78, 31.43, 27.90, 26.65, 22.44, 14.37. HRMS (ESI, m/z): $[M+H]^+$ calcd. for $C_{24}H_{30}N_2O_8$: 475.2080; found: 475.2075.

**(2R,3S,4R,5R)-2,3,4,5,6-pentahydroxy-N-(2-octyl-1,3-dioxo-2,3-dihydro-1H-benzo[de]isoquinolin-5-yl)hexanamide (GCNA2)**:

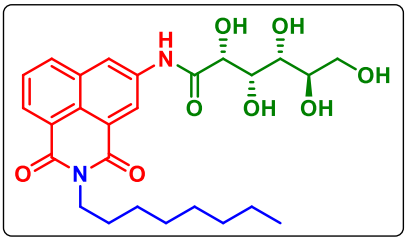

Amorphous yellow solid; yield: 93% (0.466 g); mp: 191-193 °C. IR (neat): 3450, 2921, 2849, 1703, 1672, 1503, 1336, and 1031 cm$^{-1}$. $^1$H NMR (400 MHz, DMSO-$d_6$) δ 10.24 (s, 1H), 8.86 (d, *J* = 2.0 Hz, 1H), 8.81 (d, *J* = 1.6 Hz, 1H), 8.36 (t, *J* = 8.0 Hz, 2H), 7.81 (t, *J* = 7.8 Hz, 1H), 5.76 (d, *J* = 5.2 Hz, 1H), 4.64 – 4.56 (m, 3H), 4.38 (t, *J* = 5.6 Hz, 1H), 4.29 (t, *J* = 4.4 Hz, 1H), 4.11 – 4.06 (m, 1H), 4.03 (t, *J* = 7.4 Hz, 2H), 3.65 – 3.51 (m, 4H), 1.68 – 1.58 (m, 2H), 1.32 (s, 4H), 1.24 (s, 6H), 0.85 (t, *J* = 6.8 Hz, 3H). $^{13}$C NMR (100 MHz, DMSO-$d_6$) δ 172.98, 163.88, 163.66, 137.93, 134.15, 132.40, 129.53, 127.99, 125.25, 124.62, 122.98, 122.32, 122.18, 74.74, 72.59, 72.02, 71.00, 63.78, 31.68, 29.16, 29.02, 27.91, 26.98, 22.52, 14.39. HRMS (ESI, m/z): $[M+H]^+$ calcd. for $C_{26}H_{34}N_2O_8$: 503.2393; found: 503.2389.

**(2R,3S,4R,5R)-N-(2-decyl-1,3-dioxo-2,3-dihydro-1H-benzo[de]isoquinolin-5-yl)-2,3,4,5,6-pentahydroxyhexanamide (GCNA3)**:

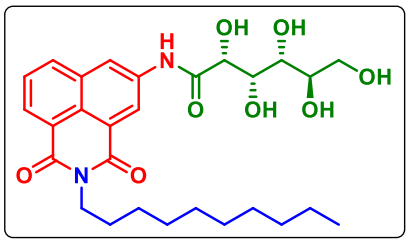

Amorphous yellow solid; yield: 94% (0.497 g); mp: 187-189 °C. IR (neat): 3450, 2922, 2849, 1703, 1672, 1503, 1336, and 1031 cm$^{-1}$. $^1$H NMR (400 MHz, DMSO-$d_6$) δ 10.23 (s, 1H), 8.85 (d, *J* = 2.0 Hz, 1H), 8.81 (d, *J* = 1.6 Hz, 1H), 8.35 (t, *J* = 7.8 Hz, 2H), 7.80 (t, *J* = 7.6 Hz, 1H), 5.76 (d, *J* = 3.6 Hz, 1H), 4.60 (s, 3H), 4.37 (s, 1H), 4.30 (s, 1H), 4.09 (s, 1H), 4.03 (t, *J* = 7.4 Hz, 2H), 3.63-3.56 (m, 3H), 3.43 (dd, *J* = 10.6, 5.4 Hz, 1H), 1.67 – 1.58 (m, 2H), 1.31 (s, 4H), 1.23 (s, 10H), 0.84 (t, *J* = 6.8 Hz, 3H). $^{13}$C NMR (100 MHz, DMSO-$d_6$) δ 172.99, 163.88, 163.66, 137.95, 134.15, 132.42, 129.51, 127.98, 125.26, 124.62, 122.99, 122.33, 122.16, 74.74, 72.60, 72.03, 71.00, 63.79, 31.73, 29.39, 29.36, 29.20, 29.13, 27.92, 26.97, 22.54, 14.40. HRMS (ESI, m/z): $[M+H]^+$ calcd. for $C_{28}H_{38}N_2O_8$: 531.2706; found: 531.2708.

**(2R,3S,4R,5R)-N-(2-dodecyl-1,3-dioxo-2,3-dihydro-1H-benzo[de]isoquinolin-5-yl)-2,3,4,5,6-pentahydroxyhexanamide (GCNA4)**:

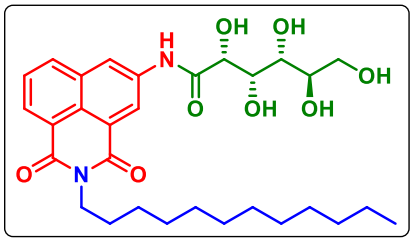

Amorphous yellow solid; yield: 96% (0.534 g); mp: 171-173 °C. IR (neat): 3450, 2922, 2849, 1703, 1672, 1503, 1336, and 1031 $cm^{-1}$. $^1H$ NMR (400 MHz, DMSO-$d_6$) δ 10.24 (s, 1H), 8.86 (d, $J$ = 2.0 Hz, 1H), 8.82 (d, $J$ = 2.0 Hz, 1H), 8.36 (t, $J$ = 7.8 Hz, 2H), 7.80 (t, $J$ = 7.6 Hz, 1H), 5.77 (d, $J$ = 5.6 Hz, 1H), 4.62 (d, $J$ = 2.4 Hz, 1H), 4.61 (s, 1H), 4.59 (d, $J$ = 5.6 Hz, 1H), 4.39 (t, $J$ = 5.6 Hz, 1H), 4.31 – 4.27 (m, 1H), 4.09 – 4.06 (m, 1H), 4.05 – 4.00 (m, 2H), 3.63 – 3.54 (m, 4H), 1.65 – 1.59 (m, 2H), 1.31 (s, 4H), 1.22 (s, 14H), 0.84 (t, $J$ = 6.8 Hz, 3H). $^{13}C$ NMR (100 MHz, DMSO-$d_6$) δ 172.99, 163.87, 163.65, 137.94, 134.15, 132.41, 129.51, 127.97, 125.25, 124.61, 122.97, 122.31, 122.15, 74.74, 72.59, 72.02, 70.99, 63.78, 31.75, 29.48, 29.45, 29.44, 29.36, 29.21, 29.16, 27.92, 26.97, 14.41. HRMS (ESI, m/z): $[M+H]^+$ calcd. for $C_{30}H_{42}N_2O_8$: 559.3019; found: 559.3026.

**(2R,3S,4R,5R)-N-(1,3-dioxo-2-tetradecyl-2,3-dihydro-1H-benzo[de]isoquinolin-5-yl)-2,3,4,5,6-pentahydroxyhexanamide (GCNA5):**

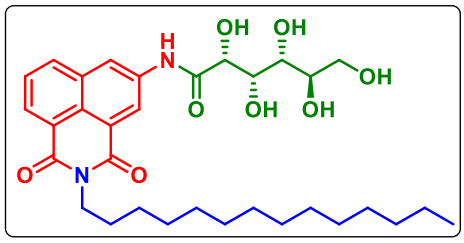

Amorphous yellow solid; yield: 90% (0.526 g); mp: 166-168 °C. IR (neat): 3449, 2922, 2849, 1703, 1672, 1503, 1336, and 1031 $cm^{-1}$. $^1H$ NMR (400 MHz, DMSO-$d_6$) δ 10.23 (s, 1H), 8.86 (d, $J$ = 2.0 Hz, 1H), 8.80 (d, $J$ = 2.0 Hz, 1H), 8.36 (t, $J$ = 7.8 Hz, 2H), 7.81 (t, $J$ = 7.6 Hz, 1H), 4.29 (d, $J$ = 4.0 Hz, 1H), 4.09 – 4.08 (s, 1H), 4.06 – 3.99 (m, 2H), 3.63 (d, $J$ = 2.6 Hz, 1H), 3.60 (d, $J$ = 2.4 Hz, 1H), 3.58 – 3.54 (m, 4H), 1.66 – 1.58 (m, 2H), 1.31 (s, 4H), 1.22 (s, 19H), 0.84 (t, $J$ = 6.8 Hz, 3H). $^{13}C$ NMR (100 MHz, DMSO-$d_6$) δ 172.98, 163.87, 163.65, 137.92, 134.15, 132.40, 129.52, 127.98, 125.23, 124.61, 122.97, 122.30, 122.17, 74.73, 72.60, 72.02, 70.99, 63.78, 31.74, 29.44, 29.41, 29.33, 29.19, 29.14, 27.91, 26.96, 22.54, 14.39. HRMS (ESI, m/z): $[M+H]^+$ calcd. for $C_{32}H_{46}N_2O_8$: 587.3332; found: 587.3329.

**(2R,3S,4R,5R)-N-(2-hexadecyl-1,3-dioxo-2,3-dihydro-1H-benzo[de]isoquinolin-5-yl)-2,3,4,5,6-pentahydroxyhexanamide (GCNA6)**:

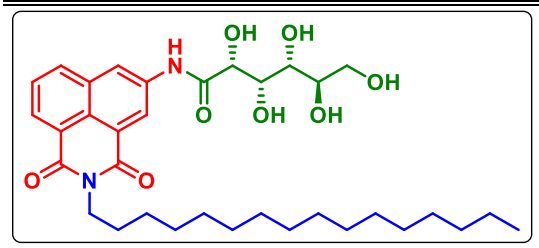

Amorphous yellow solid; yield: 92% (0.531 g); mp: 170-172 °C. IR (neat): 3453, 2922, 2849, 1703, 1672, 1503, 1336, and 1031 $cm^{-1}$. $^{1}H$ NMR (400 MHz, DMSO-$d_6$) δ 10.24 (s, 1H), 8.85 (s, 1H), 8.82 (s, 1H), 8.35 (t, $J$ = 7.8 Hz, 2H), 7.80 (t, $J$ = 7.6 Hz, 1H), 4.29 (d, $J$ = 3.6 Hz, 1H), 4.09 (s, 1H), 4.03 (t, $J$ = 6.8 Hz, 2H), 3.63-3.60 (m, 5H), 3.44-3.40 (m, 4H), 1.62 (s, 2H), 1.31 (s, 4H), 1.21 (s, 22H), 0.84 (t, $J$ = 6.2 Hz, 3H). $^{13}C$ NMR (100 MHz, DMSO-$d_6$) δ 172.98, 163.86, 163.65, 137.94, 134.15, 132.41, 129.50, 127.96, 125.24, 124.61, 122.97, 122.31, 122.15, 74.74, 72.60, 72.02, 70.98, 63.78, 31.75, 29.46, 29.16, 27.93, 26.98, 22.55, 14.39. HRMS (ESI, m/z): $[M+H]^+$ calcd. for $C_{34}H_{50}N_2O_8$: 615.3645; found: 615.3651.

**(2R,3S,4R,5R)-2,3,4,5,6-pentahydroxy-N-(2-octadecyl-1,3-dioxo-2,3-dihydro-1H-benzo[de]isoquinolin-5-yl)hexanamide (GCNA7):**

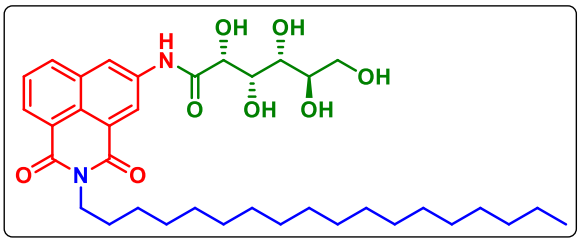

Amorphous yellow solid; yield: 94% (0.602 g); mp: 164-166 °C. IR (neat): 3452, 2922, 2849, 1703, 1672, 1503, 1336, and 1031 $cm^{-1}$. $^{1}H$ NMR (400 MHz, DMSO-$d_6$) δ 10.25 (s, 1H), 8.86 (s, 1H), 8.83 (s, 1H), 8.36 (t, $J$ = 7.4 Hz, 2H), 7.81 (t, $J$ = 7.6 Hz, 1H), 5.71 (s, 1H), 4.53 (s, 3H), 4.29 (d, $J$ = 2.8 Hz, 1H), 4.09 (s, 1H), 4.03 (t, $J$ = 6.8 Hz, 2H), 3.63-3.52 (m, 5H), 1.68 – 1.59 (m, 2H), 1.32 (s, 4H), 1.22 (s, 26H), 0.84 (d, $J$ = 6.6 Hz, 3H). $^{13}C$ NMR (100 MHz, DMSO-$d_6$) δ 172.98, 163.86, 163.65, 137.95, 134.15, 132.41, 129.51, 127.96, 125.25, 124.61, 122.98, 122.32, 122.15, 74.75, 72.60, 72.02, 70.99, 63.78, 31.75, 29.46, 29.36, 29.16, 27.93, 26.98, 22.55, 14.40. HRMS (ESI, m/z): $[M+H]^+$ calcd. for $C_{36}H_{54}N_2O_8$: 643.3958; found: 643.3953.

## 3.4. Conclusion

A simple synthesis of gluconamide-conjugated naphthalimide amphiphiles (GCNA) from commercially relevant compounds in excellent yields was achieved. GCNA self-assembled into supramolecular gel via intermolecular non-covalent interactions in DMSO-$H_2O$ to furnish nanofibrillar network. As evidenced from the experimental data, the *J*-type aggregation pattern displayed by GCNA4 substantially increased the electron density in naphthalimide moiety with the overall change in energy of $15.33x10^{-32}$ J. When compared to the amorphous GCNA4, the enriched electron density in the aggregated GCNA4 makes it as one of the effective electron-donating electrode in triboelectric nanogenerators (TENG). Furthermore, in the fabrication of

TENG, GCNA4 is fixed as the standard triboelectric layer, which offers electrons to the external circuit and changes the opposite triboelectric layers such as Al, ITO, PET, silicone, PDMS, which can accept the electrons. The optimized combination of GCNA4-PDMS system displayed 2.4 times better in performance than the corresponding amorphous GCNA4. Nevertheless, mere gelation cannot make the aggregated system electron-rich; rather, molecules' mode of aggregation and 3D orientation contribute effectively. The fabricated GCNA TENG is able to power up 240 red LEDs and small electric devices such as wristwatch, thermometer, and calculator with 4.7μF capacitor and hygrometer with 47μF capacitor. This work highlights the importance of molecular design in the bottom-up assembly process, and electron density of the aggregated system. It also underlines the promising applications of self-assembled supramolecular materials in triboelectric nanogenerators.

## 3.5. References


1. H. Wang, Z. Feng and B. Xu, *Angew. Chemie - Int. Ed.*, 2019, **58**, 5567–5571.
2. H. Kar and S. Ghosh, *Isr. J. Chem.*, 2019, 59, 881–891.
3. G. Brancato, F. Coutrot, D. A. Leigh, A. Murphy, J. K. Y. Wong and F. Zerbetto, *Proc. Natl. Acad. Sci. U. S. A.*, 2002, **99**, 4967–4971.
4. A. Priimagi, G. Cavallo, A. Forni, M. Gorynsztejn-Leben, M. Kaivola, P. Metrangolo, R. Milani, A. Shishido, T. Pilati, G. Resnati and G. Terraneo, *Adv. Funct. Mater.*, 2012, **22**, 2572–2579.
5. W. M. Heckl, in *Astrobiology*, 2002, pp. 361–372.
6. M. Barbieri, *Biosemiotics*, 2012, **5**, 411–437.
7. R. J. Brea, M. D. Hardy and N. K. Devaraj, *Chem. - A Eur. J.*, 2015, **21**, 12564–12570.
8. D. Segré, D. Ben-Eli, D. W. Deamer and D. Lancet, in *Origins of Life and Evolution of the Biosphere*, 2001, vol. 31, pp. 119–145.
9. B. Bhushan, *Philos. Trans. R. Soc. A Math. Phys. Eng. Sci.*, 2009, **367**, 1445-1486.
10. S. J. Rowan, S. J. Cantrill, G. R. L. Cousins, J. K. M. Sanders and J. F. Stoddart, *Angew. Chemie - Int. Ed.*, 2002, **41**, 898-952.
11. P. Cordier, F. Tournilhac, C. Soulié-Ziakovic and L. Leibler, *Nature*, 2008, **451**, 977-980.
12. C. S. Chin, D. H. Alexander, P. Marks, A. A. Klammer, J. Drake, C. Heiner, A. Clum, A. Copeland, J. Huddleston, E. E. Eichler, S. W. Turner and J. Korlach, *Nat. Methods*, 2013, **10**(6), 563-569.
13. J. -M Lehn, *Angew. Chemie Int. Ed. English*, 1990, **29**, 1304-1319
14. M. F. M. Sciacca, V. Romanucci, A. Zarrelli *et al.*, *ACS Chem. Neurosci.*, 2017, **8**, 1767–1778.

15. T. Imura, N. Ohta, K. Inoue, N. Yagi, H. Negishi, H. Yanagishita and D. Kitamoto, *Chem. - A Eur. J.*, 2006, **12**, 2434–2440.
16. T. J. Deming, *Adv. Mater.*, 1997, **9**, 299–311.
17. B. M. Rosen, M. Peterca, K. Morimitsu, A. E. Dulcey, P. Leowanawat, A. M. Resmerita, M. R. Imam and V. Percec, *J. Am. Chem. Soc.*, 2011, **133**, 5135–5151.
18. J. Luo and Z. L. Wang, *EcoMat*, 2020, **2**, e12059.
19. F. Arab Hassani, Q. Shi, F. Wen, T. He, A. Haroun, Y. Yang, Y. Feng and C. Lee, *Smart Mater. Med.*, 2020, **1**, 92–124.
20. Z. Li, Q. Zheng, Z. L. Wang and Z. Li, *Research*, 2020, **2020**, 8710686.
21. M. Zhu, Z. Yi, B. Yang and C. Lee, *Nano Today*, 2021, **36**, 101016.
22. L. Catacuzzeno, F. Orfei, A. Di Michele, L. Sforna, F. Franciolini and L. Gammaitoni, *Nano Energy*, 2019, **56**, 823–827.
23. J. Zhu, M. Zhu, Q. Shi, F. Wen, L. Liu, B. Dong, A. Haroun, Y. Yang, P. Vachon, X. Guo, T. He and C. Lee, *EcoMat*, 2020, **2**, e12058.
24. Z. L. Wang and A. C. Wang, *Mater. Today*, 2019, **30**, 34–51.
25. C. Wu, A. C. Wang, W. Ding, H. Guo and Z. L. Wang, *Adv. Energy Mater.*, 2019, **9**, 1802906.
26. F. R. Fan, W. Tang and Z. L. Wang, *Adv. Mater.*, 2016, **28**, 4283–4305.
27. Z. L. Wang, *ACS Nano*, 2013, **7**, 9533–9557.
28. Y. Wang, Y. Yang and Z. L. Wang, *npj Flex. Electron.*, 2017, **1**, 10.
29. D. W. Kim, J. H. Lee, J. K. Kim and U. Jeong, *NPG Asia Mater.*, 2020, **12(6)**. 1-17.
30. Q. Zheng, Y. Zou, Y. Zhang *et al*., *Sci. Adv.*, 2016, **2**, e1501478.
31. S. Chao, H. Ouyang, D. Jiang, Y. Fan and Z. Li, *EcoMat*, 2021, **3**, e12071.
32. C. Sohns, M. Khalaph, L. Bergau and P. Sommer, *Herzschrittmachertherapie und Elektrophysiologie*, 2020, **31**, 265–272.
33. M. Haghi, S. Danyali, S. Ayasseh, J. Wang, R. Aazami and T. M. Deserno, *Sensors*, 2021, **21**, 1–24.
34. M. Smuck, C. A. Odonkor, J. K. Wilt, N. Schmidt and M. A. Swiernik, *npj Digit. Med.*, 2021, **4**, 45.
35. H. Ryu, H. J. Yoon and S. W. Kim, *Adv. Mater.*, 2019, **31**, 1802898.
36. B. Shi, Z. Li and Y. Fan, *Adv. Mater.*, 2018, **30**, 1801511.
37. J. H. Lee, J. Kim, T. Y. Kim, M. S. Al Hossain, S. W. Kim and J. H. Kim, *J. Mater. Chem. A*, 2016, **4**, 7983–7999.
38. T. Huang, C. Wang, H. Yu, H. Wang, Q. Zhang and M. Zhu, *Nano Energy*, 2014, **14**, 226–235.
39. J. Wang, Z. Zhao, X. Zeng, X. Liu and Y. Hu, *Sensors*, 2021, **21**, 3634.

40. X. Ren, X. Xiang, H. Yin, Y. Tang and H. Yuan, *Nanotechnology*, 2021, **32**, 315404.
41. S. Zhao, J. Wang, X. Du, J. Wang, R. Cao, Y. Yin, X. Zhang, Z. Yuan, Y. Xing, D. Y. H. Pui and C. Li, *ACS Appl. Energy Mater.*, 2018, **1**, 2326–2332.
42. Y. Jiang, K. Dong, X. Li, J. An, D. Wu, X. Peng, J. Yi, C. Ning, R. Cheng, P. Yu and Z. L. Wang, *Adv. Funct. Mater.*, 2021, **31**, 2005584.
43. Z. Qin, Y. Yin, W. Zhang, C. Li and K. Pan, *ACS Appl. Mater. Interfaces*, 2019, **11**, 12452–12459.
44. H. J. Yang, J. W. Lee, S. H. Seo, B. Jeong, B. Lee, W. J. Do, J. H. Kim, J. Y. Cho, A. Jo, H. J. Jeong, S. Y. Jeong, G. H. Kim, G. W. Lee, Y. E. Shin, H. Ko, J. T. Han and J. H. Park, *Nano Energy*, 2021, **86**, 106083.
45. D. Godwinraj and S. C. George, *Adv. Ind. Eng. Polym. Res.*, 2021, **4**, 1–8.
46. G. Hua and K. Odelius, *ACS Sustain. Chem. Eng.*, 2016, **4**, 4831–4841.
47. A. K. Rachamalla, V. P. Rebaka, T. Banoo, R. Pawar, M. Faizan, K. Lalitha and S. Nagarajan, *Green Chem.*, 2022, **24**, 2451–2463.
48. D. Kolosov, V. Adamovich, P. Djurovich, M. E. Thompson and C. Adachi, *J. Am. Chem. Soc.*, 2002, **124**, 9945–9954.
49. W. Zeng, H. Y. Lai, W. K. Lee, M. Jiao, Y. J. Shiu, C. Zhong, S. Gong, T. Zhou, G. Xie, M. Sarma, K. T. Wong, C. C. Wu and C. Yang, *Adv. Mater.*, 2018, **30**, 1704961..
50. W. W. Stewart, *Cell*, 1978, **14**, 741–759.
51. M. Mariello, F. Guido, V. M. Mastronardi, M. T. Todaro, D. Desmaële and M. De Vittorio, *Nano Energy*, 2019, **57**, 141–156.
52. J. D. Phillips, *Front. Nanotechnol.*, 2021, **3**, 633931.
53. N. Sezer and M. Koç, *Nano Energy*, 2021, **80**.
54. C. Wei and X. Jing, *Renew. Sustain. Energy Rev.*, 2017, **74**, 1–18.
55. A. Toprak and O. Tigli, *Appl. Phys. Rev.*, 2014, **1**, 031104.
56. M. Gholikhani, H. Roshani, S. Dessouky and A. T. Papagiannakis, *Appl. Energy*, 2020, **261**, 114388.
57. J. Pei, F. Guo, J. Zhang, B. Zhou, Y. Bi and R. Li, *J. Clean. Prod.*, 2021, **288**, 125338.
58. A. R. Hirst, B. Escuder, J. F. Miravet and D. K. Smith, *Angew. Chemie - Int. Ed.*, 2008, **47**, 8002–8018.
59. K. L. Ayyapillai Thamizhanban, and S. Nagarajan, in *Emerging Nanostructured Materials for Energy and Environmental Science, Environmental Chemistry for a Sustainable World 23*, ed. R. S. et al. (eds.), Springer Nature Switzerland AG 2019, 2019, pp. 443–470.
60. J. M. Roseman, J. Lin, S. Ramakrishnan, J. K. Rosenstein and K. L. Shepard, *Nat. Commun.*, 2015, **6**, 10070.

61. Y. Zhao, F. Sakai, L. Su, Y. Liu, K. Wei, G. Chen and M. Jiang, *Adv. Mater.*, 2013, **25**, 5215–5256.
62. S. V. Stovbun and A. A. Skoblin, *Moscow Univ. Phys. Bull.*, 2012, **67**, 317–330.
63. K. Steck, S. Dieterich, C. Stubenrauch and F. Giesselmann, *J. Mater. Chem. C*, 2020, **8**, 5335–5348.
64. S. Datta and S. Bhattacharya, *Chem. Soc. Rev.*, 2015, **44**, 5596–5637.
65. A. Thamizhanban, S. Balaji, K. Lalitha, Y. S. Prasad, R. V. Prasad, R. A. Kumar, C. U. Maheswari, V. Sridharan and S. Nagarajan, *J. Agric. Food Chem*., 2020, **68**, 14896–14906.
66. Y. S. Prasad, S. Miryala, K. Lalitha, B. Saritha, C. U. Maheswari, V. Sridharan, C. S. Srinandan and S. Nagarajan, *Sci. Rep*., 2020, **10**, 18017.
67. K. Lalitha, K. Gayathri, Y. S. Prasad, R. Saritha, A. Thamizhanban, C. U. Maheswari, V. Sridharan and S. Nagarajan, *Gels,* 2018, **4**, 1.
68. K. Muthusamy, V. Sridharan, C. U. Maheswari and S. Nagarajan, *Green Chem*., 2016, **18**, 3722–3731.
69. P. R. A. Chivers and D. K. Smith, *Nat. Rev. Mater.*, 2019, **4**, 463–478.
70. Nonappa and E. Kolehmainen, *Soft Matter*, 2016, **12**, 6015–6026.
71. V. Crupi, D. Majolino, A. Mele, L. Melone, C. Punta, B. Rossi, F. Toraldo, F. Trotta and V. Venuti, *Soft Matter*, 2014, **10**, 2320–2326.
72. R. N. A. H. Lewis and R. N. McElhaney, *Chem. Phys. Lipids*, 1998, **96**, 9–21.
73. J. Heo, D. P. Murale, H. Y. Yoon, V. Arun, S. Choi, E. Kim, J. Lee and S. Kim, *Aggregate*, 2022, **3**, e159.
74. V. Grande, B. Soberats, S. Herbst, V. Stepanenko and F. Würthner, *Chem. Sci.*, 2018, **9**, 6904–6911.
75. M. Shirakawa, N. Fujita and S. Shinkai, *J. Am. Chem. Soc.*, 2005, **127**, 4164–4165.
76. H. Maeda, Y. Haketa and T. Nakanishi, *J. Am. Chem. Soc.*, 2007, **129**, 13661–13674.
77. D. Giuri, L. J. Marshall, C. Wilson, A. Seddon and D. J. Adams, *Soft Matter*, 2021, **17**, 7221–7226.
78. A. Dawn and H. Kumari, *Chem. - A Eur. J.*, 2018, **24**, 762–776.
79. S. Bianco, S. Panja and D. J. Adams, Gels, 2022, **8**, DOI 10.3390/gels8020132.
80. R. A. Shaukat, Q. M. Saqib, M. U. Khan, M. Y. Chougale and J. Bae, *Energy Reports*, 2021, **7**, 724–731.
81. P. Supraja, R. R. Kumar, S. Mishra, D. Haranath, P. R. Sankar, K. Prakash, N. Jayarambabu, T. V. Rao and K. U. Kumar, *Sensors Actuators A Phys.*, 2022, **335**, 113368.
82. H. Wu, S. Wang, Z. Wang and Y. Zi, *Nat. Commun.*, 2021, **12**, 1–8.

83. R. D. I. G. Dharmasena, J. H. B. Deane and S. R. P. Silva, *Adv. Energy Mater.*, 2018, **8**, 1802190.

84. S. Niu, S. Wang, L. Lin, Y. Liu, Y. S. Zhou, Y. Hu and Z. L. Wang, *Energy Environ. Sci.*, 2013, **6**, 3576–3583.

## 3.6. Selected NMR ($^{1}$H & $^{13}$C), and Mass spectra

**$^{1}$H NMR Spectrum of compound GCNA3 (400 MHz, DMSO-*d*$_6$)**

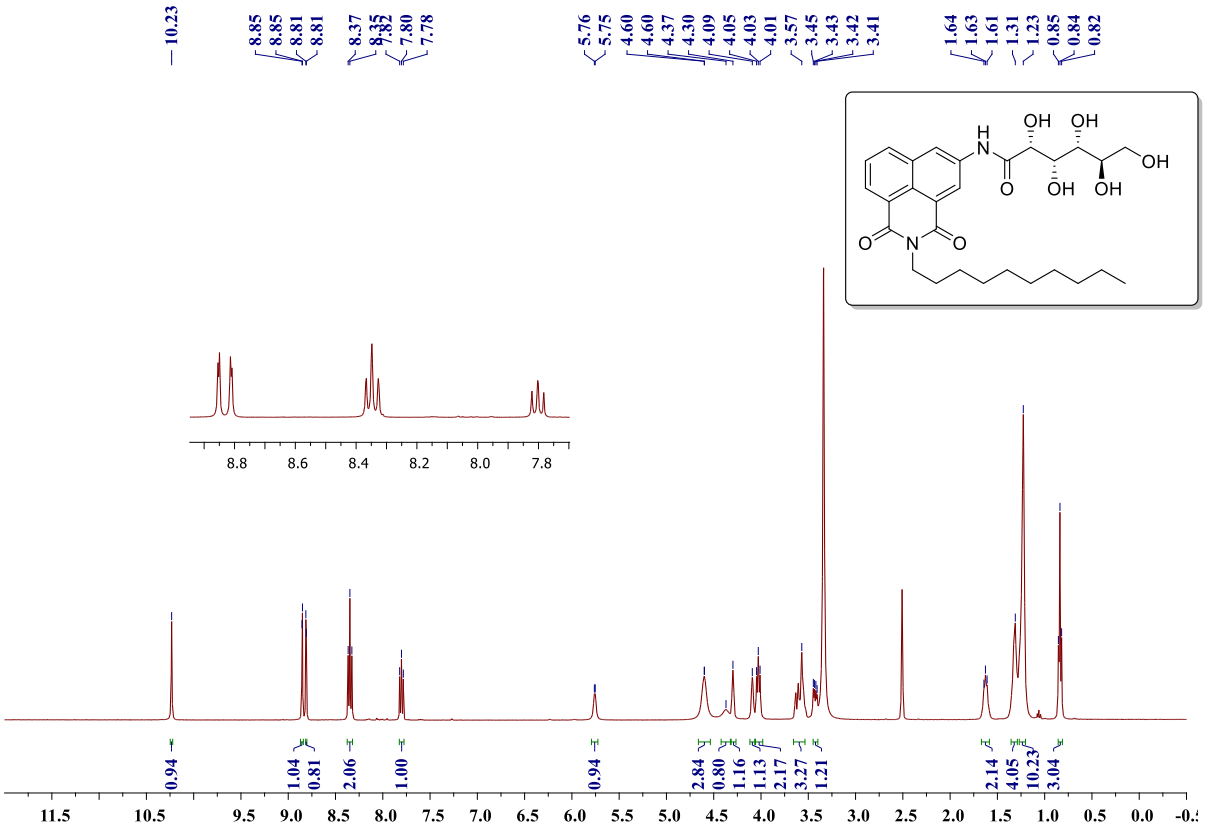

**Deuterium exchange $^{1}$H NMR Spectrum of compound GCNA3 (400 MHz, DMSO-$d_6$)**

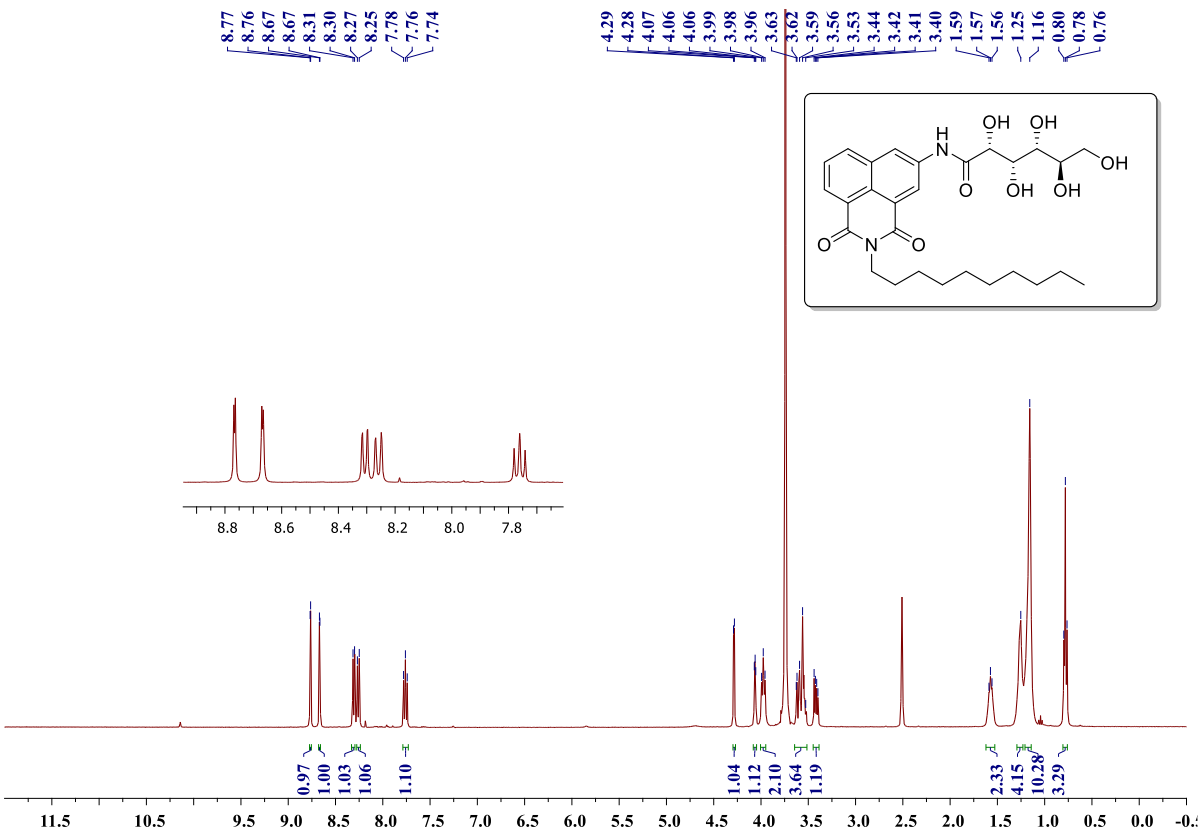


**$^{13}$CNMR Spectrum of compound GCNA3 (100 MHz, DMSO-$d_6$)**

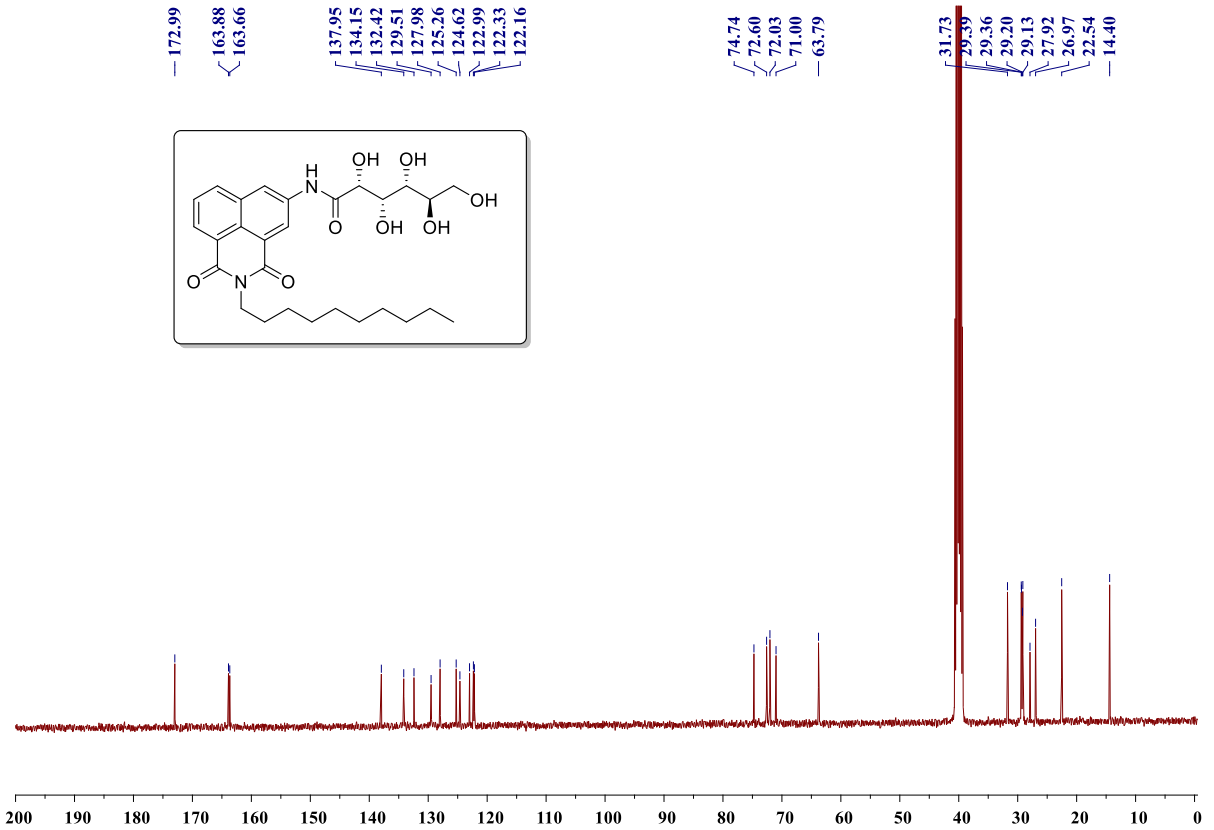

## HRMS Spectrum of GCNA3

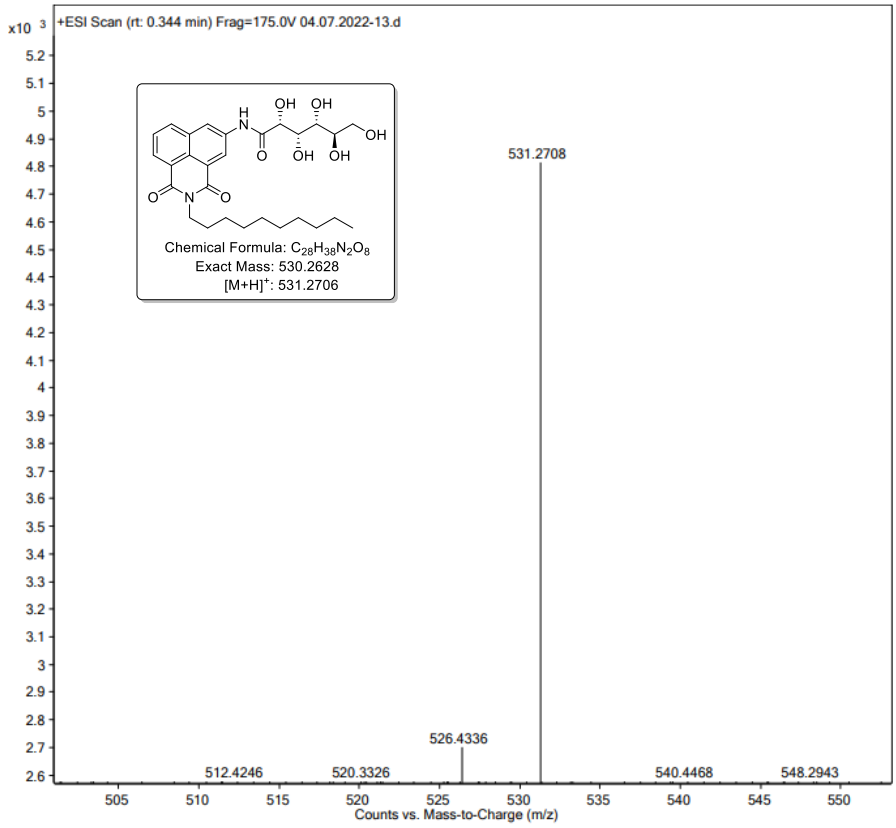


## $^1$H NMR Spectrum of compound GCNA4 (400 MHz, DMSO-$d_6$)

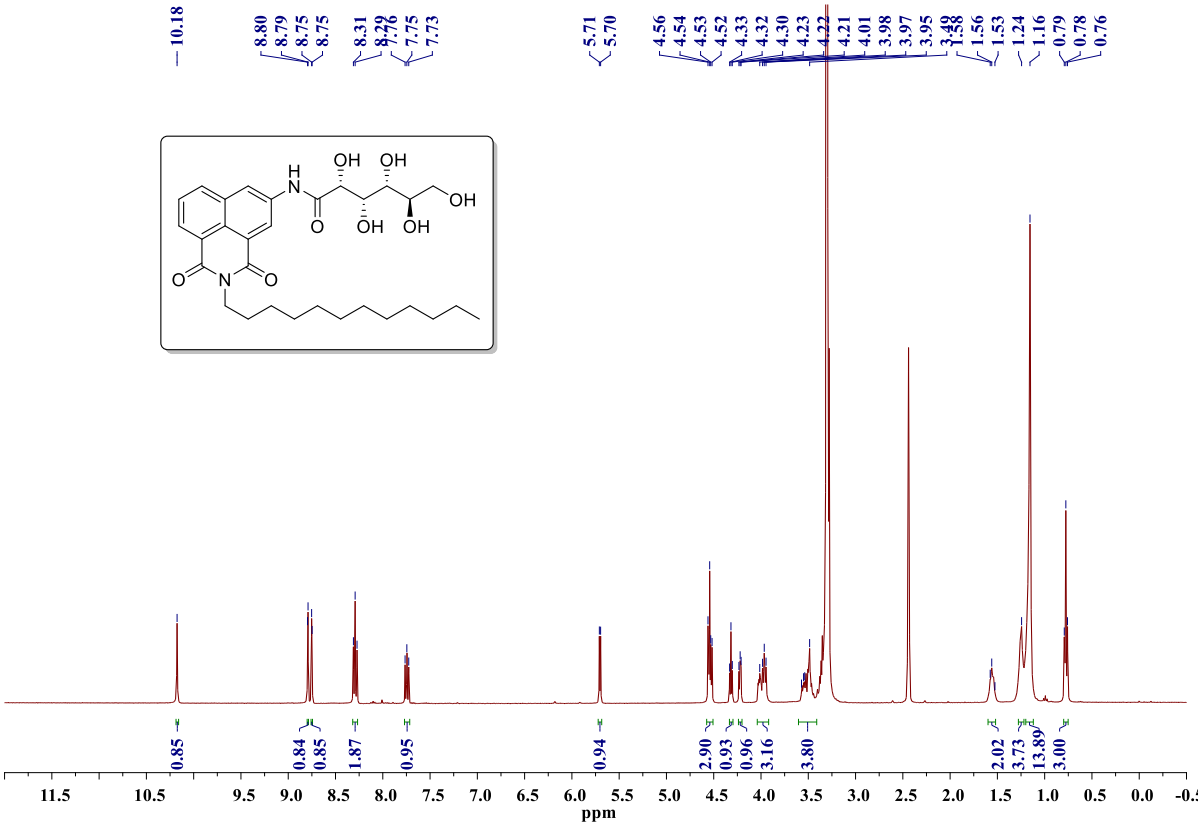

## $^{13}$CNMR Spectrum of compound GCNA4 (100 MHz, DMSO-$d_6$)

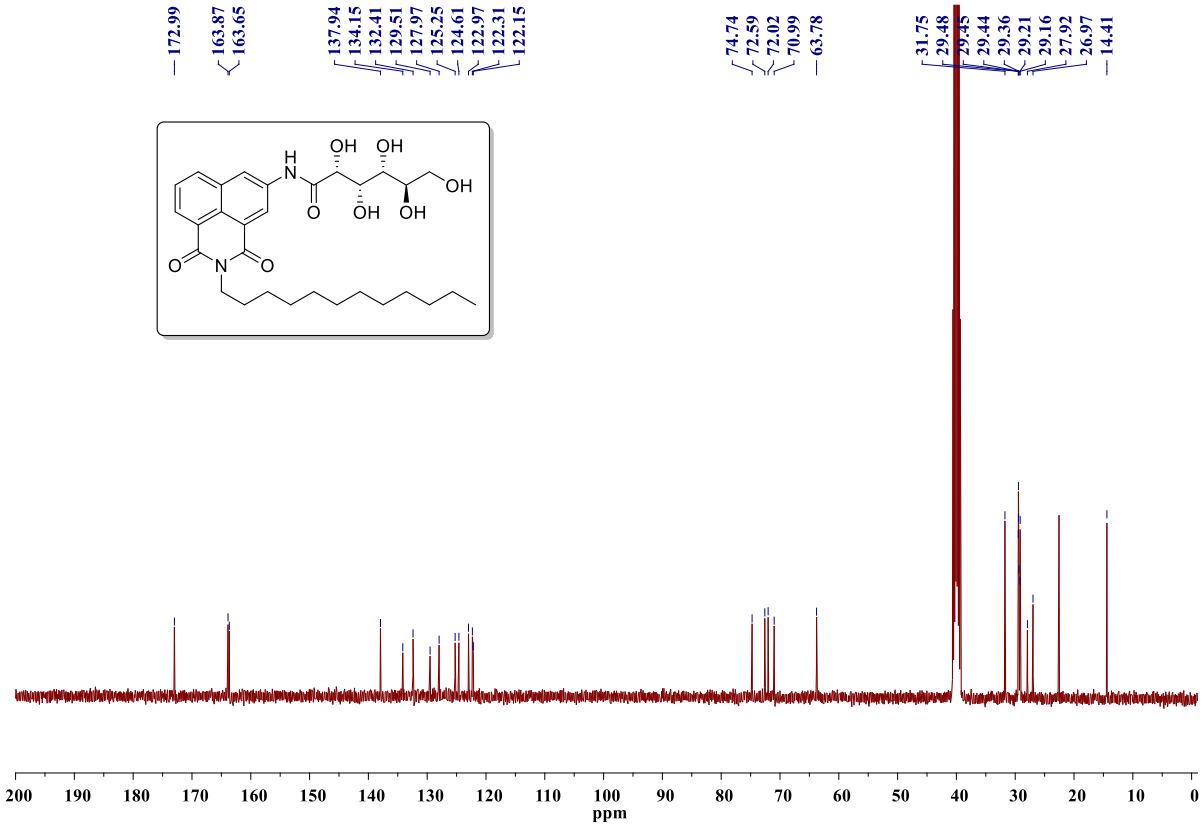


## HRMS Spectrum of GCNA4

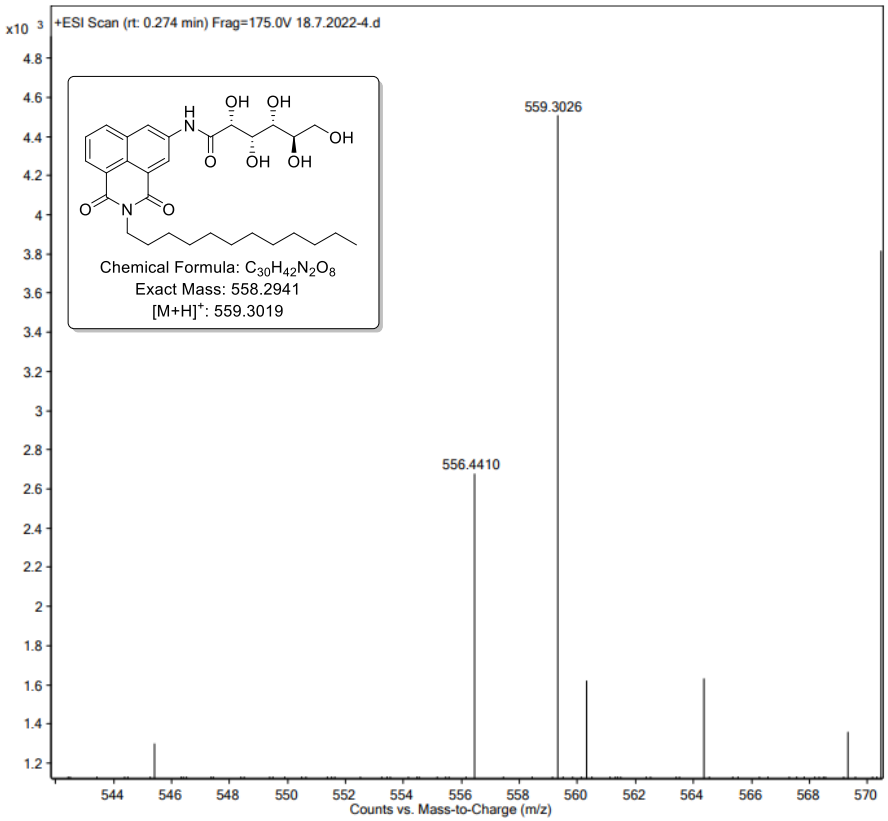

## $^{1}$H NMR Spectrum of compound GCNA7 (400 MHz, DMSO-$d_6$)

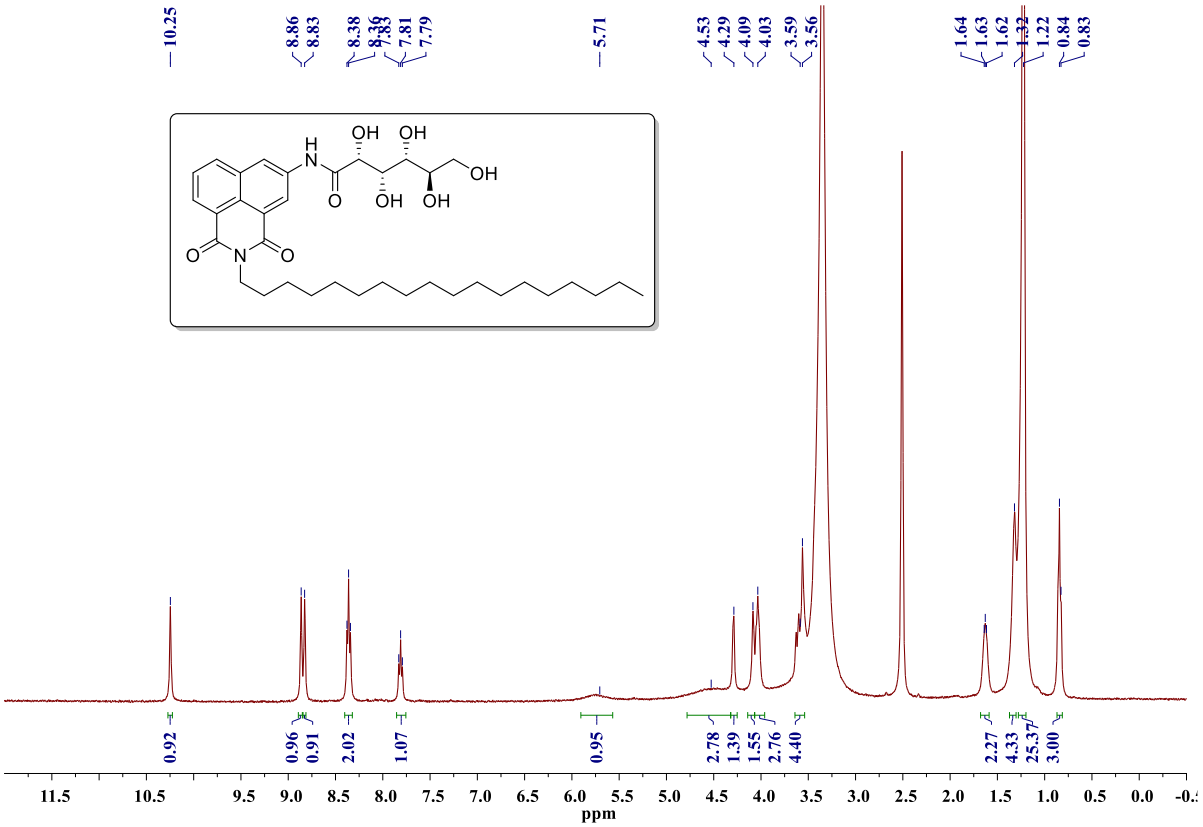


## $^{13}$CNMR Spectrum of compound GCNA7 (100 MHz, DMSO-$d_6$)

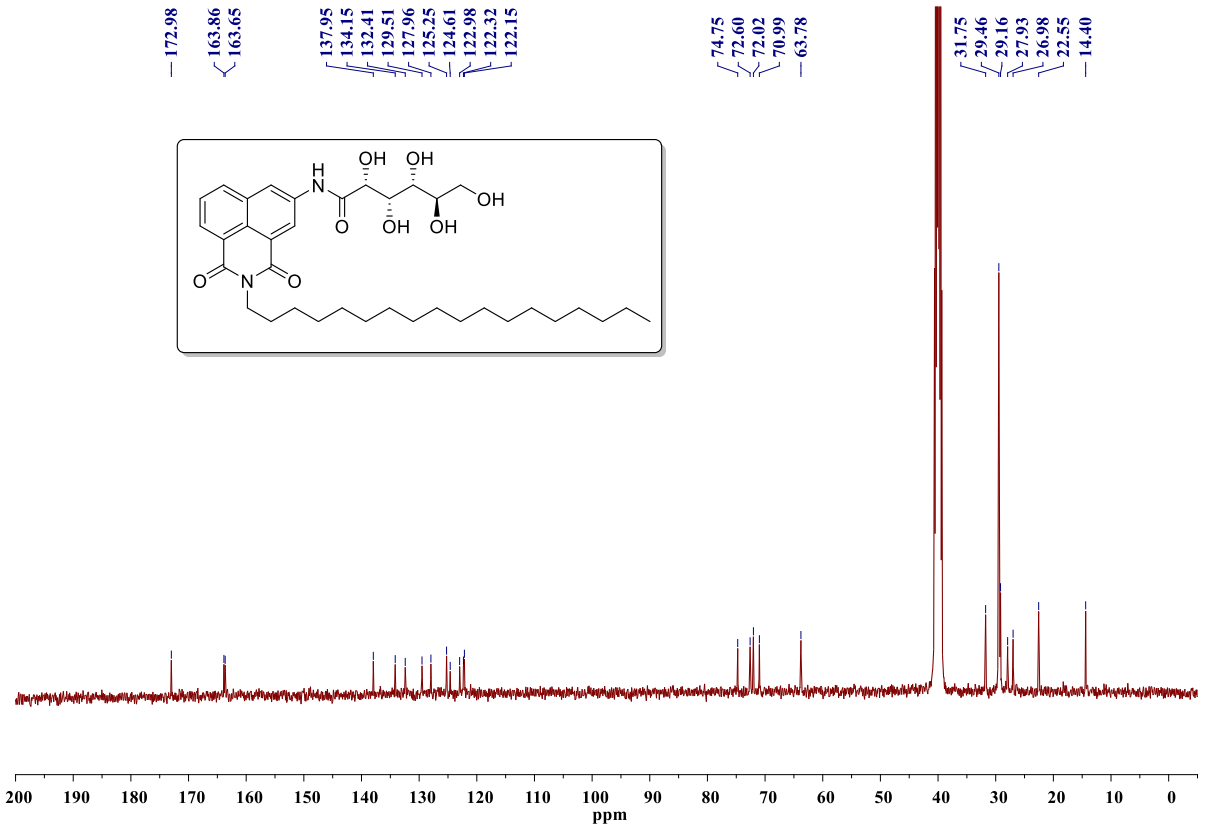

## HRMS Spectrum of compound GCNA7

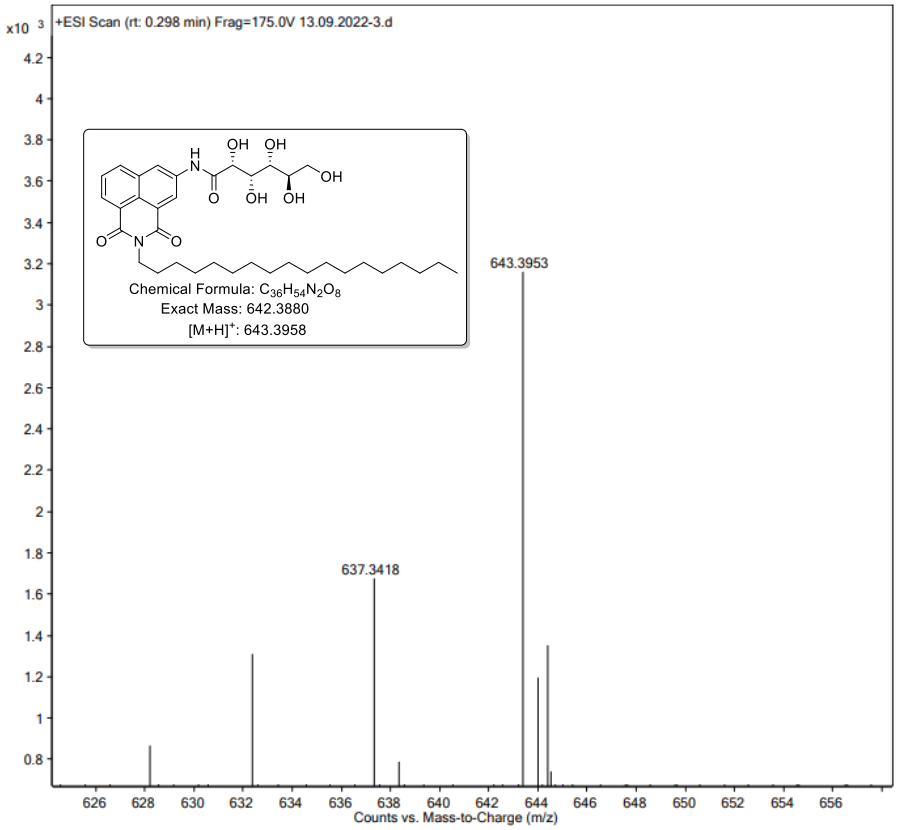

# CHAPTER-IV

## Assembled *N*-glycosyl naphthalimide ricinoleate for the fabrication of humidity sensor

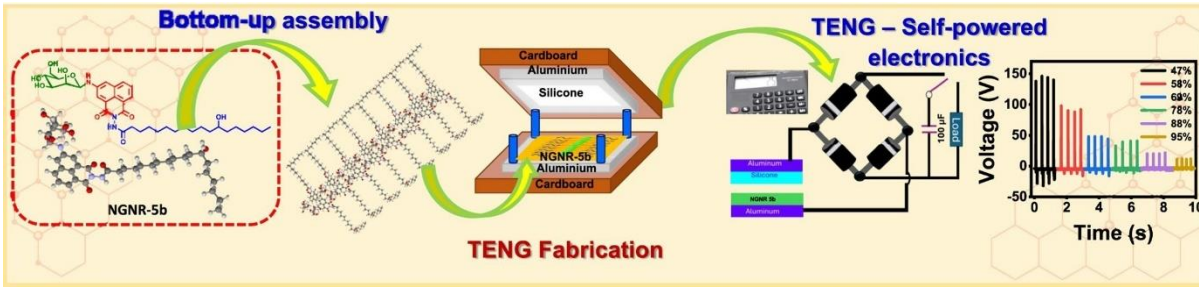

# 4.1. Introduction

The Internet of Things (IoTs) era is uprising with the overall development of artificial intelligence technology,[1] fifth-generation network, electronics,[3-5] and sensor networks,[6,7] which require abundant energy and greater precession. To fulfill the requirements of IoTs, universally sustainable, reliable, and abundant power supplies are necessitated, wherein Triboelectric nanogenerators (TENG) display several merits, including low-cost manufacturing, a broad selection of materials, high energy conversion efficiency at low motion frequencies, strong scalability, lack of pollution, and with lightweight fabrication.[8-11] It has the ability to generate electricity by harvesting random mechanical energy from the surroundings based on contact electrification and electrostatic induction phenomena.[12,13] Basically, contact electrification, or triboelectrification, is a physical phenomenon that explains the transfer of electrons between two materials when they come into physical contact, which is based on the electron affinities of the materials used. In particular, materials with higher electron affinity act as electron acceptors, whereas other materials act as electron donors. However, in the fabrication of TENG, materials selection plays a vital role in expanding the scope of green energy harvesting technologies and gaining maximum output performance with mechanical stability upon repetitive contact.[14-16] In 2012, Wang and co-workers developed the first TENG,[17] later various groups utilized synthetic, natural polymers, inorganic materials including MOFs, metal oxides, and metals. It is worth mentioning that great progress has been made in selecting materials for the fabrication of TENG; however, the potential use of assembled organic materials has yet to be explored least.[18,19] In assembled organic systems, molecular design and the resultant electron density generated by the bottom-up assembly process play a significant role.

In general, nature utilizes carbohydrates, proteins, and fats, which are widely abundant, for the generation of required energy.[20-22] Supramolecular assembly of these classes of molecules generates nano energy in nerves and muscles, which are crucial for movement, memory, and many other physiological processes.[23,24,25-28,29-32] For the fabrication of next-generation molecular materials, carbohydrates play an indispensable role as building blocks because of their biocompatibility, natural abundance, and biodegradability.[33,34] By considering the salient features of carbohydrates, in this chapter, monosaccharides were used to synthesize N-glycosyl naphthalimide ricinoleate amphiphiles (NGNRs). The significance of naphthalimides in materials fabrication is discussed in chapter 2 and 3.[35-40] However, utilizing these assembled organic materials in the fabrication of TENG opens new avenues for energy harvesting technology. Chapter 3 demonstrates the use of self-assembled gluconolactone conjugated naphthalimide amphiphiles (GCNA) as an electron donor layer in combination with the PDMS as an electron acceptor in TENG, which generated an output voltage, current, and power density

of ~ 250 V, 40 μA, and ~ 622 mW/m$^2$ respectively.[18] In this chapter, a modification is made by changing the hydrophobic unit to ricinoleic acid, generally referred to as 12-hydroxy-9-cis-octadecenoic acid obtained from castor oil. Monosaccharides and Ricinoleic acid are Generally Recognized as Safe (GRAS) by the Food and Drug Administration (FDA). In particular, the World Health Organization (WHO) and the expert committee of the Joint Food and Agriculture Organization (FAO) have approved a daily intake of castor oil, a precursor of ricinoleic acid, up to 0.7 mg/kg body weight.[41] Consequently, NGNR used for the fabrication of TENG is derived from environmentally friendly resources using a simple synthetic strategy. A TENG was constructed by a bottom-up assembly process using the molecular gelation concept through a more sustainable pathway that would open a gateway to green energy harvesting. The influence of molecular structure in the fabrication of assembled organic energy materials has not been reported to date, and our research group is exclusively working on the fabrication of assembled organic nano energy harvesting devices.

In this chapter, a series of NGNRs were generated using a sustainable protocol in good yields, whereas the literature reported methods to involve multi-step synthesis, use of highly complex protection and deprotection strategies, limited substrate scope, involving column chromatography purification, and ended up with poor yields. Molecular self-assembly studies of synthesized NGNRs generated a 3D-fibrillar network, wherein the solvent is trapped and formed a gel. Most importantly, from the application point of view, the bottom-up assembly mechanism of NGNR is proposed based on the FT-IR, SAXRD, UV-vis, and fluorescence techniques. The naphthalimide core is generally reported as an electron acceptor.[39] In contrast, in this chapter, molecular assembly significantly enhanced the electron density in the naphthalimide and turned into an electron donor, as evidenced by our studies. This work offers new insight into the fabrication of organic TENG based on the bottom-up assembly process and shows promising potential for self-powered electronics and a humidity sensor application.

## 4.2. Results and Discussion

Optimization of reaction conditions: Naphthalimides are one of the most versatile cores displaying unique optoelectronic properties.[39] Modifying naphthalimides by integrating varieties of structural units and functional groups was significant among the researchers.[42,43] In Chapter 2, the reaction condition suitable for synthesizing *N*-glycosyl naphthalimides using batch processes and conventional methods is reported. However, the research of alternative, simple, and environmentally friendly approaches for synthesizing chemicals of industrial significance is essential. In this chapter, continuous flow reactions have been performed to obtain 3-amino-*N*-(ricinoleic acid hydrazide)-1,8-naphthalimides (**3**) from 3-nitro-1,8-naphthalic anhydride (**1**) with methyl ricinoleate hydrazides (**2**), which includes condensation

followed by in situ reduction using Fe in MeOH-AcOH. In organic synthesis, control of temperature and pressure is a critical factor in achieving the requisite activation energy, leading to the effective desired product formation. A flow chemistry method that integrates the condensation and reduction processes is adopted to overcome the limitations of a conventional batch process. By harnessing the high temperature and high-pressure flow reactions in the heterogeneous phase using Fe catalyst, the desired compound **3** in good yields is generated. Initially, the reaction was carried out at 80 $^{o}$C, 2 bar pressure with a flow rate of 100 µL/min, and a 60% conversion was observed. With this interesting result on hand, a continuous generation of compound **3** in high yield using a high temperature and high-pressure flow reactor is optimized. The stainless-steel coil reactor is the obvious material of choice for high-temperature and high-pressure applications.

By fixing the flow rate of substrates at 100 µL/min, 2 bar pressure, temperature is tuned, and investigated the % of conversion into a product (**Figure 4.2a**). The subsequent increase in the temperature of the flow reactor from 80 $^{o}$C to 300 $^{o}$C with an increment of 20 $^{o}$C generated a steady rate of increase in the reaction with a maximum conversion rate of 94%. By increasing the retention time of the reactants in the steel coil flow reactor by reducing the flow rate up to 100 µL/min at 200 $^{o}$C, 2 bar pressure generated a continuous production of compound **3** with traces of polar impurities, which were purified using recrystallization in EtOH (**Figure 4.1**). In the condensation reaction using a flow reactor, the unsaturation present in the ricinoleate moiety did not interfere, and further reduction of the nitro group was facilitated smoothly. **Figure 4.1a** represents the product's response with respect to temperature at a flow rate of 100 µL/min.

Reaction of 3-Amino-*N*-(ricinoleic acid hydrazide)-1,8-naphthalimides **3** with various monosaccharides **4** using $(NH_4)_2SO_4$ as a catalyst in methanol was performed in a batch reactor at a higher temperature. Reactions performed at 80 $^{o}$C furnished the desired product after the prolonged reaction time of 24h in moderate yields (**Figure 4.1a**). Further, an increase in temperature up to 120 $^{o}$C rendered the desired product with an excellent yield within 4h. It is worth stating that a further increase in temperature results in a decrease in the yield of the desired NGNRs, which is attributed to the Amadori rearrangement. This type of non-enzymatic Amadori rearrangement occurs at high temperatures due to sugar caramelization, which is an undesired and uncontrolled event. Overall, the key features of our optimized condition involve no protection and deprotection of sugars, formation of exclusively $\beta$-anomeric product, no formation of undesired products in the entire reaction sequence, and the only side products obtained are one molecule of oxygen and two molecules of water with an excellent yield of the desired product without any complicated workup and column chromatographic purification (**Figure 4.1**).

All the synthesized NGNRs were well characterized using NMR, FT-IR, and mass spectral techniques. Generally, the anomeric proton of a sugar moiety displays a coupling constant of $J \leq 4$ Hz for $\alpha$-anomer and $J > 4$ Hz for $\beta$-anomer. The calculated coupling constant $J = 5.2$ Hz for the anomeric proton of **NGNR5a** resonating at 4.21 ppm as a doublet in the deuterium exchange $^{1}$H-NMR spectrum confirms the formation of $\beta$-anomeric product.

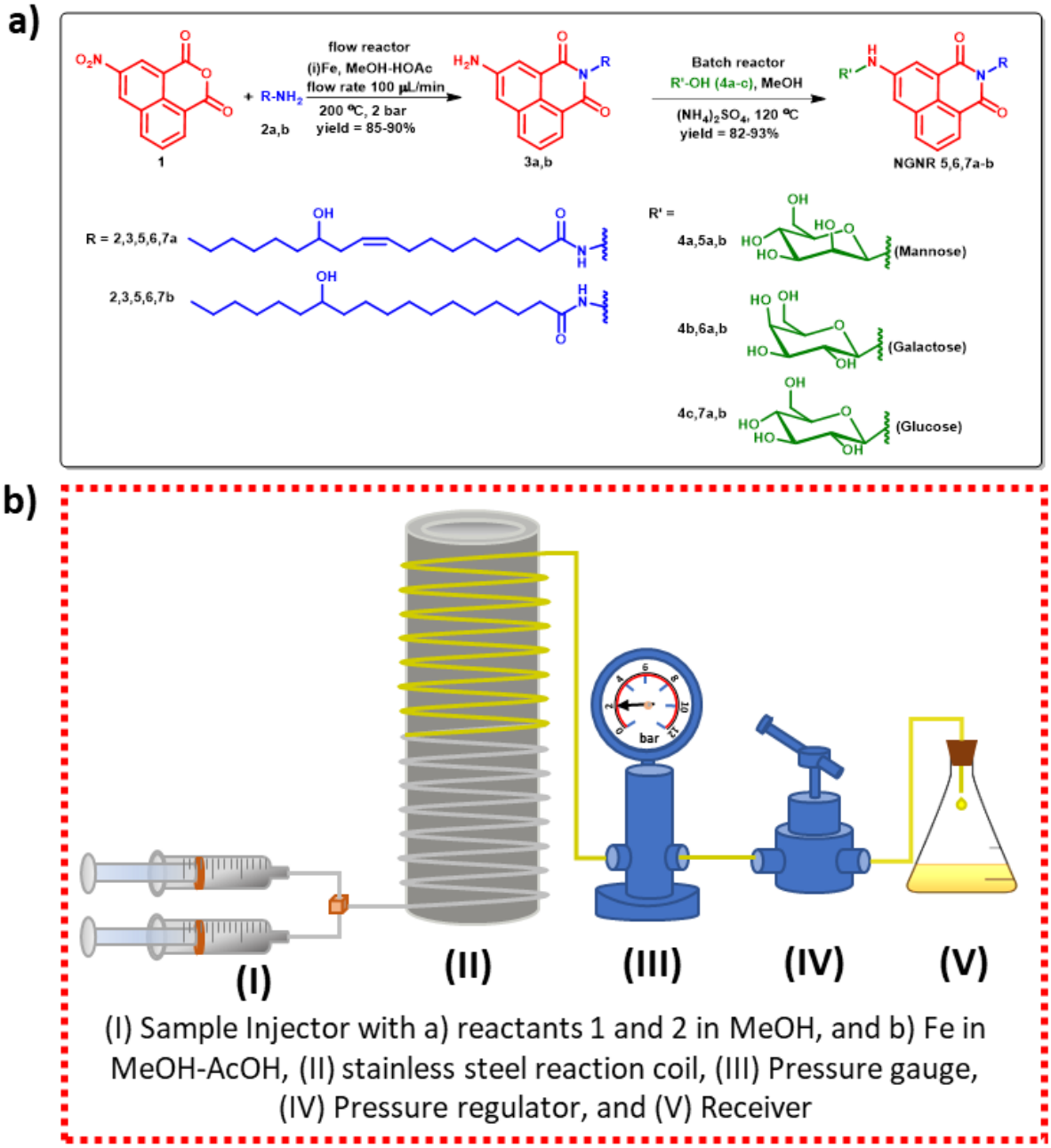


**Figure 4.1**. (a) Synthesis of *N*-glycosyl-3-amino-*N*-(ricinoleic acid hydrazide)-1,8-naphthalimides (NGNRs). (b) Pictorial representation of optimized flow reactor.

The gelation abilities of synthesized NGNR compounds were studied in a wide variety of solvents and oils (**Table 4.1**). Gelation studies revealed that the synthesized NGNRs could form organogel in xylenes and hybrid hydrogel in DMSO-$H_2O$ in the ratio of 4:6 (v/v). Organogel formed in xylenes displayed good strength, whereas the hybrid hydrogels were soft with the

CGC 6%; even a little shaking could break the gel. We were very curious to investigate the gelation capability of NGNRs in *o*-xylene, *m*-xylene, and *p*-xylene. At this juncture, the organogel formed by NGNRs in *m*-xylene is stronger than the gel formed in *o*-xylene and *p*-xylene, which is ascribed by gel-to-sol transition temperature.

**Table 4.1**. Gelation studies of **NGNR5**, **6**,**7a-b** in various solvents and vegetable oils

| S.No | Solvents/Oils | NGNR5a | NGNR6a | NGNR7a | NGNR5b | NGNR6b | NGNR7b |
|---|---|---|---|---|---|---|---|
| 1 | Linseed oil | S | S | S | S | S | S |
| 2 | Olive oil | PG | PG | PG | PG | PG | PG |
| 3 | Paraffin light | PG | PG | PG | PG | PG | PG |
| 4 | Polyethylene glycol (PEG) | S | S | S | S | S | S |
| 5 | Chloroform | S | S | S | S | S | S |
| 6 | DMSO | S | S | S | S | S | S |
| 7 | DMSO+$H_2O$ | PG | PG | PG | PG | PG | PG |
| 8 | Cyclohexane | I | I | I | I | I | I |
| 9 | Toluene | S | S | S | S | S | S |
| 10 | N-methyl-2-pyrrolidone | S | S | S | S | S | S |
| 11 | 1,4-dioxane | S | S | S | S | S | S |
| 12 | Ethanol | P | P | P | P | P | P |
| 13 | Methanol | P | P | P | P | P | P |
| 14 | Butanol | P | P | P | P | P | P |
| 15 | Isopropyl alcohol | S | S | S | S | S | S |
| **16** | **Xylene** | **G (1.5)** | **G (1.5)** | **G (1.5)** | **G (1)** | **G (1)** | **G (1)** |
| **17** | ***o*-xylene** | **G (1.5)** | **G (1.5)** | **G (1.5)** | **G (1)** | **G (1)** | **G (1)** |
| **18** | ***m*-xylene** | **G (1.5)** | **G (1.5)** | **G (1.5)** | **G (1)** | **G (1)** | **G (1)** |
| **19** | ***p-xylene*** | **G (1.5)** | **G (1.5)** | **G (1.5)** | **G (1)** | **G (1)** | **G (1)** |
| 20 | Water | I | I | I | I | I | I |
| 21 | Diesel | S | S | S | S | S | S |
| 22 | 1,2-dichloro benzene | P | P | P | P | P | P |
| 23 | 1,2-dichloroethane | S | S | S | S | S | S |
| 24 | Acetonitrile | S | S | S | S | S | S |

CGC, critical gelation concentration is given in parentheses % wt/v. S, soluble; G, Gel; PG, partial gel; P, precipitation; I, insoluble

All six **NGNR 5,6,7(a&b)** furnished an opaque yellow gel in *m*-xylene on cooling to room temperature and were stable at room temperature for more than three months. The critical gelation concentration (CGC) of **NGNR5a**, **6a**, and **7a** in *m*-xylene is 1.5%, and **5b**, **6b**, and **7b** is 1% (wt/v), respectively. The representative images of the gel formed by **NGNR5b**, **6b**, and **7b** are given in **Figure 4.3a**. Interestingly, **NGNR5b-7b** without unsaturation in the hydrophobic unit displayed better gelation ability of 1% wt/v, whereas the compounds **NGNR5a-7a** having unsaturation in the hydrophobic unit formed relatively a higher CGC of 1.5% wt/v.

The thermo-reversible nature of the organogel through repeated heating and cooling cycles was evaluated. Remarkably, even after 25 cycles, these gels remained stable because of the reversible intermolecular interactions. To ascertain the strength of the gel, meticulously identified the gel-to-sol transition temperature, $T_g$, for organogel formed by **NGNR5,6,7(a &b)**. The designed amphiphiles possess ricinoleate unit as a hydrophobic tail, naphthalimide as a π-π-stacking component, and monosaccharides as hydrophilic head groups, respectively. It is observed that the organogel formed from **NGNR5b**, having mannose as a hydrophilic unit, displayed a higher $T_g$ = 102 $^oC$ when compared to its epimer **NGNR7b**, derived from glucose (87 $^oC$). In addition, **NGNR6b**, derived from galactose, exhibited $T_g$ = 91 $^oC$, which is also an epimer of compound **NGNR7b**. These interesting results strongly indicate that the process of epimerization has the potential to significantly modify the gel strength through intermolecular interactions, which directly reflects on supramolecular architecture. An investigation of gelation ability and $T_g$ revealed that **NGNR5b**, **6b**, and **7b**, possessing a similar Hydrophilic Lipophilic Balance (HLB) level, create a gel with the same CGC. However, the strength of the gel differs due to the orientation of the -OH groups within the 3D lattice, affecting the intermolecular H-bonding. Measurements of the concentration-dependent $T_g$ exhibited a gradual rise and reached a plateau once the NGNRs solution reached saturation (**Figure 4.2b,c**). Among the various NGNRs synthesized, **NGNR5b** with higher $T_g$ = 102 $^oC$ and CGC of 1% (wt/v) has been considered as a model substrate for further investigation and represented as **NGNR5b**.

To understand the self-assembly mechanism, molecular-level insights are necessary. Various intermolecular interactions such as hydrogen bonding, π-π stacking, anionic-π and cationic-π and van der Waals displayed by a molecule play a crucial role in the assembly mechanism. Hydrogen bonding is ubiquitous in nature and plays a vital role in the structure and function of various supramolecular architecture including the assemblies of DNA and RNA helices. Fourier transform infrared spectroscopy is the best tool for studying intermolecular interactions with respect to functional groups.

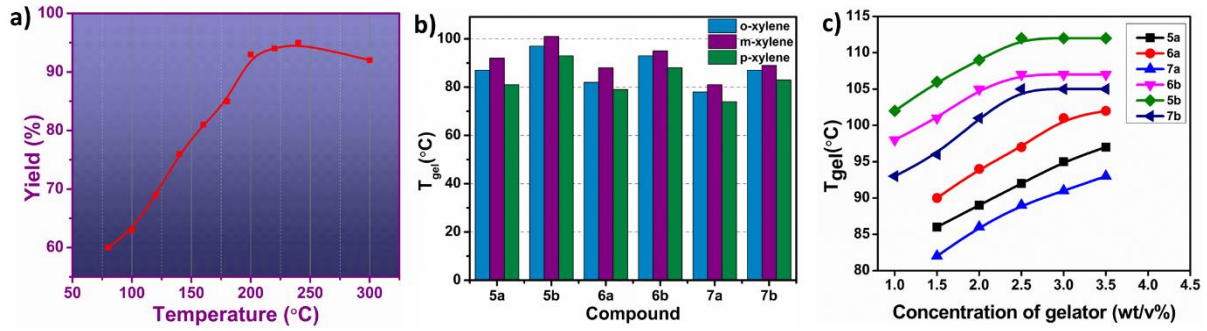


**Figure 4.2.** (a) The response of the product with respect to the temperature at flow rate of 100 µL/min. (b) Gel to sol transition temperature ($T_g$) measurements of **NGNR5a-7a** and **NGNR5b-7b** in different xylenes. (c) Concentration-dependent gel to sol transition temperature ($T_g$) measurements of **NGNR5a-7a** and **NGNR5b-7b** in *m*-xylene.

Attenuated Total Reflectance Fourier Transform Infrared Spectroscopy (ATR-FTIR) spectrum for the needle-like crystalline **NGNR5b** and its xerogel is given in **Figure 4.3b**. **NGNR5b** in crystalline state displayed peaks for -OH and -NH stretching at 3350 $cm^{-1}$ and 3234 $cm^{-1,}$ respectively. During the gelation process, owing to the entrapment of solvent and flexible fibrillar aggregation, both -OH and -NH stretching frequencies shifted towards a higher wavenumber region and were observed at 3458 $cm^{-1}$. In the crystalline state, stretching frequencies of carbonyl group, amide 1, amide 2, -C=C-, and bending frequencies of C-H appeared at 1728, 1677, 1465, 1631 and 778 $cm^{-1}$, whereas in the xerogel state, all these peaks displayed appreciable shift and observed at 1743, 1710, 1462, 1625 and 723 $cm^{-1}$ respectively. FTIR analysis clearly reveals the involvement of various groups in molecular self-assembly via intermolecular interactions. It is worth mentioning that the peak corresponds to the stretching frequency of aromatic -C=C- appeared at 1631 $cm^{-1}$ in the crystalline state displayed a shift to the lower wavenumber region, revealed the involvement of aromatic moiety of naphthalimide in π-π stacking. FTIR analysis disclosed that the molecular arrangement in the crystalline state is different from the xerogel state.

Predicting the molecular arrangement within the supramolecular gel is exceptionally challenging, as the structure and characteristics depend on the geometry and arrangement of building blocks in a three-dimensional lattice. Nonetheless, the small angle-XRD (SAXRD) technique provides an understanding of the molecular arrangement. The xerogel obtained from **NGNR5b** displayed 2θ = 2.4°, 4.7°, 7.2°, 9.8° corresponding to the interplanar spacing (d-spacing) at 3.6, 1.8, 1.2 and 0.9 nm, respectively. XRD peak analysis revealed the Bragg's reflection following a consistent pattern of 1, ½, 1/3 and 1/4 (**Figure 4.3c**). Peaks displayed at 19.9°, 21.1°, 21.9°, and 26.0° corresponds to the π-π stacking arrangement. Intermolecular interactions facilitate the molecular self-assembly, creating a 3-D fibrillar network architecture measuring a length of 3.6 nm as determined by XRD, which is higher than the end-to-end molecular length of NGNR. The end-to-end molecular length of **NGNR5b** is 2.5 nm, calculated

from the energy-minimized structure of **NGNR5b**. This result suggests the presence of a double layer stabilized by intermolecular H-bonding.

UV absorption and fluorescence characteristics are integral in the designing and functionality of a broad spectrum of electronic devices; these properties enable fine-tuned color control, data transmission, energy conversion, and substance identification. A detailed investigation of a conjugated molecule's absorption and emission characteristics opens a pathway to establish the efficiency and performance of electronic devices.

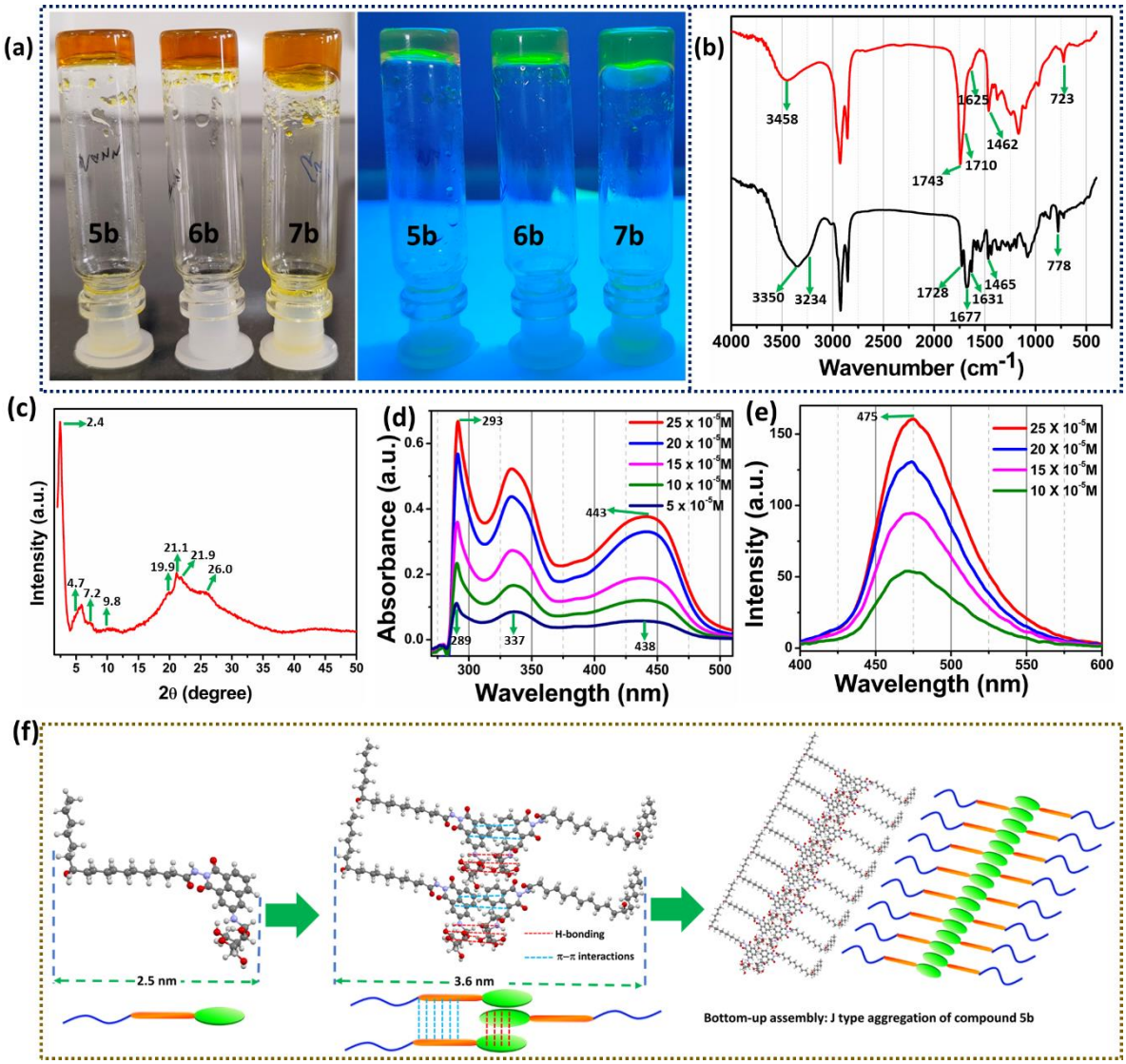


**Figure 4.3**. (a) Images of the gel formed by **NGNR5b-7b** in m-xylene under normal and UV light (CGC = 1% wt/v). (b) A comparison of FT-IR spectra of **NGNR5b** in xerogel state (red), and amorphous state (black). (c) The XRD pattern of a xerogel was obtained from **NGNR5b**. (d) UV-vis, and (e) fluorescence titration of **NGNR5b** dissolved in gelling solvent xylene [$\lambda_{ex}$ = 289 nm]. (f) A schematic representation of the bottom-up assembly of **NGNR5b** to generate *J*-type aggregated intertwined lamellar sheet structure

Absorption spectra of **NGNR5b** in gelling solvent, *m*-xylene is given in **Figure 4.3d**. In the UV-visible spectra, three distinct and well-resolved peaks centered at 289, 337 and 438 nm are observed, and these bands can be ascribed to the π–π* transition of the amide group, n–π* transition of the naphthalimide, respectively. Notably, as the concentration of the gelator

increases, the peak centered at 289 and 436 nm displayed a redshift to 293 and 443 nm, respectively. The red shift displayed by **NGNR5b** upon increase in concentration clearly indicates the emergence of *J*-type aggregation results in supramolecular organization.

Aggregation-induced emission (AIE) is a distinctive photophysical phenomenon exhibited by specific conjugated organic molecules. Aggregation-induced emission (AIE) is a distinctive photophysical phenomenon exhibited by specific conjugated organic molecules. Unlike the conventional behavior of fluorophores, which becomes less emissive upon aggregation, AIE molecules exhibit increased enhanced emission when they aggregate into an assembled state. Assembled materials displaying AIE are instrumental in a wide array of applications, including printed circuit boards, electronic gadgets, security, bio and chemical sensors, energy harvesting, and electronic communication systems. **Figure 4.3e** represents the emission behavior of **NGNR5b** in gelling solvent *m*-xylene at various dilutions. Upon increasing the concentration, a gradual increase in the emission intensity suggests the existence of AIE. Based on the FTIR, SAXRD, and UV absorption studies, the molecular self-assembly mechanism is proposed and given in **Figure 4.3f**.

Gel morphology is examined using scanning electron microscopy (SEM), as shown in **Figure 4.4a-c**. The gel formed by **NGNR5b** in *m*-xylene displayed intertwined lamellar sheet-like morphology obtained by intermolecular interactions. It is worth mentioning that SEM analysis of another **NGNR6b** in *m*-xylene generated an intertwined globule sheet (**Figure 4.4d-f**). Morphological analysis clearly revealed that even changes in the orientation of sugar hydroxyl groups can drastically affect the morphology, reflecting on the material performance. As per the literature, surface morphology plays a crucial role in TENG fabrication,[44-46] since the device efficiency, reliability, and versatility depend on how the surface characteristics are designed and engineered. These surface characteristics of materials enable TENGs to be adapted for various energy harvesting applications.[47-49] It is worth mentioning that **NGNR5b** displayed better performance than **NGNR6b**, as indicated by preliminary TENG studies.

The key consideration when utilizing gel materials to fabricate TENGs is their ability to be flexible, mechanical strength, and versatile enough to satisfy the demands of TENGs as flexible wearable electronics. The Mechanical strength is an important parameter of the materials used in TENG fabrication because it should not undergo deformations while processing, such as stress or stain, frequency, or temperature. Rheology is the best tool to measure the processability of gels and can provide important information on their strength and thermoreversibility. The frequency sweep experiment of gel formed by **NGNR5b** in *m*-xylene furnished a greater value of storage modulus G' compared to the loss modulus G'' throughout the range of analysis disclosed its strength (**Figure 4.4g**).

A stress or strain sweep experiment was conducted by varying the amplitude of the input signal at constant temperature and frequency; a slight fold or deformation in supramolecular structure was observed beyond the critical strain ($\gamma_c$) value of 0.002%, and complete gel to sol transition was observed at $\gamma$ = 0.038%, the greater value of G' compared to the G'' within the linear viscoelastic region (LVE) suggest a good mechanical strength of the gel (**Figure 4.4h**).

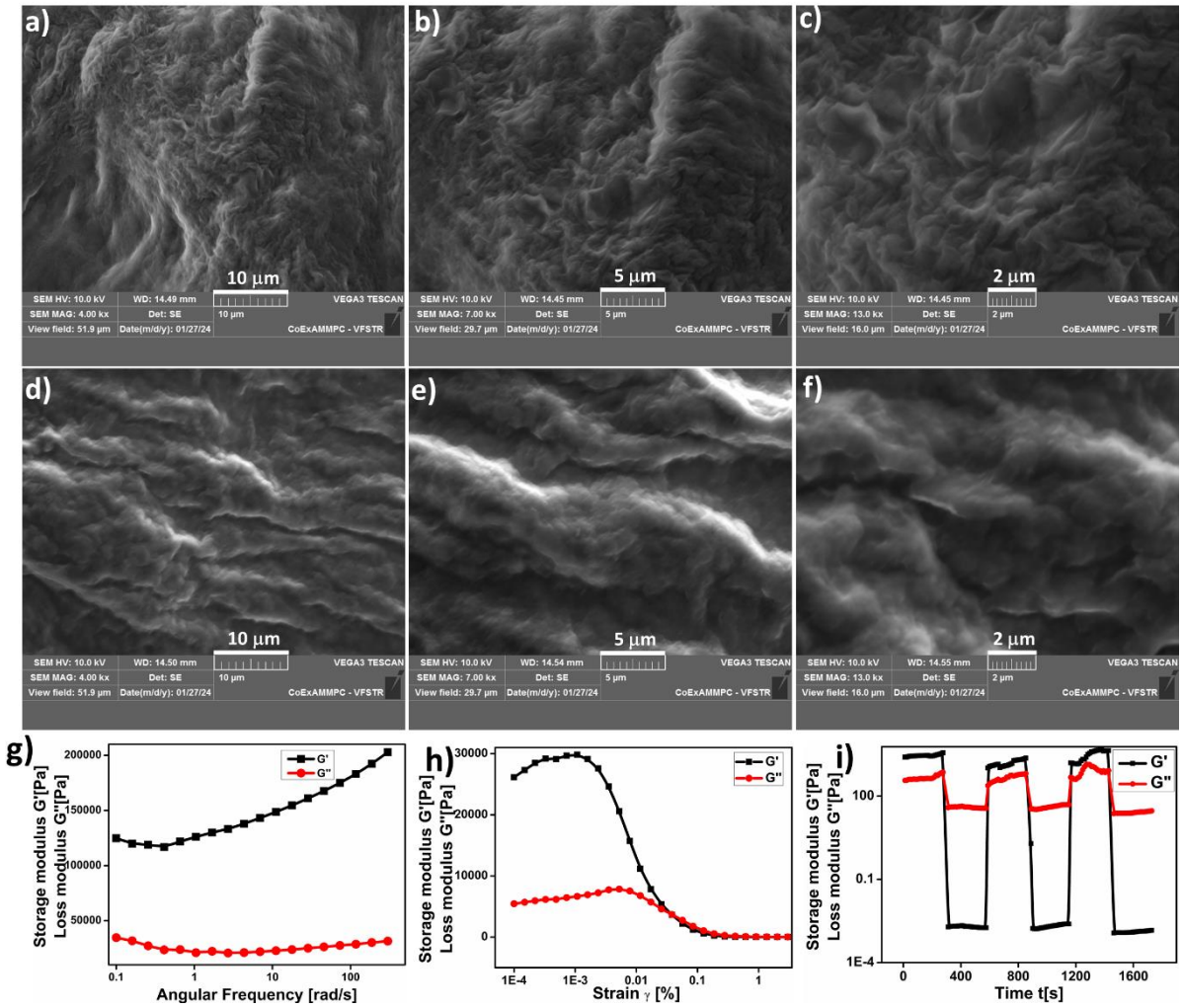


**Figure 4.4**. SEM images of the xerogel formed by **NGNR5b** (a–c) and **6b** (d-f) in *m*-xylene. (g) strain amplitude, and (h) angular frequency dependency of G' and G'' of the gel formed by **NGNR5b** in *m*-xylene. (i) Thixotropic behavior investigation using continuous strain ramp-up and ramp-down measurements of the gel formed by **NGNR5b** in *m*-xylene.

A continuous step-strain experiment investigated the thixotropic nature of the gel formed by **NGNR5b** (**Figure 4.4i**). On applying a constant strain (100%), G' is found to be lower than the G'', indicating the deformation of a 3D supramolecular network in organogel. Upon reducing the strain to 1%, the greater value of G' compared to the G'' revealed the rapid recovery nature of the gel to its original form by reconstructing the supramolecular network. The thixotropic nature of the gel was consistent even after three cycles, which clearly supports the good strength and processability of the gel for use as a triboelectric layer in the fabrication of TENG. It is worth mentioning that the gel displayed thixotropic behavior on simple shaking and resting.

The hypothesis for the thixotropic behavior of the gel is that the gelator makes the hydrogen bonding interaction between the sugar molecules stronger, establishing the one-dimensional aggregate, and weak van der Waals interactions between the long aliphatic chain form the three-dimensional architecture. The shear strain produced breaks only the weak van der Waal interaction but not the hydrogen bonding, which results in gel deformation. Upon releasing the shear strain, three-dimensional networks regenerate through the recovery of intermolecular interactions, thereby gel gets regenerated.

TENG device fabrication: **Figure 4.5** shows the schematic of the TENG and its components. The TENG device was fabricated using **NGNR5b** film and silicone rubber deposited on aluminium as triboelectric layers and aluminium as electrodes for TENG. These two triboelectric layers were attached to two cardboard sheets on top of each other and separated with sponge spacers to operate TENG in vertical contact separation mode (VCS), as shown in **Figure 4.5d**. Finally, both electrodes were connected with electrical wires, and the electrical outputs of the TENG were measured using a digital oscilloscope (GW-instek, GDS -1102B) and low noise current preamplifier (SRS, SR 570).

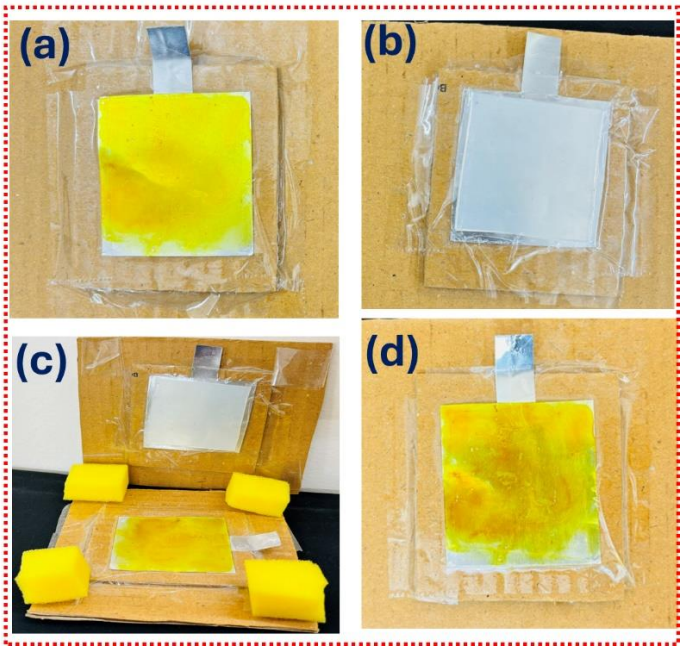


**Figure 4.5**. Fabrication of vertical contact separation mode TENG. (a) NGNR-5b film coated on aluminium substrate and attached to a Cardboard. (b) Silicone attached aluminium sheet is attached to Cardboard. (c) final vertical contact separation mode TENG device. (d) Image of the TENG device after stability test.

Further, additional TENG devices were fabricated for fixed **NGNR5b** film and variable opposite frictional layers such as aluminium, polymethyl methacrylate (PMMA), and fluorinated ethylene propylene (FEP). The stability of the TENG device was performed using an in-house developed tapping machine. The electrical characteristics of TENG devices, utilizing a fixed **NGNR5b** film against various opposing triboelectric layers, are depicted in

**Figure 4.6b**. Among these configurations, the highest performance was achieved with a device comprising an **NGNR5b** film on an aluminium substrate paired with silicone rubber, achieving an open-circuit voltage of 410 V and a short-circuit current of 100 μA. This specific pairing was selected for additional device measurements. The differential response of the TENG devices can be attributed to the electron-accepting and donating properties of the materials involved in frictional contact. The **NGNR5b** film acts as an electron donor due to its chemical bonding and surface characteristics. Consequently, the output is relatively low when the **NGNR5b** film is combined with another electron-donating material, such as aluminium. However, pairing the **NGNR5b** film with an electron-accepting material, like silicone, significantly enhances the device's output. This behavior underscores the electron-donating attribute of the **NGNR5b** film.

Further, a switching polarity test of the TENG device was performed, and the results are presented in **Figure 4.6c-d**. This confirms that the voltage and current output are generated from TENG alone, not any noise signal from the instrument. **Figure 4.6e** presents the variation of voltage and current output of the TENG at different load resistances. The voltage increases with load resistance and reaches saturation level after 10 MΩ, while the current decreases with load resistance and gets saturated after 10 MΩ. The observed load characteristics of TENG are similar to those of the existing reports.[50-52] The instantaneous power density of the TENG was calculated using the P= V*I/A formula, and the results are presented in **Figure 4.6f**. The TENG reaches a maximum power density of 5.1 W/m$^2$ at a load resistance of 10 MΩ, from the maximum power transmission theorem, which can be considered as an impedance matching condition.[53]

Moreover, the TENG device underwent a stability and durability test involving a consistent tapping force applied by a machine for 10,000 cycles, demonstrating remarkable stability. Following this, the device was subjected to manual tapping for an additional 600 cycles, with the outcomes showcased in **Figure 4.6g**. Impressively, the TENG device maintained its initial output level even after 10,600 total cycles, underscoring its durability. Furthermore, images of the **NGNR5b** film, both prior to and following the 10,000-cycle test, are displayed in **Figure 4.5d**. These visuals confirm the **NGNR5b** film's mechanical resilience and strong adhesion to the aluminium substrate, with no evidence of cracking observed on its surface. Further, we used a bridge rectifier circuit to convert the AC signal produced by the TENG into a DC signal, as shown in **Figure 4.6h**. A 100 μF capacitor was charged to 1.25 V in 280 sec using a linear motor. Later, a voltage charge was utilized for the continuous operation of the calculator (**Figure 4.6h**), and the capacitor was simultaneously charged by TENG. This demonstration shows the potential of TENG in building self-powered systems.

TENGs have a wide range of applications due to their ability to convert low-frequency mechanical energy into electricity. Further, TENG output is very sensitive to the surface condition of the frictional layers, making them suitable for applications in sensing chemicals, gases, and humidity.[54-56] TENG can be used as a sensor to make them low-maintenance and cost-effective.[57] This chapter explores TENG in humidity sensing applications using an in-house developed sensing setup, as depicted in **Figure 4.7a**.

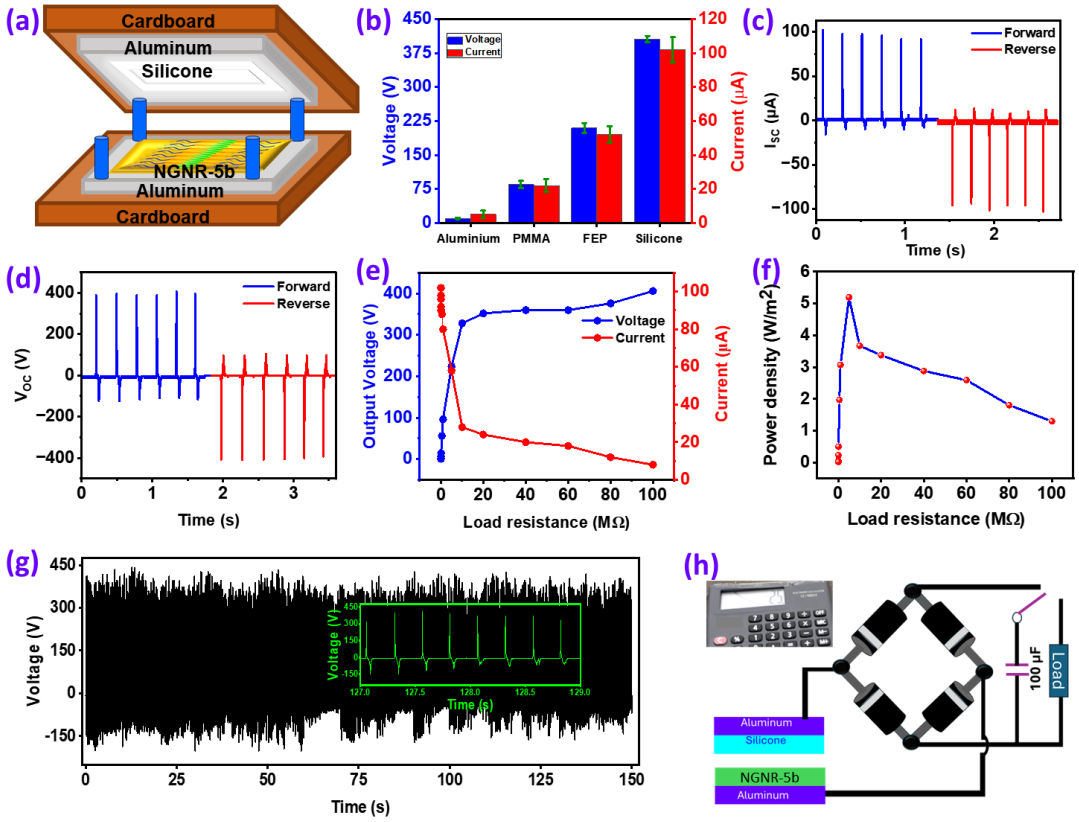


**Figure 4.6**. (a) Schematic of the TENG device, (b) TENG response with different frictional layers; switching polarity results of (c) Voc, (d) Isc, (e) load resistance versus output voltage and current, (f) the instantaneous power density as a function of load resistance, (g) stability of TENG electrical response for 600 cycles of hand tapping, (h) photograph of the digital calculator continuously powered with TENG.

During the experiments, the TENG device was manually tapped while introducing water vapor from a humidifier into the testing chamber in a controlled manner. The electrical output of the TENG was measured across different relative humidity levels ~ 47%, 58%, 69%, 78%, 88%, and 95% and the findings are presented in **Figure 4.7b**. The results clearly indicate a gradual decrease in the voltage output from 142 to 11 V as the humidity level increases (**Figure 4.7c**), illustrating a linear correlation between the output voltage and varying levels of humidity.

This linear relationship underpins the potential of TENGs as self-powered humidity sensors. **Figure 4.7d** shows the photographs of the LEDs powered by TENG under different humidity conditions and it clearly indicates the decrement in the output voltage with humidity. Typically, the performance of a humidity sensor is characterized by the device's electrical response (such as resistance, voltage, or current), as given by the formula.[58,59]

$$\text{Response}=\frac{(V_0-V_{RH})}{V_0}\times 100\%\text{-------(1)}$$

Where $V_o$ is TENG output at a low RH value (47%) when external no water vapor is introduced into the test chamber and VRH is TENG output under different humidity conditions. The TENG humidity sensing response is presented in **Figure 4.7e**.

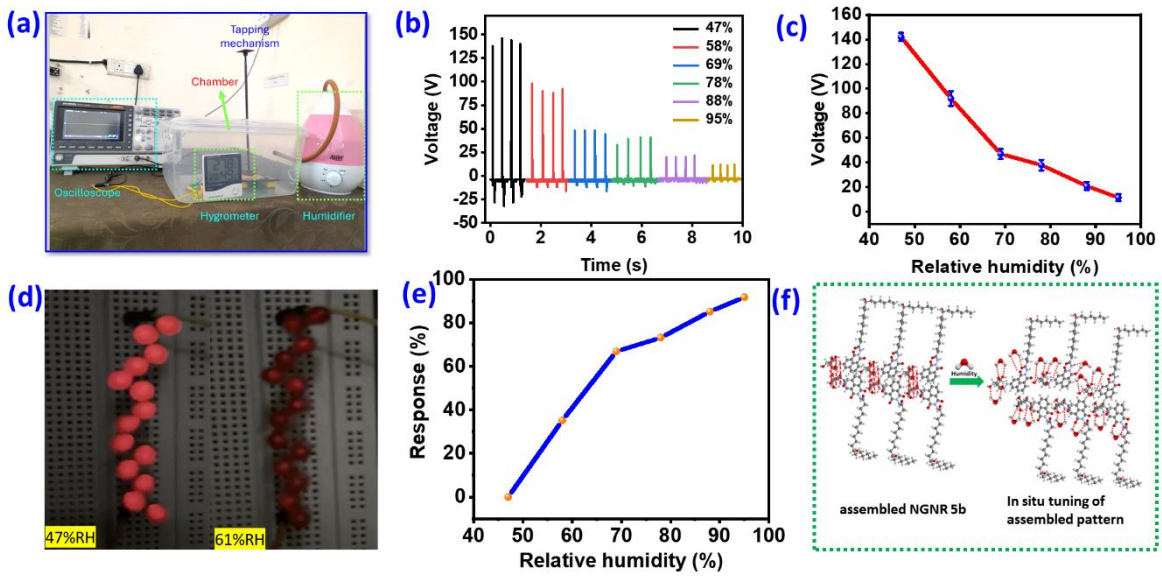


**Figure 4.7**. (a) Photograph of the humidity sensing set up, (b)-(c) TENG output voltage under different humidity conditions, (d) Photograph of the LEDs powered by TENG under two different humidity levels, (e) Response plot of TENG with humidity variation, (f) humidity sensing mechanism.

The effect of humidity on the TENG response is well-reported in the literature.[60] In most cases, the decrease in the TENG output is attributed to the neutralization of surface charges on the triboelectric layers by adsorbed water molecules, and the same can be applied to the present study.[61-66] Additionally, the presence of hydrophilic functional groups on the surface of the triboelectric layers tends to increase water adsorption, thereby improving the device's sensitivity to humidity. It has been observed that the change in TENG response is notably significant up to 70% relative humidity (RH) and becomes less pronounced beyond this point. This pattern can be explained by the increased number of water molecules adsorbed on the triboelectric layers fabricated by using assembled **NGNR5b**. At higher humidity levels, the assembled **NGNR5b** experiences a decreased electron density because of the in situ tuning of the pattern, followed by the reduction in electrostatic charges generated during contact electrification (**Figure 4.7f**).

# 4.3. Experimental

## 4.3.1. General information

A detailed general information is given in chapter 2.

### 4.3.2. General procedure for the synthesis of 3a-b:

To one of the sample injector 3-nitro-1,8-napthalic anhydride **1** (2 mmol), and methyl ricinoleate hydrazide **2** (4 mmol) in 10 mL MeOH was taken and in another sample injector Fe (5 mmol) in MeOH–HOAc (1:1) was taken. Both the injectors were subjected to the flow rate of 100 µL/min, maintaining the reaction coil temperature 200 °C at 2 bar pressure. The reaction mixture collected in the receiver was concentrated, then neutralized with saturated $Na_2CO_3$ solution, and extracted with ethyl acetate. The extracted organic layer was dried over $Na_2SO_4$ and concentrated using a rotary evaporator. A pure **3a–b** was obtained as an amorphous yellow solid.

### 4.3.3. General procedure for the synthesis of NGNR5-7a-b:

To a stirred solution of **3a–b** (0.5 mmol) in MeOH (5 mL) was added monosaccharide **4a–c** (0.75 mmol) followed by $(NH_4)_2SO_4$ (0.05 mmol) in a batch reactor. The reaction mixture was stirred at 65 °C for 24 h in an oil bath. After the completion of the reaction as identified using TLC, the reaction mixture was allowed to cool to room temperature, upon cooling a pale-yellow solid precipitated out was filtered and washed with cold methanol, and recrystallized in ethanol. Experimental details of gelation studies, morphological analysis, X-ray diffraction, molecular modelling, and rheological measurements are given in Chapter 2.

### 4.3.4. Triboelectric layers (films) preparation

Self-assembled supramolecular gel of **NGNR5b** is directly coated on the aluminium foil (thickness~100 µm) by drop casting method. The photograph of the prepared sample **NGNR5b** film on aluminium is shown in **Figure 4.5.** Further, silicone film is directly prepared on aluminium by drop casting method. Initially, the Silicone solution and catalyst were combined in a mass ratio of 10:1, and the mixture was stirred extensively for 30 minutes. Subsequently, the solution was poured into a mold with an area of 5x5 $cm^2$ and a thickness of ~1 mm, where it was allowed to dry for 24 hours to form the pure Silicone film.

## 4.4. Characterization details

**(Z)-N-(5-amino-1,3-dioxo-1H-benzo[de]isoquinolin-2(3H)-yl)-12-hydroxyoctadec-9-enamide (3a):**

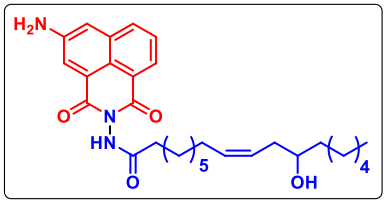


Amorphous yellow solid; yield: 89% (0.902 g); mp: 137 - 139 °C. IR (neat): 3226, 1720, 1674, 1625, 1452, and 772 $cm^{-1}$. $^1H$ NMR (400 MHz, DMSO-$d_6$) δ 10.52 (s, 1H), 8.11 (d, $J$ = 1.6 Hz, 1H), 8.09 (d, $J$ = 2.8 Hz, 1H), 8.00 (d, $J$ = 2.0 Hz, 1H), 7.65 (t, $J$ = 7.8 Hz, 1H), 7.35 (d, $J$ = 2.0 Hz, 1H), 6.06 (s, 2H), 5.49 – 5.31 (m, 1H), 4.20 (d, $J$ = 5.6

Hz, 1H), 2.33 (t, *J* = 7.2 Hz, 2H), 2.12 – 2.09 (m, 1H), 2.03 – 1.95 (m, 1H), 1.65 – 1.57 (m, 2H), 1.32 – 1.23 (m, 20H), 0.85 (t, *J* = 6.6 Hz, 3H). $[M+H]^+$ calcd. for $C_{30}H_{42}N_3O_4$: 508.3175; found: 508.3173.

**N-(5-amino-1,3-dioxo-1H-benzo[de]isoquinolin-2(3H)-yl)-12-hydroxyoctadecanamide (3b):**

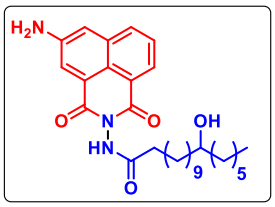

Amorphous yellow solid; yield: 86% (0.875 g); mp: 132 - 134 °C. IR (neat): 3229, 1721, 1672, 1629, 1456, and 774 $cm^{-1}$. $^1H$ NMR (400 MHz, DMSO-$d_6$) δ 10.47 (s, 1H), 8.04 (s, 1H), 8.03 (s, 1H), 7.92 (d, *J* = 2.0 Hz, 1H), 7.58 (t, *J* = 7.8 Hz, 1H), 7.27 (d, *J* = 2.4 Hz, 1H), 6.00 (s, 2H), 4.16 – 4.13 (m, 1H), 2.26 (t, *J* = 7.2 Hz, 2H), 1.57 – 1.50 (m, 2H), 1.12 – 1.16 (m, 26H), 0.77 (t, *J* = 6.8 Hz, 3H). HRMS (ESI, m/z): $[M+H]^+$ calcd. for $C_{30}H_{44}N_3O_4$: 510.3332; found: 510.3333.

**(Z)-N-(1,3-dioxo-5-(((2R,3S,4S,5S,6R)-3,4,5-trihydroxy-6-(hydroxymethyl)tetrahydro-2H-pyran-2-yl)amino)-1H-benzo[de]isoquinolin-2(3H)-yl)-12-hydroxyoctadec-9-enamide (5a):**

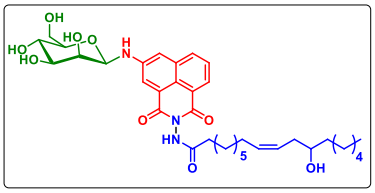

Amorphous yellow solid; yield: 91% (0.303 g); mp: 151 - 153 °C. IR (neat): 2850, 1632, 1546, 1256, and 1088 $cm^{-1}$. $^1H$ NMR (400 MHz, DMSO-$d_6$) δ 10.53 (s, 1H), 8.25 (s, 1H), 8.18 – 8.15 (m, 2H), 7.71 (t, *J* = 7.6 Hz, 1H), 7.57 (s, 1H), 6.95 (dd, *J* = 13.0, 9.0 Hz, 1H), 5.44 – 5.40 (m, 1H), 4.96 (t, *J* = 10.4 Hz, 1H), 4.87 (d, *J* = 5.2 Hz, 1H), 4.79 (d, *J* = 4.0 Hz, 2H), 4.40 – 4.34 (m, 2H), 4.19 (d, *J* = 5.2 Hz, 1H), 3.83 – 3.82 (m, 1H), 3.72 – 3.69 (m, 1H), 3.50 – 3.44 (m, 4H), 2.34 (t, *J* = 7.0 Hz, 2H), 2.11 – 2.09 (m, 1H), 2.02 – 1.99 (m, 2H), 1.65 – 1.58 (m, 2H), 1.34 – 1.22 (m, 19H), 0.85 (t, *J* = 5.6 Hz, 3H). $^{13}C$ NMR (100 MHz, DMSO-$d_6$) δ 171.57, 162.37, 162.18, 146.18, 133.93, 133.35, 131.01, 127.64, 127.10, 123.10, 122.61, 121.61, 113.14, 82.14, 81.97, 78.48, 74.85, 71.42, 70.30, 70.02, 67.52, 61.69, 37.69, 36.94, 35.68, 33.65, 31.83, 29.75, 29.57, 29.51, 29.45, 29.37, 29.34, 29.29, 29.18, 29.09, 28.96, 27.34, 25.76, 25.71, 25.66, 25.49, 22.55, 14.42. HRMS (ESI, m/z): $[M+Na]^+$ calcd. for $C_{36}H_{51}N_3O_9$: 692.3523; found: 692.3524

**(Z)-N-(1,3-dioxo-5-(((2R,3R,4S,5R,6R)-3,4,5-trihydroxy-6-(hydroxymethyl)tetrahydro-2H-pyran-2-yl)amino)-1H-benzo[de]isoquinolin-2(3H)-yl)-12-hydroxyoctadec-9-enamide (6a):**

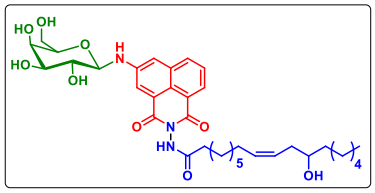

Amorphous yellow solid; yield: 93% (0.310 g); mp: 157-159 °C. IR (neat): 2851, 1630, 1544, 1254, and 1088 $cm^{-1}$. $^1H$ NMR (400 MHz, DMSO-$d_6$) δ 10.53 (s, 1H), 8.18 (s, 1H), 8.16 (s, 1H), 8.13 (s, 1H), 7.71 (t, *J* = 7.8 Hz, 1H), 7.52 (s, 1H), 7.25 (d, *J* = 7.2

Hz, 1H), 5.43 – 5.40 (m, 1H), 4.88 – 4.80 (m, 2H), 4.62 – 4.55 (m, 2H), 4.45 (d, *J* = 2.8 Hz, 1H), 4.20 (d, *J* = 5.2 Hz, 1H), 3.77 – 3.81 (m, 1H), 3.60 – 3.56 (m, 3H), 3.50 – 3.44 (m, 3H), 2.34 (t, *J* = 7.2 Hz, 2H), 2.14 – 2.08 (m, 1H), 2.08 – 1.95 (m, 2H), 1.66 – 1.57 (m, 2H), 1.32 – 1.23 (m, 19H), 0.85 (t, *J* = 5.6 Hz, 3H). $^{13}$C NMR (100 MHz, DMSO) δ 171.57, 162.38, 162.24, 146.91, 134.04, 133.28, 131.02, 127.71, 127.11, 122.73, 122.61, 121.94, 121.46, 85.63, 85.46, 76.26, 74.83, 70.57, 70.30, 70.02, 68.82, 60.93, 37.69, 36.94, 35.68, 33.64, 31.83, 29.74, 29.60, 29.51, 29.45, 29.37, 29.34, 29.29, 29.17, 29.09, 28.96, 27.34, 25.75, 25.71, 25.65, 25.48, 22.55,14.42. HRMS (ESI, m/z): $[M+H]^+$ calcd. for $C_{36}H_{51}N_3O_9$: 670.3704; found: 670.3703

**(Z)-N-(1,3-dioxo-5-(((2R,3R,4S,5S,6R)-3,4,5-trihydroxy-6-(hydroxymethyl)tetrahydro-2H-pyran-2-yl)amino)-1H-benzo[de]isoquinolin-2(3H)-yl)-12-hydroxyoctadec-9-enamide (7a):**

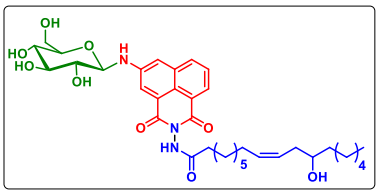

Amorphous yellow solid; yield: 88% (0.293 g); mp: 155 - 157 °C. IR (neat): 2850, 1630, 1546, 1255, and 1088 cm$^{-1}$. $^1$H NMR (400 MHz, DMSO-$d_6$) δ 10.47 (s, 1H), 8.19 (s, 1H), 8.17 (s, 1H), 8.13 (s, 1H), 7.71 (t, *J* = 7.8 Hz, 1H), 7.52 (s, 1H), 7.22 (d, *J* = 6.8 Hz, 1H), 5.43 – 5.40 (m, 1H), 4.96 – 4.84 (m, 3H), 4.62 – 4.56 (m, 1H), 4.43 – 4.39 (m, 1H), 4.31 (s, 1H), 4.13 (s, 1H), 3.72 – 3.68 (m, 1H), 3.56 – 3.50 (m, 2H), 3.45 – 3.34 (m, 3H), 2.35 (t, *J* = 7.0 Hz, 2H), 2.12 – 2.10 (m, 1H), 2.02 – 2.00 (m, 1H), 1.66 – 1.60 (m, 2H), 1.32 – 1.24 (s, 20H), 0.85 (d, *J* = 5.6 Hz, 3H). $^{13}$C NMR (100 MHz, DMSO-$d_6$) δ 171.55, 162.37, 162.23, 146.79, 134.06, 133.37, 131.01, 127.70, 127.11, 122.75, 122.60, 121.92, 121.50, 85.15, 84.95, 78.23, 77.99, 73.52, 70.54, 70.29, 70.01, 61.29, 37.70, 36.94, 35.68, 33.64, 31.84, 29.76, 29.62, 29.57, 29.52, 29.39, 29.35, 29.31, 29.19, 29.11, 28.97, 27.35, 25.77, 25.72, 25.67, 25.49, 22.56, 14.43. HRMS (ESI, m/z): $[M+H]^+$ calcd. for $C_{36}H_{51}N_3O_9$: 670.3704; found: 670.3705

**N-(1,3-dioxo-5-(((2R,3S,4S,5S,6R)-3,4,5-trihydroxy-6-(hydroxymethyl)tetrahydro-2H-pyran-2-yl)amino)-1H-benzo[de]isoquinolin-2(3H)-yl)-12-hydroxyoctadecanamide (5b):**

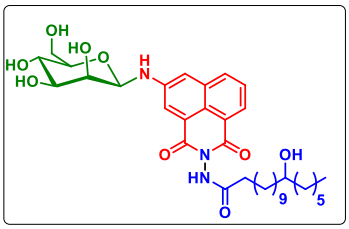

Amorphous yellow solid; yield: 90% (0.301 g); mp: 147 - 149 °C. IR (neat): 3234, 1728, 1677, 1631, 1465, and 778 cm$^{-1}$. $^1$H NMR (400 MHz, DMSO-$d_6$) δ 10.54 (s, 1H), 8.25 (t, *J* = 2.2 Hz, 1H), 8.18 – 8.15 (m, 2H), 7.71 (t, *J* = 7.8 Hz, 1H), 7.57 (d, *J* = 2.0 Hz, 1H), 6.96 (dd, *J* = 14.2, 9.0 Hz, 1H), 4.96 (dd, *J* = 12.0, 9.2 Hz, 1H), 4.88 – 4.87 (m, 1H), 4.83 – 4.78 (m, 2H), 4.41 – 4.35 (m, 1H), 4.20 (d, *J* = 5.2 Hz, 1H), 3.83 – 3.81 (m, 1H), 3.73 – 3.67 (m, 1H), 3.50 – 3.44 (m, 5H), 2.34 (t, *J* = 7.2 Hz, 2H), 1.65 – 1.58 (m, 2H), 1.28 – 1.23 (m, 26H), 0.86 (t, *J* = 6.4 Hz, 3H). $^{13}$C NMR (100 MHz, DMSO-$d_6$)

δ 171.56, 162.37, 162.18, 146.23, 133.93, 133.34, 127.63, 127.23, 123.10, 122.61, 121.90, 121.61, 113.14, 78.55, 78.49, 74.86, 71.42, 70.03, 67.53, 61.70, 37.70, 33.66, 31.84, 29.75, 29.52, 29.46, 29.38, 29.30, 28.97, 25.76, 25.71, 25.49, 14.42. HRMS (ESI, m/z): $[M+H]^+$ calcd. for $C_{36}H_{53}N_3O_9$: 672.3860; found: 672.3864.

**N-(1,3-dioxo-5-(((2R,3R,4S,5R,6R)-3,4,5-trihydroxy-6-(hydroxymethyl)tetrahydro-2H-pyran-2-yl)amino)-1H-benzo[de]isoquinolin-2(3H)-yl)-12-hydroxyoctadecanamide (6b):**

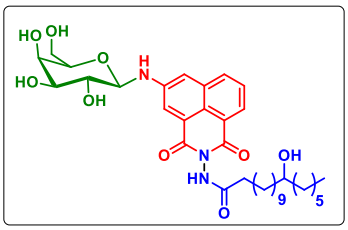

Amorphous yellow solid; yield: 91% (0.304 g); mp: 151 - 153 °C. IR (neat): 3234, 1728, 1677, 1630, 1465, and 779 $cm^{-1}$. $^1H$ NMR (400 MHz, DMSO-$d_6$) δ 10.54 (s, 1H), 8.18 (s, 1H), 8.16 (s, 1H), 8.13 (s, 1H), 7.71 (t, *J* = 7.8 Hz, 1H), 7.52 (s, 1H), 7.26 (d, *J* = 7.6 Hz, 1H), 4.85 – 4.81 (m, 2H), 4.64 – 4.61 (m, 2H), 4.47 (d, *J* = 3.2 Hz, 1H), 4.21 (d, *J* = 5.2 Hz, 1H), 3.77 (t, *J* = 3.4 Hz 1H), 3.60 – 3.54 (m, 3H), 3.49 – 3.44 (m, 3H), 2.34 (t, *J* = 7.0 Hz, 2H), 1.66 – 1.57 (m, 2H), 1.28 (s, 16H), 1.24 (s, 10H), 0.85 (t, *J* = 6.2 Hz, 3H). $^{13}C$ NMR (100 MHz, DMSO-$d_6$) δ 171.58, 162.38, 162.24, 146.90, 134.03, 133.29, 127.71, 127.11, 122.78, 122.72, 122.58, 121.92, 121.45, 76.25, 74.82, 70.55, 70.01, 68.80, 60.90, 37.69, 33.64, 31.84, 29.75, 29.61, 29.51, 29.45, 29.38, 29.29, 29.17, 28.96, 25.76, 25.71, 25.49, 22.56. HRMS (ESI, m/z): $[M+H]^+$ calcd. for $C_{36}H_{53}N_3O_9$: 672.3860; found: 672.3858.

**N-(1,3-dioxo-5-(((2R,3R,4S,5S,6R)-3,4,5-trihydroxy-6-(hydroxymethyl)tetrahydro-2H-pyran-2-yl)amino)-1H-benzo[de]isoquinolin-2(3H)-yl)-12-hydroxyoctadecanamide (7b):**

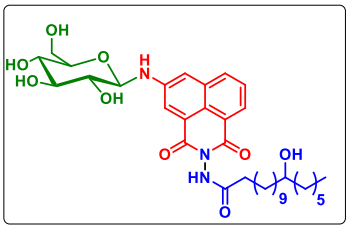

Amorphous yellow solid; yield: 82% (0.274 g); mp: 144 - 146 °C. IR (neat): 3233, 1728, 1675, 1631, 1465, and 779 $cm^{-1}$. $^1H$ NMR (400 MHz, DMSO-$d_6$) δ 10.55 (s, 1H), 8.18 (s, 1H), 8.16 (s, 1H), 8.13 (t, J = 2.4 Hz, 1H), 7.71 (t, J = 7.8 Hz, 1H), 7.52 (s, 1H), 7.27 (d, J = 7.6 Hz, 1H), 4.86 – 4.80 (m, 2H), 4.63 – 4.62 (m, 2H), 4.48 (d, J = 3.2 Hz, 1H), 4.22 (d, J = 5.2 Hz, 1H), 3.78 (s, 1H), 3.61 – 3.55 (m, 3H), 3.49 – 3.43 (m, 3H), 2.34 (t, J = 7.0 Hz, 2H), 1.63 – 1.57 (m, 2H), 1.36 – 1.23 (s, 26H), 0.85 (d, J = 6.9 Hz, 3H). $^{13}C$ NMR (100 MHz, DMSO-$d_6$) δ 171.57, 162.38, 162.24, 146.91, 134.03, 133.29, 131.01, 127.70, 127.10, 122.78, 122.61, 121.93, 121.46, 85.46, 76.26, 74.84, 70.56, 70.01, 68.85, 60.95, 37.69, 36.94, 33.64, 31.84, 31.76, 29.75, 29.62, 29.52, 29.38, 29.30, 28.97, 25.76, 25.71, 25.66, 25.49, 22.56.

## 4.5. Conclusion

Using an environmentally friendly chemical process, a continuous flow method for generating *N*-glycosyl naphthalimide ricinoleate (NGNR) amphiphiles in good yield is reported. Inspired by nature's energy harvesting using molecular assembly phenomenon, a new energy harvesting and utilization strategy is developed. An important aspect of the demonstrated system is the up-conversion of electron-deficient naphthalimides into electron-rich species by molecular assembly. A large potential can be generated and used for operating self-powered electronic devices using the fabricated nanogenerator. In addition, the device fabricated from assembled organic material is low-cost, stable, reliable, and easy to fabricate, making it potentially advantageous for practical applications. The self-powering nature avoids using an external power supply, and its highly sensitive molecular architecture facilitates the detection of relative humidity in the food processing, textile, and agriculture sectors.

## 4.6. References


1. S. Sicari, and A. Rizzardi and A. Coen-Porisini, *Comput. Networks* 2020, ***179***, 107345.
2. H. Hui, Y. Ding, Q. Shi, F. Li, Y. Song and J. Yan, *Appl. Energy* 2020, ***257***, 113972.
3. K. A. Cook-Chennault, N. Thambi and A. M. Sastry, *Smart Mater. Struct.* 2008, ***17***, 43001.
4. K. A. Cook-Chennault, N. Thambi and A. M. Sastry, *Smart Mater. Struct.* 2008, ***17***, 43001.
5. D. Zhang and Q. Liu, *Biosens. Bioelectron.* 2016, ***75***, 273–284.
6. X. Lu, P. Wang, D. Niyato, D. I. Kim and Z. Han, *IEEE Commun. Surv. Tutorials,* 2015, ***17***, 757–789.
7. J. Yick, B. Mukherjee and D. Ghosal, *Comput. Networks,* 2008, ***52***, 2292–2330.
8. Z. L. Wang, T. Jiang and L. Xu, *Nano Energy*, 2017, ***39***, 9–23.
9. Y. Zi, H. Guo, Z. Wen, M.-H. Yeh, C. Hu and Z. L. Wang, *ACS Nano,* 2016, ***10***, 4797 – 4805.
10. X. Peng, K. Dong, C. Ye, Y. Jiang, S. Zhai, R. Cheng, D. Liu, X. Gao, J. Wang and Z. L. Wang, *Sci. Adv.,* 2020, ***6***, eaba9624.
11. S. Mahalingam, A. Manap, K. S. Lau, D. Floresyona, R. Medali Rachman, S. Ayu Pradanawati, R. Rabeya, C. H. Chia, N. Afandi and A. Nugroho, *Renew. Sustain. Energy Rev.,* 2024, ***189***, 113999.
12. C. Zhang and Z. L. Wang, (Ed.: Q.-A. Huang), *Springer* Singapore, Singapore, 2018, 1335–1376.

13. G. Zhu, B. Peng, J. Chen, Q. Jing and Z. Lin Wang, *Nano Energy,* 2014, ***14***, 126–138.
14. H. Zou, Y. Zhang, L. Guo, P. Wang, X. He, G. Dai, H. Zheng, C. Chen, A. C. Wang, C. Xu and Z. L. Wang, *Nat. Commun.,* 2019, ***10***, 1427.
15. G. Khandelwal, A. Chandrasekhar, N. P. Maria Joseph Raj, S.-J. Kim, *Adv. Energy Mater.,* 2019, ***9***, 1803581.
16. S. Rathore, S. Sharma, B. P. Swain and R. K. Ghadai, *IOP Conf. Ser. Mater. Sci. Eng.,* 2018, ***377***, 12186.
17. F.-R. Fan, Z.-Q. Tian and Z. Lin Wang, *Nano Energy,* 2012, ***1***, 328–334.
18. A. K. Rachamalla, S. Potu, V. P. Rebaka, T. Banoo, Y. Kumar, C. U. Maheswari, V. Sridharan, R. K. Rajaboina and S. Nagarajan, *Chem. - A Eur. J.,* 2023, ***29***, e202301076.
19. S. M. Nawaz, M. Chatterjee, S. Chakrabarti, N. Sepay and A. Mallik, *Nano Energy,* 2023, ***117***, 108924.
20. P. C. Calder, *J. Parenter. Enter. Nutr.,* 2015, ***39***, 18-32.
21. D. A. J. Stone, *Rev. Fish. Sci,.* 2003, ***11***, 337–369.
22. J. D. Mul, K. I. Stanford, M. F. Hirshman and L. J. Goodyear, *Prog. Mol. Biol. Transl. Sci.,* 2015, ***135***, 17–37.
23. R. Tyagi, K. Singh, N. Srivastava and R. Sagar, *Mater. Adv.,* 2023, ***4***, 3929–3950.
24. B. M. Turner, *Cell,* 2002, ***111***, 285–291.
25. K. Ohtsubo and J. D. Marth, *Cell,* 2006, ***126***, 855–867.
26. A. KOBATA, *Eur. J. Biochem.,* 1992, ***209***, 483–501.
27. D. C. Fork and S. K. Herbert, *Photosynth. Res.,* 1993, ***36***, 149–168.
28. J. E. Holesh, S. Aslam and A. Martin, *Treasure Island* (FL), **2024**.
29. A. Sidar, E. D. Albuquerque, G. P. Voshol, A. F. J. Ram, E. Vijgenboom and P. J. Punt, *Front. Bioeng. Biotechnol.,* 2020, ***8***, 1–15.
30. A. Kirui, W. Zhao, F. Deligey, H. Yang, X. Kang, F. Mentink-Vigier and T. Wang, *Nat. Commun.,* 2022, ***13***, 538.
31. S. Pérez and I. Tvaroška, *Adv. Carbohydr. Chem. Biochem.,* 2014, ***71***, 9–136.
32. E. Jéquier, *Am. J. Clin. Nutr.,* 1994, ***59***, 682S-685S.
33. H. F. Oldenkamp, J. E. Vela Ramirez and N. A. Peppas, *Regen. Biomater.,* 2019, ***6***, 1–12.
34. L. Li, G. Chen, *J. Am. Chem. Soc.,* 2022, ***144***, 16232–16251.
35. M. D. Tomczyk and K. Z. Walczak, *Eur. J. Med. Chem.,* 2018, ***159***, 393–422.
36. A. Zhang, Y. Zhang, Z. Xu, Y. Li, X. Yu and L. Geng, *RSC Adv.,* 2017, ***7***, 25673–25677.
37. S. Kagatikar and D. Sunil, *J. Mater. Sci.,* 2022, ***57***, 105–139.

38. R. Greiner, T. Schlücker, D. Zgela and H. Langhals, *J. Mater. Chem. C,* 2016, ***4***, 11244–11252.
39. M. Poddar, G. Sivakumar and R. Misra, *J. Mater. Chem. C,* 2019, ***7***, 14798–14815.
40. P. Gopikrishna, N. Meher and P. K. Iyer, *ACS Appl. Mater. Interfaces,* 2018, ***10***, 12081–12111.
41. W. Johnson, *Int. J. Toxicol.,* 2007, ***26***, 31–77.
42. M. Lv and H. Xu, *Curr. Med. Chem.,* 2009, ***16***, 4797–4813.
43. A. L. Berhanu, I. Mohiuddin, A. K. Malik, J. S. Aulakh, V. Kumar and K.H. Kim, *TrAC - Trends Anal. Chem.,* 2019, ***116***, 74–91.
44. Y. Wang, X. Zhao, Y. Liu and W. Zhou, *Beilstein J. Nanotechnol.,* 2022, ***13***, 298–312.
45. Y. Zou, J. Xu, K. Chen and J. Chen, *Adv. Mater. Technol.,* **2021**, ***6***, 2000916.
46. M. Ibrahim, J. Jiang, Z. Wen and X. Sun, *Nanoenergy Adv.,* 2021, ***1***, 58–80.
47. Y. Zheng, L. Cheng, M. Yuan, Z. Wang, L. Zhang, Y. Qin and T. Jing, *Nanoscale,* 2014, ***6***, 7842 – 7846.
48. T. Bhatta, S. Sharma, K. Shrestha, Y. Shin, S. Seonu, S. Lee, D. Kim, M. Sharifuzzaman, S. M. S. Rana and J. Y. Park, *Adv. Funct. Mater.,* 2022, ***32***, 2202145.
49. X. Pu, L. Li, H. Song, C. Du, Z. Zhao, C. Jiang, G. Cao, W. Hu and Z. L. Wang, *Adv. Mater.,* 2015, ***27***, 2472–2478.
50. S. Potu, N. Madathil, S. Mishra, A. Bora, Y. Sivalingam, A. Babu, M. Velpula, L. Bochu, B. Ketharachapalli, A. Kulandaivel, R. K. Rajaboina, U. K. Khanapuram, H. Divi, P. Kodali, B. Murali and R. Ketavath, *ACS Appl. Eng. Mater.,* 2023, ***1***, 2663–2675.
51. M. Navaneeth, S. Potu, A. Babu, B. Lakshakoti, R. K. Rajaboina, U. Kumar K, H. Divi, P. Kodali and K. Balaji, *ACS Sustain. Chem. Eng.,* 2023, ***11***, 12145–12154.
52. M. Rakshita, N. Madathil, A. A. Sharma, P. P. Pradhan, D. P. Kasireddi A.K, U. K. Khanapuram, R. K. Rajaboina and H. Divi, *ACS Appl. Electron. Mater.,* **2024**, **6**, 3, 1821–1828.
53. P. Supraja, R. R. Kumar, S. Mishra, D. Haranath, P. R. Sankar, K. Prakash, N. Jayarambabu, T. V. Rao and K. U. Kumar, *Sensors Actuators A Phys.,* 2022, ***335***, 113368.
54. S. Panda, H. Jeong, S. Hajra, P. M. Rajaitha, S. Hong and H. J. Kim, *Sensors Actuators B Chem.,* 2023, ***394***, 134384.
55. D. Zhang, Y. Yang, Z. Xu, D. Wang and C. Du, *J. Mater. Chem. A,* 2022, ***10***, 10935–10949.
56. C. Huang, G. Chen and A. Nashalian, J. Chen, *Nanoscale,* 2021, ***13***, 2065–2081.
57. Z. L. Wang, *ACS Nano,* 2013, ***7***, 9533–9557.

58. Sardana, Z. Singh, A. K. Sharma, N. Kaur, P. K. Pati and A. Mahajan, *Sensors Actuators B Chem.,* 2022, ***371***, 132507.
59. F. Ejehi, R. Mohammadpour, E. Asadian, S. Fardindoost and P. Sasanpour, *Mikrochim. Acta,* 2021, ***188***, 251.
60. Z. Duan, Y. Jiang and H. Tai, *J. Mater. Chem. C,* 2021, ***9***, 14963–14980.
61. D. Jung, J. Kim and G. S. Lee, *Sensors Actuators, A Phys.,* 2015, ***223***, 11–17.
62. S. Panda, H. Jeong, S. Hajra, P. M. Rajaitha, S. Hong and H. J. Kim, *Sensors Actuators B Chem.,* 2023, ***394***, 134384.
63. V. Mohan, V. K. Mariappan, P. Pazhamalai, K. Krishnamoorthy and S. J. Kim, *Carbon N. Y.,* 2023, ***205***, 328–335.
64. L. Zhang, H. Li, Y. Xie, J. Guo and Z. Zhu, *Beilstein J. Nanotechnol.*, 2020, ***11***, 1394–1401.
65. S. Sardana, Z. Singh, A. K. Sharma, N. Kaur, P. K. Pati and A. Mahajan, *Sensors Actuators B Chem.,* 2022, ***371***, 132507.
66. V. Nguyen and R. Yang, *Nano Energy*, 2013, ***2***, 604–608.

# 4.7. Selected NMR ($^{1}$H & $^{13}$C), and Mass spectra

$^{1}$H NMR Spectrum of NGNR5b (400 MHz, DMSO-$d_6$)

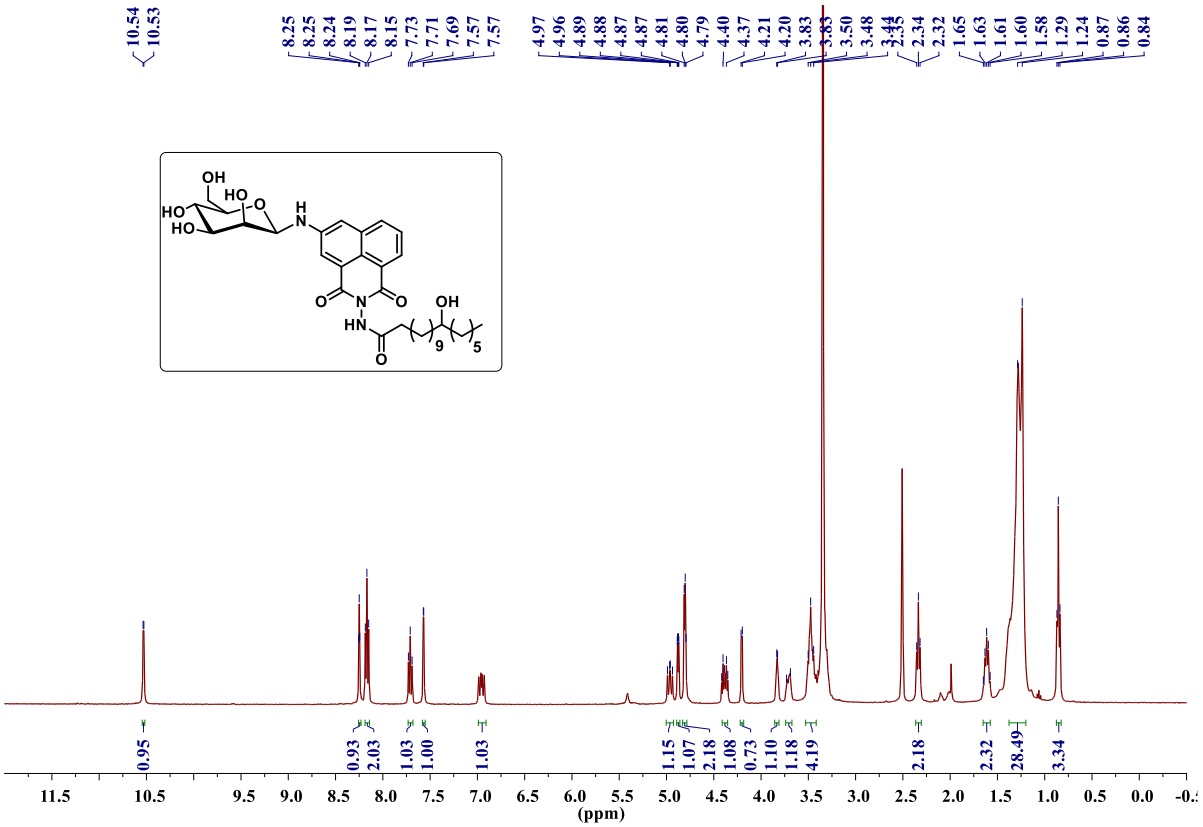


$^{13}$C NMR Spectrum of NGNR5b (100 MHz, DMSO-$d_6$)

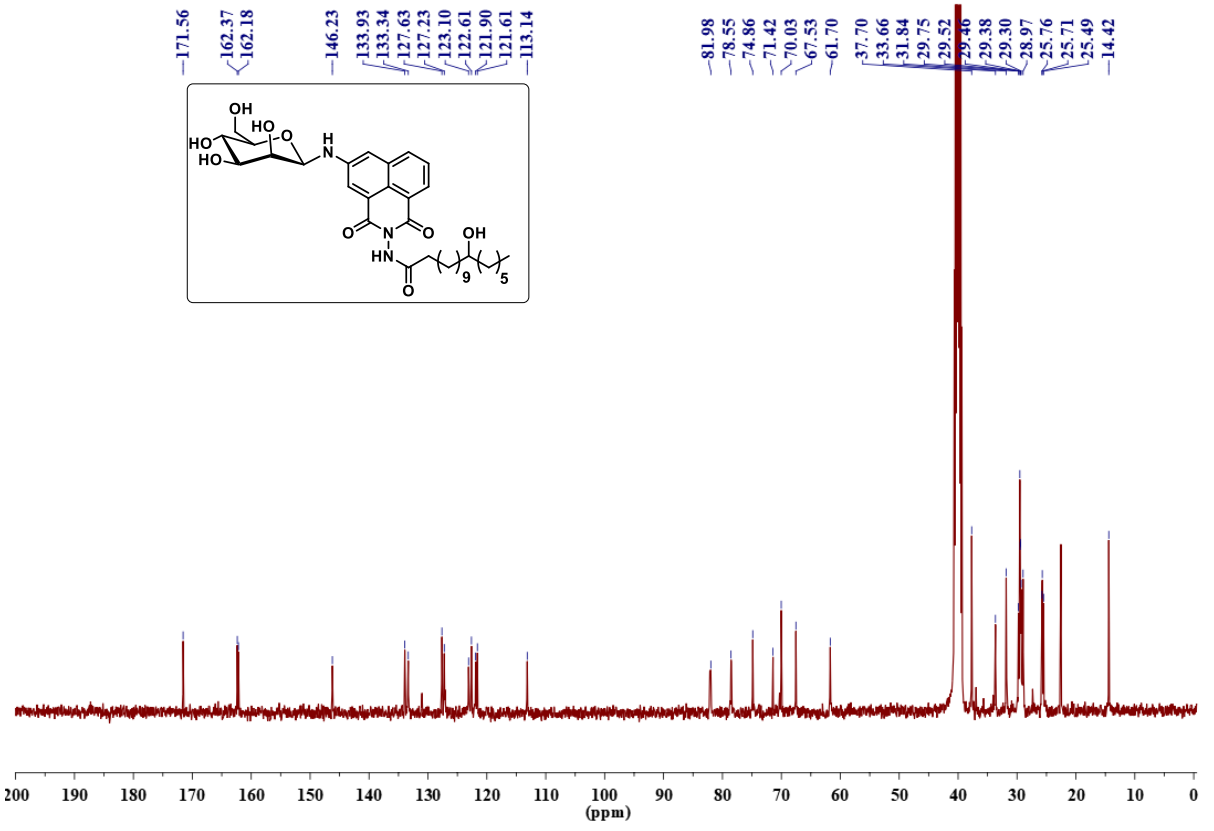

## HRMS spectrum of NGNR5b

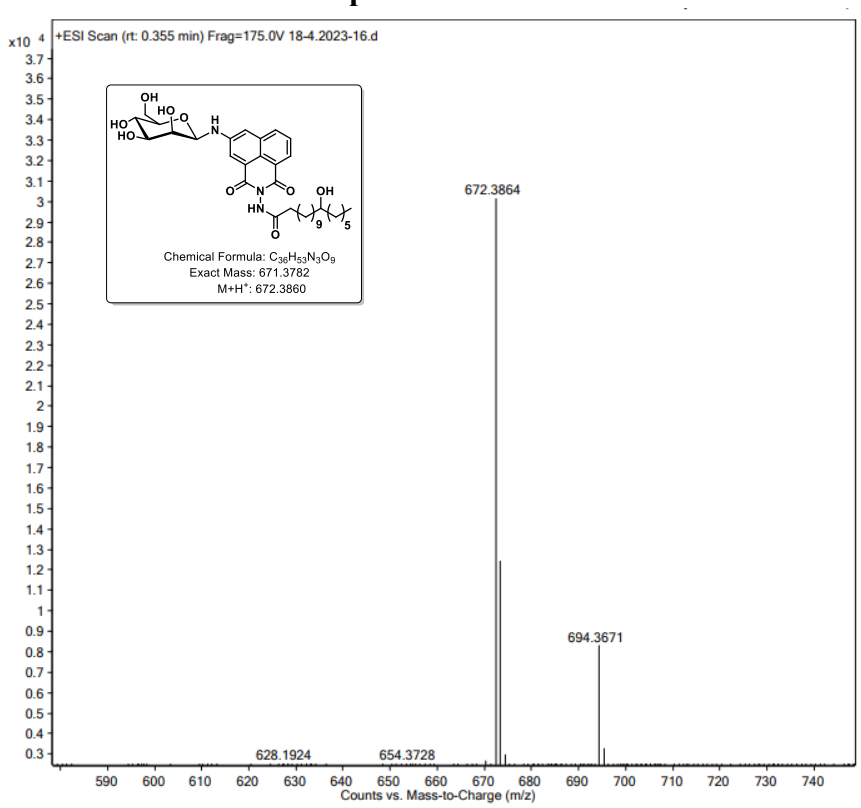


## $^1$H NMR Spectrum of NGNR6b (400 MHz, DMSO-$d_6$)

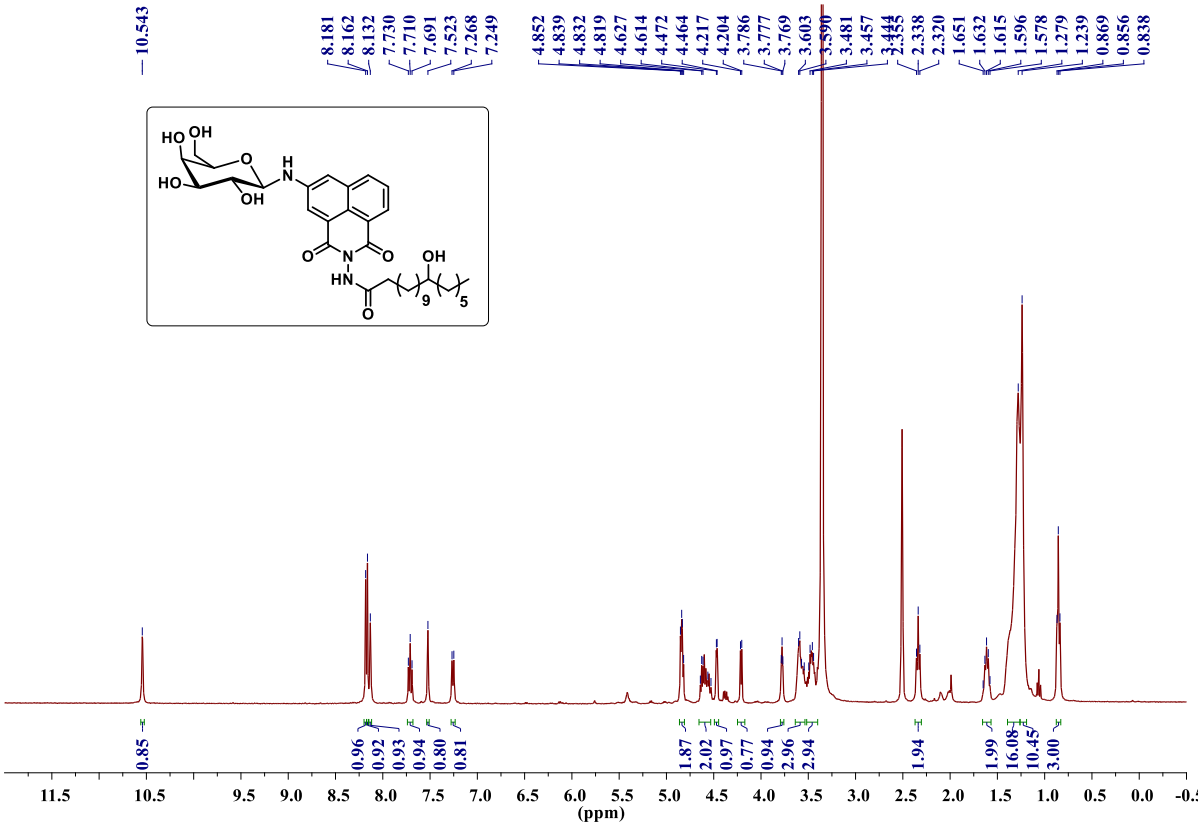

## $^{13}$C NMR Spectrum of NGNR6b (100 MHz, DMSO-*d*$_6$)

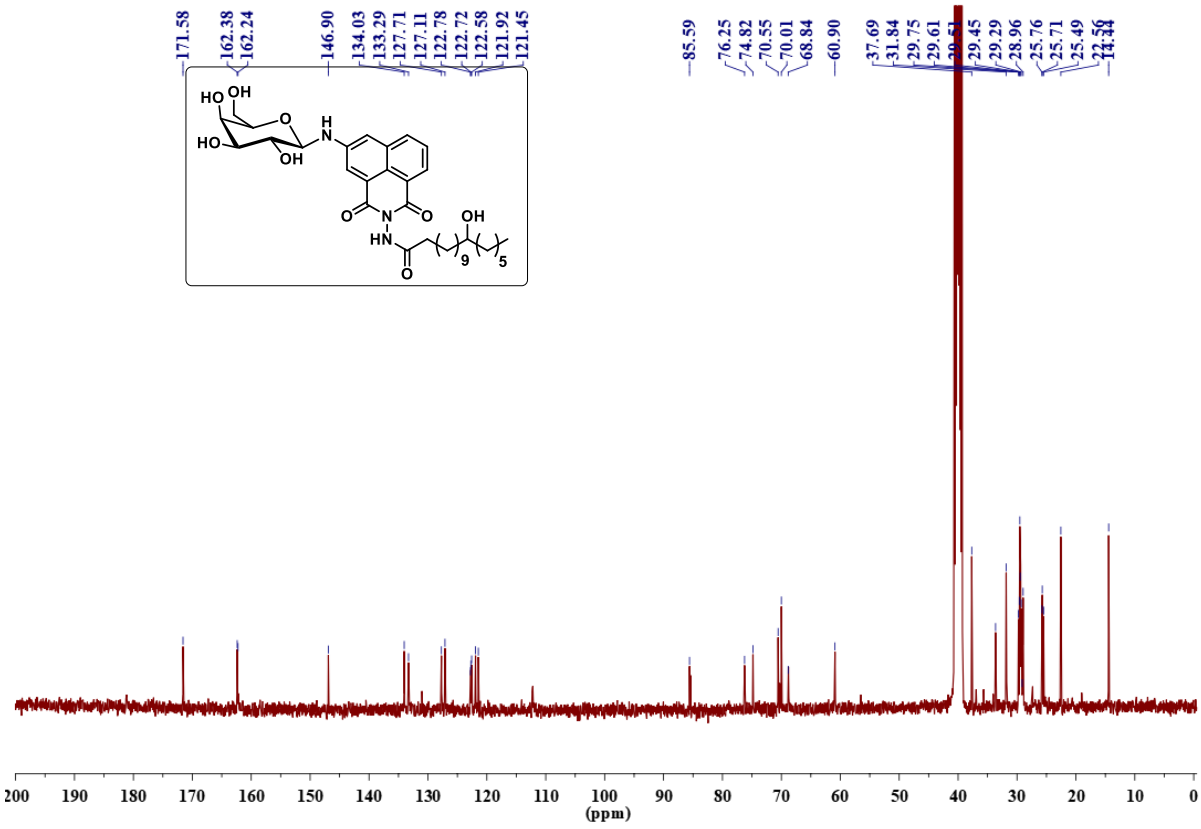


## HRMS spectrum of NGNR6b

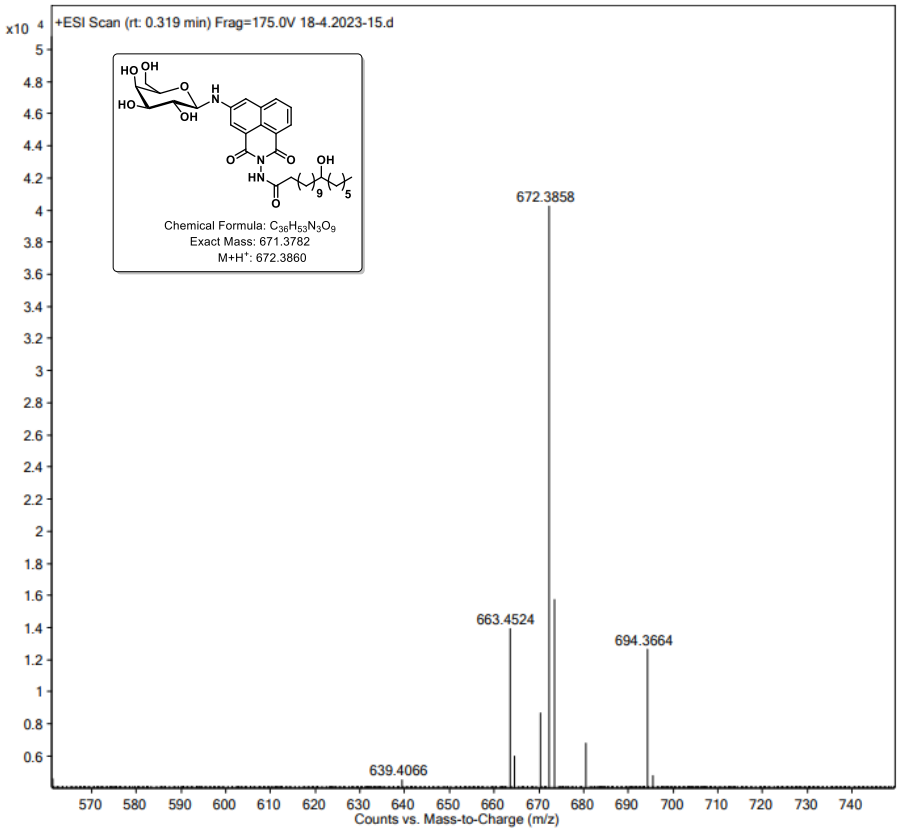

## $^{1}$H NMR Spectrum of NGNR7b (400 MHz, DMSO-$d_6$)

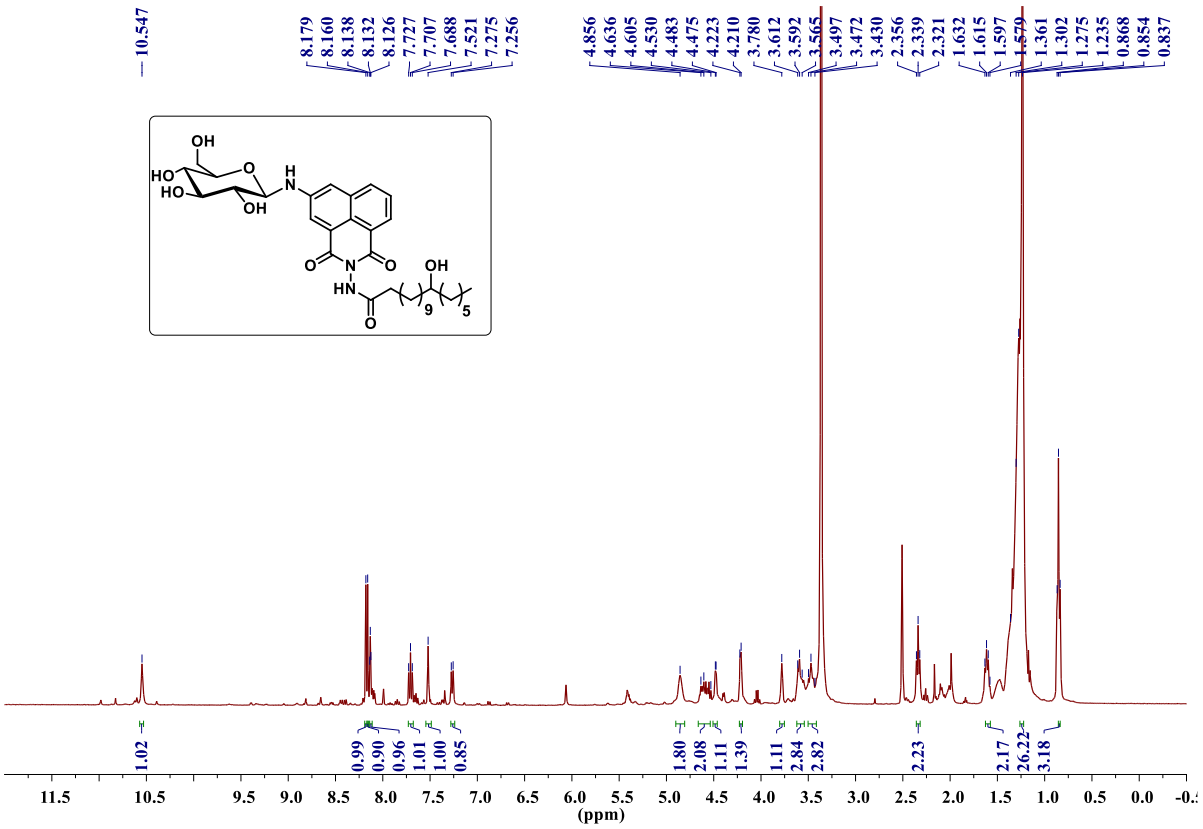


## $^{13}$C NMR Spectrum of NGNR7b (100 MHz, DMSO-$d_6$)

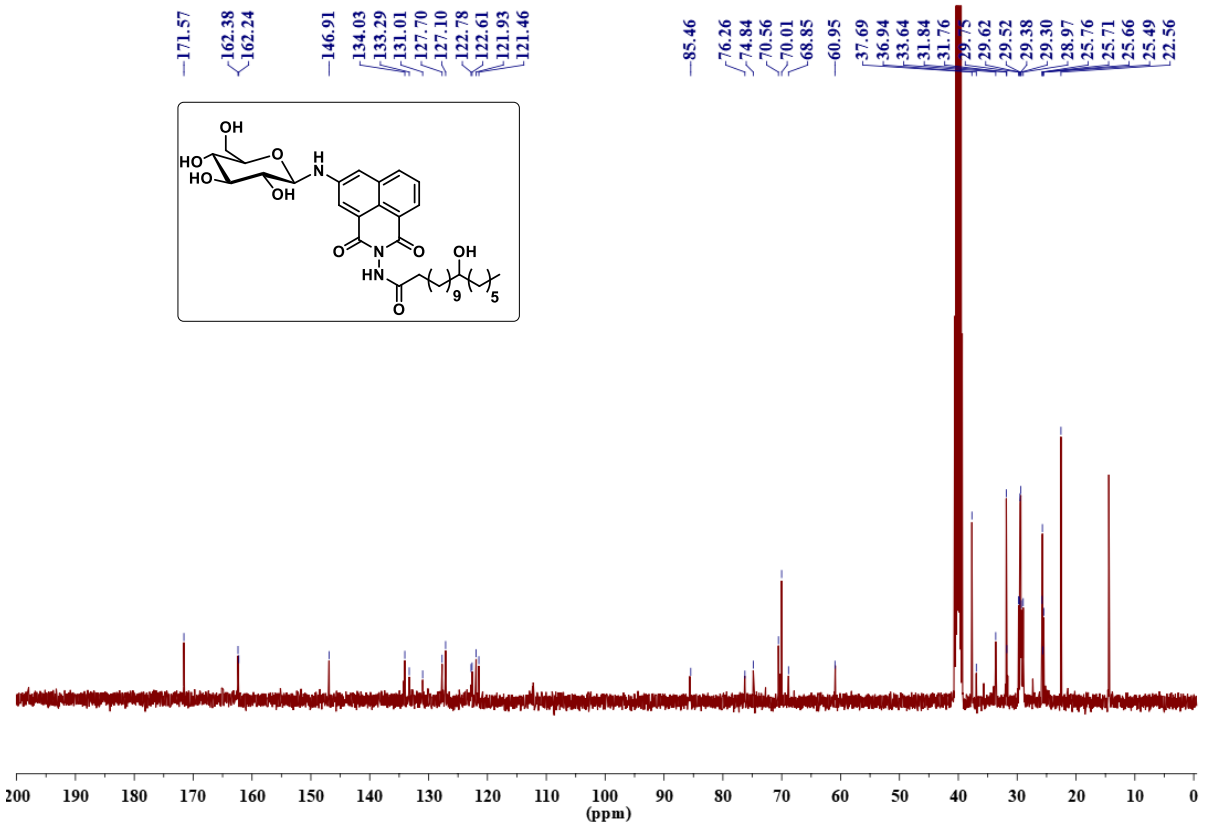

## HRMS spectrum of NGNR7b

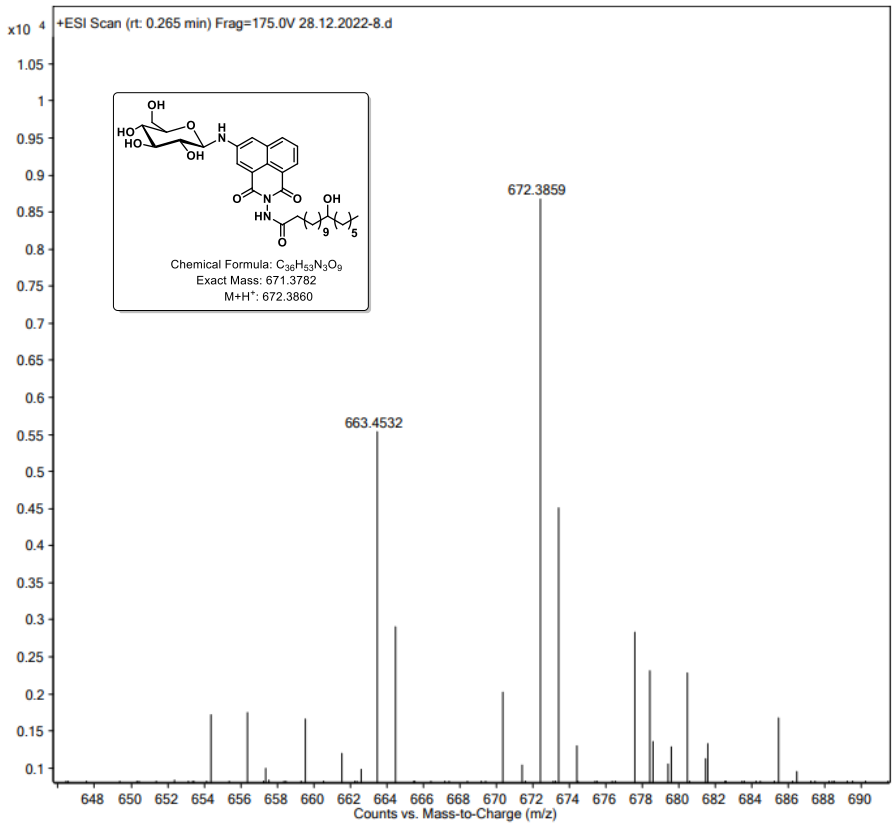

# CHAPTER-V

## Diglycosyl naphthalimide for the fabrication of green energy device

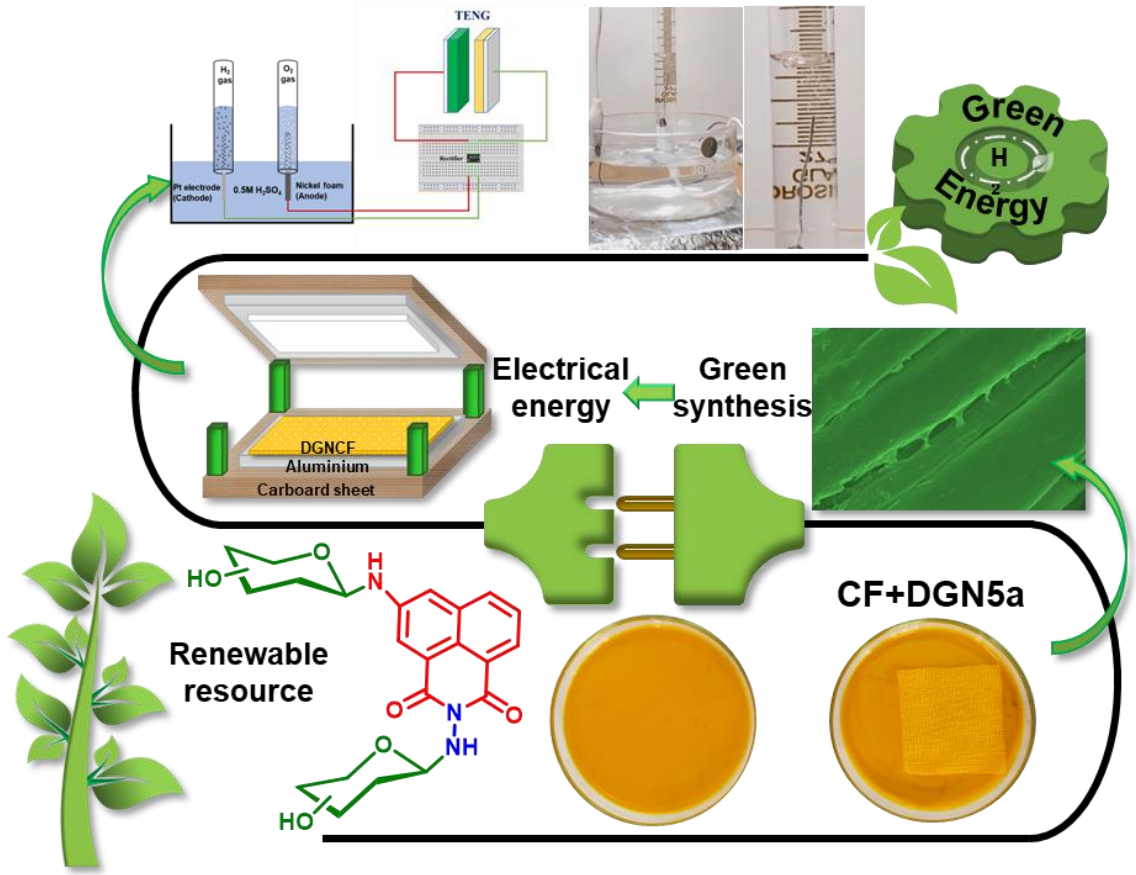

# 5.1. Introduction

Mechanical energy stands out among the energy sources available in our daily environment for its widespread availability and high-power output, making it a prime candidate for fuelling future autonomous smart systems.[1,2] Triboelectric nanogenerators have emerged as promising candidates among the various technologies developed to capture this energy.[3–5,6,7–11] Notably, TENGs can generate electricity from common mechanical actions such as touching, impact, sliding, rotation, and vibration, underscoring their efficiency in practical and commonplace scenarios. Flexible TENGs, in particular, have gained attention for their simplicity, affordability, and adaptability for integration into human environments, offering a compelling solution for mechanical energy harvesting in everyday life.[12–16] As research in TENG technology progresses, continued development and refinement hold promise for advancing the capabilities of self-powered systems and driving innovation in energy harvesting.

The advancement of high-performance TENGs employing environmentally friendly materials, such as carbohydrates, resonates with the escalating focus on sustainability within technology innovation. By utilizing renewable resources, researchers not only mitigate the environmental footprint of energy harvesting devices but also play a pivotal role in driving the global agenda toward a more ecologically sound future. In the pursuit of carbon neutrality, using low-carbon or carbon-free energy sources emerged as a critical strategy.[17,18] Among these, hydrogen ($H_2$) stands out as a promising resource due to its clean combustion, yielding only water. Presently, industrial $H_2$ production primarily relies on reforming fossil fuels, which, although cost-competitive, poses a sustainability challenge due to dependence on non-renewable coal and oil resources.[19,20] To address this, sustainable production methods such as electrochemical hydrogen evolution reaction (HER) offer a pathway forward. However, HER processes are energy-intensive, with electricity consumption comprising a significant portion of production costs.[21,22] In this context, a self-powered electrochemical system (SPECS) represents a compelling solution. By harnessing distributed energy sources autonomously, SPECS minimizes reliance on external power inputs, thus enhancing the economic and environmental feasibility of sustainable $H_2$ production and thereby advancing the overarching goal of carbon neutrality.[23–28]

Nature predominately utilises carbohydrates, proteins, and fats to generate energy essential for physiological processes. Carbohydrates are particularly interesting due to their multiple chiral centers and presence in various forms, such as glycolipids, glycoproteins, and proteoglycans. These molecules are crucial for functions related to cellular architecture, energy metabolism,

and molecular interactions. The biocompatibility, natural abundance, and biodegradability of carbohydrates make them ideal candidates for next-generation molecular materials.[29–33] Conjugating carbohydrates with other functional moieties significantly expands their range of applications, attracting considerable scientific interest. This functionalization enhances their utility in diverse fields such as drug delivery, bioimaging, and material science.[34–40] By modifying carbohydrates, their inherent biocompatibility, natural abundance, and structural versatility can be harnessed more effectively, highlighting their potential as key components in advanced technologies and biomedical applications.[41–48] By considering the salient features of carbohydrates in the materials field, a series of diglycosyl naphthalimides (DGN) were synthesized from monosaccharides and naphthalimides. The justification for the selection of naphthalimides is given in Chapter 1.[49–56] This work offers new insight into the fabrication of organic TENG based on the template-assisted assembly (TASA) process and shows promise in the development of self-powered electronics. This innovative approach highlights the synergistic benefits of combining carbohydrates with naphthalimides and opens new avenues for creating efficient, next-generation molecular materials for energy solutions.

## 5.2. Results and Discussion

As discussed in the previous chapters, naphthalimides have emerged as promising candidates for the development of electronic devices. A series of DGN were synthesized from monosaccharides and naphthalimides using a straightforward synthetic method. The condensation of 3-nitro-1,8-naphthalic anhydride **1** with hydrazine hydrate **8** in methanol under reflux conditions followed by reduction using Fe in MeOH–AcOH in one pot furnished the corresponding diamino-naphthalimides **9** in 96% yield. Further, the *N*-glycosylation of compound **9** with various monosaccharides using glacial acetic acid as a catalyst in methanol under reflux conditions rendered the desired DGN, **5a-d** in excellent yields (**Scheme 5.1)**

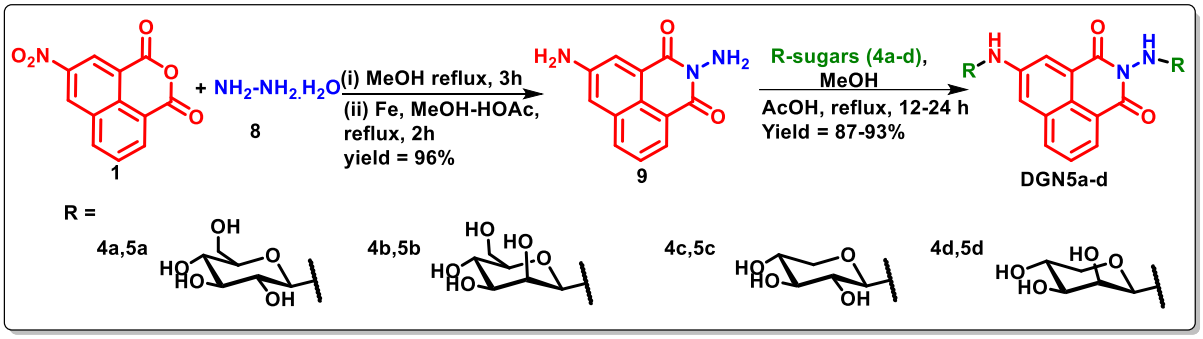


**Scheme 5.1.** Synthesis of Diglycosyl Naphthalimides

All the synthesized DGNs were well characterized using NMR, FT-IR, and Mass Spectral analysis. Typically, the anomeric proton of a sugar moiety exhibits a coupling constant of $J \leq$

4.0 Hz for α-anomer and $J > 4.0$ Hz for $\beta$-anomer. In the case of **DGN5c**, the observed coupling constant $J = 8.4$ Hz for the anomeric proton, resonates at 4.58 ppm as a doublet in deuterium exchanged $^1$H-NMR spectrum, confirming the formation of $\beta$-anomeric product. Based on the solubility displayed by DGNs in water, a flexible TENG is developed using cotton fabric by adopting the TASA process. In this experiment, initially, the cotton fabric is dipped into a hot solution of **DGN5a** in $H_2O$ at 0.03M concentration and allowed to cool down. Upon cooling, hydroxyl groups of **DGN5a** form multiple hydrogen bonds with cellulose fibers of cotton, thereby generating a stable assembled pattern with strong adherence. After 10 min, the dipped cloth was taken out and rinsed very well with distilled water to ensure the complete removal of any adhered substances and dried under a desiccator, thereby generating a **DGN5a** coated flexible Cotton fabric (**DGNCF**) (**Figure 5.1**).

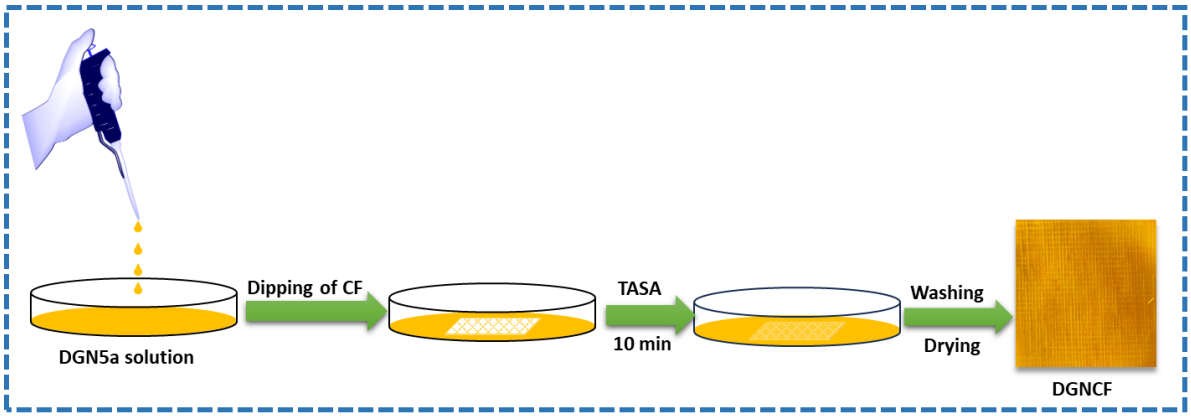


**Figure 5.1**. Schematic representation of fabrication of DGNCF

DGN-coated cotton fabric obtained by TASA process is characterized by XRD, UV, Fluorescence, and morphological studies. As presented in **Figure 5.2a**, the XRD patterns of CF, **DGN5a**, and **DGNCF** reveal significant insights into these materials' structural characteristics and interactions. The XRD diffraction pattern, showing the 2θ values at 15°, 16.7°, 23.1°, and 34.6° for both the cotton and DGN-coated fabric, indicative of crystalline structure of cellulose. The consistent 2θ values for both CF and **DGNCF** indicate that the fundamental crystalline structure of the cellulose I is maintained even after the coating of **DGN5a**. Although the crystalline structure remains largely unchanged, a noticeable change in peak can be attributed to the interaction between the cotton fibers and **DGN5a**. Specifically, the abundant hydroxyl (-OH) groups present in the cellulose structure of cotton are likely engaging in hydrogen bonding with -OH and -NH groups of **DGN5a** molecules. The formation of hydrogen bonds can influence the XRD patterns, especially in the highly ordered hydrogen bonding network within the cellulose. The interaction between **DGN5a** and cotton fibers affects the crystalline regions and promotes the extension of amorphous regions within the material.

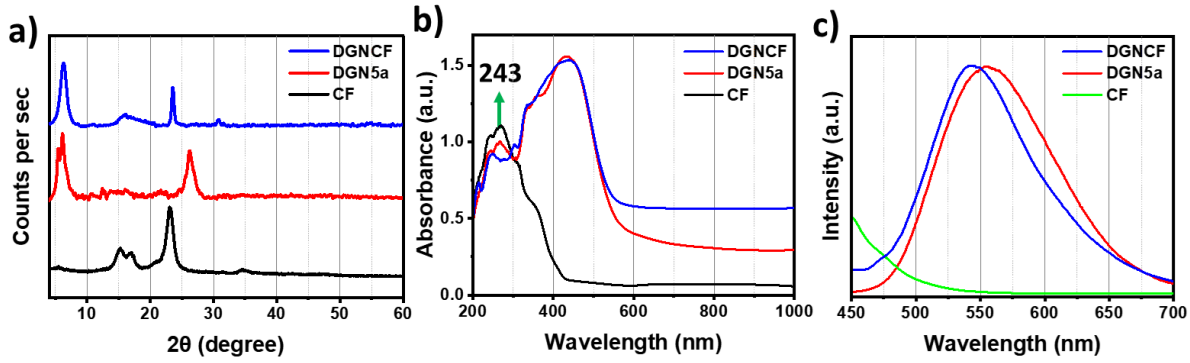


**Figure 5.2**. (a). The XRD pattern of **CF**, **DGN5a**, **DGNCF**. (b) UV–vis, and (c) fluorescence spectra of **CF**, **DGN5a**, and **DGNCF** [$\lambda_{ex}$ = 420 nm].

UV-vis spectroscopy is a versatile analytical technique that has proven invaluable in the study of self-assembling organic molecules. This tool enables monitoring the formation and structural characteristics by leveraging the distinctive absorption profiles exhibited by the constituent molecules within the UV-vis spectrum. By comparing the spectra of coated and uncoated substrates it is possible to detect the presence and relative abundance of UV-vis absorbing materials within the assembled systems, providing essential insights into the self-assembly process. A solid-state UV-vis analysis of **CF** and **DGNCF** was conducted to assess the TASA of **DGN5a** onto CF. **Figure 5.2b** illustrates the UV-vis absorption spectra of **CF DGNCF**, and **DGN5a**. The UV-vis studies revealed the characteristic peaks of cellulose at 243 nm in both the **CF** and **DGNCF**. In addition to this characteristic peak, DGNCF displayed a peak at 438nm, which can be attributed to the n-π*–transition of the naphthalimide moiety of the **DGN5a**, corroborated by the **DGN5a** absorption band at 429nm.

The fluorescence emission of **DGN5a** was attributed to the intramolecular charge transfer (ICT) transition. The fluorescence spectra of the **CF** and **DGNCF** were measured and presented in **Figure 5c**. **DGNCF** displayed emission at 545 nm, whereas its precursor **DGN5a** displayed emission at 553 indicating the interaction of the sugar unit of **DGN5a** with CF, followed by the stacking of naphthalimides core. In contrast, no emission was observed for the simple CF under the same excitation wavelength.

The surface morphologies of **CF** and **DGNCF** were investigated using SEM, as shown in **Figure 5.3**. The SEM images reveal that the surface of pure **CF** is relatively smooth, indicative of its natural, untreated state with tightly packed cellulose fibers. In contrast, the SEM images of **DGNCF** exhibited a surface morphological change. Interestingly, the **DGNCF** retains the original structural features of **CF** without apparent surface cracks or flaws, demonstrating the effectiveness of the TASA process. This preservation of structural integrity ensures the retention of the fabrics' inherent properties, such as breathability, softness, flexibility, and stretchability.

From the XRD, UV, Fluorescence, and morphology analysis, it is clear that **DGN5a** is uniformly coated onto the **CF** by the TASA process and generated the **DGNCF** (**Figure 5.3c**).

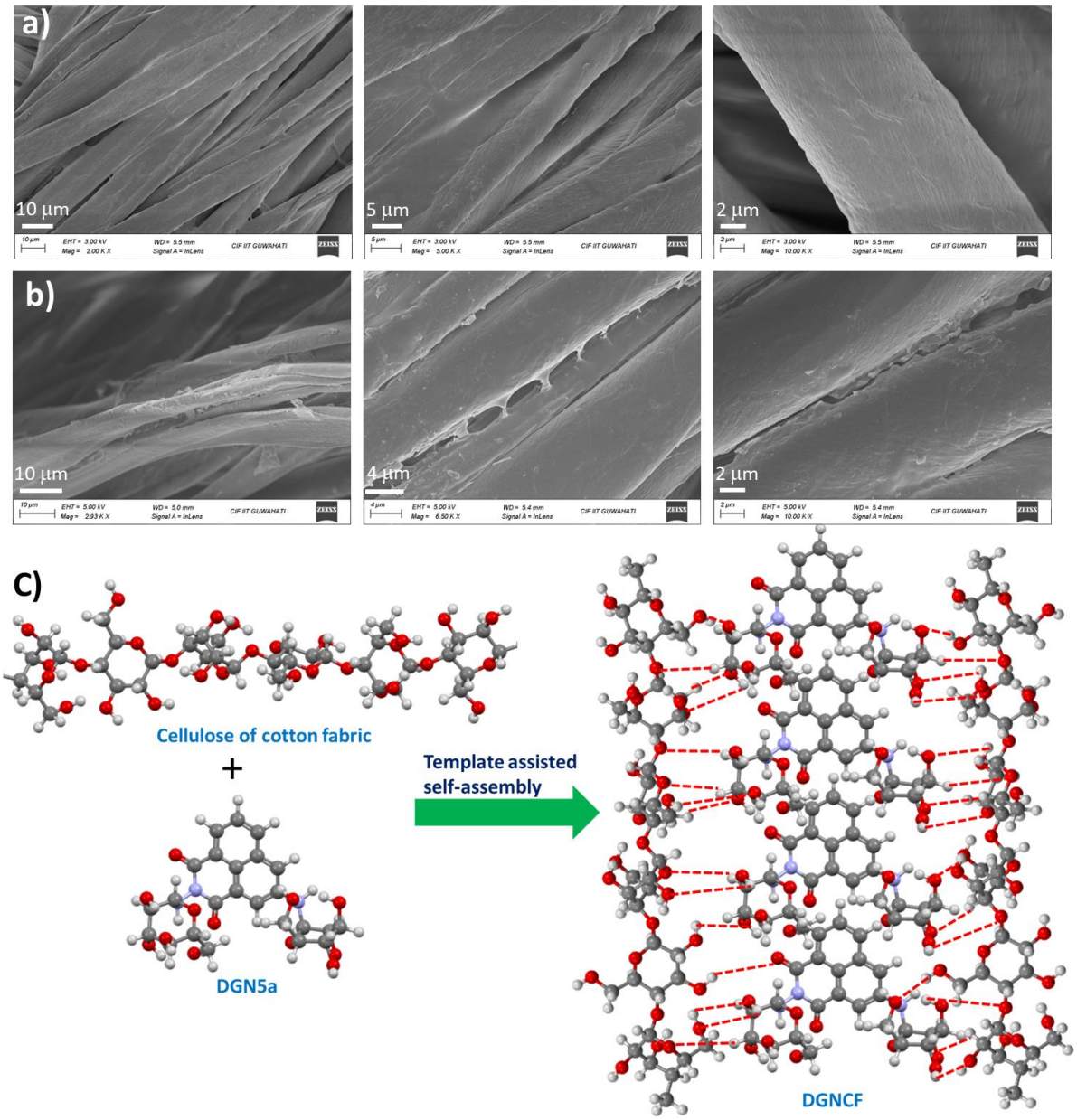


**Figure 5.3**. SEM images of the (a) CF, and (b) DGNCF at different magnifications. (c) A schematic representation of TASA of **DGN5a** on **CF** to generate **DGNCF**

TENG device fabrication and testing**: DGNCF** of 3x3 $cm^2$ was attached to the aluminium electrode using a conductive carbon tape for better adhesion and conductivity and FEP (fluorinated ethylene propylene) sheet was used as the opposite triboelectric layer. These two triboelectric layers were mounted on cardboard sheets and separated by sponge spacers to enable the TENG to function in vertical contact separation (VCS) mode (**Figure 5.4a**). To assess the performance of the TENG, the bottom, and top aluminium electrodes were connected with

two electrical wires and tested in vertical contact separation mode under hand-tapping. For optimization, various triboelectric layers, including Kapton, silicone polymer, PTFE, and PMMA, were also tested while keeping the DGNCF constant. The electrical outputs of the TENG device were measured using a digital storage oscilloscope (TBS-1102) and a low noise current preamplifier (SR 570). The long-term stability and durability of the **DGNCF**-TENG were evaluated over 10,000 cycles using an in-house built tapping machine.

**Figure 5.4b** shows the electrical responses ($V_{oc}$, $I_{sc}$) of the TENG with various opposing triboelectric layers, while keeping **DGNCF** layer constant, subjected to repeated hand-tapping force. Among the tested materials, the maximum voltage and current were observed for **DGNCF** paired with FEP, which was chosen for further studies. The area-dependent studies revealed an increase in output voltage and current with an increase in surface area **Figure 5.4c**. The TENG was able to produce an open-circuit voltage of 364 V and a short-circuit current of 113 μA. The differing responses of the TENG devices with different dielectric layer combinations can be attributed to the electron-accepting and donating properties of the materials in frictional contact.

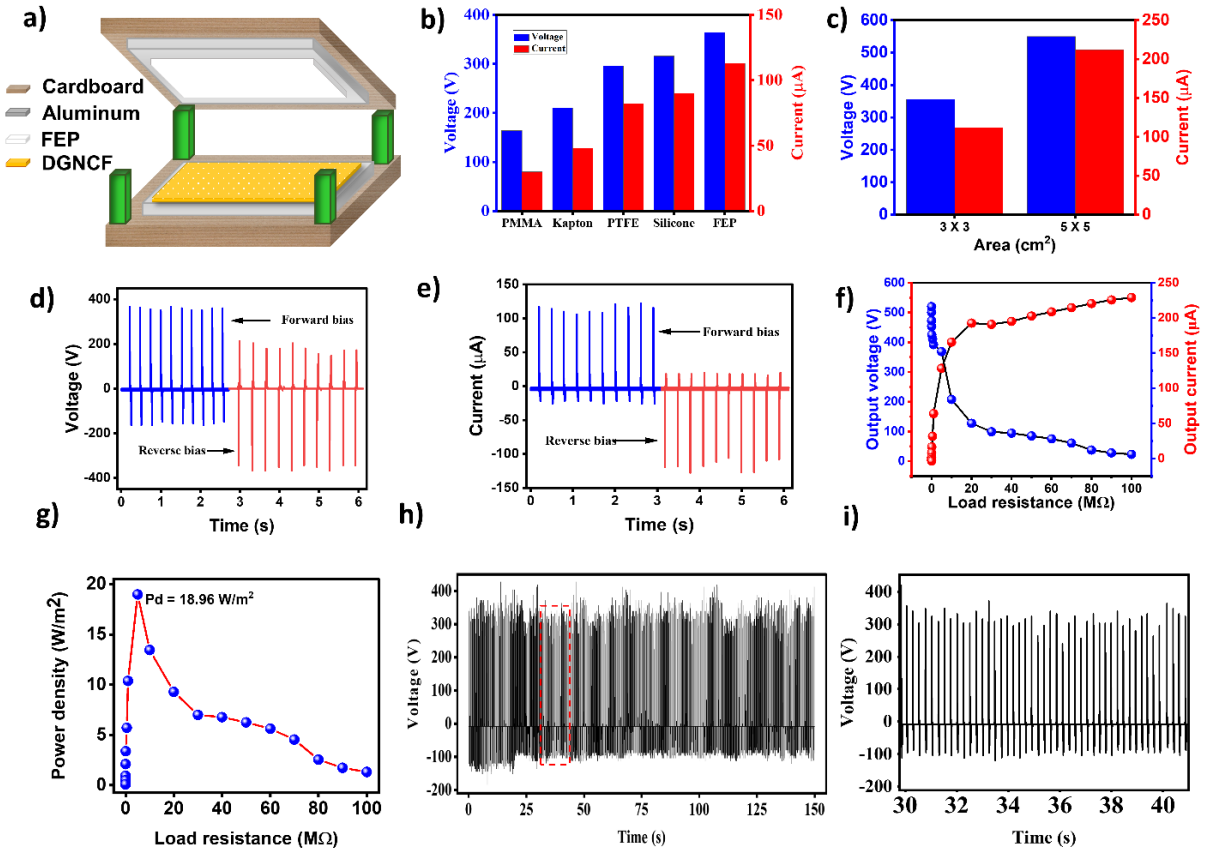


**Figure 5.4.** (a) Schematic representation of the fabricated TENG device. (b) TENG response of **DGNCF** with different frictional layers. (c) Area-dependent TENG response. (d-f) switching polarity results of (d) Voc, (e) Isc, (f) load resistance versus output voltage and current. (g) the instantaneous power density as a function of load resistance. (h,i) stability of TENG electrical response for 600 cycles of hand tapping.

The **DGNCF** acts as an electron donor due to its chemical bonding and surface characteristics as discussed in chapters 2-4. Consequently, the output is relatively low when the **DGNCF** is combined with another electron-donating material, such as PMMA. However, pairing the **DGNCF** with an electron-accepting material, like silicone rubber, PTFE, FEP significantly enhances the device's output, highlighting the electron-donating attribute of the **DGNCF**. **Figure 5.4c&d** illustrates the open-circuit voltage and short-circuit current graphs for both forward and reverse bias conditions. This polarity test confirms that the signal is generated solely from the TENG and not from any noise signal from the instrument. **Figure 5.4e** illustrates the variation of voltage and current output of the TENG at different load resistances. The voltage increases with load resistance and saturates after 10 MΩ, while the current decreases with load resistance and saturates after 10 MΩ. These observed load characteristics of the TENG align with findings in existing literature. The instantaneous power density of the TENG was calculated using the formula P = V * I / A, with results presented in **Figure 5.4f**. At a load resistance of 10 MΩ, the TENG achieves a maximum power density of 18.96 W/m², in accordance with the maximum power transmission theorem, indicating an impedance matching condition. The stability of the fabricated TENG is tested over 600 hand-tapping cycles ofand found to be stable **Figure 5.4h,i**. **Figure 5.5.** shows the schematic representation of a self-powered hydrogen production setup developed utilizing the fabricated TENG through water splitting. This innovative system harnesses mechanical energy from TENGs to drive the electrochemical decomposition of water into hydrogen and oxygen. The TENG converts mechanical motion into electrical energy, which is then used to electrolyze water without the need for external power sources. A DB 107 bridge rectifier was used to convert the AC signal from the TENG into DC. Notably, the TENG was able to produce hydrogen directly without the assistance of a capacitor. In this setup, the electrolyte used is 0.5M sulfuric acid ($H_2SO_4$).

The cathode consisted of a platinum electrode, where the reduction reaction occurs:

Cathode (Reduction): $2\ H^+_{(aq)} + 2\ e^- \rightarrow H_2\ (g)$

At the anode, a nickel foam electrode was employed, where the oxidation reaction takes place.

Anode (Oxidation): $2\ H_2O\ (l) \rightarrow O_2\ (g) + 4\ H^+_{(aq)} + 4\ e^-$

In this process, the addition of sulfuric acid ($H_2SO_4$) to water plays a crucial role in enhancing the overall efficiency and effectiveness of the system. $H_2SO_4$ dissociates into hydrogen ions ($H^+$) and sulphate ions ($SO_4^{2-}$) when dissolved in water, significantly increasing the solution's ionic conductivity. This enhanced conductivity facilitates the flow of electric current generated by the TENG through the electrolyte, which is essential for driving the electrochemical reactions involved in water splitting. The high concentration of $H^+$ ions provided by the $H_2SO_4$

is vital for the reduction reaction at the cathode, where hydrogen gas ($H_2$) is produced, thereby accelerating the reaction rate.

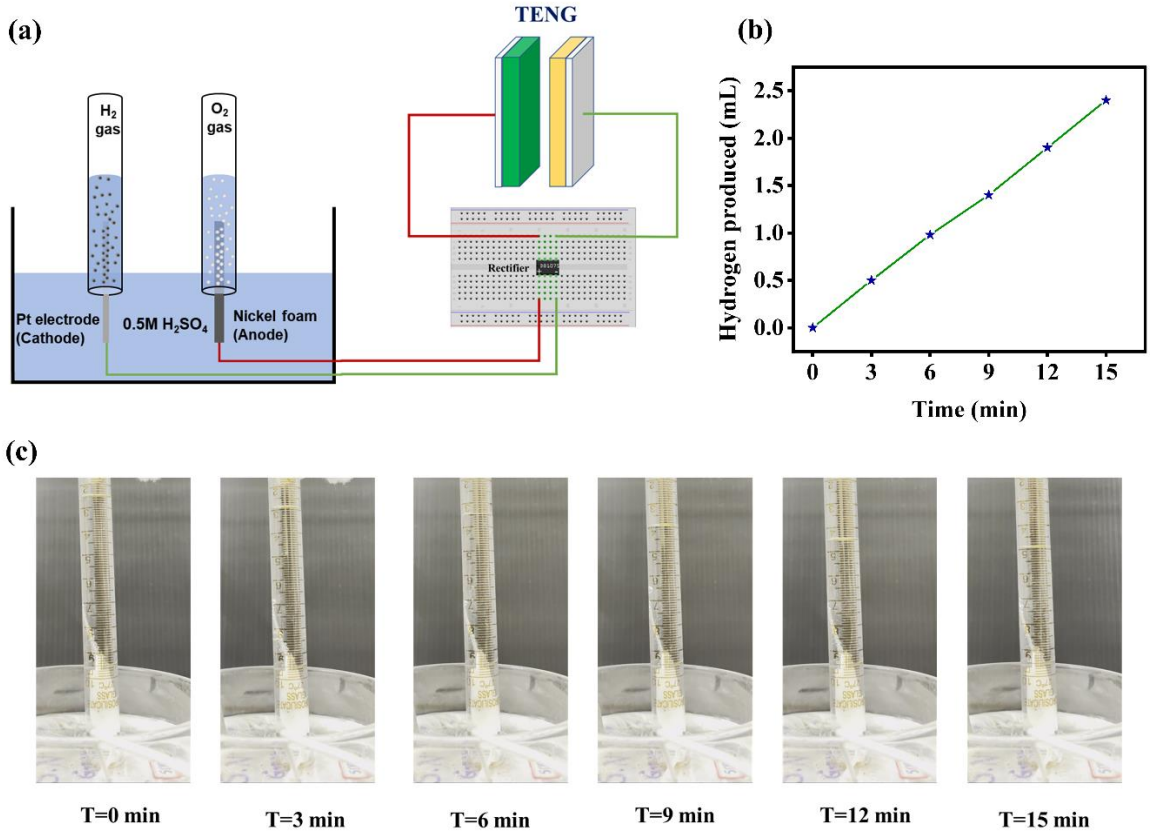


**Figure 5.5**. (a) Schematic representation of the self-powered electrochemical workstation for the Hydrogen evolution reaction utilizing the fabricated TENG. (b) Production of $H_2$ gas with respect to time.

The generated electrical energy from the TENG drives splitting water into hydrogen and oxygen. To measure the hydrogen production rate, the TENG was connected to a linear motor operating at a tapping frequency of 6 Hz. It was found that, under this machine tapping, the hydrogen production rate was determined to be ~ 173.4μL/min. **Figure 5.5b** displays the amount of hydrogen gas produced at the cathode as a function of time. Images of the production of $H_2$ gas with various time intervals is given in **Figure 5.5c**. The fixation of the fabricated TENG onto the mechanical devices performing a function can generate energy, even without a separate energy component for this operation. This report highlights the utility of the fabricated TENG in sustainable hydrogen production. This setup represents a significant advancement in clean energy technologies, offering a pathway towards efficient and environmentally friendly hydrogen generation.

## 5.3. Experimental Section

### 5.3.1. General Information

A detailed general information is given in Chapter 2.

### 5.3.2. General procedure for the synthesis diamino naphthalimide (9)

To a stirred solution of 3-nitro-1,8-napthalic anhydride **1** (1 mmol) in 5 mL of methanol, hydrazine hydrate **8** (2 mmol) was added and refluxed for 3h. After the completion of the reaction as identified by TLC, the reaction mixture is directly subjected to reduction using Fe powder in MeOH-HOAc and continued the reflux for 2h. After the completion of the reduction reaction, as identified using TLC, the reaction mixture was cooled to room temperature, neutralized with saturated $Na_2CO_3$ solution, and extracted with ethyl acetate. The organic layer was dried over $Na_2SO_4$ and the solvent was removed under reduced pressure using a rotary evaporator. A pure diamino-naphthalimides (**9**) was obtained as an amorphous yellow solid.

### 5.3.3. General procedure for the synthesis of diglycosyl naphthalimides (DGN5a-d))

To a stirred solution of diamino naphthalimide **9** (1.0 mmol) in MeOH (10 mL) was added monosaccharide **4a-d** (1.5 mmol) followed by $(NH_4)_2SO_4$ (0.1mmol). The reaction mixture was stirred at 65 ºC for 24h in an oil bath. During the progress of the reaction, a pale-yellow solid precipitated out was filtered and washed with cold methanol and recrystallized in ethanol

## 5.4. Characterization Data

**Diglucosyl naphthalimide (DGN5a):** Amorphous yellow solid; yield: 93% (0.768g); mp: 185 - 187 °C. IR (neat): 3261, 2881, 1696, and 1623 $cm^{-1}$. $^1H$ NMR (400 MHz, DMSO-$d_6$) δ 8.15

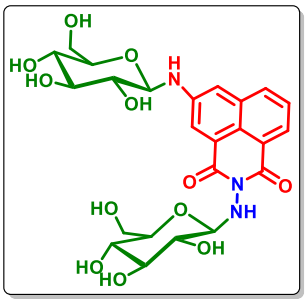


(m, 2H), 8.10 (d, $J$ = 2.4 Hz, 1H), 7.69 (t, $J$ = 7.6 Hz, 1H), 7.47 (d, $J$ = 2.0 Hz, 1H), 7.24 (d, $J$ = 7.6 Hz, 1H), 6.58 (d, $J$ = 7.6 Hz, 1H), 5.05 (d, $J$ = 4.8 Hz, 1H), 5.02 – 4.96 (m, 4H), 4.89 (d, $J$ = 4.8 Hz, 1H), 4.58 (t, $J$ = 7.8 Hz, 1H), 4.49 (t, $J$ = 6.0 Hz, 1H), 4.33 (t, $J$ = 8.0 Hz, 1H), 4.13 (t, $J$ = 5.4 Hz, 1H), 3.77 – 3.68 (m, 1H), 3.55 – 3.45 (m, 2H), 3.30 – 3.15 (m, 7H), 3.06 – 2.98 (m, 2H). $^{13}C$ NMR (100 MHz, DMSO-$d_6$) δ 162.45, 162.24, 146.33, 133.40, 132.42, 127.17, 126.44, 122.43, 122.15, 121.76, 120.63, 111.30, 88.86, 84.74, 78.29, 77.76, 77.54, 77.01, 73.08, 72.86, 70.26, 70.09, 61.16, 60.88. HRMS (ESI, m/z): $[M+Na]^+$ calcd. for $C_{24}H_{29}N_3O_{12}$: 574.1651; found: 574.1651.

**Dimannosyl naphthalimide (DGN5b):** Amorphous yellow solid; yield: 90% (0.743 g); mp: 177 - 179 °C. IR (neat): 3261, 2880, 1695, and 1623 $cm^{-1}$. $^1H$ NMR (400 MHz, DMSO-$d_6$) δ

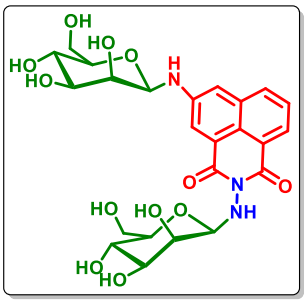

8.17 – 8.13 (m, 2H), 8.11 (d, $J$ = 2.4 Hz, 1H), 7.69 (t, $J$ = 7.6 Hz, 1H), 7.47 (d, $J$ = 2.0 Hz, 1H), 7.23 (d, $J$ = 8.0 Hz, 1H), 6.58 (d, $J$ = 7.6 Hz, 1H), 5.04 (d, $J$ = 4.4 Hz, 1H), 4.99 – 4.95 (m, 4H), 4.88 (d, $J$ = 4.8 Hz, 1H), 4.58 (t, $J$ = 8.0 Hz, 1H), 4.48 (t, $J$ = 5.8 Hz, 1H), 4.33 (t, $J$ = 7.8 Hz, 1H), 4.11 (t, $J$ = 5.0 Hz, 1H), 3.72 – 3.68 (m, 1H), 3.55 – 3.49 (m, 2H), 3.37 (d, $J$ = 2.0 Hz, 1H),3.29 – 3.20 (m, 6H), 3.05 – 2.98 (m, 2H). $^{13}C$ NMR (100 MHz, DMSO-$d_6$) δ 162.43, 162.28, 146.33, 133.40, 132.42, 127.17, 126.44, 122.43, 122.15, 121.76, 120.63, 111.30, 88.86, 84.74, 78.29, 77.76, 77.54, 77.01, 73.08, 72.86, 70.26, 70.09, 61.16, 60.88. HRMS (ESI, m/z): $[M+Na]^+$ calcd. for $C_{24}H_{29}N_3O_{12}$: 574.1651; found: 574.1650.

**Dixylosyl naphthalimide (DGN5c):** Amorphous yellow solid; yield: 89% (0.655 g); mp: 180 - 182 °C. IR (neat): 3260, 2881, 1695, and 1623$cm^{-1}$. $^1H$ NMR (400 MHz, DMSO-$d_6$) δ 8.18 –

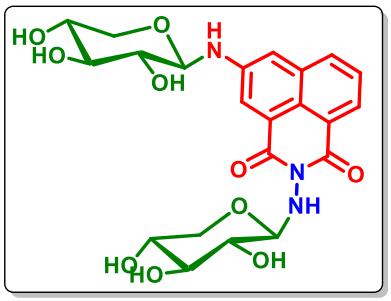

8.14 (m, 2H), 8.07 (dd, $J$ = 5.0, 2.2 Hz, 1H), 7.68 (td, $J$ = 7.8, 2.6 Hz, 1H), 7.46 (d, $J$ = 6.8 Hz, 1H), 7.22 (t, $J$ = 9.2 Hz, 1H), 6.73 (d, $J$ = 7.6 Hz, 1H), 5.75 (s, 1H), 5.17 (d, $J$ = 4.0 Hz, 1H), 5.10 (d, $J$ = 4.4 Hz, 1H), 5.07 (d, $J$ = 4.4 Hz, 1H), 5.04 – 5.02 (m, 2H), 4.97 (d, $J$ = 4.8 Hz, 1H), 4.58 – 4.53 (m, 1H), 4.34 (t, $J$ = 7.4 Hz, 1H), 3.74 – 3.68 (m, 2H), 3.57 – 3.52 (m, 1H), 3.30 (s, 1H), 3.26 – 3.20 (m, 4H), 2.95 (t, $J$ = 9.8 Hz, 1H). $^{13}C$ NMR (100 MHz, DMSO-$d_6$) δ 161.93, 161.79, 146.05, 133.63, 133.00, 127.68, 127.07, 122.61, 122.43, 121.84, 120.86, 112.69, 85.72, 82.52, 74.39, 74.17, 71.39, 69.21, 68.50, 67.42, 67.01, 65.09. HRMS (ESI, m/z): $[M+Na]^+$ calcd. for $C_{22}H_{25}N_3O_{10}$: 514.1440; found: 514.1438.

**Dilyxosyl naphthalimide (DGN5d):** Amorphous yellow solid; yield: 87% (0.640 g); mp: 184 - 186 °C. IR (neat): 3260, 2881, 1695, and 1623$cm^{-1}$. $^1H$ NMR (400 MHz, DMSO-$d_6$) δ 8.18 –

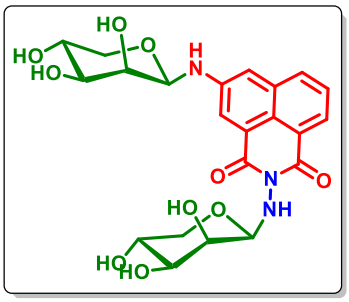

8.14 (m, 3H), 7.69 (t, $J$ = 7.8 Hz, 1H), 7.52 (d, $J$ = 2.4 Hz, 1H), 7.14 (d, $J$ = 11.2 Hz, 1H), 6.90 (d, $J$ = 8.8 Hz, 1H), 5.11 (d, $J$ = 5.6 Hz, 1H), 5.02 (d, $J$ = 4.8 Hz, 1H), 4.99 – 4.95 (m, 3H), 4.89 (d, $J$ = 4.8 Hz, 1H), 4.78 (d, $J$ = 4.8 Hz, 1H), 4.66 (d, $J$ = 11.2 Hz, 1H), 3.89 – 3.85 (m, 2H), 3.76 – 3.72 (m, 1H), 3.64 – 3.58 (m, 3H), 3.52 – 3.47 (m, 2H), 3.27 (t, $J$ = 8.6 Hz, 1H), 2.82 (t, J = 9.6Hz, 1H). $^{13}C$ NMR (100 MHz, DMSO-$d_6$) δ 161.95, 161.80, 146.05, 133.65, 133.00, 127.68, 127.07,

122.61, 122.43, 121.84, 120.86, 112.69, 85.72, 82.52, 74.39, 74.17, 71.39, 69.21, 68.50, 67.42, 67.01, 65.09. HRMS (ESI, m/z): $[M+Na]^+$ calcd. for $C_{22}H_{25}N_3O_{10}$: 514.1440; found: 514.1442.

## 5.5. Conclusion

A series of diglycosyl naphthalimides (DGNs) were synthesized using environmentally friendly chemical processes in good yields. A flexible DGNCF fabric is generated by template-assisted self-assembly of DGN onto the cotton fabric. The flexible DGNCF displayed potential in the fabrication of TENG, which produces a significant potential, enabling the operation of self-powered electronic devices. Using the fabricated TENG, self-powered hydrogen production from water is demonstrated.

## 5.6. References


1. M. Germer, U. Marschner and A. Richter, *IEEE Internet Things J.*, 2022, **9**, 7700–7714.
2. R. De Fazio, M. De Giorgi, D. Cafagna, C. Del-Valle-Soto and P. Visconti, *Energies*, 2023, **16**, 3016.
3. Z. L. Wang, *ACS Nano*, 2013, **7**, 9533–9557.
4. F. R. Fan, W. Tang and Z. L. Wang, *Adv. Mater.*, 2016, **28**, 4283–4305.
5. C. Wu, A. C. Wang, W. Ding, H. Guo and Z. L. Wang, *Adv. Energy Mater.*, 2019, **9**, 1802906.
6. S. Wang, L. Lin and Z. L. Wang, *Nano Lett.*, 2012, **12**, 6339–6346.
7. T. Liu, M. Liu, S. Dou, J. Sun, Z. Cong, C. Jiang, C. Du, X. Pu, W. Hu and Z. L. Wang, *ACS Nano*, 2018, **12**, 2818–2826.
8. Z. Lin, B. Zhang, H. Guo, Z. Wu, H. Zou, J. Yang and Z. L. Wang, *Nano Energy*, 2019, **64**, 103908.
9. D. Zhang, Z. Xu, Z. Yang and X. Song, *Nano Energy*, 2020, **67**, 104251..
10. X. Liang, T. Jiang, G. Liu, Y. Feng, C. Zhang and Z. L. Wang, *Energy Environ. Sci.*, 2020, **13**, 277–285.
11. W. Xu, L.-B. Huang, M.-C. Wong, L. Chen, G. Bai and J. Hao, *Adv. Energy Mater.*, 2017, **7**, 1601529.
12. Y. Wang, Y. Yang and Z. L. Wang, *npj Flex. Electron*, 2017, **1**, 10.
13. X. Ding, H. Cao, X. Zhang, M. Li and Y. Liu, *Sensors,* 2018, **18**, 1713.
14. W. Yang, H. Chen, M. Wu, Z. Sun, M. Gao, W. Li, C. Li, H. Yu, C. Zhang, Y. Xu, Y. Xu

and J. Wang, *Adv. Mater. Interfaces*, 2022, **9**, 2102124..

15. Z. Sun, H. Chen, M. Wu *et al*., *Materials*, 2022, **15**, 6770.
16. D. Yan, D. Tao, D. Xu, Y. Sun, B. Deng, G. Cao, J. Fang and W. Xu, *Nano Energy*, 2024, 129, 110000.
17. N. S. Lewis and D. G. Nocera, *Proc. Natl. Acad. Sci.*, 2006, **103**, 15729–15735.
18. M. R. Shaner, H. A. Atwater, N. S. Lewis and E. W. McFarland, *Energy Environ. Sci.*, 2016, **9**, 2354–2371.
19. A. Nikkhah, B. Emadi, H. Soltanali, S. Firouzi, K. A. Rosentrater and M. S. Allahyari, *J. Clean. Prod.*, 2016, **137**, 843–849.
20. M. Luo, Y. Yi, S. Wang, Z. Wang, M. Du, J. Pan and Q. Wang, *Renew. Sustain. Energy Rev.*, 2018, **81**, 3186–3214.
21. J. R. Bartels, M. B. Pate and N. K. Olson, *Int. J. Hydrogen Energy*, 2010, **35**, 8371–8384.
22. A. Boretti, *Int. J. Hydrogen Energy*, 2010, **35**, 8417–8424.
23. L. Zhou, D. Liu, L. Liu, L. He, X. Cao, J. Wang and Z. L. Wang, *Research*, 2021, **2021**, 4673028.
24. N. Zhai, Z. Wen, X. Chen, A. Wei, M. Sha, J. Fu, Y. Liu, J. Zhong and X. Sun, *Adv. Energy Mater.*, 2020, **10**, 2001041.
25. S.-F. Leung, H.-C. Fu, M. Zhang, A. H. Hassan, T. Jiang, K. N. Salama, Z. L. Wang and J.-H. He, *Energy Environ. Sci.*, 2020, **13**, 1300–1308.
26. X. Cao, Y. Jie, N. Wang and Z. L. Wang, *Adv. Energy Mater.*, 2016, **6**, 1600665.
27. G. Zhu, C. Pan, W. Guo, C.-Y. Chen, Y. Zhou, R. Yu and Z. L. Wang, *Nano Lett.*, 2012, **12**, 4960–4965.
28. Y. Quan, J. Zhu and G. Zheng, *Small Sci.*, 2021, **1**, 2100043.
29. J. Zhou, J. Li, X. Du and B. Xu, *Biomaterials*, 2017, **129**, 1–27.
30. P. S. Chauhan, V. Shrivastava and R. S. Tomar, *Turkish J. Pharm. Sci.*, 2018, **15**, 238–247.
31. R. Nagarkar, M. Singh, H. X. Nguyen and S. Jonnalagadda, *J. Drug Deliv. Sci. Technol.*, 2020, 59, 101923.
32. L. Li and G. Chen, *J. Am. Chem. Soc.*, 2022, **144**, 16232–16251.
33. A. Masudi, O. Muraza, N. W. C. Jusoh and U. Ubaidillah, *Environ. Sci. Pollut. Res.*, 2023, **30**, 14104–14125.
34. Y. Guo, X. Xu, Y. Shang and B. Gao, *Environ. Sci. Pollut. Res.*, 2018, **25**, 27982–27991.
35. L. C. Reyes-Alvarado, N. N. Okpalanze, E. R. Rene, E. Rustrian, E. Houbron, G. Esposito and P. N. L. Lens, *J. Environ. Manage.*, 2017, **200**, 407–415.
36. D. R. Jayasundara, T. Duff, M. D. Angione, J. Bourke, D. M. Murphy, E. M. Scanlan and P. E. Colavita, *Chem. Mater.*, 2013, **25**, 4122–4128.

37. S. Kubo, R. Demir-Cakan, L. Zhao, R. J. White and M.-M. Titirici, *ChemSusChem*, 2010, **3**, 188–194.
38. S. Gim, Y. Zhu, P. H. Seeberger and M. Delbianco, *Wiley Interdiscip. Rev. Nanomedicine Nanobiotechnology*, 2019, **11**, e1558.
39. R. Ahmad, Y. Deng, R. Singh, M. Hussain, M. A. A. Shah, S. Elingarami, N. He and Y. Sun, *J. Biomed. Nanotechnol.*, 2018, **14**, 20–43.
40. M. Izumi and H. Uzawa, *Trends Glycosci. Glycotechnol.*, 2005, **17**, 107–119.
41. L. Su, Y. Feng, K. Wei, X. Xu, R. Liu and G. Chen, *Chem. Rev.*, 2021, **121**, 10950–11029.
42. M. Alibolandi, M. Mohammadi, R. Teimouri, M. Babaei, J. Movaffagh and M. Ramezani, *Carbohydrate-based materials in tissue engineering applications*, 2021, vol. 2–2.
43. M. A. Khalilzadeh, S. Y. Kim, H. W. Jang, R. Luque, R. S. Varma, R. A. Venditti and M. Shokouhimehr, *Mater. Today Chem.*, 2022, **24**, 100869.
44. W. Wang, M. Gao, M. Cao, X. Liu, H. Yang and Y. Li, *Bioresour. Technol.*, 2021, 332, 125059.
45. R. K, V. K. S, P. Saravanan, R. Rajeshkannan, M. Rajasimman, H. Kamyab and Y. Vasseghian, *Environ. Res.*, 2024, **240**, 117521..
46. G. Wang, A. Chen, P. Aryal and J. Bietsch, *Org. Biomol. Chem.*, 2024, **22**, 5470–5510.
47. R. S. Bhadale and V. Y. Londhe, *J. Mater. Sci. Mater. Med.*, 2021, **32**, 89.
48. X. Cao, X. Du, H. Jiao, Q. An, R. Chen, P. Fang, J. Wang and B. Yu, *Acta Pharm. Sin. B*, 2022, **12**, 3783–3821.
49. D. Kolosov, V. Adamovich, P. Djurovich, M. E. Thompson and C. Adachi, *J. Am. Chem. Soc.*, 2002, **124**, 9945–9954.
50. J.-A. Gan, Q. L. Song, X. Y. Hou, K. Chen and H. Tian, *J. Photochem. Photobiol. A Chem.*, 2004, **162**, 399–406.
51. J. Liu, G. Tu, Q. Zhou, Y. Cheng, Y. Geng, L. Wang, D. Ma, X. Jing and F. Wang, *J. Mater. Chem.*, 2006, **16**, 1431–1438.
52. S. Chen, P. Zeng, W. Wang, X. Wang, Y. Wu, P. Lin and Z. Peng, *J. Mater. Chem. C*, 2019, **7**, 2886–2897.
53. M. Poddar, G. Sivakumar and R. Misra, *J. Mater. Chem. C*, 2019, **7**, 14798–14815.
54. Y. Qin, G. Li, T. Qi and H. Huang, *Mater. Chem. Front.*, 2020, **4**, 1554–1568.
55. T. Gunnlaugsson, M. Glynn, G. M. Tocci (née Hussey), P. E. Kruger and F. M. Pfeffer, *Coord. Chem. Rev.*, 2006, **250**, 3094–3117.
56. X. Chen, T. Pradhan, F. Wang, J. S. Kim and J. Yoon, *Chem. Rev.*, 2012, **112**, 1910–1956.

# 5.7. Selected NMR ($^{1}$H & $^{13}$C), and Mass spectra

$^{1}$H NMR Spectrum of DGN5a (400 MHz, DMSO-$d_6$)

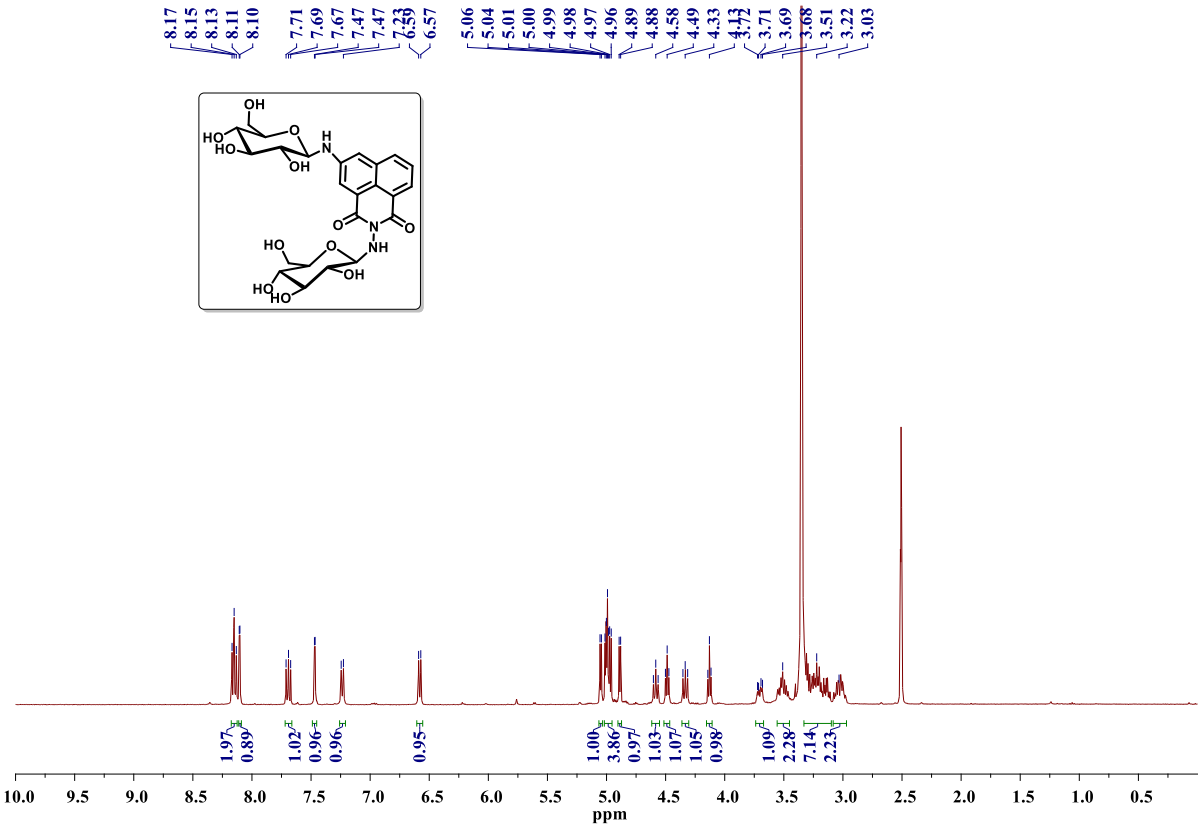


$^{13}$C NMR Spectrum of DGN5a (100 MHz, DMSO-$d_6$)

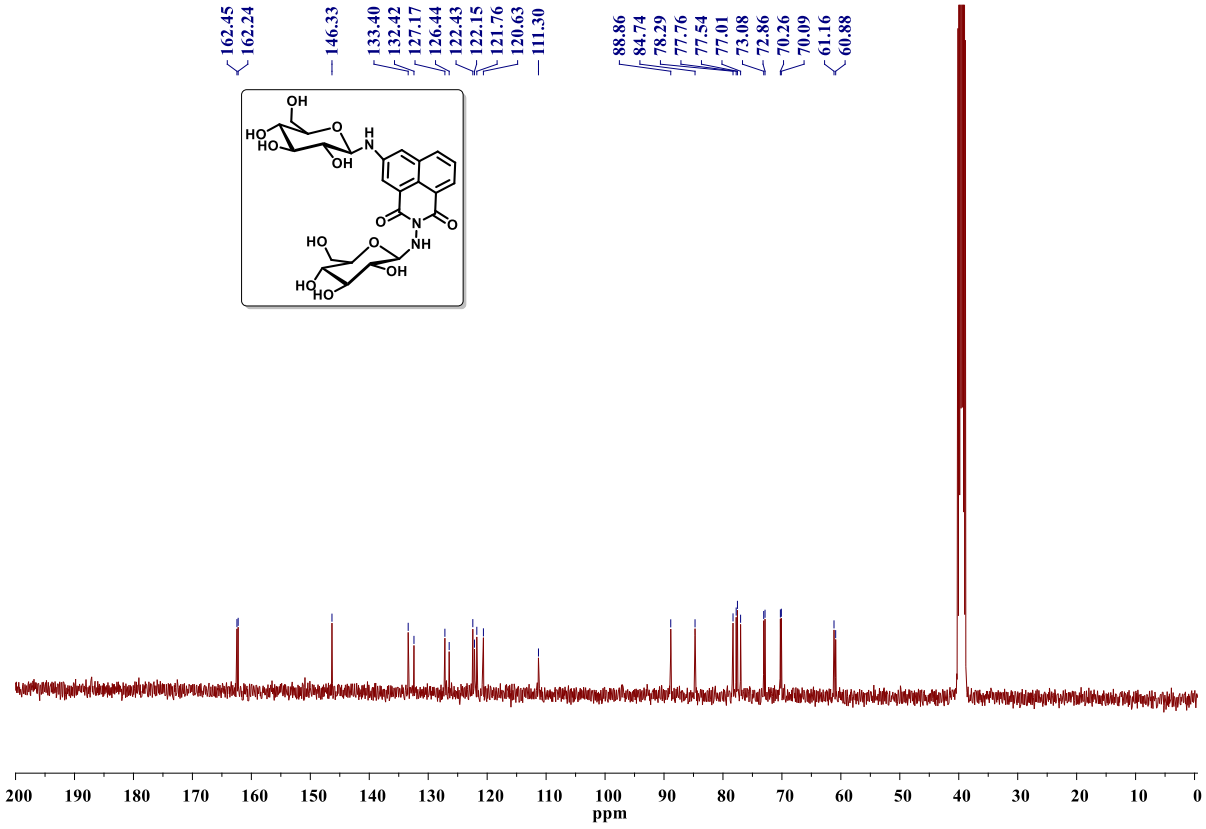

## HRMS spectrum of DGN5a

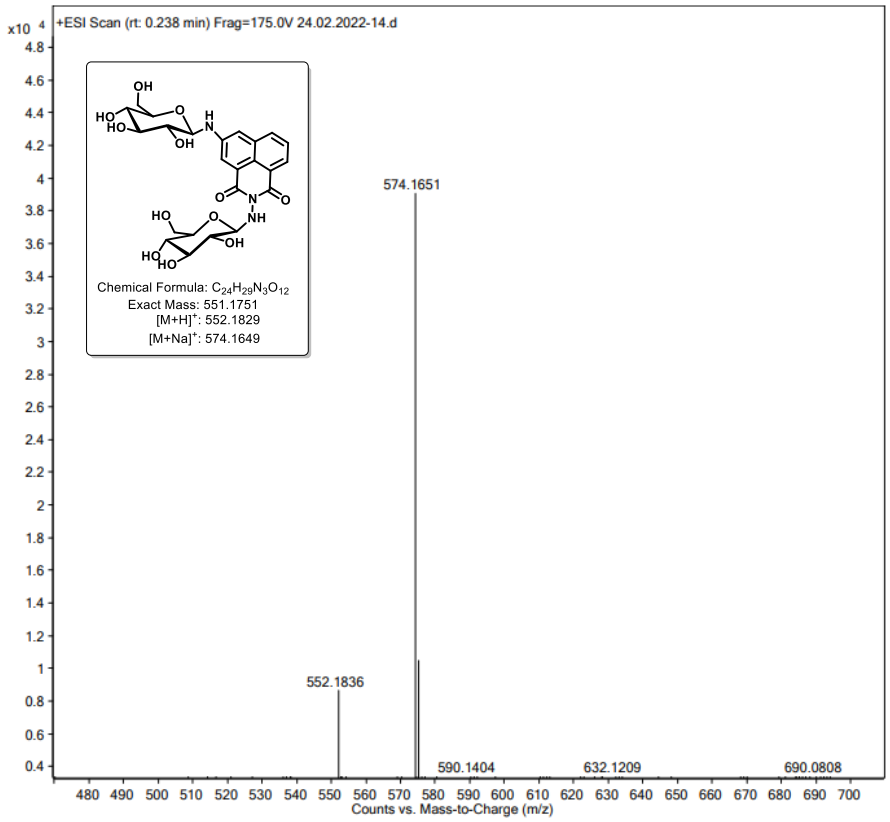


## $^1$H NMR Spectrum of DGN5c (400 MHz, DMSO-$d_6$)

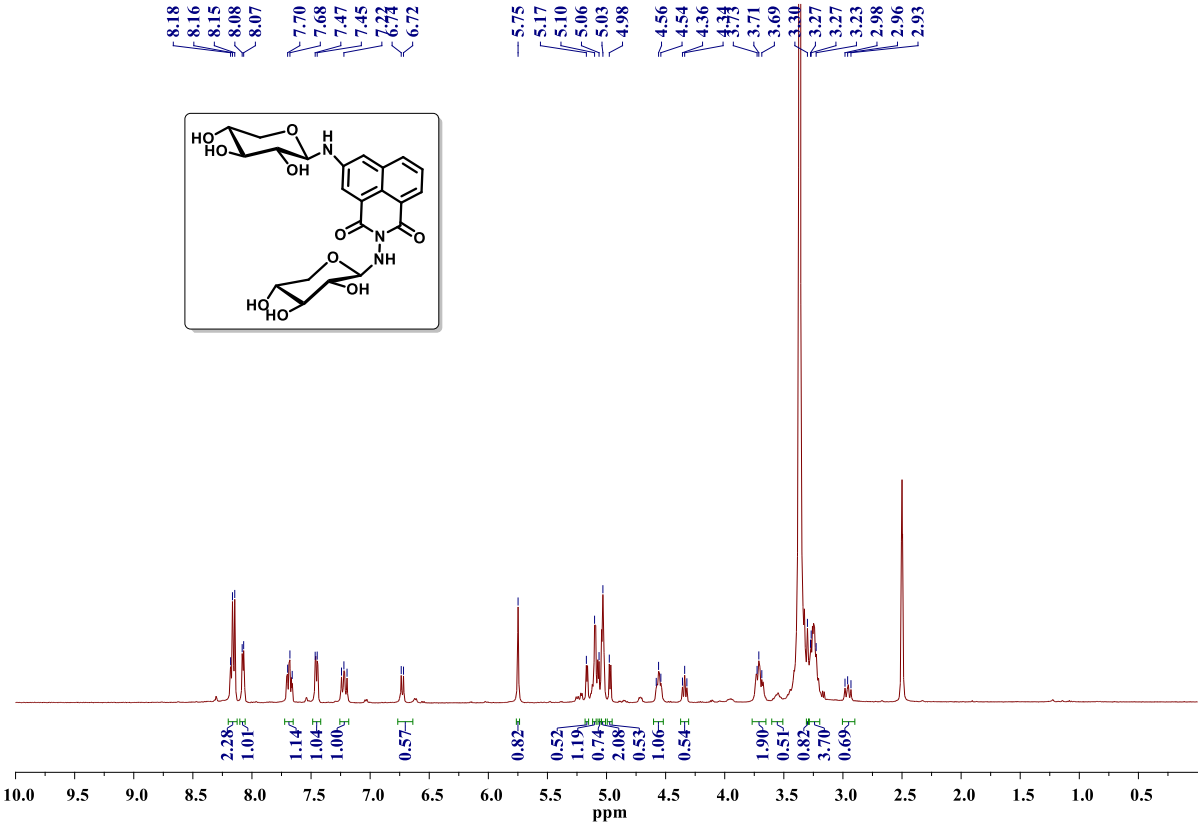

**Deuterium exchange $^{1}$H NMR Spectrum of DGN5c (400 MHz, DMSO-$d_6$)**

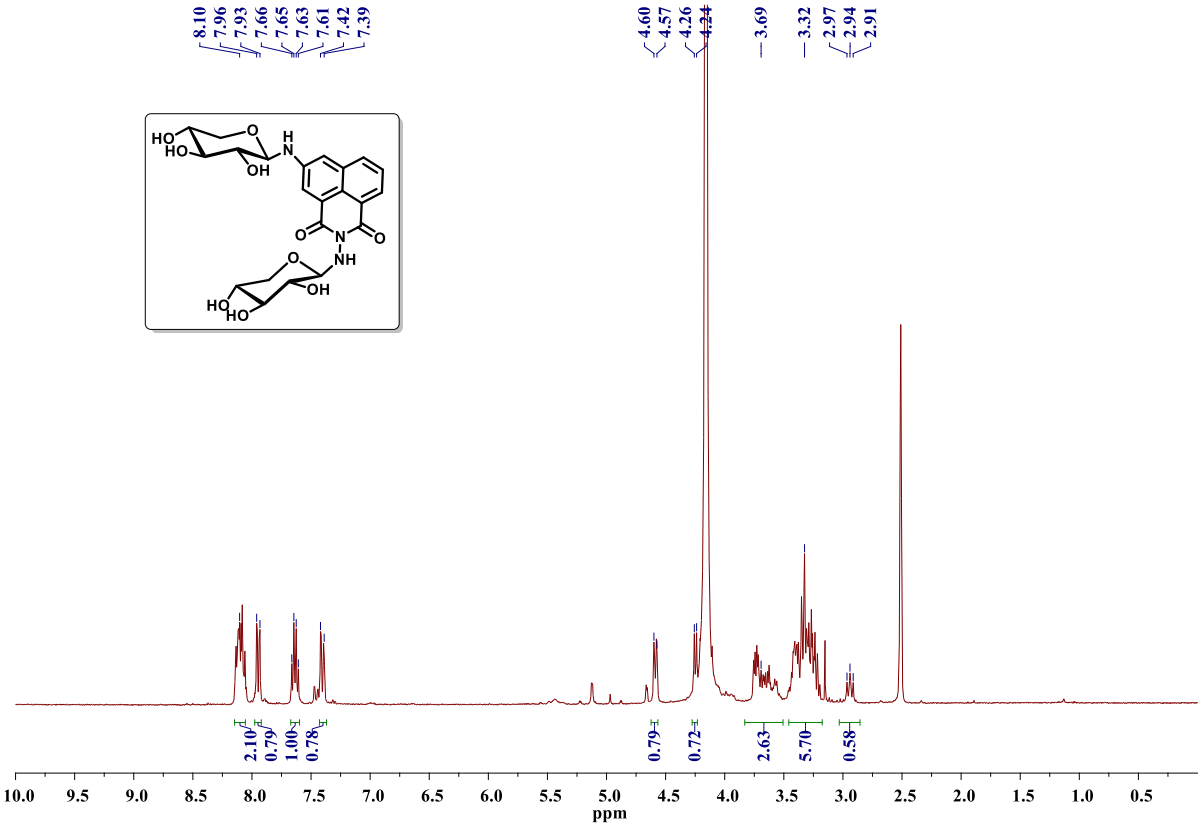


**$^{13}$C NMR Spectrum of DGN5c (100 MHz, DMSO-$d_6$)**

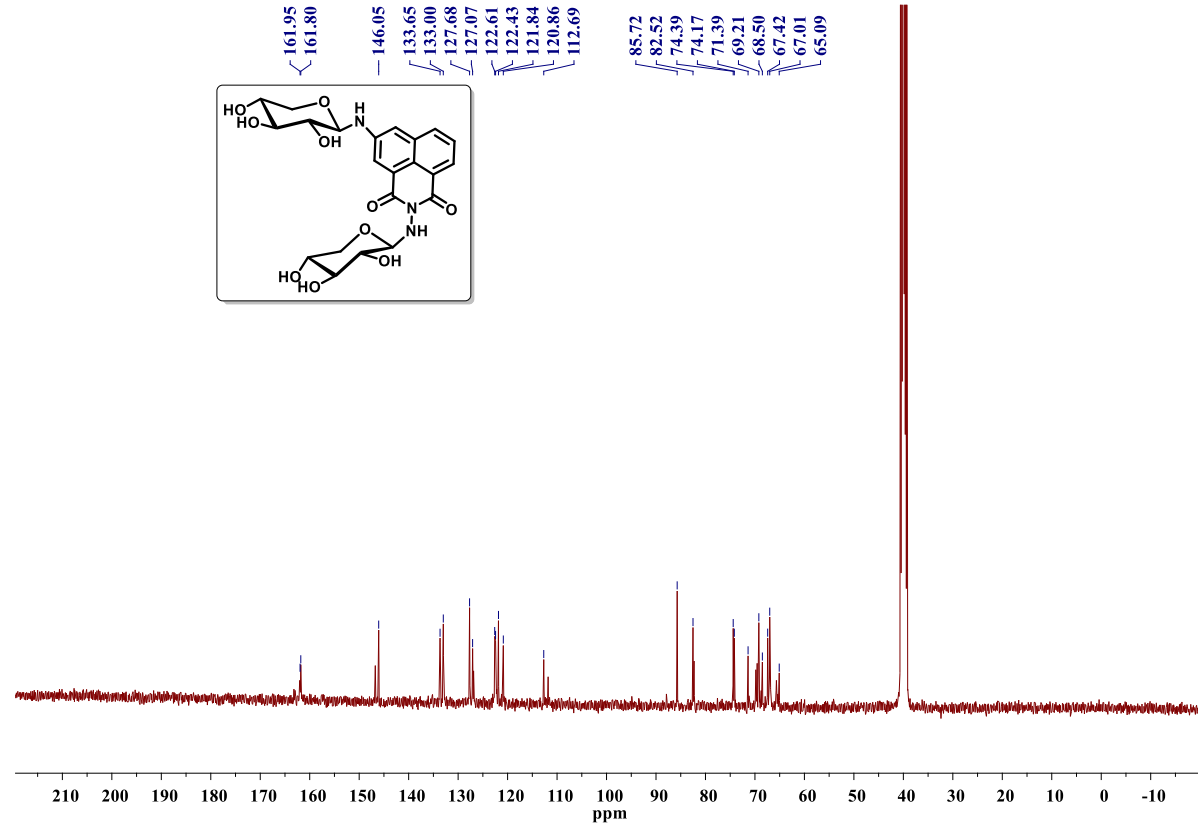

## HRMS spectrum of DGN5c

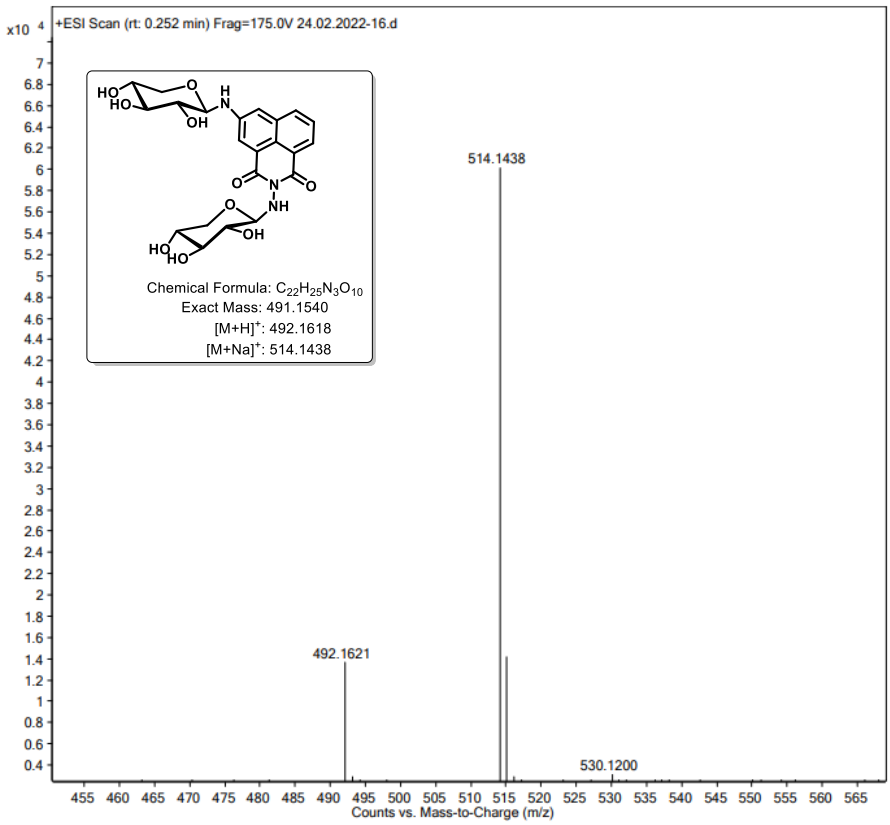

# SUMMARY

A series of carbohydrate naphthalimide derivatives were synthesized using environmentally benign protocols and studied its self-assembly. Self-assembled carbohydrate naphthalimides displayed potential in the fabrication of flexible semiconductors and triboelectric nanogenerators (TENG). A remarkable effect in electronics could be arrived at by a fine-tuning of the molecular structure.

# SCOPE FOR FUTURE WORK

Further investigation of self-assembled carbohydrate naphthalimide scaffolds could render scientific knowledge on the molecular aspect of assembled organic materials. The development of molecular-level concepts in assembled materials can deliver optoelectronic devices, organic LEDs, bioelectronics, fluorescent sensors, Anticancer agents, and drug-delivery systems.

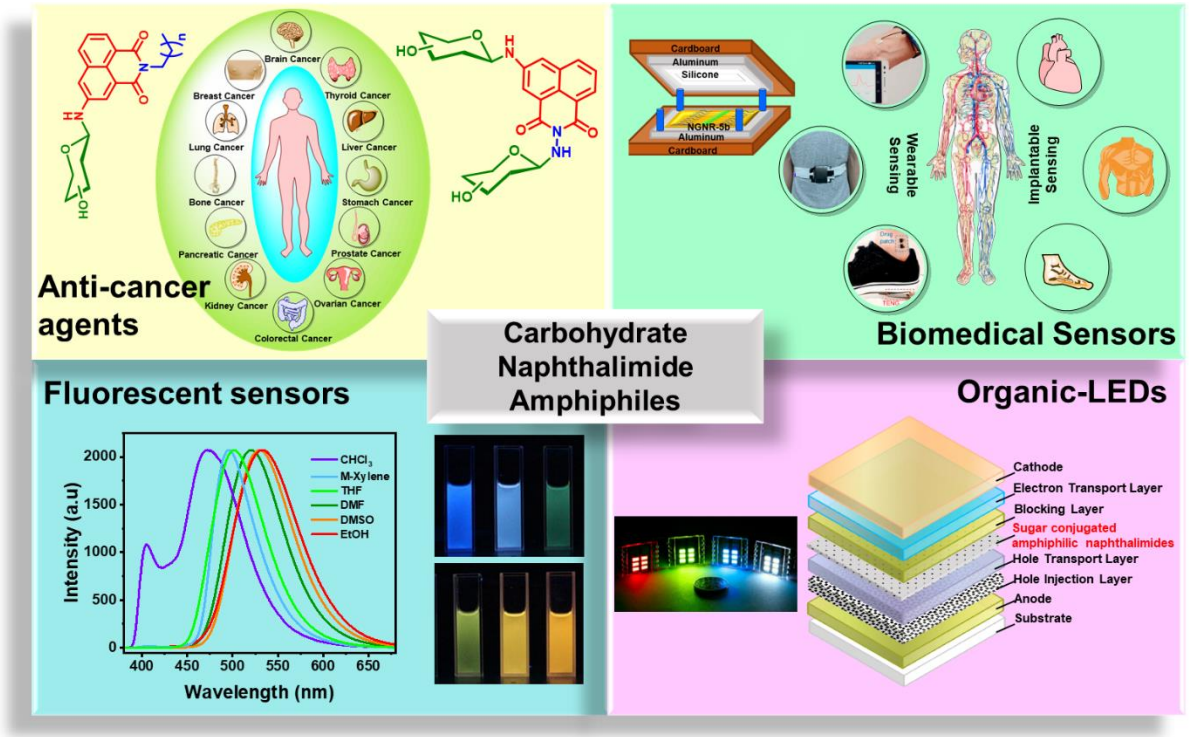

# APPENDICES

# List of Publications

1. **A high performance triboelectric nanogenerator using assembled sugar naphthalimides for self-powered electronics and sensors**

   **R. Arun Kumar**, M. Navaneeth, T. Banoo, Deepshikha, V. Prasad Rebaka, Y. Kumar, R. Kumar Rajaboina and S. Nagarajan*, ***Chem. Eng. J.*, 2024, 490, 151800**.

2. **Electronically Robust Self-Assembled Supramolecular Gel as a Potential Material in Triboelectric Nanogenerators**

   **R. Arun Kumar**, S. Potu, V. P. Rebaka, T. Banoo, Y. Kumar, C. U. Maheswari, V. Sridharan, R. K. Rajaboina and S. Nagarajan*, ***Chem. – A Eur. J.*, 2023, 29, e202301076**.

3. **A facile synthesis of amphiphilic *N*-glycosyl naphthalimides and fabrication of flexible**
   **semiconductors using molecular self-assembly**

   **R. Arun Kumar**, V. P. Rebaka, Tohira Banoo, Ravinder Pawar, Mohmmad Faizan, Krishnamoorthy Lalitha, and Subbiah Nagarajan*. ***Green Chem.*, 2022, 24, 2451-2463.**

4. **Facile Synthesis and Self-Assembly of Pharmaceutically Important Oligobenzylidine-D-Sorbitol Dialdehydes: Direct Encapsulation and Stimuli Responsive Delivery of $H_2S$.**

   V. P. Rebaka, Y. Kumar, T. Banoo, **R. Arun Kumar**, and S. Nagarajan*, ***Mater. Adv., 2024, 5, 5471-5481***.

5. **Regioselective synthesis of 4-arylamino-1, 2-naphthoquinones in eutectogel as a confined reaction medium using LED light**

   R. Vara Prasad, Y. Kumar, **R. Arun Kumar**, T. Banoo and S. Nagarajan*, ***Org. Biomol. Chem*., 2024, 22, 3876–3881**.

6. **Self-assembling nanoarchitectonics of twisted nanofibers of fluorescent amphiphiles as chemo-resistive sensor for methanol detection**

   V. Singh, A. Thamizhanban, K. Lalitha, D. K. Subbiah, **R. Arun Kumar**, V. P. Rebaka, T. Banoo, Y. Kumar, V. Sridharan, A. Ahmad, U. Maheswari Chockalingam, J. B. Balaguru Rayappan, A. A. Khan and S. Nagarajan*, ***Gels* 2023, 9, 442**.

7. **Hybrid hydrogels derived from renewable resources as a smart stimuli responsive soft material for drug delivery application**

   Vandana Singh, Yadavali Siva Prasad, **R. Arun Kumar**, Vara Prasad Rebaka, Tohira Banoo, C. Uma Maheswari, Vellaisamy Sridharan, Krishnamoorthy Lalitha, and Subbiah Nagarajan*. ***RSC Adv.*, 2022, 12, 2009-2018**.

8. **Supramolecular gels of gluconamides derived from renewable resources: Antibacterial and anti-biofilm applications**

   Yadavali Siva Prasad, S. Manikandan, Krishnamoorthy Lalitha, Miryala Sandeep, R. Vara Prasad, **R. Arun Kumar**, C.S. Srinandan, C. Uma Maheswari, Vellaisamy Sridharan, Subbiah Nagarajan*. ***Nano Select*, 2020, 1, 510– 524**.

9. **Glycolipid-Based Oleogels and Organogels: Promising Nanostructured Structuring Agents**

   Ayyapillai Thamizhanban, Srikanth Balaji, Krishnamoorthy Lalitha, Yadavali Siva Prasad, R. Vara Prasad, **R. Arun Kumar**, C. Uma Maheswari, Vellaisamy Sridharan, and Subbiah Nagarajan*. ***J. Agric. Food Chem*., 2020, 68, 50, 14896–14906.**

## Book Chapters:

1. **Anti-biofilm activities against food pathogens**

   **R. Arun Kumar**, Rebaka Vara Prasad, Subbiah Nagarajan*, Applications of Next Generation Biosurfactants in the Food Sector, **Elsevier, 2023, 479-508**.

2. **Sophorolipids and rhamnolipids as a biosurfactant: Synthesis and applications**

   Rebaka Vara Prasad, **R. Arun Kumar**, Devendra Sharma, Atul Sharma, Subbiah Nagarajan*. Green Sustainable Process for Chemical and Environmental Engineering and Science, **Elsevier,2021, Pages 423-472**.

3. **State of the Art and New Perspectives in Oleogels and Applications**

   Vara Prasad Rebaka, **R. Arun Kumar**, Srishti Batra, Nagarajan Subbiah*, Sustainable Green Chemical Processes and their Allied Applications. Nanotechnology in the Life Sciences. **Springer, Cham, 2020, Pages 151-182**.

## Patent:

1. **Synthesis of amphiphilic *N*-glycosyl naphthalimides and fabrication of flexible semiconductors using molecular self-assembly**

**R. Arun Kumar**, Nagarajan Subbiah. **IN Patent** 524,613.

## Manuscripts Under Preparation:

1. **From Sugars to Hydrogen: Harnessing the Power of Triboelectric Nanogenerator Using Assembled-Sugar Naphthalimides for Hydrogen Production**

   **R. Arun Kumar**, Nagarajan Subbiah

**List of International and National Conferences Attended**

1. Presented Poster in International Conference on **Innovations in Materials Science** and Workshop on Characterization Techniques (I-MAT-2024), during April 24-27, 2024, organized by IIT Roorkee, Uttarakhand.
2. Presented Poster in International Conference on **Chemistry and Applications of Soft Materials (CASM-2022)**, during 25-27$^{th}$ July 2022, organized by CSIR-NIIST, Thiruvananthapuram.
3. Participated in three day online International Conference on "**Conventional and Digital Methods in Chemical Education**", Organized by the Department of Chemistry, National Institute of Technology-Warangal, during 29$^{th}$-31$^{st}$ July 2021.
4. Participated in three day International Conference on A**dvances in Chemical Sciences and Technologies** organized by the Department of Chemistry, NIT-Warangal, held on 23$^{rd}$-25$^{th}$ September 2019.

**<u>Workshops and Webinars Attended</u>**

1. Online one-day workshop for faculty development program (FDP) on "**Atomically thin metal membrane: A computational study**" organized by the Department of Chemistry, National Institute of Technology, Warangal on 05$^{th}$ March 2022.
2. Online One-Day Faculty Development Workshop on "**Green Chemistry: A Solution for Sustainable Future** " organized by the Department of Chemistry, National Institute of Technology Warangal on 4$^{th}$ March, 2022.
3. "Teaching and Learning of **Green Chemistry: Nurturing a New Generation of Chemists**", Organized by the Department of Chemistry, National Institute of Technology-Warangal, from 26$^{th}$ Feb-3$^{rd}$ March 2021.
4. "Teaching and Learning of **NMR spectroscopy for Structure Determination**", Organized by the Department of Chemistry, National Institute of Technology-Warangal, from 19$^{th}$-24$^{th}$ February 2021.

## BRIEF BIOGRAPHY OF THE AUTHOR

**Mr. Rachamalla Arun Kumar** was born in Donipamula, Nalgonda district of Telangana State, India. He has completed his secondary school education in APSWRS Bhongir, and intermediate in Alpha Junior College, Nalgonda. After completing his B.Sc. (Osmania University), and M.Sc. (Organic Chemistry) from Mahatma Gandhi University, Nalgonda, he joined the Ph.D., program under the guidance of Dr. S. Nagarajan (Associate Professor), Department of Chemistry, National Institute of Technology Warangal with the financial assistance from the NITW, MoE in July 2019. He has published nine research articles in peer-reviewed international journals, one patent, and three book chapters. His research interest lies in the synthesis and self-assembly of organic molecules to generate functional organic materials for various applications.